

2023 Merck Research Grant

Green Hydrogen

Sponsored by Group Corporate Sustainability and Science & Technology Office

Science and technology are at the heart of everything we do, driving innovations that enable us to contribute to a sustainable future. **In this endeavor, we are seeking for research proposals in the field of Green Hydrogen.**

Progress is currently made in green hydrogen production, e.g.:

- innovative electrolysis technologies
- system and industrial integration of hydrogen technologies, e.g., storage, distribution and application areas
- fuel cell development

Submitted proposals should include a proof of concept (Technology Readiness Level 3) and describe the innovativeness of the proposal as well as the impact on the future implementation of green hydrogen supply to the chemical and pharmaceutical industry.

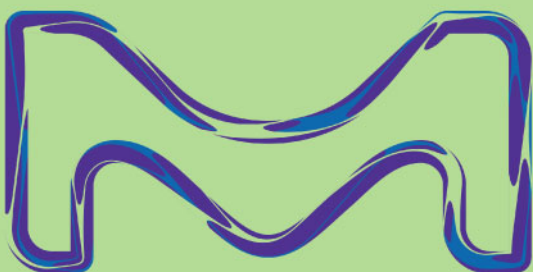


The best proposal will be awarded with one grant up to 200K € for one year with potential further collaboration

Apply now to become part of our green hydrogen journey!




Researchgrants.merckgroup.com



REVIEW

Metal-organic framework derived porous structures towards lithium rechargeable batteries

Sang A Han¹ | Hamzeh Qutaish¹ | Jong-Won Lee² | Min-Sik Park³ | Jung Ho Kim¹ 

¹Institute for Superconducting and Electronic Materials, Australian Institute for Innovative Materials, University of Wollongong, North Wollongong, New South Wales, Australia

²Department of Energy Science and Engineering, Daegu Gyeongbuk Institute of Science and Technology, Daegu, South Korea

³Department of Advanced Materials Engineering for Information and Electronics, Integrated Education Institute for Frontier Science & Technology (BK21 Four), Kyung Hee University, Yongin, South Korea

Correspondence

Jong-Won Lee, Department of Energy Science and Engineering, Daegu Gyeongbuk Institute of Science and Technology, 333 Techno Jungang-daero, Hyeonpung-eup, Dalseong-gun, Daegu 42988, South Korea.

Email: jongwon@gdinst.ac.kr

Min-Sik Park, Department of Advanced Materials Engineering for Information and Electronics, Integrated Education Institute for Frontier Science &

Abstract

Batteries are a promising technology in the field of electrical energy storage and have made tremendous strides in recent few decades. In particular, lithium-ion batteries are leading the smart device era as an essential component of portable electronic devices. From the materials aspect, new and creative solutions are required to resolve the current technical issues on advanced lithium (Li) batteries and improve their safety. Metal-organic frameworks (MOFs) are considered as tempting candidates to satisfy the requirements of advanced energy storage technologies. In this review, we discuss the

Abbreviations: 2-MIM, 2-methylimidazole; AAT, α 1-antitrypsin; ASSB, All solid-state battery; ATA, 2-aminoterephthalic acid; BDC, 1,4-benzenedicarboxylic acid or terephthalic acid; BHT, benzenehexathial; BP, 4,4'-bipyridine; BPDC, 4,4'-biphenyldicarboxylic acid; BSA, bovine serum albumin; BTB, 1,3,5-tris(4-carboxyphenyl)benzene; BTC, 1,3,5-benzenetricarboxylic acid; BZC, Bimetallic ZIF-derived carbon; CAU, Christian-Albrechts University; CB, carbon black; CE, Coulombic efficiency; CNT, carbon nanotube; CSUST, Changsha University of Science and Technology; CV, cyclic voltammetry; dace, trans-1,4-diaminocyclohexane; DEF, diethylformamide; DFT, density functional theory; diimpym, 4,6-di(1H-imidazol-1-yl)pyrimidine; DMF, dimethylformamide; DMSO, dimethyl sulfoxide; DNi, dimethylglyoxime nickel; dobdc, 1,4-dioxido-2,5-benzenedicarboxylate; EtOH, ethanol; FE-SEM, field emission scanning electron microscopy; FSS, Fish-scale structure; FTZB, 2-fluoro-4-(tetrazol-5-yl)benzoate; GF, glass fiber; GITT, galvanostatic intermittent titration technique; GO, graphene oxide; HDNC, hollow dodecahedral nanocages; HHTP, 2,3,6,7,10,11-hexahydroxytriphenylene; HITP, 2,3,6,7,10,11-hexaminitriphenylene; HKUST, Hong Kong University of Science and Technology; IL, ionic liquid; ILAG, ion-and-liquid assisted grinding; IRMOF, isoreticular MOF; KOH, potassium hydroxide; L1, 1,4-bis(imidazol-1-ylmethyl)benzene; L2, 1,1'-(1,4-butanediyl)bis(imidazole); L3, 1,1'-(1,4-hexanediyl)bis(imidazole); LAB, lithium air battery; LAG, liquid-assisted grinding; LAS, Lewis acid sites; LIB, lithium-ion battery; LiOH, lithium hydroxide; LiTFSI, lithium bis(trifluoromethylsulfonyl)imide; LMB, lithium-metal battery; LSB, lithium-sulfur battery; LSV, linear sweep voltammetry; MD, molecular dynamics; MeOH, methanol; MHN, metal hydroxide nanostrands; MIL, Materials of Institute Lavoisier; MOFs, metal-organic frameworks; NCW, N-doped carbon nanoweb; NDC, 1,2-benzenedicarboxylate; NG, neat grinding; NGA, N-doped graphene aerogel; NGN, N-doped graphene network; Nickel-MH, nickel-metal hydride; npta, 5-nitroisophthalic acid; oba, 4,4'-oxybisbenzoic acid; OCV, open-circuit voltage; OMS, open metal moieties; PAN, polyacrylonitrile; PBA, Prussian blue analogues; PCF, porous carbon framework; PCN, porous coordination network; PE, polyethylene; PEO, poly(ethylene oxide); PP, polypropylene; ppy, polypyrrole; PTFE, polytetrafluoroethylene; PVDF, polyvinylidene fluoride; PVDF-HFP, PVDF-co-hexafluoropropylene; PVP, poly(vinylpyrrolidone); PXRD, powder X-ray diffraction; rGO, reduced graphene oxide; SBU, secondary building unit; SEI, solid-electrolyte interphase; SPE, solid polymer electrolyte; SSE, solid-state electrolyte; TATB, 4,4',4''-s-triazine-2,4,6-triyltribenzoate; TCPP, tetrakis(4-carboxyphenyl)-porphyrin; TDPAT, 2,4,6-tris(3,5-dicarboxylphenyl-amino)-1,3,5-triazine; TEA, triethylamine; t_{Li^+} , Li^+ transference number; TMO, transition metal oxide; TMU, Tarbiat Modares University; UiO, University of Oslo; UTSA, University of Texas at San Antonio; ZC, ZIF-derived carbon; ZIF, zeolitic imidazolate framework.

This is an open access article under the terms of the [Creative Commons Attribution](https://creativecommons.org/licenses/by/4.0/) License, which permits use, distribution and reproduction in any medium, provided the original work is properly cited.

© 2022 The Authors. *EcoMat* published by The Hong Kong Polytechnic University and John Wiley & Sons Australia, Ltd.

Technology (BK21 Four), Kyung Hee University, 1732 Deogyong-daero, Giheung-gu, Yongin 17104, South Korea.
Email: mspark@khu.ac.kr

Jung Ho Kim, Institute for Superconducting and Electronic Materials, Australian Institute for Innovative Materials, University of Wollongong, Squires Way, North Wollongong, NSW 2500, Australia.
Email: jhk@uow.edu.au

Funding information

National Research Foundation of Korea, Ministry of Science, ICT, Grant/Award Number: NRF-2021M1A2A2038145

characteristics of MOFs for application in different types of Li batteries. A review of these emerging studies in which MOFs have been applied in lithium storage devices can provide an informative blueprint for future MOF research on next-generation advanced energy storage devices.

KEYWORDS

lithium-air battery, lithium-ion battery, lithium-metal battery, lithium-sulfur battery, metal-organic frameworks, porous structure

1 | INTRODUCTION

The term “secondary battery” refers to a rechargeable battery that can be used for converting electrical energy into the form of chemical energy, storing it, and then converting it back into the form of electrical energy when necessary. A lithium (Li) secondary battery is one type of rechargeable battery and is a device that stores and generates electricity through charging and discharging using Li^+ . Currently, lithium-ion batteries (LIBs) are used as a universal power source for various portable electronic devices, leading the era of smart devices. Some say that the battery of things era has arrived, saying that energy can now be used anytime, anywhere without being constrained by time and space through innovation in secondary battery technology. The largest demand for LIBs is coming from the need to power digital devices such as mobile phones, laptop computers, and the demand is expanding from portable information and communication devices to large-scale applications such as space and aviation, electric vehicles, hybrid vehicles, and advanced energy storage systems for supporting electrical grids.^{1–9}

Figure 1 is a schematic diagram showing the history and development direction of secondary batteries starting with lead-acid batteries. In recent years, the market has been growing, largely based on the development of electric vehicles. Research on secondary batteries has continued, starting with lead-acid batteries in the 1900s, nickel-metal hydride (MH) batteries in the 1950s, and LIBs in the 1990s. After Sony first developed LIBs in 1991, it spurred research on secondary battery development. Taking advantage of these opportunities, LIBs are currently being applied as essential power sources for mobile electronic devices, leading to the era of smart devices. LIBs are free from the environmental hazards of lead-acid batteries and the memory effect that is a fatal weakness of nickel-metal hydride (nickel-MH) batteries, and they

have superior gravimetric and volumetric energy densities compared to conventional secondary batteries.^{10–16}

The energy density limitations of LIBs, however, have raised the need for more advanced types of new battery. In order to meet the rapidly diversifying needs for secondary batteries, a technological innovation that encompasses issues of high energy, safety, and functionality is required. Current research on the next-generation batteries can be divided into LIB-related research, which corresponds to the mature stage, and future battery-related fields, corresponding to the introduction/growth stage, in consideration of the technological cycle. Lithium-sulfur battery (LSB),^{17–25} lithium-metal battery (LMB),^{26–35} and lithium-air battery (LAB)^{36–48} have been studied to overcome the limitations of LIB energy density, and all-solid-state batteries have been developed to overcome safety issues of battery. In addition, other next-generation battery technologies are emerging such as flexible batteries^{49–62} that can bend, and sodium-ion^{63–74} and zinc-air batteries^{41,75–86} for price and supply stability. Accordingly, the development direction of the next-generation battery will be the mainstream all-solid-state battery^{87–96} along with the improvement and evolution of the performance of each component constituting the battery. In addition, commercialization of LMBs and LSBs will be attempted, and ultimately, the development of LABs, called dream batteries, will proceed.

Li-ion secondary batteries are composed of four core components: an anode material, a cathode material, a separator, and an electrolyte. The movement of electrons through the external circuit, the electrochemical reactions that occur in the electrodes, and the movement of Li^+ ions in the electrolyte occur simultaneously, and through this process, the battery is charged/discharged. During charging, electrons and ions are released from the cathode material, the electrons flow through the external circuit, and the Li^+ ions move to the anode material

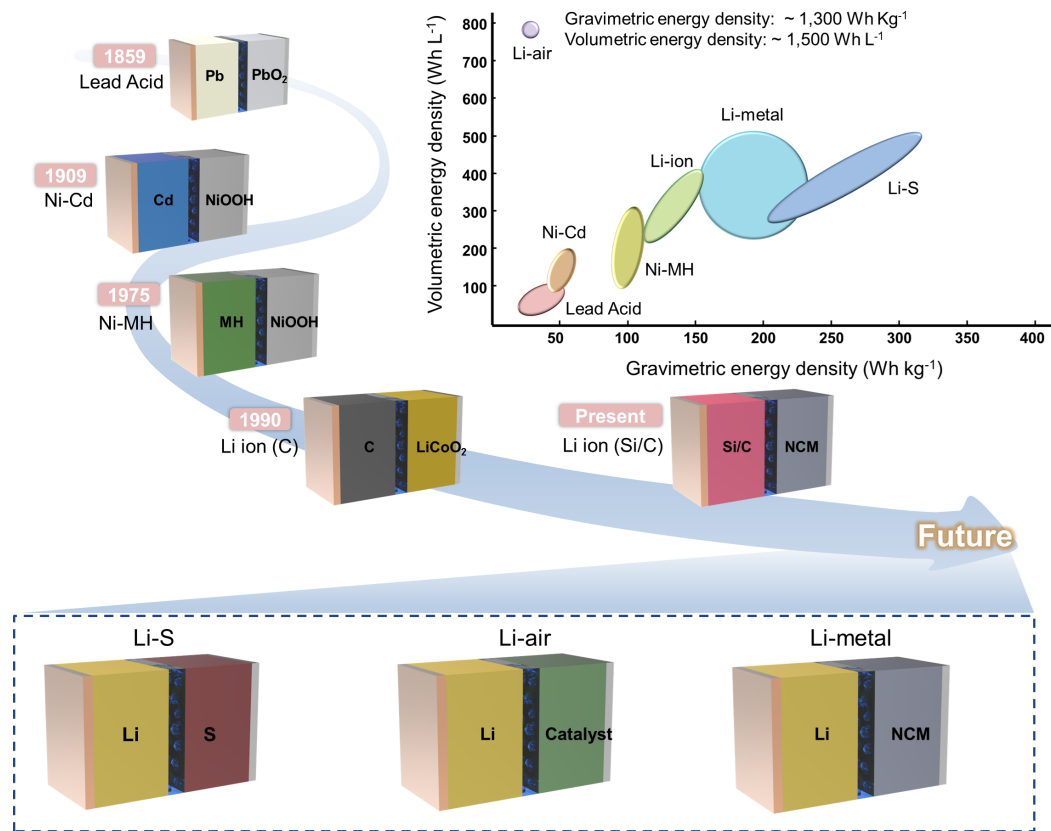


FIGURE 1 Schematic diagram showing the history and development direction of secondary batteries, with the inset showing the energy densities of the different types

through the electrolyte. This electrochemical charge transfer creates a potential difference between the cathode and the anode, and means that electrical energy is converted into chemical energy and stored. Discharge is achieved through a spontaneous electrochemical reaction of the electrode material without the addition of external energy, and chemical energy is converted into electrical energy through a process opposite to that of charging.

Each battery system, such as the LIB, LMB, LSB, and LAB systems, has its own problems. Therefore, it is important to develop suitable electrode materials with appropriate physical and electrochemical properties (e.g., electronic and ionic conductivity, redox potentials, capacity, catalytic activity, etc.) and to implement novel structures and chemical compositions. To realize this, new and creative solutions are needed for the development of materials. Polymeric and conductive carbon (C) materials, which are relatively low-cost and whose properties can be controlled to some extent through synthesis, suffer from a lack of chemical and physical stability for practical device implementation. Solid inorganic materials (e.g., silicon and metal oxides) with a redox active sites and robust structure can also be used as electrode materials for Li battery. Their slow ionic diffusion limits the charge–discharge

rate, however, and induces large volume changes during cycling, leading mechanical fragility. These shortcomings are inspiring the development and discovery of new types of advanced energy storage materials.

Metal–organic frameworks (MOFs) are considered as tempting candidates to satisfy the demands of advanced energy storage technologies.^{5,33,97–109} MOFs, which have great advantages such as large surface area, large pore volume, and can be design with desired properties by selecting and processing appropriate building blocks during synthesis, are porous material composed of a metal nodes and organic linker.^{110–117} Because the material properties required for each type of Li battery are different, this synthetic versatility of being able to synthesize variously through the combination of metal nodes and organic linkers constituting the MOF provides a way to overcome material limitations and optimize them for devices. In addition, porosity, one of the greatest characteristics of MOFs, also plays a significant role in energy storage and charge transport. The easily tunable capabilities of MOFs make them suitable for use as templates and precursors, allowing the synthesis of functional materials having desired properties, chemical composition, and unique morphology.

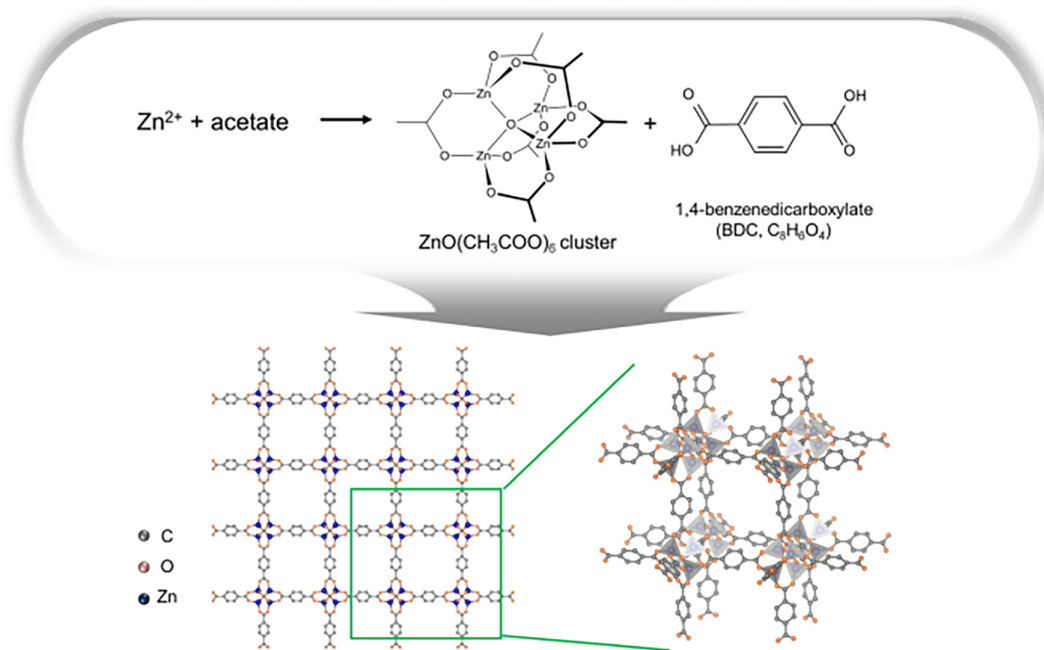


FIGURE 2 Synthesis process and structure of MOF-5

In this review, the origin, nomenclature, and structure of MOFs are first described, various methods of synthesizing MOFs are explained, and recent synthesis studies are summarized. In addition, we discuss the characteristics of MOFs, which are significant for their application in Li-based energy storage devices, and review studies on the applications of MOF materials in advanced batteries, including LIBs, LMBs, LSBs, and LABs. We focus on the properties of MOFs that can serve as variable factors as Li storage materials and describe research trends applying them to energy storage devices. We conclude with a review of novel Li storage technologies resulting from these properties of MOFs and hope that they will provide an informative roadmap as promising materials for upcoming advanced energy storage devices.

2 | OVERVIEW OF METAL-ORGANIC FRAMEWORKS

MOFs are classified porous crystalline materials consisted with covalently bonding metal ‘hubs’ and polytope organic ‘struts’. With special chemical and physical properties based on abundant inorganic and organic components that can be changed according to their composition, size, shape, geometry, and manner of branching, MOFs enable a variety of applications, including gas separation,^{118–122} storage,^{97,117,123–128} sensing,^{129–135} catalysis,^{110,136–142} and drugs.^{143–155}

2.1 | Origin of MOFs and nomenclature

Research results on the structure of MOFs, which are coordination compounds, were published in the late 1950s and early 1960s.^{156–158} After the announcement of an infinitely linked polymer skeleton in a three-dimensional (3-D) structure by R. Robson et al. of the University of Melbourne in 1989,¹⁵⁹ Omar H. Yaghi’s group at Arizona University rediscovered MOFs in 1995.¹⁶⁰ Later, the Yaghi group reported one of the most well-known MOFs, MOF-5, in 1999, which paved the foundation for the advancement of MOF research.¹¹² At the time of the rediscovery of MOFs by the Yaghi group, they used 1,3,5-benzenetricarboxylate (BTC) as a building block, which has three equally spaced carboxylate groups linked to aromatic rings to give it a hard disk-like morphology. They subsequently reported in 2003 MOF-5 with a composition of $Zn_4O(BDC)_3$ ($BDC = 1,4\text{-benzenedicarboxylate}$) favorable for hydrogen storage.¹⁶¹ It was confirmed that the generated colorless cubic compound had the formula $Zn_4O(BDC)_3 \cdot (DMF)_8 \cdot (C_6H_5Cl)$. This structure is shown in Figure 2. Simply reacting metal ions (Zn^{2+}) with various acetates creates $ZnO(CH_3COO)_6$ clusters, and combining these clusters with organic ligands (H_2BDC) creates the MOF-5 structure. The use of multi-dentate ligands such as H_2BDC contributed significantly to the anomalous thermal stability of this material and showed the possibilities for the application of molecular chemistry in the design of frameworks with selected properties.

TABLE 1 Summary of the names, metal ions, ligands, and formulas of most well-known MOFs, such as those form the HKUST, MIL, ZIF, UiO, and CAU series.

Name	Metal center	Organic ligand	Formula	References
MOF-5	Zn	BDC = 1,4-benzodicarboxylate (C ₈ H ₆ O ₄)	Zn ₄ O(BDC) ₃ (DMF) ₈ (C ₆ H ₅ Cl),	161
HKUST-1 (MOF-199)	Cu	TMA = benzene-1,3,5-tricarboxylate (C ₉ H ₆ O ₆)	Cu ₃ (TMA) ₂ (H ₂ O) ₃	174
HKUST-1	Ru	btc = 1,3,5-benzenetricarboxylate (C ₉ H ₆ O ₆)	Ru ₃ (btc) ₂	188
HKUST-1	Fe	btc = 1,3,5-benzenetricarboxylate (C ₉ H ₆ O ₆)	Fe ₁₂ (BTC) ₈ (S) ₁₂ Cl ₆ ·xFeTMPyPCL ₅	178
TUDMOF-1	Mo	btc = 1,3,5-benzenetricarboxylate (C ₉ H ₆ O ₆)	Mo ₃ (BTC) ₂	212
Zn-HKUST-1	Zn	btc = 1,3,5-benzenetricarboxylate (C ₉ H ₆ O ₆)	Zn ₃ (btc) ₂	213
MIL-53 (Al)	Al	BDC = 1,4-benzodicarboxylate (C ₈ H ₆ O ₄)	Al(OH)[O ₂ C-C ₆ H ₄ -CO ₂]	173
MIL-47	V	Dimethylformamide (DMF) (C ₃ H ₇ NO)	V ^{III} (OH){O ₂ C-C ₆ H ₄ -CO ₂ } _x (HO ₂ C-C ₆ H ₄ -CO ₂ H) (x ~ 0.75)	214
MIL-53 (Cr)	Cr	BDC = 1,4-benzodicarboxylate (C ₈ H ₆ O ₄)	Cr ^{III} (OH)·{O ₂ C - C ₆ H ₄ - CO ₂ }·{HO ₂ C - C ₆ H ₄ - CO ₂ H} _{0.75}	171
MIL-53 (Fe)	Fe	BDC = 1,4-benzodicarboxylate (C ₈ H ₆ O ₄)	C _{12.25} H _{9.25} FeN _{0.85} O ₅	181
MIL-53 (In)	In	BDC = 1,4-benzodicarboxylate (C ₈ H ₆ O ₄)	In(OH)BDC·0.75BDCH ₂	215
MOF-71	Co	BDC = 1,4-benzodicarboxylate (C ₈ H ₆ O ₄)	Co(1,4-BDC)(DMF)	194
MIL-53 (Ga)	Ga	BDC = 1,4-benzodicarboxylate (C ₈ H ₆ O ₄)	Ga(OH)(C ₈ H ₄ O ⁴⁻)·0.74C ₈ H ₆ O ₄	216
MIL-53 (Mn)	Mn	BDC = 1,4-benzodicarboxylate (C ₈ H ₆ O ₄)	Mn(BDC)L ⁿ L = pyridine N-oxide (PNO)	190
MOF-177	Zn	btc = 1,3,5-benzenetricarboxylate (C ₉ H ₆ O ₆)	Zn ₄ O(1,3,5-benzenetribenzoate) ₂	217
MIL-68	Fe	BDC = 1,4-benzodicarboxylate (C ₈ H ₆ O ₄)	Fe(OH)(BDC)	218
MIL-88	Fe	BDC = 1,4-benzodicarboxylate (C ₈ H ₆ O ₄)	Fe ₃ O(H ₂ O) ₂ Cl(BDC) ₃ ·nH ₂ O	219
MIL-125 (Ti)	Ti	BDC = 1,4-benzodicarboxylate (C ₈ H ₆ O ₄)	C ₄₈ H ₃₄ N ₆ O ₃₆ Ti ₈	220
ZIF-8	Zn	2-methylimidazolate (C ₄ H ₆ N ₂)	C ₈ H ₁₂ N ₄ Zn	205
ZIF-6	Co	2-methylimidazolate (C ₄ H ₆ N ₂)	C ₄ H ₆ CoN ₂	205
MOF-74	Mg	dobdc ⁴⁻ = 1,4-dioxido-2,5-benzenedicarboxylate ((HO) ₂ C ₆ H ₂ -1,4-(CO ₂ H) ₂)	Mg ₂ (dobdc)	221
Al-Td-MOF-1	Al	4-hydroxybenzoxonitrile (C ₇ H ₅ NO)	Li[Al(C ₆ H ₄ O ₂) ₂]	222
UiO-66	Zr	BDC = 1,4-benzodicarboxylate (C ₈ H ₆ O ₄)	Zr ₆ O ₄ (OH) ₄	223
MOF-525(Cu)	Cu	Tetracarboxyphenylporphyrin (H ₄ -TCPP-H ₂) (C ₄₈ H ₃₀)	Zr ₆ O ₄ (OH) ₄ (TCPP-H ₂) ₃	224
MIL-101 (Cr)	Cr	N-amino-2-pyridones and pyrano (C ₅ H ₆ N ₂ O and C ₈ H ₆ O ₂)	C ₂₄ H ₁₇ O ₁₆ Cr ₃	225
CAU-1	Al	BDC = 1,4-benzodicarboxylate (C ₈ H ₆ O ₄)	Al ₆ (OH) ₆ (OCH ₃) ₁₂ (BDC-NH ₂)	202
CAU-4	Al	BTB = 1,3,5-benzenetrisbenzoate (C ₆ H ₃ (CO ₂ H) ₃)	[Al(BTB)]	203

The basic structure of a MOF is composed of a secondary building unit (SBU) composed of metals or metal clusters and a linker, an organic compound that connects them. By having coordinatively unsaturated sites, the inorganic connector itself contains a functional group or exhibits semiconductor properties. Since almost all kinds of organic components can be used as linkers, the applicability of MOFs has been further developed.^{162–168}

Based on this foundation, the number of MOFs that can be synthesized is practically infinite, so it is necessary to explain how they are named. Omar M. Yaghi, a pioneer in MOF development, named his MOFs by assigning serial numbers to them, and MOF-5 is a representative example. It is also denoted as Isoreticular MOF (IRMOF-n), in the sense that it has a network of isotropic symmetry.¹⁶⁹ UiO, MIL, HKUST, and CAU are types of MOFs named after the institution in which they were

discovered. The Institute Lavoisier de Versailles in France developed a series of MOFs, and serialized them with an abbreviation for the name Materials of Institute Lavoisier (MIL) followed by a serial number after their institution, MIL-53 being the most well-known example.¹⁷⁰⁻¹⁷³ Hong Kong University of Science and Technology (HKUST) also developed MOFs and named them HKUST-*n* (*n* = 1, 2, ...). In addition to HKUST-1 discovered in 1999,¹⁷⁴⁻¹⁷⁶ where the metal center is Cu, various MOFs using iron (Fe),¹⁷⁷⁻¹⁸¹ chromium (Cr),¹⁸²⁻¹⁸⁶ nickel (Ni),¹⁸⁷ ruthenium (Ru),^{188,189} manganese (Mn),¹⁹⁰⁻¹⁹³ cobalt (Co),¹⁹⁴⁻¹⁹⁷ and so forth, as metal centers have been reported. The Zr-based MOF developed by the University of Oslo was named UiO-66,^{198,199} and later, UiO-67,²⁰⁰ UiO-68,²⁰¹ and so forth, were also reported. MOFs developed by Christian-Albrechts University (CAU) in Germany are named after it, and CAU-1²⁰² and CAU-4²⁰³ are representative examples. CAU MOFs were developed until quite recently, starting with CAU-1, and the latest example was named CAU-50.²⁰⁴ Zeolitic-like MOFs are called zeolitic imidazolate frameworks (ZIFs). These MOFs have a structure in which transition metal ions such as tetrahedrally coordinated Fe, Co, and Zn are linked with imidazole linkers, and more than 100 types of ZIFs have been reported so far.²⁰⁵ In one of the other types of nomenclature a serial number after PCN, which means porous coordination network.

Another way is to write first the metal ion to which the ligand is bound to clarify the structure of MOFs. For example, MIL-100 using Cr as this metal ion is sometimes referred to as Cr-MIL-100,^{206,207} and Ni-HKUST-1,²⁰⁸ Ni-MOF-14,²⁰⁹ and so forth, belong to this category. In the case of functionalization with a specific chemical group, the chemical group is indicated after the name of the MOF, for example, Al-MIL-53-NH₂²¹⁰ or Fe-MIL-53-NH₂.²¹¹ Table 1 summarizes the names, metal ions, ligands, and formulas of most well-known MOFs, such as the HKUST, MIL, ZIF, UiO, and CAU series.^{161,171,173,174,178,181,188,190,194,202,203,205,212-225}

2.2 | Structure of MOFs

MOFs composed of metal clusters and organic ligands are classified as porous inorganic-organic hybrid components. MOF design begins with the selection of appropriate metal ions and organic ligands to elicit the properties required for the target application. Combinations of various metal centers and ligands can produce an uncountable number of MOF molecular building blocks, providing a suitable strategy for modifying chemical and physical properties of MOFs.²²⁶⁻²²⁹ MOFs can be used as a platform for catalysts, and also be tuned to have high selectivity for specific chemical reactions.²³⁰⁻²³⁴

MOF-5, one of the most well-known MOFs, as mentioned briefly above, will be used as an example to explain the structure of MOFs. As shown in Figure 2, ZnO(CH₃COO)₆ clusters are generated by reacting metal ions (Zn²⁺) with various acetates, and these clusters are combined with organic ligands to create a 3D framework structure. The organic ligand part of the benzene structure is the spacer, and the Zn₄O(CH₃COO)₆ cluster part is the node. The structure forming the MOF-5 is originated from a cubic six-connection network.¹¹² The nodes in the net are substituted by SBUs clusters, and then the links in the net are substituted by finite rods consisting of BDC molecules. Then, the cores of the clusters form regular zinc oxide (ZnO) tetrahedra consisting of a single O atom bonded to four Zn atoms.

Based on this basic structure, in some cases, during the removal of guest molecules, often solvents, the pores are stable and can be refilled with other compounds. Therefore, the storage of gases such as hydrogen and carbon dioxide has composed the largest share of applications for MOFs. In addition, applications involving gas purification/separation, catalysts, conductive solids, and supercapacitors are the subjects of intensive research.¹⁶²⁻¹⁶⁸ MOFs are very popular and promising materials for various applications because they can be synthesized with countless different structures and properties through the combination of metal clusters and ligands. Also, since almost all kinds of organic components can be used as linkers, MOFs have continued to be developed for further applicability.¹⁶² Table 2 summarizes the molecular structures, names, and molecular formulas of various organic ligands used as linkers in synthesizing MOFs.¹⁶⁹

2.3 | Synthesis of MOFs

Numerous MOFs of various sizes and structures are required depending on the application, and this can be achieved through various synthesis methods. For example, it is possible to synthesize large MOF crystals by changing the pH/solvent at room temperature to accelerate precipitation.²³⁵ For certain applications, however, the development and understanding of novel gentle and rapid synthesis methods that could enable continuous production are still essential in order to process large volumes of homogeneous samples for rapid and reproducible synthesis.

2.3.1 | Synthesis methodology

A simple, consistent, and easily adaptable synthesis method is recognized as the ideal method for creating

TABLE 2 Molecular structures, names, and molecular formulas of various organic ligands used as linkers in synthesizing MOFs.

Organic structure	Name (Formula)	Organic structure	Name (Formula)	Organic structure	Name (Formula)
	Imidazole (C ₃ N ₂ H ₄)		2-methylimidazole (CH ₃ C ₃ H ₂ N ₂ H)		Benzimidazole (C ₇ H ₆ N ₂)
	Benzene-1,2-dicarboxylic acid (C ₆ H ₄ (CO ₂ H) ₂)		Dimethylformamide (DMF, [CH ₃] ₂ NCH)		Benzene-1,3-dicarboxylic acid (C ₁₂ H ₁₆ N ₂ O ₄)
	1,3,5-benzenetricarboxylic acid (TMA, BIC, H3BTC, C ₆ H ₃ (CO ₂ H) ₂)		Tetramethyltetrahydrofuran (TTF, C ₁₀ H ₁₂ S ₄)		Pyridine-2,4,6-tricarboxylic acid (H3PTC, C ₈ H ₅ NO ₆)
	5-aminoisophthalic acid (C ₈ H ₇ NO ₄)		2,3,3',3'-tetrafluoroterephthalic acid (C ₈ H ₂ F ₄ O ₄)		5-nitroisophthalic acid (H ₂ npta, O ₂ NC ₆ H ₃ -1,3-(CO ₂ H) ₂)

(Continues)

TABLE 2 (Continued)

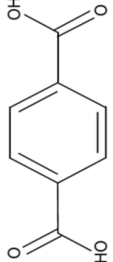
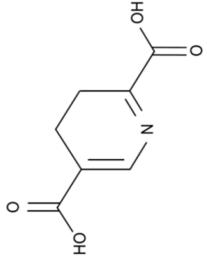
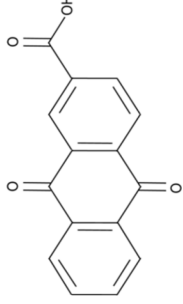
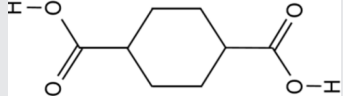
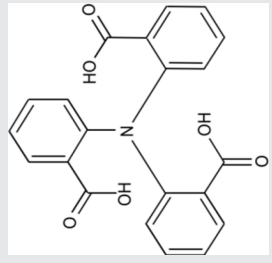
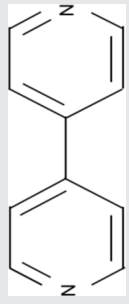
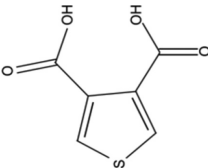
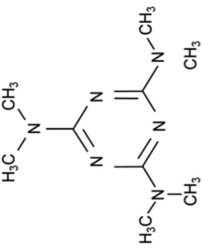
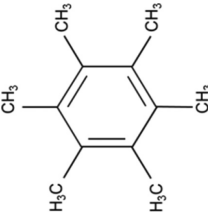
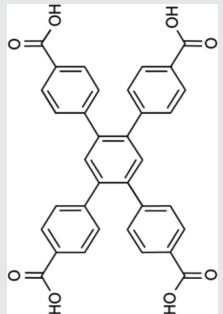
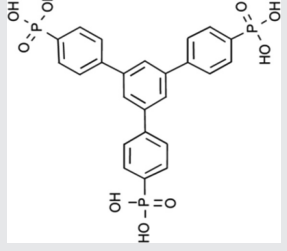
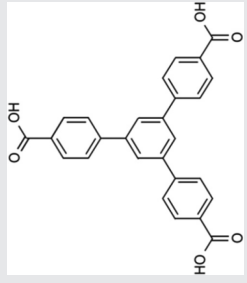
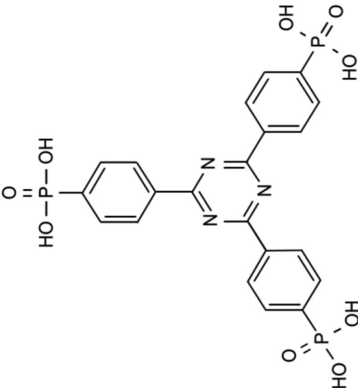
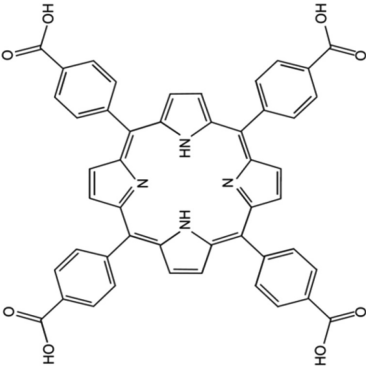
Organic structure	Name (Formula)	Organic structure	Name (Formula)	Organic structure	Name (Formula)
	1,4-benzenedicarboxylate (BDC, C ₈ H ₆ O ₄)		2,5-pyrazinedicarboxylic acid (C ₆ H ₈ N ₂ O ₆)		Anthraquinone-2-carboxylic acid (C ₁₆ H ₈ O ₆)
	1,4-cyclohexanedicarboxylic acid (H2CDC, C ₆ H ₁₀ (CO ₂ H) ₂)		Triphenylamine (H ₃ TCA, C ₁₈ H ₁₅ N)		4,4'-bipyridyl (C ₉ H ₄ N ₂)
	2,5-thiophenedicarboxylic acid (C ₆ H ₄ O ₄ S)		2,4,6-tris(dimethylamino)-1,3,5-triazine (H6TDPAT, C ₉ H ₁₈ N ₆)		Benzene hexamethyl (BHT, C ₁₂ H ₁₈)
	1,2,4,5-tetrakis(4-carboxyphenyl)benzene (H4TCPP, C ₃₄ H ₂₂ O ₈)		1,3,5-tris(4-phosphono phenyl)benzene (H ₆ PPB, C ₂₄ H ₂₁ O ₉ P ₃)		1,3,5-tris(4-carboxyphenyl)benzene (H3BTB, C ₂₇ H ₁₈ O ₆)

TABLE 2 (Continued)

Organic structure	Name (Formula)	Organic structure	Name (Formula)
	2,4,6-tri-(phenylene-4-phosphonic acid)-s-triazine (H6PPT, C ₂₄ H ₂₄ N ₃ O ₉ P ₃)		4-tetracarboxyphenylporphyrine (H6TCPP, C ₄₈ H ₃₀ N ₄ O ₈)

materials. The principles of MOF synthesis have basic properties and depend on the appropriate selection of metal centers and ligands. The vast diversity of choice of metal centers and ligands constituting MOFs can ensure an infinite hybrid organic-inorganic combination. Previous studies have shown that some regular structural motifs exist in MOF synthesis and that they help predict the architecture.^{236–240} MOFs with the desired properties can be synthesized by incorporating functions into linkers to apply specific reactive groups, or chiral or redox centers. The size of the metal center, its hardness, electronic composition, coordination modes, and so forth, affect the topology of the final synthesized MOF.^{241–246} Another concept that is undoubtedly highly relevant to the final structure and properties of MOFs relates to the choice of basic building blocks. Also, various synthesis parameters such as solvent, temperature, pressure, pH, reaction time, and so forth, must be considered. There are various synthesis approaches, such as conventional solution,^{247–251} hydrothermal,^{252–255} microwave-assisted,^{256–261} electrochemical,^{262–264} mechanochemical,^{265–267} and sonochemical methods.^{268–272} Figure 3 is a schematic diagram that briefly illustrates various MOF synthesis methods.

Conventional solution method

The solution method is the most common, simple method for obtaining large single crystal MOFs at room temperature and under atmospheric pressure. Yaghi et al. synthesized MOFs in low yields using a diffusion synthesis method.¹¹² This was a very early method for MOF synthesis. Since then, numerous types of MOFs such as MIL-53, MIL-88, MIL-110, CAU-1, ZIF-8, ZIF-67, and UiO-66 were synthesized using water, methanol (MeOH), and DMF as solvents.^{202,273} Li et al. have reported the effects of solvents on the synthesis of MIL-96(Cr) and MIL-100(Cr).²⁷⁴

Dinç et al. investigated the factors governing the critical steps of cation exchange in MOFs by studying the effects of various solvents by inserting Ni²⁺ into MOF-5 and Co²⁺ into MFU-4 L, where MFU stands for Metal-Organic Framework Ulm-University.²⁷⁵ In conclusion, it was found that although solvents affect the cation exchange mechanism, only a select group of relevant parameters was correlated with exchange rates. This approach establishes a method for understanding important aspects of cation exchange in different MOFs and other materials.

Hydrothermal method

The hydrothermal method, also called solvothermal synthesis, is the most widely used method for the synthesis of MOFs.^{276–281} The reaction proceeds by using a soluble metal salt, a free linker, and an organic high-boiling-

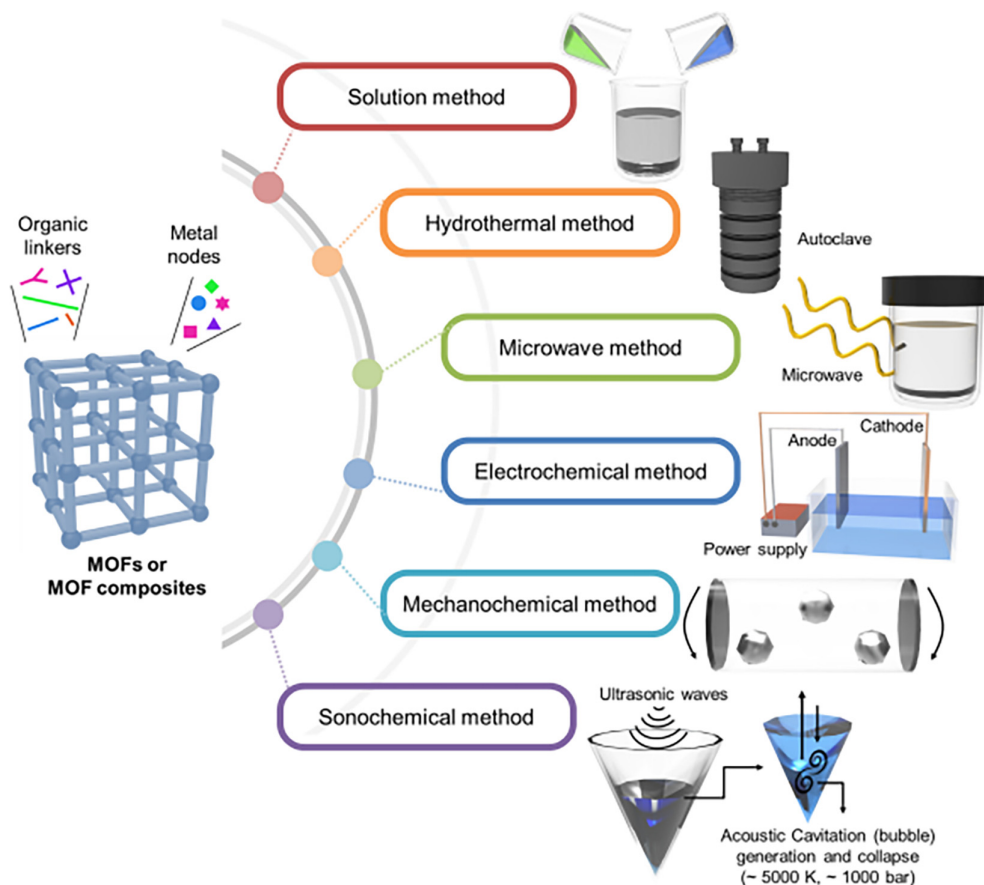


FIGURE 3 Schematic diagram briefly showing various MOF synthesis methods

point solvent in a sealed container and heating the solvent above its boiling point. Then, the product is recovered and washed, and the solvent is removed from the pores of the MOFs. This method has the advantages of being able to produce homogeneous MOFs particles with high crystallinity, a small crystallite size distribution, and high phase purity due to the fast reaction kinetics.^{280,282–285} The Yaghi group, a pioneer in MOF development, synthesized crystalline MOF-5 with a yield of 90% by heating (85 ~ 105°C) an N,N'-diethylformamide (DEF) solution of $\text{Zn}(\text{NO}_3)_2 \cdot 4\text{H}_2\text{O}$ and the acid form of BDC in a sealed container.²⁸⁶ Zheng et al. synthesized six types of MOF by the hydrothermal method using Zn, Co, and Ni as metal ions and H_3BTC , H_2NDC , L1, L2, and L3 as ligands (NDC = 1,2-benzenedicarboxylate, L1 = 1,4-bis(imidazol-1-ylmethyl)benzene, L2 = 1,1'-(1,4-butanediyl)bis(imidazole), L3 = 1,1'-(1,4-hexanediyl)bis(imidazole)).²⁵² The six MOFs synthesized in this way are as follows; (1) $\{\text{Co}_3(\text{L1})_3(\text{BTC})_2(\mu\text{-H}_2\text{O})_3 \cdot 2\text{H}_2\text{O}\}_n$, (2) $\{\text{Zn}_2(\text{L2})(\text{HBTC})_2 \cdot 2\text{H}_2\text{O}\}_n$, (3) $\{\text{Co}(\text{L3})(\text{HBTC})\}_n$, (4) $\{\text{Co}(\text{L1})(\text{NDC})\}_n$, (5) $\{\text{Ni}(\text{L2})(\text{NDC})\}_n$, (6) $\{\text{Co}(\text{L3})(\text{NDC})\}_n$. It was confirmed that structure (1) has a rare 4-connected self-penetrating network, (2) has a two-dimensional (2D) (3,4)-connected network,

(3) has a 2D (3,5)-connected network, (4) and (5) have a 4-connected MOF structure with CdSO_4 type topology, and (6) has a 2D 4-connected net structure. Although solvothermal synthesis has significant advantages, it has several disadvantages, such as the use of solvents with hazardous effects on the environment, the use of expensive stainless-steel autoclaves and Teflon reactors, limited mass production possibilities, and difficulties in product cleaning.²⁷⁹

In the hydrothermal process, a chemical reaction occurs between organic and inorganic components, and the backbone of the material is formed by solvent molecules that act as “pore templates”, which are then washed at high temperatures to remove the trapped solvent from the pores.²⁸⁷ Depending on the reaction conditions, however, reactive media such as reaction solvents, residual reactants, and by-products are incompletely removed from the MOF product, resulting in clogging of the pores in the process. Recently, Pré et al. proposed to improve the washing process by introducing optimized centrifugation conditions at two different stages: after the reaction and after washing the product.²⁸⁸ Nickel (Ni)-based MOF-74 (Ni-MOF-74) was selected as a target material for this study. The process is summarized in Figure 4.

During the step of the first batch synthesis, the washing process was repeated as indicated by the green box in Figure 4, which improved the separation of the product from the reactive medium. The second batch synthesis introduced centrifugation at two points where the solvent was drained, as indicated by the red arrows in Figure 4. Optimization studies of the centrifugation time and rotational speed between the reaction and product washing (1) and between product washing and product washing (2) were also performed to obtain the best separation quality. The first centrifugation introduced into the synthesis route removes the reactive medium from the product and the second centrifugation separates the contaminated MeOH from the product after washing. It can be confirmed that the separation in the washing process is improved through the process proposed in this study, and it leads to the complete activation of the MOF pores, which provides a way to expand the possibilities for future applications.

Microwave method

For various applications of MOFs, a small-sized MOF is sometimes required. The microwave assisted method is a useful method for generating small metal and oxide particles. Compared to the hydrothermal synthesis method, this method has the advantages of reducing the time required for synthesis by more than 10 times, making the size and composition of the synthesized MOFs uniform, and producing MOFs with more diverse compositions.^{289–294} Recently, Wright et al. synthesized zirconium (Zr) based MOFs (UiO-66) in the form of thin films using a simple and rapid microwave assisted synthesis.²⁹² In this study, a rapid synthesis method using microwaves was proposed to bake oriented UiO-66 thin films on gold (Au) and silicon (Si) substrates. The reaction time on Au and Si substrates was greatly shortened, and it was confirmed that the MOF in the form of a thin film could be synthesized with an easy method.

A method for synthesizing MOFs by combining the microwave method with other methods was proposed by Han et al.²⁹³ MOF crystals suggested in this study were successfully produced on polyacrylonitrile (PAN)/MOF fiber mats using a method that combines electrospinning with microwave irradiation. The electrospinning method is a facile, scalable, and versatile technique for manufacturing continuous fibers with diameters of several nanometers to several micrometers using various types of solution or molten polymers, and can be applied to various ceramics, polymers, and carbon type materials.^{295–303} By combining the microwave and electrospinning techniques, MOF-based nanofiber structures were created. To establish the optimal conditions for the

development of PAN/MOF fiber composites, the MOFs UTSA-16 (University of Texas at San Antonio [UTSA]) such as UTSA-16(Co) and UTSA-16(Zn) were used. The preparation way for UTSA-16 (Co) and UTSA-16 (Zn) was microwave method. The precursor containing metal ions (cobalt[II] acetate and zinc acetate) was dissolved in a mixed solvent, heated in a microwave oven, washed and then dried. The manufacturing method for the PAN/UTSA-16(M) (M = Co or Zn) fiber precursor was sonicated by mixing the synthesized UTSA-16 (M) powder with DMF, and after complete dispersion, PAN is added and sonicated. After spinning the fibers from this electrospinning solution on an aluminum foil metal plate, the electrospun PAN/MOF fiber mat was obtained. A PAN/UTSA-16 fiber mat was prepared by varying the weight ratio of PAN to UTSA-16(X), which is expressed as PAN/UTSA-16(M)-X%, where M stands for Co or Zn, and X stands for wt% of UTSA-16. UTSA-16 powders with different ratios were dispersed in the PAN fiber network and the seed growth of UTSA-16 was promoted under microwave irradiation to create a UTSA-16 crystal layer. The product was denoted as PAN/UTSA-16 (X)-1st, and the sample repeating the above process for secondary growth was denoted as PAN/UTSA-16(X)-2nd. Figure 5 shows sequentially the fabrication process for the PAN-UTSA-16 fiber mat consisting of UTSA-16 synthesis, fiber mat preparation, and seed growth on the fiber. PAN/UTSA-16(Co) and PAN/UTSA-16(Zn) fibers had micropores in the range of 0.4–1.5 nm and 0.4–1.8 nm, respectively, which are similar to those in pristine UTSA-16(Co) (0.3–1.45 nm) and pristine UTSA-16 (Zn) (0.3–1.79 nm).³⁰⁴ The method to produce flexible MOF polymer fiber mats through the combination of microwave and electrospinning techniques proposed in this study opens up valuable opportunities for a variety of applications such as energy storage, decomposition of hazardous chemicals, filtration, and sensor and biomedical applications.

Electrochemical method

The electrochemical synthesis method involves synthesizing compounds in an electrochemical cell, and has the advantage that synthesis can take place under gentle conditions than general solvothermal or microwave synthesis. In addition, this method is one of the synthesis methods that is scalable to the industrial scale by providing improved selectivity and yield because the reaction temperature is low and the synthesis rate is fast.^{262,305–307} Several typical MOFs, such as HKUST-1,³⁰⁶ ZIF-8,³⁰⁸ MIL-100(Fe),³⁰⁹ and MIL-53(Al)³¹⁰ were synthesized through this method. The principle is to supply metal ions by dissolving the anode into a synthesis mixture

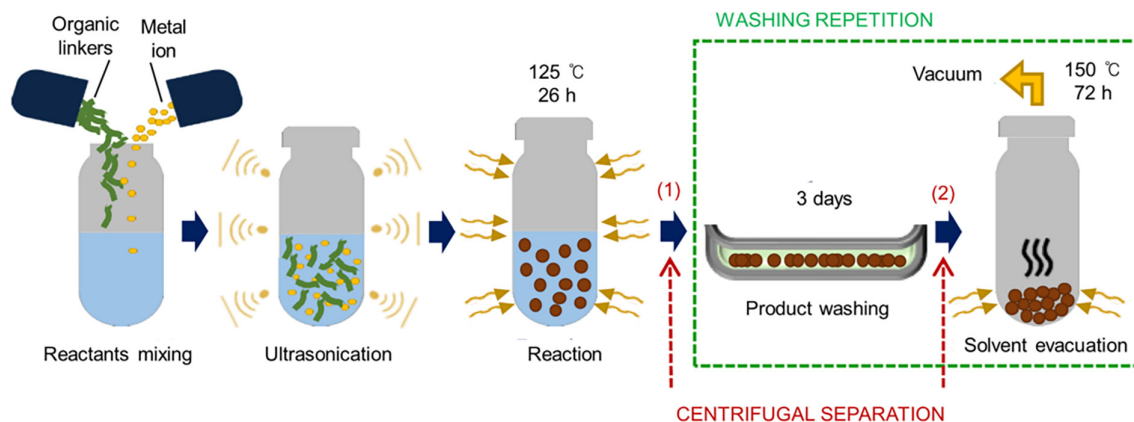


FIGURE 4 Schematic illustration of solvothermal synthesis with repeated washing processes or with additional centrifugal separation. Reproduced with permission.²⁸⁸ Copyright 2020, MDPI

containing an organic linker and electrolyte. Because the electrochemical synthesis is performed without the application of pressure, it allows more control over the concentration of the reactants in the synthesis over time. It can also control anodic oxidation to add metals at different rates, as well as continuously adding linkers to the solution. In addition, by controlling the voltage applied to the electrode, the oxidation state of the metal can be carefully controlled.

Creating thin MOF film coatings on electrodes by electrochemical methods is also an attractive feature. Liu et al. proposed a method for manufacturing a large-area 2D MOF film by using an electrochemical method.³¹¹ It is difficult to completely disperse ultra-thin MOF nanocrystals due to the strong interlayer interaction, however, so various methods have been proposed for this purpose.^{312–315} In this study, it was demonstrated that a large-area 2D $\text{Cu}_3(\text{HHTP})_2$ (HHTP: 2,3,6,7,10,11-hexahydroxytriphenylene) film could be grown on Cu foil through a controllable electrochemical assembly technique. Two pieces of Cu foil were used as anode and cathode, and they were immersed in a solution of dissolved HHTP powder to construct an electrochemical cell. When voltage was applied, Cu^{2+} ions were released from the Cu anode, and these ions reacted with the anions of HHTP to deposit a $\text{Cu}_3(\text{HHTP})_2$ MOF film on the Cu anode. Figure 6 shows the film-type MOF synthesis method using the electrochemical method. The method proposed in this study can be universally applied even when benzene-1,3,5-triyltrihydroxyboronic acid, meso-tetra(4-carboxyphenyl)porphine, or 2,4,6-trihydroxy-1,3,5-benzenetricarboxaldehyde are used as ligands. This MOF film can be transferred to any substrate without damage by poly(methyl methacrylate) transfer technology. This will provide an effective and controllable electrochemical synthesis technique for the industrial-scale production of MOF films, allowing for application in nanoelectronic devices as well as for broader applications.

Mechanochemical method

The mechanochemical synthesis method is based on a combination of mechanical and chemical phenomena on the molecular scale and is undoubtedly considered one of the best techniques that can be applied to implement the large-scale production of MOFs.³¹⁶ The reason why MOF synthesis via mechanochemical methods is of interest is that the reaction proceeds under room temperature and solvent-free conditions and (at least without additional heat), and the reaction takes 10–60 min to complete, leading to a quantitative yield. Mechanochemical methods can be divided into three main categories: (1) neat grinding (NG) that does not use a solvent in the reaction process, (2) liquid-assisted grinding (LAG) uses a catalytic amount of liquid phase to increase the mobility of reagents, and (3) ion-and-liquid assisted grinding (ILAG) uses a catalytic liquid containing trace amounts of salt additives to accelerate MOF formation.

In 2006, James et al. demonstrated microporous MOFs produced via NG for the first time.²⁶⁵ Later, James et al. also synthesized HKUST-1 by milling copper(II) acetate monohydrate and H_3BTC .^{317–319} The NG method has been successfully applied with other metal ions such as cadmium-based MOFs.^{320,321} A significant benefit of this approach is that the method leaves only water as a by-product and requires no purification.^{322,323}

Some MOFs that can be prepared with a solvent-free NG approach, but compared to metal acetates and nitrates, metal carbonates and metal oxides without crystal water require the addition of some solvent to aid the reaction process.^{324,325} Thus, the LAG method has been proposed and Braga et al. reported that crystallization and the reaction rate of MOFs can be improved in the presence of small amounts of solvent.³²⁶ In this study, one-dimensional (1D) porous coordination polymer- CuCl_2 (trans-1,4-diaminocyclohexane, denoted as dace)

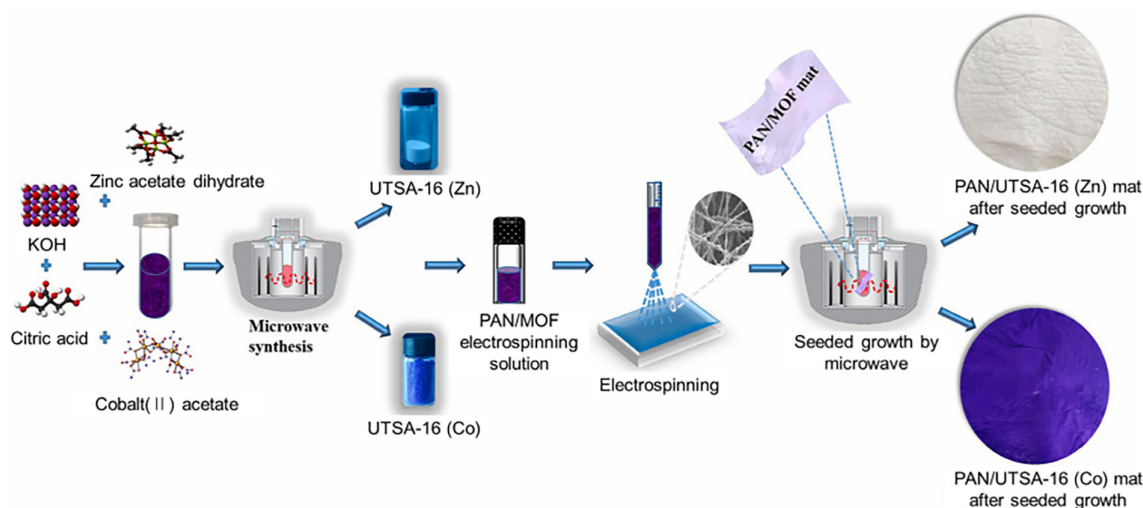


FIGURE 5 Manufacturing process for PAN-UTSA-16 fiber mat consisting of UTSA-16 synthesis, fiber mat preparation, and seed growth of fibers by combining electrospinning technology and microwave irradiation. Reproduced with permission.²⁹³ Copyright 2020, Elsevier

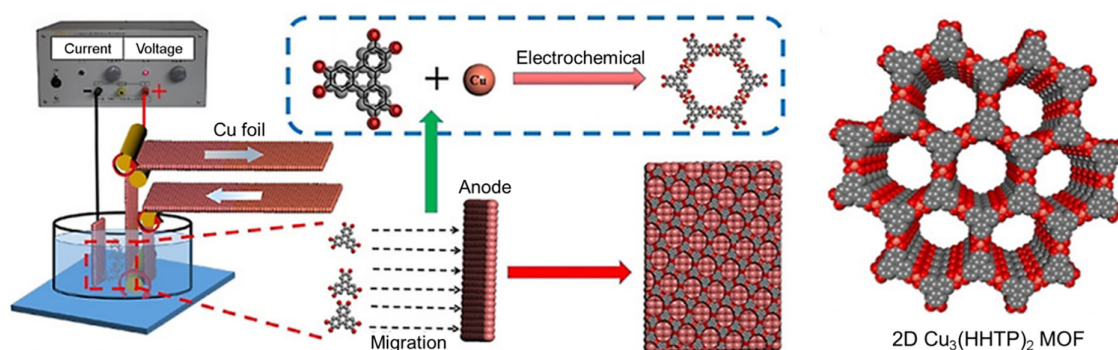


FIGURE 6 Process of synthesizing film-type 2D $\text{Cu}_3(\text{HHTP})_2$ MOF using the electrochemical method. Reproduced with permission.³¹¹ Copyright 2021, WILEY-VCH

was synthesized by grinding $\text{CuCl}_2 \cdot \text{H}_2\text{O}$ and dace in existence of water or dimethyl sulfoxide (DMSO), and then heat and vacuum treatment removed the water or the DMSO. Jone et al. revealed that some inorganic salts can assist MOF synthesis via LAG.³²⁷ Since then, researches have been reported on the synthesis of MOFs by the ILAG method, using a catalytic liquid containing trace amounts of salt additives. ZIFs were synthesized using DMF, EtOH, and DEF as a grinding solution with $\text{NH}_4\text{CH}_3\text{SO}_3$, NH_4NO_3 , and $(\text{NH}_4)_2\text{SO}_4$ as salt additives.³²⁸

Ni-based MOFs have attracted considerable attention and have been mainly synthesized by hydrothermal synthesis³²⁹ and precursor calcination in the air.³³⁰ These synthesis processes, however, generally require high temperatures, bulk solvents, and long reaction times.^{331,332} Jin et al. reported a simple solution-phase method for synthesizing $\text{Ni}_3(\text{BTC})_2 \cdot 12\text{H}_2\text{O}$ in a short time, but it was cumbersome to deprotonate the linker and also use an organic solvent.³³³ Since then, there have been studies

that synthesized Ni-MOF based on mechanochemical methods, but there were weaknesses in each study, and satisfactory results have not been reported.^{266,328,334–343} Wang et al. synthesized a Ni-based MOF in a very short time of 1 min by maximizing the advantages of the mechanochemical method.³⁴⁴ Changing the grinding time did not significantly affect the yield, which was in the range of 66%–72%. Regardless of the type of auxiliary liquid (water, MeOH, EtOH, or DMF) added in small amounts, the product was synthesized in 1 min and the synthesized yield was between 60% and 70%. In conclusion, it was confirmed that the method proposed in the above study is fast, efficient, eco-friendly, inexpensive, and has excellent scalability, and it was also suggested that the yield and reaction can be enhanced by controlling the synthesis conditions.

ZIF-8 is one of the most extensively studied types of MOF due to its facile synthesis and excellent structural stability.^{345,346} ZIF-67 has the same topology as ZIF-8, in which Zn is replaced by Co in the structure of ZIF-8.

Bimetallic ZIFs can be synthesized through appropriate control of Zn and Co, and several studies have demonstrated a synthetic route for bimetallic CoZn-ZIFs in liquid-based synthetic system.^{347–349} Another approach is to convert ZnO to ZIF via a solvent-free approach for mechanochemical applications.^{322,350,351} Tanaka et al. reported a simple acetate-assisted mechanochemical synthesis using cobalt acetate to approach the large-scale production of bimetallic CoZn-ZIFs.³⁵² Figure 7 is a schematic illustration showing the mechanochemical method and photographs of Zn-ZIF and bimetallic-ZIF powders synthesized through this method. Zn-ZIF obtained by mechanical synthesis is a white powder, ZIF-67 has a dark purple color, and $\text{Co}_x\text{Zn}_{(1-x)}$ -ZIF has a light to dark purple color depending on x . Cobalt acetate which added in acetate-assisted mechanosynthesis released acetic acid reacted with 2-MIM. Then, the solubility of ZnO in acids and mass transfer with hydrated water and autoacetic acid promote the complexation reaction between the ionized metal and 2-MIM.³⁵³ The acetate-assisted milling method proposed in this study can control the Co/Zn ratio by adjusting the amount of acetate added, and it is advantageous when there are no solvents and the starting materials and products are treated as solids. It is also expected to help revitalize the industrial applications of ZIF, opening up new opportunities for the creation of multimetal ZIF nanomaterials.

Sonochemical method

The sonochemical method is based on the chemical effect generated by the application of high-energy ultrasound to the mixture during the reaction. The main advantages of the ultrasound-assisted method in the synthesis of MOFs are rapid reaction, environmental friendliness, energy efficiency, and ease of use. It can be applied to the mass production of MOFs in the future because a quick reaction is required for the scaling up of MOFs.^{354–358} Ahn et al. synthesized MOF-177 by the sonochemical method in 2010.²⁶⁹ CuTATB- n (TATB = 4,4',4''-s-triazine-2,4,6-triyl-tribenzoate; n = power level), also called PCN-6 with the isorecticular structure of HKUST-1, was synthesized through a novel sonochemical pathway.³⁵⁵ In this study, catenated PCN-6 and non-catenated PCN-6' were synthesized by adjusting only the ultrasonic power level within 1 h in DMF solution with copper nitrate dihydrate and H_3TATB . In addition, IRMOF-9 (catenated) and IRMOF-10 (non-catenated) were synthesized in the same way using 4,4'-biphenyldicarboxylic acid (BPDC) as a ligand. The surface area increased with the applied ultrasonic power level, and the product synthesized via the sonochemical method exhibited improved porosity. It was observed that particle size of the product was gradually increased along with increasing ultrasonic power levels.

Morsali et al. synthesized TMU-5 (where TMU stands for Tarbiat Modares University, $[\text{Zn}(\text{oba})(4\text{-bpdh})_{0.5}]_n \cdot (\text{DMF})_{1.5}$) and TMU-6 ($[\text{Zn}(\text{oba})(4\text{-bpmb})_{0.5}]_n \cdot (\text{DMF})_{1.5}$) (oba: 4,4'-oxybisbenzoic acid; 4-bpdh = 2,5-bis(4-pyridyl)-3,4-diaza-2,4-hexadiene; 4-bpmb = 1,4-bis(pyridine-4-ylmethoxy)benzene) by the sonochemical method and studied the effects of the ultrasonic irradiation time and the initial reagent concentration on the size and shape of the MOF particles.³⁵⁸ It was confirmed that a high concentration of the initial reagent increases the size of the generated particles and induces a non-uniform particle size distribution. Conversely, a small concentration of the initial reagent decreases the size of MOF particles. Triethylamine (TEA) was added to increase the nucleation rate, and when TEA was used, rapid nucleation of the product occurred due to the deprotonated oba ligand, and the rapid nucleation decreased the particle size.

Various metal ions are readily incorporated inside molecular units to provide a wide range of optoelectronic and catalytic functions, and the porphyrin units in the ligand moiety of MOFs form stronger coordination bonds with expensive metal nodes, improving chemical stability.^{359–362} Because it has well-dispersed and isolated porphyrin units, rigid porphyrinic MOFs can avoid inactivation of catalyst due to dimerization of the porphyrin molecules, so porphyrin is widely used in MOFs composed of tetrakis (4-carboxyphenyl)-porphyrin (TCPP) and metal nodes such as Fe, Al, and Zr.³⁶³ Zr based MOFs such as MOF-525, MOF-545 (also named PCN-222), PCN-221, PCN-223, PCN-224, PCN-225, and NU-902 are also being studied.^{364–372} Among them, MOF-525 and MOF-545 are synthesized using the same substrate as for the Zr metal source and TCPP,²²⁴ since mixed phase particles are often observed, so it takes various efforts, such as high-throughput synthesis, seed-mediated synthesis, solvent-assisted separation, investigation of the modulator, and kinetic and thermodynamic control^{373–376} to get their pure phase.

Ahn et al. reported a facile single-step synthetic procedure for pure phase MOF-525 and MOF-545 synthesized through modulation synthesis via the sonochemical pathway.³⁷⁷ Zirconyl chloride octahydrate, benzoic acid, trifluoroacetic acid, DMF and TCPP were used for synthesis of MOF-525 and MOF-545. The samples thus obtained were named S-MOF-525 and S-MOF-545, respectively, and for comparison, MOF-525 and MOF-545 were synthesized by the conventional solvothermal method and denoted as C-MOF-525 and C-MOF-545. Figure 8 shows a schematic illustration of the sonochemical method, the structures of MOF-525 and MOF-545, and scanning electron microscopy (SEM) images of MOF-525 and MOF-545 synthesized under optimal conditions. After checking the morphology of S-MOF-525 and S-MOF-545 grown under each condition, cubic- and

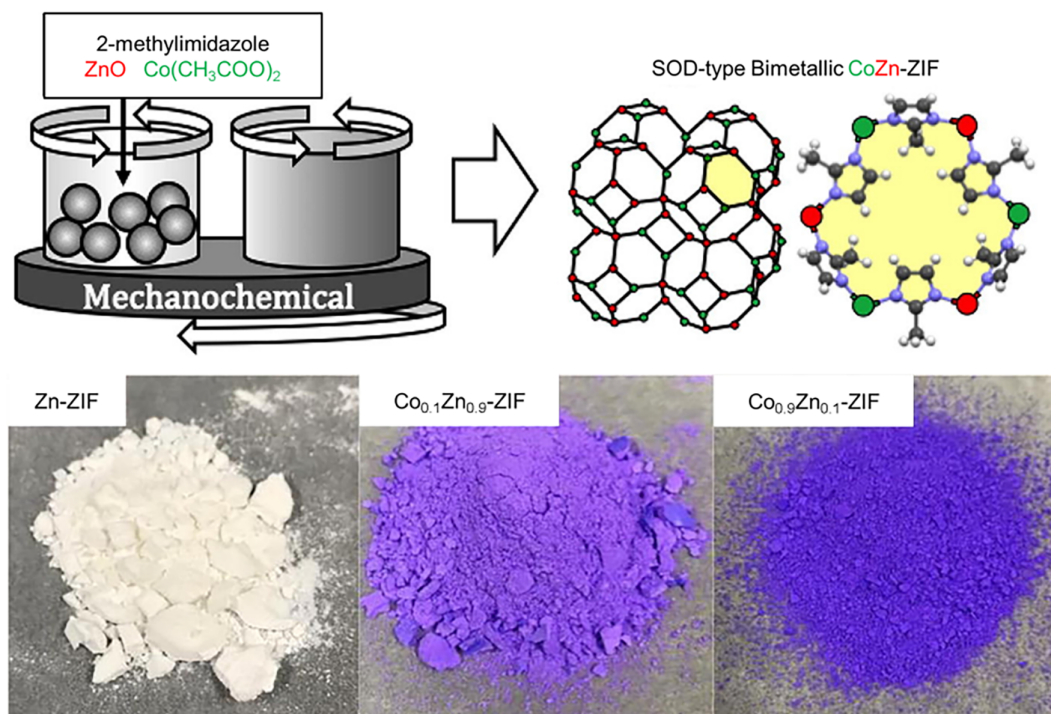


FIGURE 7 Schematic diagram of mechanochemical method for the synthesis of Zn-ZIF and bimetallic-ZIFs, with photographs of the resulting products. Reproduced with permission.³⁵² Copyright 2019, Elsevier

needle-shapes or their mixture were seen depending on the synthesis conditions (for the mixture: SEM middle image of Figure 8). MOF-525 consists of $Zr_6(O-H)_4O_4(CO_2)_{12}$ clusters in ftw topology, and MOF-545 consists of $Zr_6O_8(CO_2)_8(H_2O)_8$ clusters in csq topology, while the mixed-form particles appeared due to the varying connectivity of Zr_6 clusters during synthesis.^{373,378} In conclusion, the acoustic cavitation generated during sonochemical synthesis produced a very high local temperature, as well as pressure accompanying fast heating and cooling rates, so it induced accelerated homogeneous nucleation and significant reductions in crystallization times.^{269,270,379} This method has advantages including short synthesis time, low energy consumption, defect site formation, improved textural properties of the product, and the possibility of large production scales.^{276,380,381} This study showed that the use of sonochemical methods in synthesizing Zr- and porphyrin-based MOFs can produce particles with high crystal purity and uniform size while significantly reducing the synthesis time.

2.3.2 | Scaling-up production

Mass synthesis is required for the application of MOFs in real life. For the practical application of MOFs, mass synthesis is essential, and the production of MOF in the solvent-free or solid state has been applied to mass production, showing very encouraging results for the synthesis

and molding of MOFs. Coronas et al. described a solvent-free synthesis to prepare ZIF-8 from ZnO in just 2 min at high pressure and room temperature.³⁸² The ZIF-8, which took only 2 min to synthesize, showed a typical rhombic dodecahedral morphology with no significant difference compared to the ZIF-8 synthesized by the conventional solvothermal method for comparison. This methodology can be applied to the synthesis of other MOFs and covalent organic frameworks as well, and it enables the rapid synthesis of MOF materials and provides new insights into practical applications. Maspoch et al. reported enhanced results of a spray drying methodology that enabled the coinciding synthesis and shaping of microspherical highly nucleated MOF beads.³⁸³ This method has the advantages of being able to provide good yields with good porosity and high-density cores, as well as being capable of fabricating a variety of MOFs, allowing fine-tuning of porosity. In addition, the simple recovery of spent solvent makes the process cost-effective and waste-efficient.

Flow chemistry has the advantage that accurate and reproducible results for defined reaction times can be achieved by varying the volume or flow rate of each reactor.³⁸⁴ Recently, it has been demonstrated that it is possible to mass-produce MOFs with controlled particle size using flow technology.^{385–389} Among the various types of MOFs, ZIF-8 was produced using a variety of different sorts of equipment and procedures.^{390–393} Falcaro et al. reported a method of synthesizing a ZIF-8 composite structure including bio-macromolecules as well as

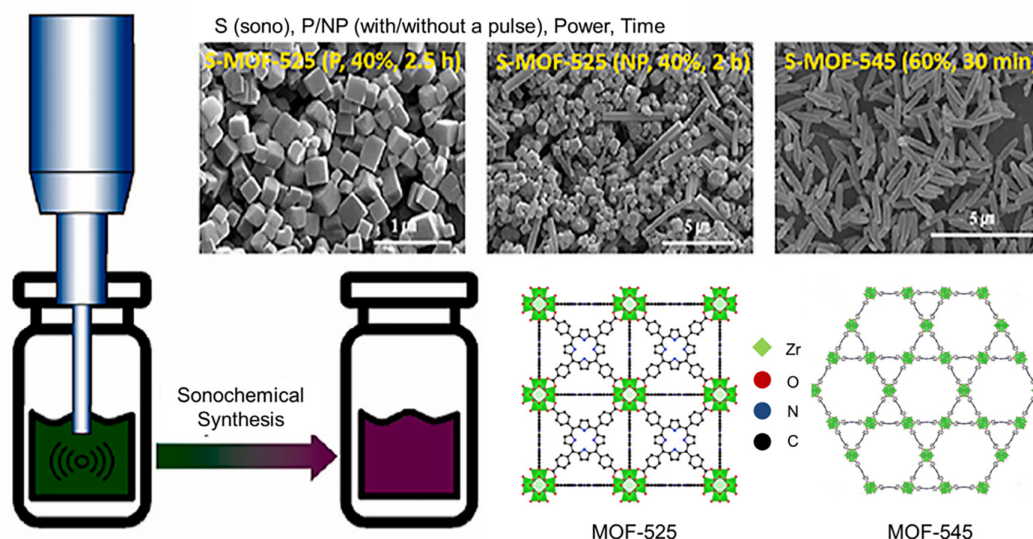


FIGURE 8 Schematic illustration of the sonochemical method and SEM images and structures of MOF-525 and MOF-545. Reproduced with permission.³⁷⁷ Copyright 2021, Elsevier

allowing control of the particle size by controlling the residence time of EtOH during synthesis using this continuous process.³⁹⁴ In this study, bovine serum albumin (BSA) was used as a model protein, which helped to develop a continuous flow procedure and understand the growth kinetics of ZIF-8-based composites. Figure 9 shows a schematic illustration of the synthesis system used in the continuous process. Three solutions are prepared: a solution in which the Zn source is dissolved, a solution in which BSA + 2-MIM is dissolved, and EtOH, and the solutions are injected while controlling the flow. The effect of the EtOH/water flow rate ratio on initial crystal size was studied by varying the EtOH flow rate through fixing the residence time in a continuous flow setup. Based on previous findings that alcoholic solvents promote crystallization of ZIF-8,³⁹⁵ it was supposed that fast injection of EtOH could inhibit the growth of amorphous particles and cause crystallization of ZIF-8, and continuous process conditions were established. The higher the EtOH flow rate, the smaller the crystallites that are yielded will be as shown in the SEM images in Figure 9. Then, by adjusting the residence time (from 0.33 to 120 s), it was possible to synthesize various size of BSA@ZIF-8 crystals with ranging from 40 to 100 nm. To demonstrate the scalability of the proposed method, the synthesis was carried out continuously for 5 h, resulting in the synthesis of BSA@ZIF-8 with an average particle size of 60 nm. A productivity of 2.1 g h⁻¹ was achieved, which is comparable to previous pure MOF synthesis results where synthesis was conducted on a laboratory scale.³⁹⁶ The continuous process applied to BSA@ZIF-8 was applied with α 1-antitrypsin (AAT), and it was confirmed that AAT was successfully encapsulated in the ZIF-8 particles. This study not only showed the

potential for mass production due to the continuous reaction, but also showed its applicability to the synthesis of ZIF-8-based composites for clinical biotherapeutics by easily controlling the particle size to make it suitable for intravenous drug delivery administration.

James et al. describe the continuous synthesis of MOFs containing Ni(salen), nickel(II)bis(triphenylphosphine)dichloride (NiCl₂[PPh₃]₂), HKUST-1, ZIF-8, and Al(fumarate)(OH) via twin screw and single screw extruders.³⁹⁷ This study reported practical application potential by successfully synthesizing MOFs with high yield, purity, and crystallinity at a rate of kilogram per hour with no added solvent or a minimum amount of solvent.

Table 3 summarizes the advantages and disadvantages of the MOF synthesis methods described so far. The MOFs show tremendous promise for a wide range of applications, so for their future, laboratory-scale studies and industrial implementation must go hand in hand. Fortunately, as noted in the review so far, new synthesis methods have evolved and are breaking down the laboratory-scale boundaries.^{398,399} It is not yet clear whether MOFs can compete with today's well-known industrial compounds such as zeolite, silica, or activated carbon, but since many researchers have focused on MOF applications, the possibility is considered close enough.

3 | FAVORABLE PROPERTIES OF MOFs FOR LITHIUM-BASED ENERGY STORAGE SYSTEMS

Before describing Li storage-related studies using MOFs, we would like to discuss the favorable characteristics

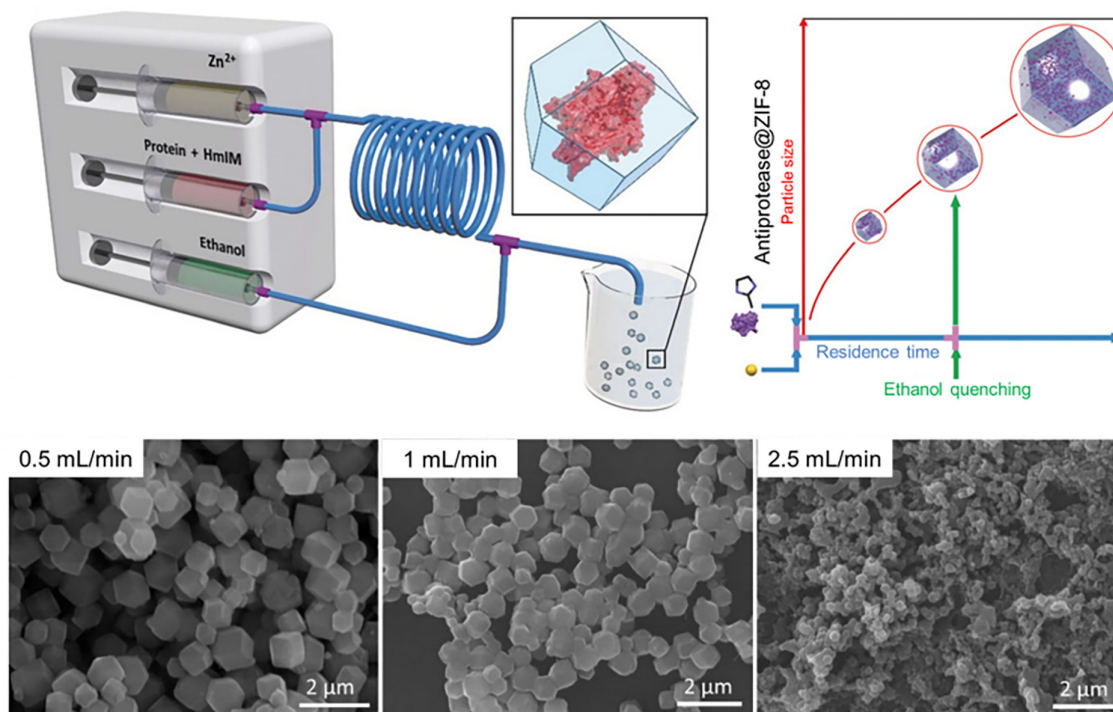


FIGURE 9 Schematic illustration of the continuous synthesis process for biocomposites encapsulated in ZIF-8 particles, and SEM images of the resulting products according to the EtOH flow rate. Reproduced with permission.³⁹⁴ Copyright 2020, WILEY-VCH

required for Li storage and the MOFs, materials that satisfy them. The favorable properties of materials required for Li storage can be divided into (1) physical and chemical stability, (2) high electronic/ionic conductivity, (3) excellent porosity and high-surface area, and (4) mass production potential as shown in Figure 10. Now, we will explain why each characteristic is important for storing lithium and in what sense the MOF satisfies it.

3.1 | Physical and chemical stability



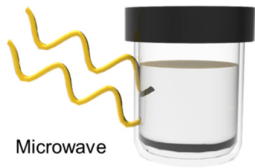
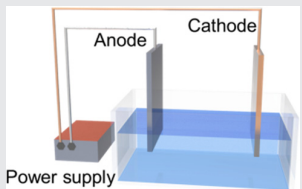

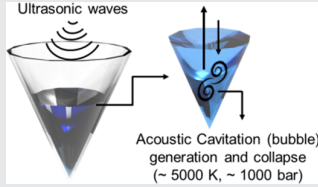
For stable Li storage, physicochemical stability is the first essential. This is because the active material must maintain its structural integrity in devices that undergo volume expansion and contraction. MOFs are famous for being variable enough that their properties can be tuned to your liking by choosing a suitable linker and metal node. Many reviews and papers have already discussed the physical and chemical stability of MOFs, and various synthetic strategies for controlling them have been reported.^{100,168,400} During synthesis, physicochemical properties can be controlled by adjusting, replacing, changing, or removing the composition of linkers and metal nodes. It is also possible to control the crystallographic phase and crystal size/morphology to select and adjust the surface chemistry of the MOFs.⁴⁰¹ This

easy-to-control functionality is a strength of MOFs as they provide a strategy for the synthesis of materials with the properties required for each energy storage applications. Therefore, it is important that the physical and chemical stability, an important characteristic of materials used in lithium storage devices, can be improved by selecting an appropriate synthesis medium for MOFs. One example is that MOFs composed of redox inactive nodes and short, rigid linkers show more thermochemical stability. Mechanical properties can be adjusted through the application of flexible linkers, control of the strength of host-guest interactions, adjustment of crystal size, and multi-metal framework construction.^{402,403}

3.2 | Electronic/ionic conductivity

Electron and ion transport are the most important parameters in any electrochemical devices. Especially in batteries, large overvoltages caused by high internal resistance affect the output reduction. Ionic conductivity affects the Li content that needs to be stored, which is one of the key parameters for achieving high-power and high-capacity lithium batteries. Since MOFs generally use metal-oxygen bonds, however, they have insulating properties, so need to be tuned. As one way to overcome this problem, studies have been conducted to tune the

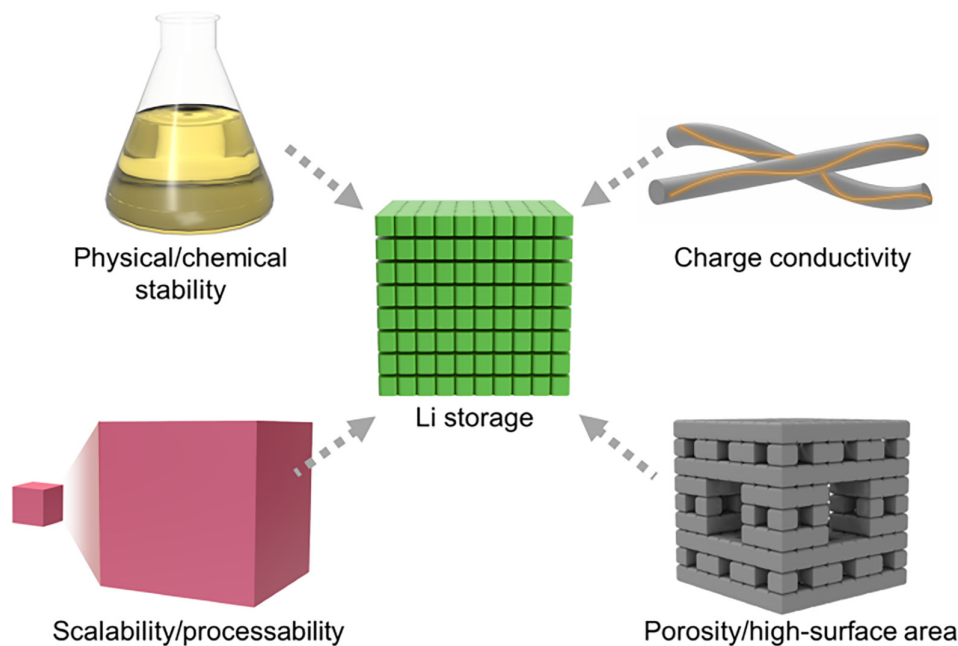
TABLE 3 Advantages and disadvantages of the MOF synthesis methods.

Synthesis method	Advantages (+) & Disadvantages (-)
Conventional solution 	(+) Normal, simple, easy (+) The crystallinity of MOFs occurs in a short period (+) Synthesized at room temperature and atmospheric pressure (-) Relatively slow process (-) Small amount synthesis
Hydro(solvo)thermal 	(+) Wide operating temperature range (e.g., 80–250 °C) (+) A heating and cooling process can help crystal growth (+) Easy industrial transposition (-) High cost of purchasing the equipment needed for the synthesis (-) High energy consumption (-) Long reaction time
Microwave assisted 	(+) Simple and energy-efficient approach (+) Short synthesis time and improved yield (+) Controllable morphology, phase selectivity, and particle distribution (+) Easy transformation and tight control of response parameters (-) Difficulty separating large single-crystals
Electrochemical 	(+) Useful for industrial scale synthesis by providing improved selectivity and yield (+) Fast and clean synthesis (+) Uniform MOF growth and deposited directly on platforms (+) Accurate layer deposition thickness growth
Mechanochemical 	(+) Solvent-free method (+) No specific pressure and temperature required (-) Difficulty separating large single-crystals (-) Secondary phases are usually obtained
Sonochemical 	(+) Responsive, environmentally friendly, energy efficient, and easy (+) Uniform particle size and shape can be obtained in a short time (+) A suitable method for the fabrication of nanosize MOFs (-) Ultrasonication can break the crystallites and prevent the formation of large single crystal

electronic structure through the control of the metal nodes and organic linkers using an approach called “through-bond” conductivity.⁴⁰⁴ For example, comparing the Mn^{2+} and Fe^{2+} analogs of the material family known as MOF-74, the use of *d*-electrons loosely coupled to Fe^{2+} and soft sulfur linkers significantly improves the electronic conductivity. The conductivity of electronically tuned MOFs can be improved through the modulation of metals and linkers. Another approach for improving electron conductivity is passing through space or electron hopping into guest molecules through

π - π interactions.^{405,406} Strategies exist to modulate ionic and proton conductivities as well as electronic conductivity. Incorporating ionic guest species that can facilitate the transport of ions and protons can be a straightforward approach. The polarity function is incorporated into the framework after synthesis, allowing the possibility of spatial and directional transmission control.^{407,408} Another method is to use an ionic framework with a mobile counterion to substantially increase the ionic conductivity.^{222,409,410} These novel synthetic strategies to enhance electronic and ionic conductivity

FIGURE 10 Favorable properties of materials suitable for lithium storage



in MOFs have provided new molecular insights for the discovery of materials beyond porous organic frameworks, as well as enabling novel materials for charge transport applications.

3.3 | Porosity and surface area

Porosity is important for the storage and transport of electrochemically active species, and high surface area is essential for catalytic processes. The large surface area and excellent porosity of MOFs are the most well-known characteristics. It has been already reported that the topology and pore size of MOFs can be adjusted through choosing appropriate metal nodes and organic linkers.^{286,411} Enormous control over the pore size, surface area, and chemical characteristics of MOFs gives the ability to observe and control their structural and chemical factors that influence electrochemical processes. The combination of micropores and mesopores in MOF is advantageous for Li storage because they create strategic channels and spaces that can affect to the molecular diffusion. The large surface area is advantageous for catalytic process in LABs, and the MOFs with high porosity enables the storage of polysulfide active species in LSBs. The high porosity is also particularly useful for devices that depend on chemical transformation of small molecules, such as oxygen in LABs. The ability to tune surface area and porosity has been poor for conventional inorganic solids, but these relatively easy-to-tune MOFs could further expand the opportunities for electrochemical applications.

3.4 | Scalability and processability

For practical applications, the material must have the potential to be mass-produced. In terms of scalability, mass synthesis of MOFs has been demonstrated by several companies (BASF, MOFWORX, MOF Technologies, and NuMat).^{387,398,399} The above companies utilized flow chemistry, electrochemical, and mechanochemical methods for bulk synthesis. First, the electrochemical synthesis method has the advantages of promoting uniform and fast growth of MOF and direct deposition on conductive platforms with accurate layer deposition to achieve a chosen thickness. The mechanochemical MOF synthesis method is based on using physical mixing (e.g., grinding, ball milling, etc.) of linker and metal node components without prolonged heating or the use of solvents, so that it has the advantages of mass production, reduced costs, and reduced chemical waste.⁴¹² This method also has the advantage of being able to produce a bulk of mixed metal MOFs by changing the component reagents. Another advantage is that production costs can be lowered by using inexpensive metal sources such as oxides, carbonates, hydroxides, and metal salts. Another creative method to improve the mass production potential of MOFs is microwave irradiation, which allows rapid growth of MOFs from precursor solutions.^{289,412} This method requires less energy than solvothermal methods because it relies on local heating instead of heating the entire solution. Solution-phase layer-by-layer deposition followed by material classes, another high-volume synthesis method, the products of which are also called surface-mounted MOFs, enables molecular and structural precision and control of

film thickness.^{413–415} In addition to solution-phase layer-by-layer deposition method, chemical vapor deposition and atomic layer deposition allow finer control over film thickness. The large-scale synthesis of MOFs with the versatility of possible substrates and wide control of combinable substrates expands the possibilities for their electrochemical applications.

The properties described so far are basic properties for improving Li storage and applicability. Each Li storage device, including LIBs, LMBs, LSBs, and LABs, which will be described below, has different priorities of properties required for the applied material. Therefore, it is important to identify the required characteristics of each device components and select the appropriate design element and synthesis strategy for materials.

In addition, as a method of synthesizing a safe MOF considering economic feasibility without relying on expensive or rare raw materials has been recently studied, it is known that MOF has advantages in cost-effectiveness, environmental friendliness, easy access, safety, and stability compared to other existing energy storage materials.^{199,289,305,400} According to BASF's experience, the main cost drivers of MOFs are linker costs, space time yield, down-stream processing effort, and solvents used. The BASF team described large-scale production, toxicity of reagents and solvents, cost of raw materials, availability/purity of chemicals, and safety as evaluation criteria for commercialization of MOFs.³⁰⁷ By meeting this criterion, MOFs are cost-effective and environmentally friendly materials compared to other energy storage materials, which means they also have advantages in terms of stability.

4 | APPLICATIONS OF MOFs IN LITHIUM-BASED ENERGY STORAGE SYSTEMS

After MIL-177 was first applied as an anode material for a Li-ion battery, the possibility of MOFs was confirmed. Since then, various MOF series materials, including MIL-53, MIL-10, HKUST-1, and so forth, have been used for Li storage applications (Figure 11). For each Li storage device, the priority of the characteristics required for the applied material is different, and MOFs have been used for the anode, cathode, separator, and so forth. MOFs are broadly classified into basic pristine MOFs and structures derived from MOFs. Besides direct utilization of pristine MOFs, they can perform as a self-sacrificial template for generating various nanostructured electrode materials. It is one of an effective method to accomplish enhanced electrochemical behavior for various applications. Numerous MOF-derived nanoarchitectures/nanoarchitectonics materials have been reported including nanostructured carbon

materials, metal compounds, and their composites. MOFs also show good performance for lithium storage, however, MOF-derived materials especially containing carbon components, have great potential as electrode materials owing to the improved electrical conductivity and stability. Now, we will explain the latest researches using pristine MOFs and MOF-derived structures applying to Li storage devices, including LIBs, LSBs, LABs, and LMBs.

4.1 | Lithium-ion battery

LIBs are devices that store and generate electricity through charging/discharging processes using Li^+ , and they play an essential role in our daily life. In the charging process, Li atoms in the cathode are ionized into lithium cations and move through the electrolyte to the anode, where Li^+ is stored, and it is released again in the reverse process. LIBs are widely used as energy storage devices in mobile information technology (IT) applications such as laptop computers, cellphones, and so forth, and they are currently utilized as power sources for electric vehicles. As utilization increases, the required performance standards, such as for the energy density, cost, lifespan, power output, and safety of LIBs, are also increasing. Related research on LIBs is expected to continue to expand as the scope of applications and demands increase, but there are constraints such as limited energy density and safety issues, which are caused by thermal runaway of the electrolyte. In order to resolve this issue and further meet the urgent and diverse demands on the battery industry, large-scale technological innovation is required, covering high energy, safety, and functionality.

MOFs can be promising advanced materials for LIBs to storage Li due to their distinct structure, high specific surface area, and well-developed porosity.²⁸⁶ Metal cations act as active sites in the MOFs for redox reactions, and the open crystal structure supports effective and reversible insertion/extraction of Li^+ .^{221,416} The intrinsic porosity of MOF enables the reversible storage of Li, and its high specific surface area promotes transport of Li^+ by increasing interfacial contact with the electrolyte solution. Redox-active metal nodes in MOFs are fairly standard and it has been extensively studied as both anode and cathode materials in previous studies.^{5,107,417,418} MOFs and MOF-based composites offer both advantages and limitations to LIBs systems as electrode materials. Figure 12 briefly explains the application of MOF-based materials to LIB components, and the notable features of MOFs, that play an important role in this case.

Since applying MOF-177²¹⁷ as an anode and MIL-53 (Fe)⁴¹⁹ as a cathode material for the first time, MOFs have received much attention and have been widely

studied as advanced materials for LIBs. MOFs offer remarkable performance as anode materials for LIBs without compromising structural changes even at significantly high current densities.⁴²⁰ First, the studies using MOFs as cathode materials for LIBs are explained. Early studies of MOFs as cathode materials for LIBs focused mainly on Fe-based MOFs. This was because they have $\text{Fe}^{3+}/\text{Fe}^{2+}$ redox pairs allowing reversible Li storage.^{419,421–424} In 2007, Tarascon et al. studied Fe-based MOF, MOF-53(Fe), which was the first demonstration of a cathode material featuring the MOF structure in LIBs as shown in Figure 13A.⁴¹⁹ Fe-based MOFs such as MIL-53(Fe) and MIL-68(Fe)⁴²³ have limitations in their reversible capacities, however, due to the restricted number of

inserted Li^+ ions per MOF formula. For MIL-53(Fe), for example, theoretical calculations show that, when the concentration of intercalated Li^+ is high, additional lithiation destabilizes the limited environment of the metal ions and causes a dramatic loss of cohesive interactions, which eventually leads to irreversible structural loss and destruction.^{421,422}

The capacity can be improved by introducing additional electroactive sites into the structure of MOFs. Tarascon et al. reported a method to increase the initial capacity by adsorbing electroactive molecule, 1,4-benzoquinone, on MIL-53(Fe) to generate a new MOFs compound (MIL-53(Fe)-quinone₁).⁴²⁰ This group previously used MOF-53(Fe) as a cathode material for

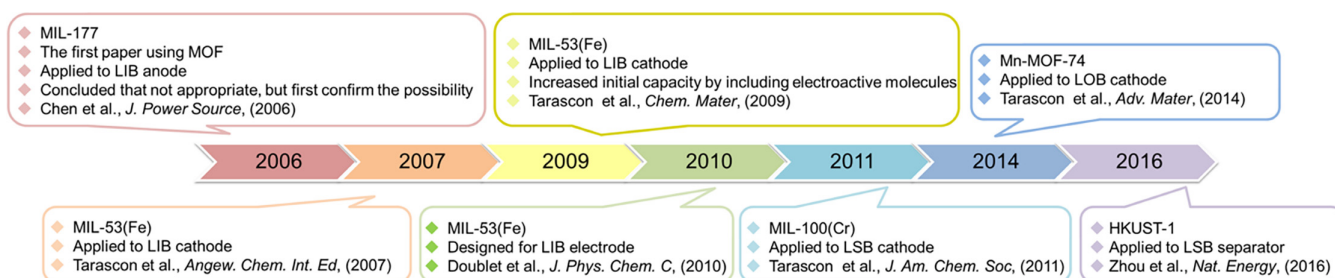


FIGURE 11 A brief history of research on the application of MOFs in Li batteries

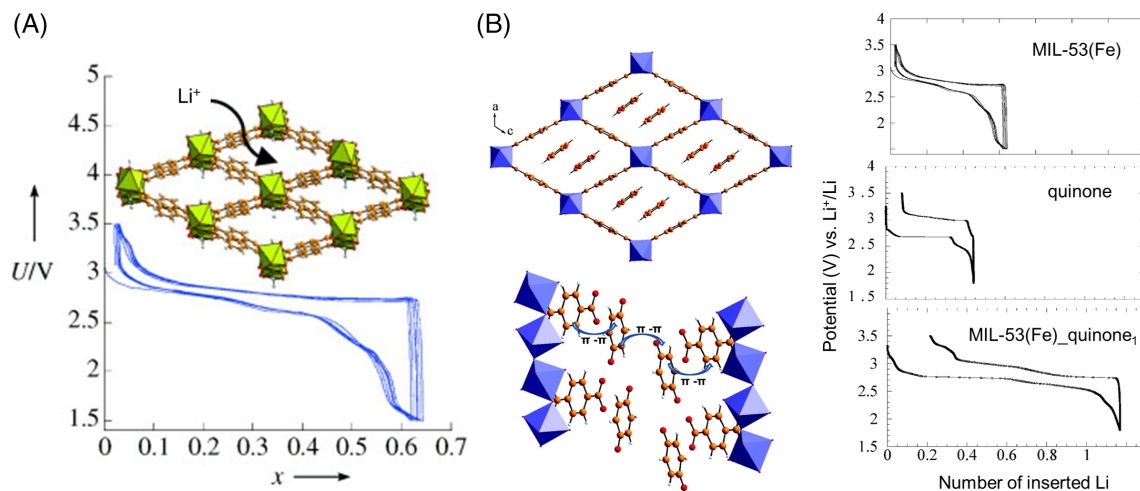
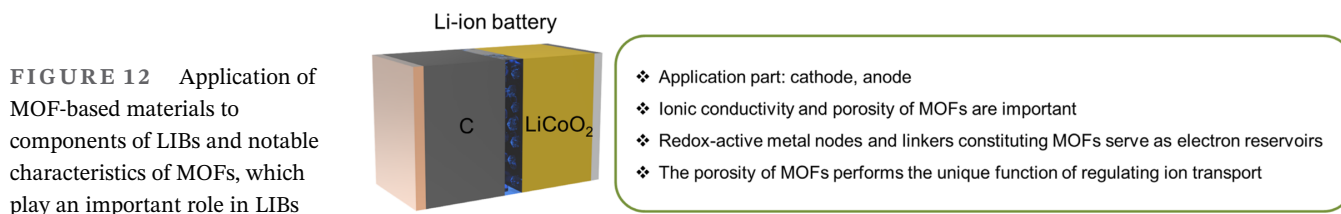


FIGURE 13 (A) Structure of MOF-53 and voltage profile applied to LIB cathode. Reproduced with permission.⁴¹⁹ Copyright 2007, WILEY-VCH. (B) The structure of MOF-53 including the electroactive molecule 1,4-benzoquinone, and the initial capacity before and after inclusion of the electroactive molecule. Reproduced with permission.⁴²⁰ Copyright 2009, American Chemical Society

LIBs for the first time. Because of the low density of the material, however, and the limited number of intercalated Li^+ , neither volumetric (mAh cm^{-3}) nor gravimetric (mAh g^{-1}) capacity were as high as for commercial cathode materials. In addition, the problem of limited rate capability at high current densities, which was induced by the poor electron conductivity of the structure, remains an open problem. To solve these problems, the adsorption of 1,4-benzoquinone, an electroactive molecule that can theoretically capable of two electrons per molecule but can also act as a redox mediator, was applied as shown in Figure 13B. Unfortunately, the additional capacity was rapidly dissipated during cycling, due to the gradual exchange between dimethyl carbonate molecules and quinone when the MIL-53(Fe) electrode was in contact with the electrolyte. Although the above study concluded that the electrochemical performance of the quinone-loaded material was rather disappointing, the π - π interaction between the quinone and the benzene ring of the MOF ligand was optimized.

Another approach is to employ both redox-active ligands and redox-active metal centers in the structure of MOFs.⁴²⁵ $\text{Cu}_2(\text{Ac})_4$ paddlewheel-cluster SBUs were used as nodes, and 2,7-anthraquinonedicarboxylic acid (2,7- H_2AQDC), one of the anthraquinone groups, was used as a bridging ligand. By in-situ Cu K-edge X-ray absorption near edge structure (XANES) analysis and cyclic voltammetry (CV), it was found that $\text{Cu}_2(\text{Ac})_4$ paddlewheel and anthraquinone groups were involved in the reduction during the discharge process. As well as quinone type ligands, tricarboxytriphenyl amine⁴²⁶ and tetrathiafulvalene tetracarboxylic acid⁴²⁷ can be used as electroactive ligands to increase the reversible capacity.

Prussian blue (PB, $\text{Fe}_4[\text{Fe}(\text{CN})_6]_3$) and its analogues, which have a cyanide-bridged perovskite type framework with large niche sites, have also been considered as potential alternatives. Various Prussian blue analogues (PBAs,) with different alkali metal and transition metal components were manufactured and applied as cathode materials for LIBs.^{428–431} Honma et al. reported the electrochemical Li^+ insertion/extraction of $\text{A}_x\text{Mn}_y[\text{Fe}(\text{CN})_6]$ (A: K, Rb), a valence tautomeric PBA.⁴²⁹ PBA is a material of the MOF family whose physical, electrochemical, and structural properties have been thoroughly studied.

The generalized formula for PBA can be written as $\text{A}_x\text{B}^{\text{II}}_{1.5-0.5x}[\text{B}^{\text{III}}(\text{CN})_6]_{\square_{0.5-0.5x}}\cdot n\text{H}_2\text{O}$ (A: alkali metal, B, B': transition metal, $0 < x < 1$), and where $[\text{B}^{\text{III}}(\text{CN})_6]^{3-}$ has fractional occupancy of the sites to form intrinsic vacancies (\square) occupied by coordinating and crystal water molecules. PBA has the basic structure of perovskite in which metal centers are interconnected each other, and the metal centers are connected by cyanide bridges as shown in Figure 14A.

$\text{Rb}_x\text{Mn}^{\text{II}}_y[\text{Fe}^{\text{III}}(\text{CN})_6]\cdot n\text{H}_2\text{O}$ exhibits a pressure-, temperature-, and photoinduced phase transition from cubic phase $\text{Rb}_x\text{Mn}^{\text{II}}_y[\text{Fe}^{\text{III}}(\text{CN})_6]\cdot n\text{H}_2\text{O}$ to tetragonal phase $\text{Rb}_x\text{Mn}^{\text{III}}_y[\text{Fe}^{\text{II}}(\text{CN})_6]\cdot n\text{H}_2\text{O}$,⁴³² which means strong interatomic interaction between Fe and Mn ions.⁴¹⁹ So, $\text{A}_x\text{Mn}^{\text{II}}_y[\text{Fe}^{\text{III}}(\text{CN})_6]\cdot n\text{H}_2\text{O}$ is a possible contender for Li^+ storage. The PBA compound was obtained through the precipitation method of adding an $\text{MnCl}_2\cdot 4\text{H}_2\text{O}$ aqueous solution to a $\text{K}_3[\text{Fe}(\text{CN})_6]$ and RbCl aqueous solution. Since rapid precipitation often leads to non-uniformity of the resulting compound, the addition rate of the aqueous solution was kept constant at 1 ml s^{-1} to control the crystal size. Quantitative Li^+ insertion/extraction was investigated by an electrochemical method using synthesized $\text{K}_{0.14}\text{Mn}_{1.43}[\text{Fe}(\text{CN})_6]\cdot 6\text{H}_2\text{O}$ and $\text{Rb}_{0.7}\text{Mn}_{1.15}[\text{Fe}(\text{CN})_6]\cdot 2.5\text{H}_2\text{O}$. Reversible Li^+ insertion/extraction in the aqueous electrolyte cannot be performed because the hydration radius (2.37 \AA) of Li^+ is larger than the lattice channel size of PBA. In this study, a nonaqueous electrolyte (ethylene carbonate and diethyl carbonate) was used. Figure 14B shows the open-circuit voltage (OCV) curves obtained by the galvanostatic intermittent titration technique (GITT) of $\text{K}_{0.14}\text{Mn}_{1.43}[\text{Fe}(\text{CN})_6]\cdot 6\text{H}_2\text{O}$ and $\text{Rb}_{0.7}\text{Mn}_{1.15}[\text{Fe}(\text{CN})_6]\cdot 2.5\text{H}_2\text{O}$. In both compounds, an almost complete amount of Li^+ can be inserted/extracted at 3.3 V versus Li/Li^+ . Although the obtained capacity was slightly lower than that of MIL-53, the Li^+ insertion/extraction voltage was higher, resulting in similar energy densities.⁴¹⁹ Reversible Li^+ insertion/extraction was observed for both K and Rb salts, but the redox-active sites could be converted by valence tautomerism. It has been shown that K salts without valence tautomerism exhibit Li^+ insertion/extraction with redox processes of Fe ions, whereas Rb salts with valence tautomerism exhibit redox processes of Mn ions.

Although PBA has a moderate initial capacity, cycling performance is unstable due to structural instability and phase transformation during the charging/discharging process.^{428,433} Improvement of the cycling stability of PBA can be accomplished by inhibiting formation of vacancy,⁴²⁸ manufacturing a core-shell structure,⁴³³ or integrating the PBA with conductive additives.⁴³⁴ Kojima et al. fabricated a vacancy-free PBA framework $\text{Mn}^{\text{III}}[\text{Mn}^{\text{III}}(\text{CN})_6]$ by removing K^+ ions from $\text{K}_2\text{Mn}^{\text{II}}[\text{Mn}^{\text{II}}(\text{CN})_6]$.⁴²⁸ $\text{K}_2\text{Mn}[\text{Mn}(\text{CN})_6]$ was obtained by the precipitation method of adding $\text{MnCl}_2\cdot 4\text{H}_2\text{O}$ aqueous solution to KCN aqueous solution in N_2 atmosphere, centrifuging the precipitate, washing with distilled water, and vacuum drying. The exact composition of the synthesized product was confirmed to be $\text{K}_{1.72}\text{Mn}[\text{Mn}(\text{CN})_6]_{0.93}\square_{0.07}\cdot 0.65\text{H}_2\text{O}$ (\square : $[\text{Mn}(\text{CN})_6]^{4-}$ vacancy) by elemental analyses. It can be seen that $[\text{Mn}(\text{CN})_6]^{4-}$ vacancy represents about 7%, which is significantly

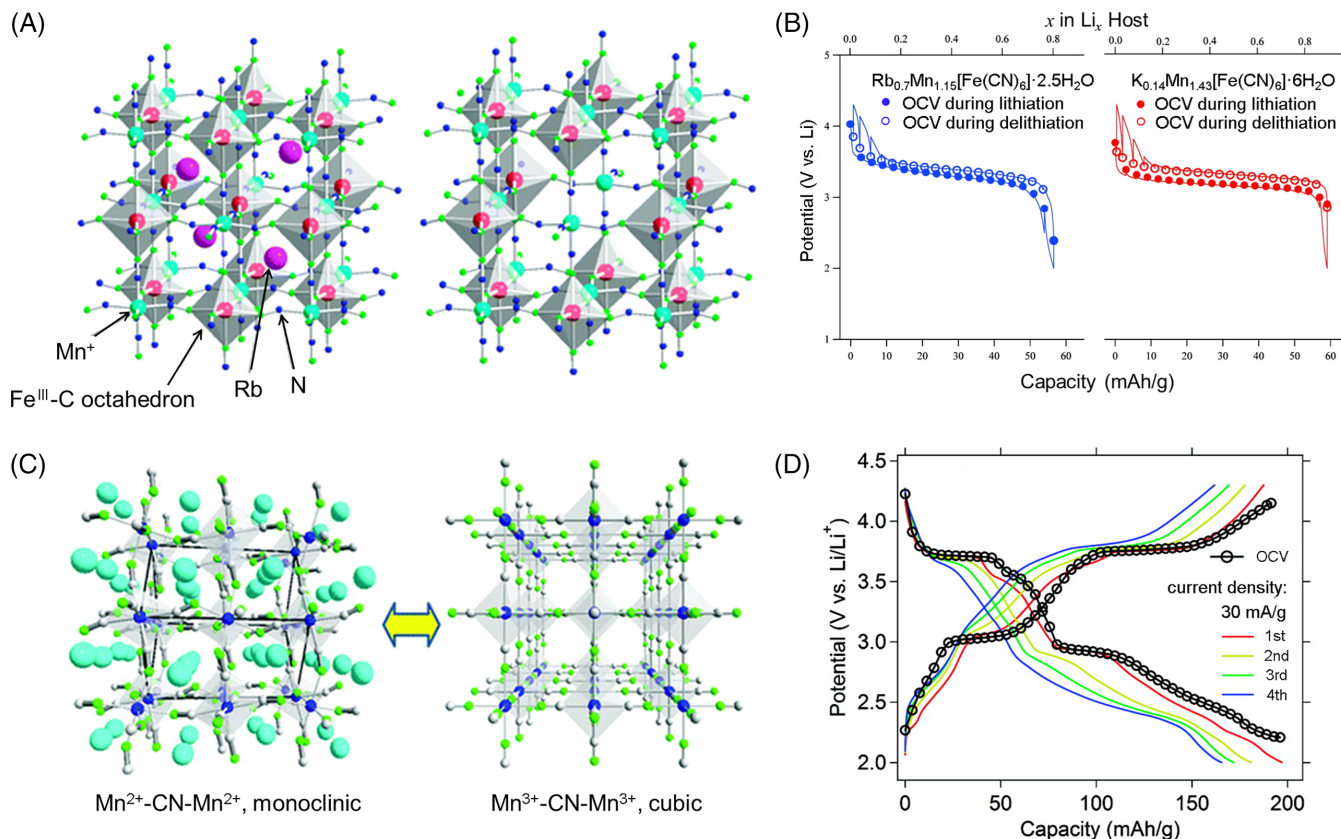


FIGURE 14 (A) Schematic structure of $\text{Rb}_1\text{Mn}[\text{Fe}(\text{CN})_6]$ without $[\text{Fe}(\text{CN})_6]^{3-}$ vacancies and $\text{Mn}_{1.5}[\text{Fe}(\text{CN})_6] \cdot n\text{H}_2\text{O}$ with $[\text{Fe}(\text{CN})_6]^{3-}$ vacancies. (B) Open-circuit voltage (OCV) curves obtained by the galvanostatic intermittent titration technique (GITT) using an intermittent current rate of 18 mA g⁻¹ and periodic interruption for 30 min. Reproduced with permission.⁴²⁹ Copyright 2010, American Chemical Society. (C) Crystal structure of $\text{K}_{1.72}\text{Mn}[\text{Mn}(\text{CN})_6]_{0.93} \square_{0.07} \cdot 0.65\text{H}_2\text{O}$ and cubic phase crystal structure from which K-ions were extracted. (D) OCVs obtained by the GITT method and discharge/charge curves for $\text{Mn}[\text{Mn}(\text{CN})_6]_{0.93} \square_{0.07} \cdot 0.65\text{H}_2\text{O}$ during Li⁺ insertion/extraction. (\square : $[\text{Mn}(\text{CN})_6]^{4+}$ vacancy) Reproduced with permission.⁴²⁸ Copyright 2012, American Chemical Society

suppressed compared to the vacancies of general PBA (e.g., MnFe-PBA contains 30% vacancies). It is expected that the presence of a small amount of $[\text{Mn}(\text{CN})_6]^{4-}$ vacancies is due to the rapid precipitation of PBA (due to the high rate of addition of the Mn solution to the KCN solution). The vacancy-suppressed PBA framework was fabricated by electrochemically extracting K-ions from the compound, applying a low-density current for 10 min, and interrupting for 60 min repeatedly. The compound from which K ions were extracted is named Mn $[\text{Mn}(\text{CN})_6]_{0.93} \square_{0.07} \cdot 0.65\text{H}_2\text{O}$. When K ions are extracted, its crystal structure changes from a monoclinic phase to a cubic phase. Figure 14C shows the structure of $\text{K}_{1.72}\text{Mn}[\text{Mn}(\text{CN})_6]_{0.93} \square_{0.07} \cdot 0.65\text{H}_2\text{O}$ with a cubic crystal structure in which the 3D cyanide-bridged framework and 3D porous channel exist simultaneously and K ions are extracted. Figure 14D shows the OCV and discharge-charge curves during Li⁺ insertion/extraction obtained with GITT at a constant current density of 30 mA g⁻¹. The OCV curve shows two potential plateaus at 3.7 and 3.0 V for Li⁺ insertion/extraction reactions, similar to the response during K ion extraction. The first discharge

capacity (1.91 Li⁺; 197 mAh g⁻¹) is higher than the theoretical value for $\text{Mn}[\text{Mn}(\text{CN})_6]_{0.93} \square_{0.07} \cdot 0.65\text{H}_2\text{O}$ (1.72 Li⁺; 176 mAh g⁻¹), which is presumed to be caused by electrochemical side reactions. Due to the reversible Li⁺ insertion/extraction, the discharge capacity and the charge capacity are almost the same.

Now, studies using MOFs and MOF-based materials as anode materials for LIBs are described. Most LIBs use graphite anodes, which allow reversible intercalation of Li⁺ in a layered structure. Graphite anode has a relatively low capacity of 372 mAh g⁻¹, however, by forming the intercalation compound LiC₆ during the charging process.^{435,436} Silicon anodes with a very large capacity of 3580 mAh g⁻¹ (Li₁₅Si₄) are suggested as an alternative, but large volume expansion during charging and discharging poses a serious safety problem.⁴³⁷ As alternatives to the graphite anode materials, tin (Sn)-based composites,^{438,439} phosphorous (P)-based composites,⁴⁴⁰ and transition metal oxides (TMO)^{441,442} have been studied, which have a higher capacity and superior rate capability compared to graphite. These materials suffer from significant volume changes upon the lithiation/delithiation

processes, however, causing particle agglomeration or structural collapse during cycling, which eventually leads to a rapid capacity loss. These technological hurdles require creative treatments and the exploration of advanced materials.

In 2006, the first study applying MOF-177 as an anode material for LIBs was conducted.²¹⁷ In this study, MOF-177 was synthesized through the facile solvothermal route, and its electrochemical properties were examined. As a result, it was found that the MOF-177 sample featured a high irreversible capacity during the first discharge process and good cyclability after the first cycle, but the reversible capacity was relatively low. Structural destruction of the sample was observed after Li storage, and the formation of metallic Zn during discharge was confirmed. Therefore, the performance of MOF-177 was not impressive due to its limited cycling stability, but this study opened up the possibility of the applicability of MOFs as anode materials for LIBs. Afterwards, various MOF materials, such as MOF-5,^{443–445} ZIF-8,⁴⁴⁶ ZIF-67,^{447,448} MIL-88,²¹⁹ MIL-125(Ti),^{449,450} MOF-177,²¹⁷ and so forth, have been explored for practical use in LIBs.

Their high porosity, versatile structure, redox-active functions, and excellent host-guest chemistry allow MOFs to play an important role in LIBs. For example, the reversible capacity of Li^+ can be increased by increasing the amount of Li^+ stored in the redox-active metal center and Li-stabilizing ligand moiety. A Li-intercalated MOF electrode is constructed by applying a ligand containing a carboxylate group, an amide group, an aromatic ring, an imidazole ring, or a pyridine ring that can provide an insertion site for Li^+ . BDC,^{451,452} BTC,^{453–455} 5-amino-isophthalic acid (AIPA),⁴⁵⁶ 2,3,5,6-tetrafluoroterephthalic acid⁴⁵⁷ are examples. In MOFs using them as ligands, Li^+ can be reversibly inserted/dissociated into organic moieties without direct bonding of metal centers. Some ligand structures and formulas mainly used in the synthesis of MOFs are given in Table 2.

In 2016, Hu et al. applied an Mn-BDC MOF synthesized by the solvothermal method with 1,4-BDC and manganese(II) chloride (MnCl_2) as an anode material for LIBs.⁴⁵² Mn has been studied as an energy storage material with great potential because of its low toxicity, stability, and low cost from an economic point of view. Figure 15A shows the structure of the ligand used for the synthesis, synthesized Mn-1,4-BDC, and the structure of Mn-1,4-BDC@200 treated at 200°C, respectively. The carboxylate functional group of 1,4-BDC can serve as a nucleation site for the growth of Mn^{2+} and subsequently enables Mn-1,4-BDC crystal growth. DMF used as a solvent was removed through the process of drying Mn-1,4-BDC in a vacuum oven, and it was confirmed that the

coordinated DMF molecules were sufficiently removed in this process. The specific surface area slightly increased after the removal of DMF molecules. This may benefit LIB performance as it can prevent electrolyte-related side reactions at lower potentials compared to Li/Li^+ . The electrochemical behavior of Mn-1,4-BDC and Mn-1,4-BDC@200 was analyzed by CV and constant current charge–discharge cycling. A comparison of the rate capability and the electrochemical cycling performance of Mn-1,4-BDC and Mn-1,4-BDC@200 is shown in Figure 15B. Mn-1,4-BDC@200 maintained a reversible capacity of 974 mAh g^{-1} after 100 cycles, which exhibited a Coulombic efficiency (CE) of over 98%. In the initial cycle, the CE was relatively low, but as the number of cycles increased, the charge and discharge capacity gradually increased. It maintained high capacity even after 12 charge/discharge cycles and showed high CE. As a result of confirming the change in capacity at various charge and discharge rates, the Mn-1,4-BDC@200 anode material recovered the charge and discharge capacity of approximately 939.1.2 and 945.2 mAh g^{-1} , respectively without significant loss of reversible capacity.

Chen et al. synthesized Co-BTC in various morphologies and dimensions using three types of reaction solvent in the hydrothermal method and examined its feasibility as an anode material for LIB.⁴⁵⁵ Figure 15C shows the structure of BTC, a ligand used for synthesis, and the structure of synthesized Co-BTC. To investigate the influence of solvents in the synthesis of anode materials on LIB performance, three types of reaction solvents were selected: EtOH, DMF, and mixed solvent of EtOH and DMF with a 1:1 ratio, vol%. By using three different types of solvents, it was confirmed that the solvent plays a important work in the hydrothermal synthesis, and the coordination solvent molecules trapped inside the pores of the MOFs can have a injurious effect on the reversible Li^+ insertion/extraction. The reaction product using EtOH as a solvent (represented as CoBTC-EtOH) presents monodispersed hollow microspheres structure, diameter range of 3–8 μm , and relatively rough surface. The MOF obtained using DMF as a solvent (denoted as CoBTC-DMF) showed a 2D layered architecture with irregular walls, and the MOF obtained using mixed solvent of EtOH and DMF with a 1:1 ratio, vol% (denoted as CoBTC-DMF/EtOH) exhibited a nanorod structure with a nanorod length of 50–300 nm and a width of ~ 50 nm. This shows that the morphology and dimensions of the product are highly dependent on the reaction solvent. The cycling behavior of the CoBTC-DMF, CoBTC-EtOH, and CoBTC-DMF/EtOH electrodes was tested under the low current density of 100 mA g^{-1} from 0.01 to 3.0 V versus Li/Li^+ . After 100 cycles, the reversible capacity retention of CoBTC-EtOH was 856 mAh g^{-1} : this corresponds

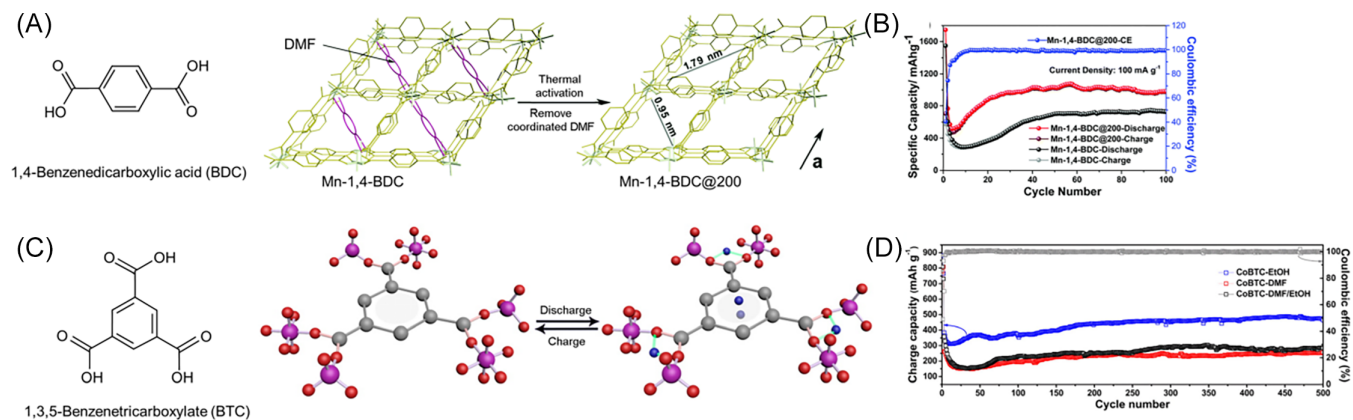


FIGURE 15 (A) Structures of 1,4-benzenedicarboxylic acid (BDC), Mn-1,4-BDC, and Mn-1,4-BDC@200. (B) A comparison of the electrochemical cycling performance and rate capability of Mn-1,4-BDC@200 and Mn-1,4-BDC. Reproduced with permission.⁴⁵² Copyright 2016, ROYAL SOCIETY OF CHEMISTRY. (C) Structures of 1,3,5-benzenetricarboxylate (BTC) and Co-BTC. (D) Cycling performances of EtOH, CoBTC-DMF, and CoBTC-DMF/EtOH at the high current density of 2 A g⁻¹. Reproduced with permission.⁴⁵⁵ Copyright 2016, American Chemical Society

to approximately 97.4% of the initial charge capacity (879 mAh g⁻¹). There was no appreciable difference between the cycling stabilities of CoBTC-DMF, CoBTC-EtOH, and CoBTC-DMF/EtOH. Relatively low initial CE was observed, which is associated with electrolyte decomposition and formation of an unavoidable solid-electrolyte interface (SEI) film.^{458–460} After cycling, however, all the samples, CoBTC-DMF, CoBTC-EtOH, and CoBTC-DMF/EtOH, showed nearly 100% of CE, which suggests the formation of a stable SEI layer and efficient Li⁺ transport from/into the anode.^{461–463} It showed outstanding rate capability over a wide range of charge/discharge rates, and when the current density was returned to 100 mA g⁻¹, the average charge capacity was restored and remained stable up to 90th cycles without significant decrease. Figure 15D shows the cycling performances of CoBTC-DMF, CoBTC-EtOH, and CoBTC-DMF/EtOH at the high current density of 2 A g⁻¹. A sample synthesized using EtOH among the three solvents, Co-BTC-EtOH electrode exhibited a reversible capacity as high as 473 mAh g⁻¹ at a current density of 2 A g⁻¹ after 500 cycles, maintaining near 100% CE. On the other hand, CoBTC-DMF and CoBTC-DMF/EtOH anodes showed excellent cycling stability at high current density, but their reversible capacity was 257 and 285 mAh g⁻¹ after 500 cycles, respectively, which are quite lower than that of CoBTC-EtOH. Therefore, it can be concluded that the Co-BTC synthesized using EtOH showed superior electrochemical performance. The macroporous void space of CoBTC-EtOH spheres, accessible specific regions, and the absence of coordinating solvents may be responsible for these results. The macroporous void space of CoBTC-EtOH spheres facilitates electrolyte impregnation and ion/electron transport, while accommodating expansion/contraction, so the

material showed distinguished cycling stability at high current density with a high reversible capacity.

The surface area, particle size, and morphology of MOFs can affect their electrochemical behavior when applied to LIBs. MOFs with numerous shapes, such as hollow microspherical,⁴⁵⁵ lamellar,⁴⁵⁷ shell-like,⁴⁶⁴ and pillar-layer⁴⁶⁵ have been reported, and they have porous structure that is beneficial to effective accommodation of volume changes, penetration of electrolytes, and transport of Li⁺. The particle size and homogeneity affect the surface area of the MOFs, but their effect on electrochemical behavior is opposite. The large surface area and high porosity form a large interface between the electrode and the electrolyte, which leads to a shorter Li⁺ diffusion length,^{454,466} but there is also a negative aspect that causes excessive side reactions with the electrolyte, leading to electrolyte degradation and performance degradation.^{452,464}

To overcome this, by leveraging the advantages of the controllable composition and shape/structure of MOFs, MOFs can be used on their own, but can also serve as a platform for the construction of nanostructured carbon composites and TMOs. Existing TMOs have problems with large volume changes during cycling and low electrical conductivity, resulting in poor rate capability and cycling stability. By constructing an appropriate nanostructure, and embedding the TMO in a conductive porous carbon matrix, the effects of fast Li⁺ transport and effective buffering of volume variations were attained, and as a result, greatly improved cycling performance was reported.⁴⁶⁷ This can be an efficient approach to achieve the enhanced electrochemical behavior required for applying MOFs and MOF-based materials to practical LIBs. MOFs can be used as a platform for TMO synthesis as it enables a uniform distribution of

nanostructures in a porous carbon matrix after controlled thermal deformation. Thus, TMOs synthesized using MOF as a platform can maintain structural integrity, accommodate volume changes, and facilitate electron and ion transport. TMOs with various nanostructures, such as ZnO,⁴⁴³ iron(III) oxide (Fe₂O₃),⁴⁶⁸ iron(II,III) oxide (Fe₃O₄),⁴⁶⁹ and cobalt oxide (Co₃O₄)⁴⁷⁰ were embedded in a porous carbon matrix with MOFs composed of corresponding transition metal nodes as precursors, and they showed high reversible capacity as anode materials for LIBs. Co₃O₄ is considered the most attractive alternative anodes materials for LIBs due to its high specific capacity (890 mAh g⁻¹), which is more than twice that of graphite (372 mAh g⁻¹), excellent electrochemical stability, and low cost.^{471,472} There is a problem that the cycling performance is not good, however, because the volume change during cycling is large. In particular, carbonaceous materials used in metal oxides and composites improve their electrochemical performance, so Co₃O₄ containing carbon can be considered as an alternative. In addition, nitrogen (N), which has a similar atomic diameter to carbon but has a higher electronegativity, is a very attractive dopant for carbon because N-doping can create external defects and enhance the electronic conductivity and reactivity carbon materials. The enhancement of the interaction between Li⁺ and the carbon structure is achieved by significantly altering the electron performance of doped N atoms and providing more active sites to adsorb Li⁺.

Sun et al. designed Co MOF ([Co(diimpym)(npta)]_n), where (diimpym = 4,6-di(1H-imidazol-1-yl)pyrimidine, an N-rich bidentate ligand; H₂-npta = 5-nitroisophthalic acid).⁴⁷⁰ This structure crystallized into an orthorhombic *Pbca* space group, and the asymmetric unit consisted of one Co(II) ion, one diimpym, and one npta²⁻. The diimpym has four potential N coordination sites, at which two N_{imidazole} atoms were used to link the Co atoms in a zigzag [Co(diimpym)]_n chain along the *c* axis. The N-rich Co-MOF obtained by hydrothermal reaction was subjected to the calcination process at 500°C under a flow of ultrapure N₂, followed by washing with deionized water and EtOH. This porous Co₃O₄/N-C structure looked similar to fish-scales, so it was named FSS-Co. Figure 16A shows the schematic illustration of Co₃O₄/N-C composite by heat treatment of Co-MOF (rich N) under N atmosphere, and Figure 16B shows the transmission electron microscopes (TEM) image of FSS-Co. As shown in magnified TEM image, the surface of FSS-Co is rough, and forms closely packed 3D porous nanoparticle structure with a size of about 20 nm. Two sets of gratings with the spacing of 0.243 and 0.467 nm can be seen, which were well matched with the *d*-spacing and orientation of the (311) and (111) planes of the Co₃O₄ phase cubic lattice.

The origin of a porous structure can be ascribed to the outgassing due to the decomposition of [Co(diimpym)(npta)]_n. Since the highly porous structure provides sufficient active sites for electrolyte contact, it can be used as an electrode material for energy storage. And also structural stability can be ensured during operation by favoring the tolerance of its active substances to volume changes. The electrochemical performance of FSS-Co was confirmed by CV conducted at a scan rate of 0.1 mV s⁻¹ in the potential window of 0.01–3.0 V versus Li/Li⁺ and discharge/charge profiles at a current density of 1000 mA g⁻¹. The initial charge and discharge capacities were 613 and 1210 mAh g⁻¹, respectively, giving an CE of 51.0%. After 200 cycles, the charge capacity was 579 mAh g⁻¹, indicating close to 100% CE. Reversible electrochemical behavior was exhibited after 200 cycles, and the specific capacity was almost maintained with a stable value of 612 mAh g⁻¹ within 500 cycles. By disassembling a LIB, it was confirmed that the Co₃O₄/N-C fish scale structure was preserved even after cycling, and there was no obvious crushing or agglomeration of the material, confirming that the FSS-Co structure showed excellent structural stability. As a result, FSS-Co demonstrated astonishing electrochemical properties as an anode material for LIBs, due to the synergistic effects between the N-doped C coating and the assembled porous Co₃O₄ nanoparticles.

Besides Co₃O₄, Fe₃O₄ is also considered a potential candidate for LIBs due to its high theoretical capacity (926 mAh g⁻¹), low cost, good stability, high abundance, and environmental friendliness.^{473–476} Like Co₃O₄, Fe₃O₄, also suffers from significant volume changes during cycling, and a method to optimize the Fe₃O₄-based anode by rational nanoengineering its structure and composition is proposed. One approach is to assemble nanoscale building blocks into a robust 3D architecture that combines the advantages of nanostructures and microstructures.⁴⁷⁷

Zheng et al. reported a 3D hierarchical structure assembled from microscopic Fe₃O₄ nanodots within MOFs consisting of Fe-based ZIF (Fe-ZIF, [Fe(MeIm)₂]_n), where MeIm = 2-MIM) with N-rich organic ligands as precursor/template.⁴⁶⁹ First, supramolecular self-assembly of Fe-ZIF take places on the surface of 3D N-doped carbon nanowebs (NCWs). In this case, 2-MIM molecules act as both organic linkers and structure-directing agents. The core-shell NCW@Fe-ZIF is then obtained, a 3D hierarchical structure with ultrafine Fe₃O₄ nanodots embedded in the NCW (denoted as NCW@Fe₃O₄/NC) was obtained after carbonization. In the novel 3D porous structure constituted by coordination bonds between Fe²⁺ and 2-MIM, the Fe center is tetrahedrally coordinated by the 1,3-position N atom of 2-

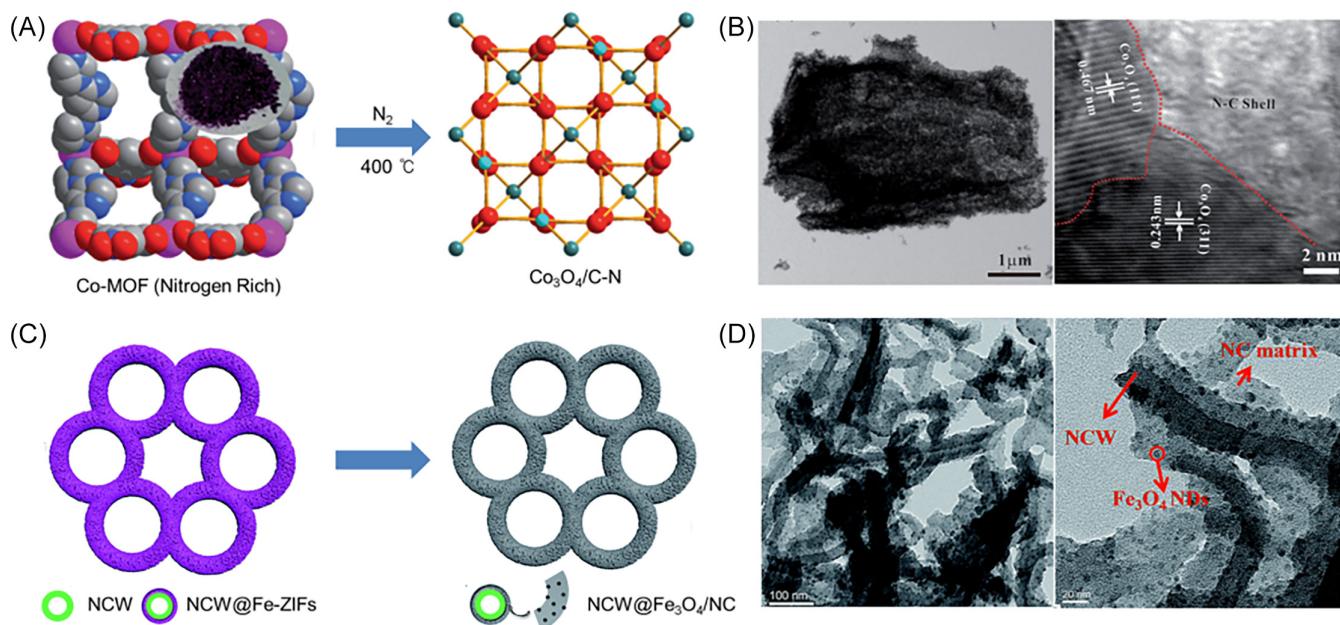


FIGURE 16 (A) Schematic illustration of structural change to Co₃O₄/N-C composite by heat treatment of Co-MOF (N-rich) under N atmosphere. (B) Transmission electron microscopy (TEM) images of porous Co₃O₄/N-C structure. Reproduced with permission.⁴⁷⁰ Copyright 2016, ROYAL SOCIETY OF CHEMISTRY. (C) Schematic diagram of the NCW@Fe₃O₄/NC participation strategy for constructing iron oxide-based storage materials with 3D structures. (D) TEM images of NCW@Fe₃O₄/NC. Reproduced with permission.⁴⁶⁹ Copyright 2018, ROYAL SOCIETY OF CHEMISTRY

MIM. And the 2-MIM ring serves as a bridging unit between the Fe centers, providing an infinite 3D framework. Figure 16C shows a schematic diagram of the MOF participation strategy for constructing iron oxide-based storage materials with 3D structures, and Figure 16D shows a TEM image of the finally synthesized NCW@Fe₃O₄/NC. A significant number of 2-MIM molecules are adsorbed on the surface of NCWs due to the strong π - π stacking interaction between the aromatic backbones of 2-MIM and NCW in MeOH solutions containing Fe²⁺ and 2-MIM. Coordination of 2-MIM with Fe²⁺ ions induces self-assembly of Fe-ZIF on the NCW substrate, resulting in a core-shell NCW@Fe-ZIF composite. Upon pyrolysis of NCW@Fe-ZIF in an inert atmosphere at 500°C, the Fe-ZIF is converted to Fe₃O₄ contained within an amorphous NCW matrix derived from 2-MIM, resulting in NCW@Fe₃O₄/NC. Since the underlying polypyrrole (ppy) precursor exhibits a 3D nanoweb-like structure composed of interconnected nanofibers, both core-shell NCW@Fe-ZIF composite and NCW@Fe₃O₄/NC retain their unique structure. In the right TEM image of Figure 16D, it can be seen that the surface of NCW@Fe₃O₄/NC is uniformly covered with some novel materials, and very small Fe₃O₄ nanodots with a size of about 5 nm are well trapped in the NC matrix. The pore size of NCW@Fe₃O₄/NC shows a relatively broad distribution centered around 30 nm, and these pores can withstand the volume changes of Fe₃O₄

nanoparticles during cycling, so an improved electrochemical performance can be expected.^{478–481} The electrochemical behavior of the NCW@Fe₃O₄/NC electrode was confirmed by analyzing the discharge/charge profiles at a current density of 0.05 C. In the first cycle, the charge and discharge capacities are 1585 and 2867 mAh g⁻¹, respectively, with a CE of 55.3%. The low initial CE can be explained by the following reasons: (1) irreversible Li⁺ consumption of NCW, (2) irreversible Li⁺ consumption of Fe₃O₄ during the first cycle, (3) Super-P added as conducting agent that contributes to part of the irreversible Li⁺ consumption, and (4) formation of a suitable SEI film. Considering all these factors, it was expected that the initial CE of the NCW@Fe₃O₄/NC anode could be improved by reducing the content of NCW and conducting agent, and the synergistic effect of the carbon and the Fe₃O₄ components was experimentally confirmed. The rate capability of the NCW@Fe₃O₄/NC anode was tested at a constant discharge rate of 0.1 C and various range of charge rates (0.1, 0.2, 0.5, 1, 2, 3, and 5 C). It exhibited a capacity of 723 mAh g⁻¹ at high charge rates, showing excellent potential as a high-power anode material for LIBs. The capacity of NCW@Fe₃O₄/NC electrode fully recovers its initial capacity, when the charge rate was returned to 0.1 C, which indicates resistant to high current operation. The capacities of the NCW@Fe₃O₄/NC electrode were 1963 mAh g⁻¹ after 170 cycles at 0.1 C discharge/0.1 C charge, 1298 mAh g⁻¹ after 130 cycles at

0.2 C discharge/0.5 C charge, and 1741 mAh g⁻¹ after 600 cycles at 1 C discharge/1 C charge. This result indicates that NCW@Fe₃O₄/NC has good rate capability at both high and low discharge/charge rates. The excellent Li⁺ storage capacity of NCW@Fe₃O₄/NC can be explained by the rational structure and composition favorable for Li⁺ storage. It is believed that the MOF-assisted synthetic protocol proposed in this study can be extended to design controllable properties of not only Fe-based MOFs but also other functional materials.

In addition to single-metal TMOs, the compositional and conformational diversity of MOF precursors enables the preparation of MOF-derived TMOs with complicated structure and chemical composition such as nanocubes,^{482,483} nanocages,^{484,485} hollow polyhedra,^{486–488} and hollow nanocages.^{489,490} Ma et al. synthesized cubic and stellated octahedron-shaped SnO/C polyhedra using Sn-based MOFs as templates and applied them in Li⁺ storage.⁴⁸⁸ Sn-based anode materials are attracting great attention due to their high theoretical capacity (994 mAh g⁻¹), low cost, and low operating potential,^{491–493} but when alloying with Li⁺ proceeds, extremely large volume changes (almost 300%) become a problem. One effective solution is to form composite structures with carbon-based materials.^{460,494–496} In this study, BDC and lithium hydroxide (LiOH) were dissolved in a mixed solvent of deionized water and DMF with the volume ratio of 1:1, and then SnSO₄ aqueous solution was added, and after stirring, the precipitate was collected, washed with DMF, and vacuum dried to obtain Sn-MOF. The products obtained with stirring bath temperatures of 25 °C and 50 °C were denoted as Sn-MOF-1 and Sn-MOF-2, respectively. The SnO/C composites obtained by heat-treating Sn-MOF-1 and Sn-MOF-2 at 500 °C in N₂ atmosphere were denoted as SnO/C-1 and SnO/C-2, respectively. Figure 17A shows the overall synthesis process for the Sn-MOF polyhedra and derivatives. By adjusting the temperature of the stirring bath, 1 μm sized cubes (Sn-MOF-1) and a 2 μm sized stellated octahedra (Sn-MOF-2) could be synthesized. The samples showed high stability, with the cubic and stellated octahedral shapes retained even after pyrolysis. TEM and high-resolution TEM (HRTEM) analysis confirmed that the SnO nanorods were uniformly dispersed in the polyhedral carbon matrix. Both micropores and mesopores exist in SnO/C-1 and SnO/C-2, but there are differences in their surface areas and pore volumes. During the pyrolysis process, anisotropic shrinkage, and decomposition of precursors with different crystal orientations and shapes occurred, which can be expected to cause differences in surface areas and pore volumes. The cycling performance and rate capability of SnO/C-1 and SnO/C-2 were analyzed by the galvanostatic charge/discharge

method. In Figure 17B, the reversible specific capacities of SnO/C-1 and SnO/C-2 were 950 and 900 mAh g⁻¹, respectively, and they are much higher than that of the theoretical values (724 mAh g⁻¹ for SnO/C-1 and 72 mAh g⁻¹ for SnO/C-2). This is due to the interfacial interaction between carbon matrix and the nanocrystalline SnO and the abundance of defects that can provide many active sites for Li⁺ storage.⁴⁹⁷ Both SnO/C-1 and SnO/C-2 showed excellent rate capability at various current densities (0.05, 0.1, 0.2, 0.5, 1, and 2 A g⁻¹). The specific capacity of the SnO/C-1 with a cubic structure is slightly higher than that of the SnO/C-2 with a stellated octahedral structure. The impedance analysis indicated that the Li⁺ transport kinetics of SnO/C-1 through the SEI film was faster. The polyhedral morphology of the MOFs was obtained by adjusting the reaction temperature in the relatively low temperature range of 0–75 °C, and the electrodes showed high reversible capacity and excellent rate capability. The results of this study can be extended to the synthesis strategy of precursors that control the shape of MOFs for the synthesis of MOF-derived nanomaterials with various structures and morphologies.

Lei et al. reported an N-doped carbon matrix derived from a core-shell ZIF featuring single-atom Co/Ni double active sites.⁴⁸⁹ Carbon materials derived from MOFs contain more pyridinic N, which is known to be able to better anchor and incorporate more favorable single-atom metals into the carbon matrix.⁴⁹⁸ For this reason, the core-shell ZIF-8@DNi-ZIF-67 structure, which starts from ZIF-8 followed by the introduction of cobalt(II) nitrate and dimethylglyoxime nickel (DNi), was used as the MOF precursor. DNi was adopted to create a Co/Ni single-atom double site and used as a Ni source in the shell construction process. These atoms took part in the coordination reaction, and some Co²⁺ of ZIF-67 was replaced by Ni²⁺ by ion exchange reaction, and which occupied the node positions forming the bimetal organic backbone of ZIF-8@DNi-ZIF-67. After high-temperature annealing and acid etching of ZIF-8@DNi-ZIF-67, N-doped carbon-based composites with hollow nanocage structures and single atom Co/Ni active sites were fabricated. The final product had a hollow dodecahedral nanocage (HDNC) structure and was named N-C@Co/Ni HDNC. It can be confirmed that numerous short-carbon nanotubes (CNTs) protruded from the surface of the dodecahedra due to the catalytic effect of Co/Ni nanoparticles, while the microstructure and morphology of the dodecahedra framework were maintained. CNTs can enhance the conductivity of composite materials and construct 3D conductive networks capable of facilitating fast electron and Li⁺ transport. From the TEM image in Figure 17C, it can be confirmed that the Co or Ni metals were uniformly embedded in the polyhedral carbon

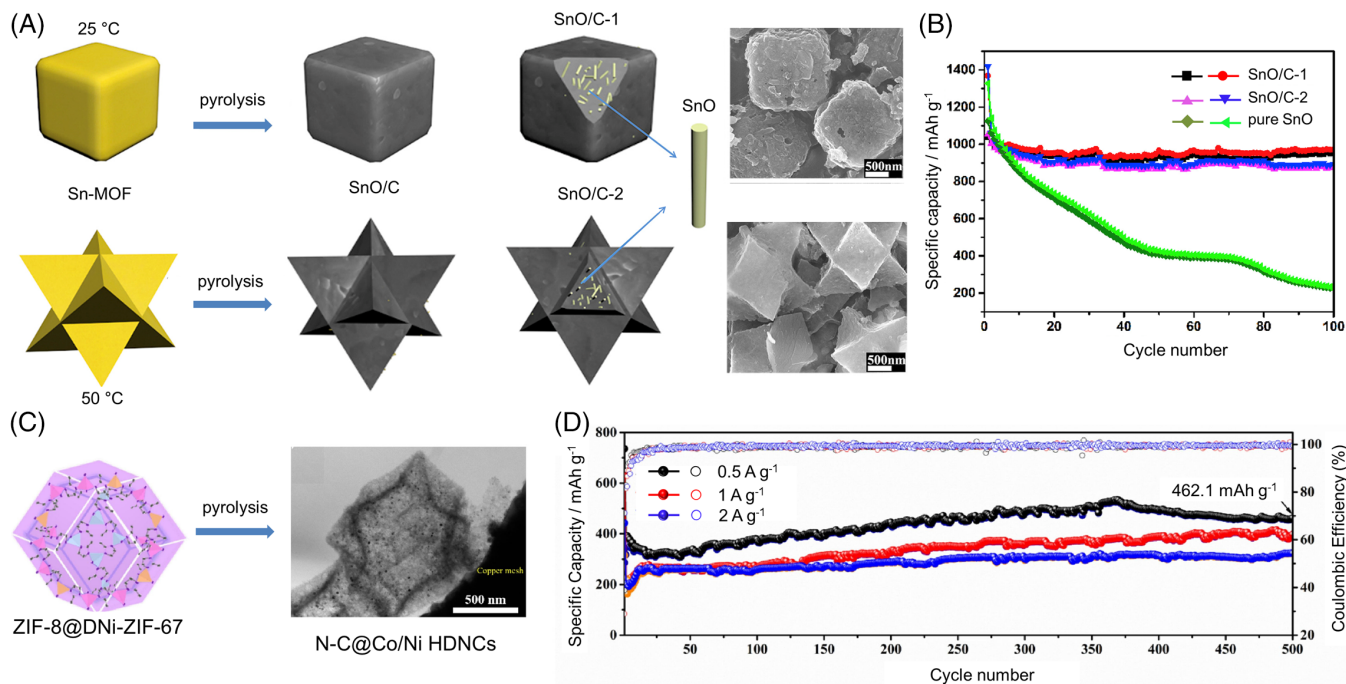


FIGURE 17 (A) Synthesis procedure for the Sn-MOF polyhedra and derivatives and SEM images of the product. (B) Cycling performances of the SnO/C polyhedral composites. Reproduced with permission.⁴⁸⁸ Copyright 2018, Elsevier. (C) Schematic illustration of the structure and TEM image of N-doped carbon-based composite with a hollow nanocage structure. (D) Cycling performance test and the corresponding Coulombic efficiencies of N-C@Co/Ni HDNCs. Reproduced with permission.⁴⁸⁹ Copyright 2021, Elsevier

skeleton with the formation of nanoparticles. The hollow structure is the preferred nanostructure for Li⁺ storage to reduce volume expansion. The ZIF-8 precursor can provide an abundant source of pyridinic N sufficient to anchor the Co/Ni, and at the same time, forming single-atom active sites with high loading. The abundant single-atom active sites can improve the catalytic activity of the electrode material, as well as changing the electronic structure of the N-doped carbon material, which favors the insertion and extraction of Li⁺ during cycling. Mesopores are present in N-C@Co/Ni HDNC, and the large surface area and rich pore structure are favorable for the fast transport of Li⁺/electrons and the penetration of the electrolyte. Utilizing this structural advantage, the N-C@Co/Ni HDNC composite showed excellent Li⁺ storage performance based on an investigation of the half-cell configuration. The image on the right in Figure 17D demonstrates the cycling performance of N-C@Co/Ni HDNCs at different current densities. After several tens of cycles, both charge and discharge capacities tend to increase, and at 369 cycles, the discharge capacity was at a maximum of 535.3 mAh g⁻¹ at 0.5 A g⁻¹. After 500 cycles at 0.5, 1, and 2 A g⁻¹, the discharge capacity was well continued without significant decrease. It can be inferred that the excellent cycling performance results from the synergy between the single Co/Ni atoms that modified the electronic structure of the N-doped carbon, the Li⁺ affinity of the composite material, and the favorable

nanostructure. The rate capability was also evaluated at various current densities, and the material showed good rate performance due to the swift insertion and extraction of Li⁺.

The multi-component TMO structure, which can diminish the diffusion length of Li⁺ and mitigate volume change during the Li⁺ insertion/extraction process, can provide improved abundant redox active sites and electrical conductivity. CNTs or graphene networks are mainly used for self-supporting 3D conductive anode materials that can expedite transport of electron and ion.^{499–503} They show significantly improved Li⁺ storage performance, compared to products without a conductive substrate. MOF-derived metal oxides have the disadvantages of low electrical conductivity and mechanical deformation. To overcome this, Han et al. reported an N-doped graphene network (NGN) structure derived from ZIF-67 with embedded Co₃O₄ particles.⁵⁰² The graphene sheets used in this study composed of 3D graphene aerogels synthesized from graphene oxide (GO) precursors through hydrothermal process,^{504,505} which have high conductivity, large surface areas, and hierarchical porous structures including macropores, mesopores, and micropores.⁵⁰⁶ A general strategy to fabricate Co₃O₄ embedded NGN (Co₃O₄@NGN) composite is schematically shown in Figure 18A. When inorganic Co²⁺ salts and N-doped graphene aerogel (NGA) are mixed, Co²⁺ was adsorbed on the graphene sheet. ZIF-67 microparticles are formed by

adding a MeOH solution with 2-methylimidazolate into NGA, and ZIF-67@NGA in which ZIF-67 is immobilized on the graphene surface is fabricated. When ZIF-67@NGA is calcined under air atmosphere, it is transformed into a Co_3O_4 @NGN composite. It can be confirmed that ZIF-67 particles about 600 nm in size are uniformly fixed on graphene sheets in the 3D architecture of NGA and embedded in the aerogel pores. NGA has a large amount of functional groups, which readily adsorbs metal ions to promote nucleation, and this application of the manufacturing method can be expanded to the preparation of ZIF-67 and other MOF@NGA hybrids. The Co_3O_4 @NGN composite exhibits a specific surface area of $50 \text{ m}^2 \text{ g}^{-1}$ and a total pore volume of $0.25 \text{ cm}^3 \text{ g}^{-1}$, which is lower than that of ZIF-67@NGA ($780 \text{ m}^2 \text{ g}^{-1}$ and $1.21 \text{ cm}^3 \text{ g}^{-1}$). The decrease in the pore volume and the specific surface area of Co_3O_4 @NGN composite compared to ZIF-67@NGA can be explained that it is because porous structure of ZIF-67@NGA partial collapse after calcination in air. Nevertheless, the result of high N adsorption suggests the presence of macropores and mesopores and the pore size distribution of the Co_3O_4 @NGN composite shows a broad hierarchical porous structure. A moderate surface area facilitates interfacial contact between the electrode and the electrolyte, and the hierarchical porous structure can buffer volume changes and promote Li^+ diffusion and electrolyte penetration. In addition, Co_3O_4 @NGN composites with a high N content can supply extra active sites and defects favorable for Li^+ storage.⁵⁰⁶ The electrochemical behavior of Co_3O_4 @NGN was analyzed over the voltage range of 0.01–3.0 V versus Li/Li^+ . The CE, which was 52.3% for the first discharge and charge capacity, rose to 97% in the fifth cycle and remained above 97% in subsequent cycles. The stable and reversible insertion/extraction of Li^+ leads to high CE, and it is because the volume expansion effect of Co_3O_4 was mitigated by the conductive network of N-doped graphene. As shown in the results on the right in Figure 18B, the average discharge capacities of Co_3O_4 @NGN at 100, 200, 400, 600, and 1000 mA g^{-1} were 1030, 924, 885, 785, and 681 mAh g^{-1} , respectively, which was higher rate performance compared to Co_3O_4 and NGN. The cycling performance showed a high first discharge capacity of 966 mAh g^{-1} at the current density of 200 mA g^{-1} , achieving a discharge capacity of 955 mAh g^{-1} even after 100 cycles. The superior electrochemical behavior of Co_3O_4 @NGN can be found for the following four reasons. First, N-doped graphene sheets have electronic properties and excellent electrical conductivity that can reduce the internal resistance of batteries. Second, the introduction of graphene prevents the agglomeration of Co_3O_4 , thereby buffering the stress caused by the volume changes and preserving splendid

cycling stability and rate performance. Third, the small size of Co_3O_4 nanoparticles derived from ZIF-67 shortens the diffusion paths of the electrolyte, improving the electrochemical active ability. Fourth, the hierarchical porous structure of the Co_3O_4 @NGN composite with macropores and mesopores provides a large electrode/electrolyte interface and also provides a large number of pores to facilitate the penetration of electrolyte and at the same time relieve the stress caused by the volume change of Co_3O_4 .

Fe_2O_3 and Fe_3O_4 are remarkable candidates for LIBs because of their excellent theoretical capacity and environmental friendliness, but, like most TMOs, their enormous volume expansion and low electrical conductivity result in significant degradation of their performance when they are applied as anode materials. Song et al. reported a rapid and simple way to fabricate porous carbon octahedral by using Fe-MOF/GO precursors.⁴⁹⁹ Most synthesis methods for preparing porous carbon composites derived from TMOs/MOFs involve high-temperature calcination, which consumes great amounts of energy and time, so they are not suitable for rapid preparation.^{507,508} In this study, $\text{Fe}_2\text{O}_3/\text{Fe}_3\text{O}_4$ @carbon/G nanocomposites ($\text{Fe}_2\text{O}_3/\text{Fe}_3\text{O}_4$ @C/G) were rapidly prepared by combusting Fe-MOFs/GO precursors with TEA. The manufacturing process for $\text{Fe}_2\text{O}_3/\text{Fe}_3\text{O}_4$ @C/G nanocomposite is shown in Figure 18C. GO was prepared by oxidizing graphite powder, which was dissolved in DMF solvent and then subjected to continuous sonication. Then, $\text{FeCl}_3 \cdot 6\text{H}_2\text{O}$ and BDC were added to the solution while stirring. In the process of stirring this mixture in an oil bath, Fe-MOFs was attached to the GO surface. The precipitate was collected by centrifugation, washed, and dried, and the obtained sample was named Fe-MOF/GO-X. (X is a number depending on the mass ratio of $\text{FeCl}_3 \cdot 6\text{H}_2\text{O}:\text{GO}$, $X = 5, 10, 20$). TEA was then added to the Fe-MOF/GO and combusted in air atmosphere to obtain porous $\text{Fe}_2\text{O}_3/\text{Fe}_3\text{O}_4$ @C/G nanocomposites. During combustion, some oxygen-containing groups are removed from GO with the formation of some active groups. TEA is burned and transformed into some active N, which reacts with the active groups in graphene to form pyridinic and pyrrolic structures.⁵⁰⁹ Combustion also releases a large amount of thermal energy, transforming Fe-MOF into $\text{Fe}_2\text{O}_3/\text{Fe}_3\text{O}_4$ @C. Fe-MOFs/GO-10 showed a clear octahedral structure, and it can be seen that the shape is maintained even after combustion. The surface area of $\text{Fe}_2\text{O}_3/\text{Fe}_3\text{O}_4$ @C/G was $19.9 \text{ m}^2 \text{ g}^{-1}$, which is larger than that of $\text{Fe}_2\text{O}_3/\text{Fe}_3\text{O}_4$ @C ($9.1 \text{ m}^2 \text{ g}^{-1}$). The pore sizes were 35.3 and 23.7 nm, respectively, and it can be seen from the pore size distribution that there are many mesopores. The pores provide more active sites and a larger surface, and can cushion the volume changes of

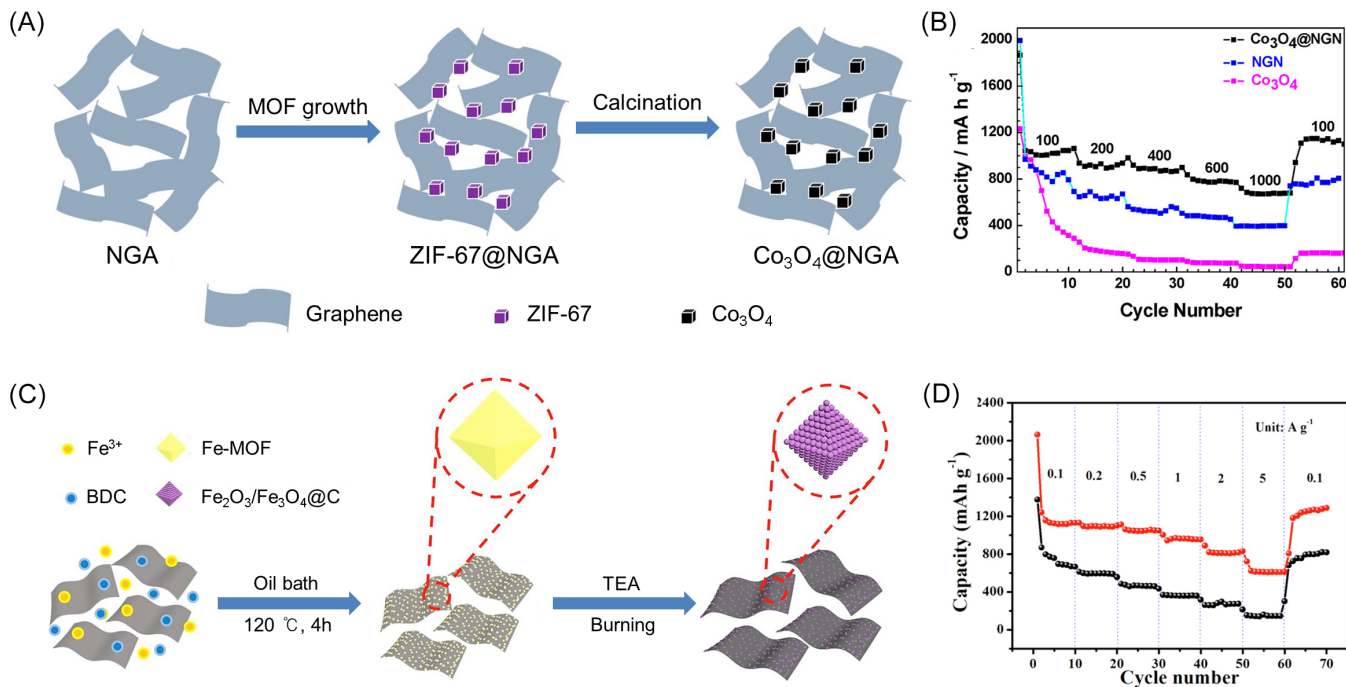


FIGURE 18 (A) Schematic illustration of the fabrication processes for hierarchically porous Co_3O_4 @NGN composite. (B) Rate capability of the as-prepared nitrogen graphene network (NGN), Co_3O_4 , and Co_3O_4 @NGN composite at various charge/discharge rates. Reproduced with permission.⁵⁰² Copyright 2017, American Chemical Society. (C) Schematic illustration of the preparation of $\text{Fe}_2\text{O}_3/\text{Fe}_3\text{O}_4$ @C/G nanocomposite. (D) Rate capability at different current densities of $\text{Fe}_2\text{O}_3/\text{Fe}_3\text{O}_4$ @C/G nanocomposite. Reproduced with permission.⁴⁹⁹ Copyright 2019, Elsevier

$\text{Fe}_2\text{O}_3/\text{Fe}_3\text{O}_4$ nanoparticles during insertion/extraction by improving transport pathways. The cycling stability of $\text{Fe}_2\text{O}_3/\text{Fe}_3\text{O}_4$ @C/G was evaluated at a current density of 0.5 A g^{-1} . $\text{Fe}_2\text{O}_3/\text{Fe}_3\text{O}_4$ @C/G exhibited a high initial discharge capacity of 1582 mAh g^{-1} and a charge capacity of 876 mAh g^{-1} , resulting in an initial CE of 55.4%. In the next cycle, the capacity increased again, achieving a CE of nearly 100% and retaining remarkable discharge capacity of 1210 mAh g^{-1} even after 200 cycles. This material showed stable cycling performance over 400 cycles, even at the high current density of 5 A g^{-1} . As shown in Figure 18D, $\text{Fe}_2\text{O}_3/\text{Fe}_3\text{O}_4$ @C/G exhibited discharge capacities of 1130, 1102, 1049, 954, 830, and 611 mAh g^{-1} at 0.1, 0.2, 0.5, 1, 2, and 5 A g^{-1} , respectively. The intact octahedral structure, even after the cycling test, indicates that the porous structure greatly relieved the structural deformation during cycling. The reason why $\text{Fe}_2\text{O}_3/\text{Fe}_3\text{O}_4$ @C/G has good performance can be explained as follows. First, the porous structure and nanoscale building units can mitigate the crushing and agglomeration of $\text{Fe}_2\text{O}_3/\text{Fe}_3\text{O}_4$ nanoparticles. Second, the electrically conductive network of 3D graphene coupled with $\text{Fe}_2\text{O}_3/\text{Fe}_3\text{O}_4$ provides a pathway for faster electron and ion transport. Third, the improvement of the content of N element and the synergistic effect of Fe_2O_3 and Fe_3O_4 after TEA combustion are advantageous for electrochemical properties.

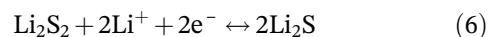
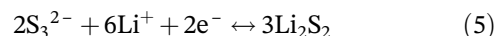
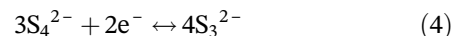
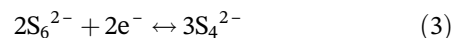
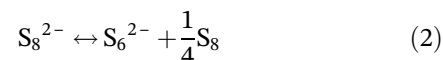
Besides TMO, transition metal sulfides,^{510,511} phosphides,⁵¹² nitrides,⁴⁴⁹ and selenides⁵¹³ derived from MOFs have been studied as anode materials for LIBs. In addition to the materials mentioned so far, sulfide is attracting attention as promising advanced materials for LIBs because of their excellent capacity and abundance in nature.⁵¹⁴ The low electronic conductivity and poor structural stability of sulfides during the charging/discharging processes, however, limit their actual specific capacity and cycling performance. One way to overcome this is to design novel porous sulfide composites, such as porous sulfide/carbon materials. Whang et al. synthesized reduced GO (rGO)@ CoS_x and CoS_x -rGO- CoS_x composites through thermal sulfurization of ZIF-67/GO precursors for use in LIBs.⁵¹⁰ The initial specific capacities of CoS_x -rGO- CoS_x and rGO@ CoS_x composites exhibited 1248 and 1320 mAh g^{-1} at the current density of 100 mA g^{-1} , respectively. They also showed stable cycling capacity after 100 cycles and good rate capability. Like sulfides, transition metal phosphides are also being studied as promising anode materials for LIBs. Most of their synthesis is conducted in a boiling organic solvent at a high temperature or through the reaction of a phosphorus source and a precursor placed in a separate location from the combustion boat, so they have not been widely applied. Their low intrinsic electrical conductivity prevents rapid chemical diffusion in the electrode.

Reducing the phosphide down to the nanoscale or coating a carbon layer could be a way to solve this problem.⁵¹⁵ Chen et al. synthesized cobalt phosphide nanoparticles (ZIF-67 derived $\text{Co}_x\text{P-NC}$) encapsulated in an N-doped carbon matrix using ZIF-67, a Co-based MOF, as its own template, and reported excellent electrochemical performance for LIB anode material.⁵¹² ZIF-67 derived $\text{Co}_x\text{P-NC}$ exhibited a high capacity of 1224 mAh g^{-1} at a current density of 0.1 A g^{-1} and an ultra-long lifespan of 1800 cycles. Table 4 summarizes recent studies in which MOFs or MOF derived materials were applied as the anode or cathode materials for LIBs.^{217,219,419,424–426,431,434,443,446,449,452–455,457,464,466,469,470,483,485–487,489,490,501,502,512,516–524}

So far, various research works on the application of MOF as anode or cathode materials for LIBs have been explained. The classes of MOFs suitable as the anode or cathode materials are as follows: (1) Unmodified MOFs applied as anode or cathode materials; (2) MOFs synthesized by changing a ligand that can provide an insertion site for Li^+ ; (3) MOFs with a modified morphology; and (4) MOFs as a platform for nanostructured TMO and carbon composites. There are two major problems, however: (1) Due to the high surface area and porosity, which are the most characteristic features of MOF-derived materials, the contact with the electrode/electrolyte interface is increased and the tap density is lowered, resulting in lower volumetric energy density and initial CE; (2) They use expensive precursors and also use high-energy synthesis processes such as high-temperature pyrolysis, which increases the manufacturing cost of MOF derived materials, limiting large-scale applications. Nevertheless, as demonstrated, future MOFs to be designed for applications in LIBs could be strategically improved by careful selection of properties such as porosity, composition, conductivity, and morphology. As a result, they are likely to offer a great advantage from the increased electron/ion storage capacity, so MOFs have potential as advanced materials for next-generation LIBs.

4.2 | Li-sulfur battery

The LSB with a high energy density of about 300 Wh kg^{-1} , a high theoretical capacity of about 1675 mAh g^{-1} , and easy supply and demand to use sulfur (S) that is abundant in nature, has received considerable attention as a rising candidate for next-generation lithium storage devices following LIBs.⁵²⁵ Different from LIBs, the Li-S cathode has an unusual theoretical specific capacity (1675 mAh g^{-1}) due to the multi-electron conversion of elemental S to polysulfides. The working principle of the LSB is as follows.



The practical application of LSBs is limited by several issues, however: (1) The insulating properties of discharge products such as Li_2S_2 and Li_2S slow the electrochemical reaction, resulting in lower S utilization and poor performance; (2) The high solubility of long chain polysulfides in the electrolyte causes an internal “shuttle” phenomenon, which leads to irreversible loss of active material due to low charging efficiency and rapid capacity fading; (3) Large volume change during cycling, up to about 80%, crush the cathode and separates the S from the conductive matrix and result permanent capacity loss. In this regard, MOFs and MOF-derived materials with tunable pore structures and compositions have great potential to solve few issues mentioned above by providing optimized pore spaces and an optimized chemical environment to store S, limit polysulfides, and accommodate volume changes. MOF-derived carbon materials not only promote electron transport and host S, but also can physically and chemically capture the polysulfide molecules during electrochemical processes due to their high electrical conductivity, high pore volume, and features that allow heteroatom (e.g., N, S, and O) doping. MOFs are mainly applied in the cathode and separator in LSBs. Figure 19 explains the application parts of MOF-based materials to LSB before detailed explanation, and the characteristic and noticeable factor of MOF, which plays a key role in this case.

The first reports of the use of MOFs in LSB were studies in which MIL-100(Cr) was used.⁵²⁶ In this study, Tarascon et al. used highly porous MIL-100(Cr) as a host material for S impregnation. This material consisted of oxocentered trimers of Cr octahedra linked with 1,3,5-benzenetricarboxylate ligands, and it was shown to be a good alternative substance for encapsulation of S and equivalent reduction state species due to its large pore volume and small window limiting the diffusion process. Using the melt-diffusion process, S permeated/integrated MIL-100(Cr) composites were created (denoted as MIL-100(Cr)/S@155, where 155 refer to the

TABLE 4 Summary of recent studies in which MOFs or MOF derived materials were applied in the anode or cathode of LIBs.

MOF	Application part	Reversible capacity (mAh g ⁻¹)	Rate (mA g ⁻¹)	Cycle number	References
MIL-53 (Fe)	Cathode	70	0.025 C	—	419
L-101 (Fe)	Cathode	72	0.2 C	100	424
Cu(2,7-AQDC)	Cathode	105	1 mA s ⁻¹	50	425
Cu-TCA	Cathode	45	2 C	200	426
Fe-BTC MOF	Anode	120	30	35	434
Co ₃ (1,3,5-BTC) ₂	Anode	1020	100	100	454
Mn[Fe(CN) ₆] _{0.6667} ·nH ₂ O	Anode	473	2000	500	455
Mn-1,4-BDC	Anode	295	200	100	466
Cu ₃ (BTC) ₂	Anode	974	100	100	452
Co ₂ (OH) ₂ BDC	Anode	474	383	50	453
Co-TFBTC	Anode	435	1000	1000	464
NNU-11	Anode	1074	100	50	457
Zn ₃ (HCOO) ₆	Anode	750	50	200	516
Mn-BTC MOF	Anode	560	60	60	517
MOF-177	Anode	694	103	100	217
MOF-5	Anode	105	—	—	443
Co-MOF	Anode	1200	75	50	519
PB	Anode	1192	200	100	520
Co-MOF derived porous Co ₃ O ₄ nanosheets	Anode	300	20 000	2000	521
PCFO-NC CoFe ₂ O ₄ nanocubes	Anode	152	2500	500	483
Zn _x Co _{3-x} O ₄ hollow nanoboxes	Anode	1141	500	800	486
N-C@Co/Ni HDNCs	Anode	462	500	500	489
Sn-based MOFs	Anode	950	50	100	488
leaf-Co ₃ O ₄ /GF	Anode	986	100	250	501
ZIF-67-derived Co ₃ O ₄	Anode	955	200	100	502
ZIF-8 derived ZnSNR@HCP	Anode	840	600	300	524
ZIF-67 derived Co _x P-NC	Anode	820	100	100	512
PB	Anode	945	200	30	522
PB	Anode	500	200	100	523
ZIF-8	Anode	699	500	100	446
ZIF-67	Anode	1200	200	400	219
MIL-88	Anode	980	200	400	219
Zn-Co-ZIF	Anode	990	100	50	487
Ni ₂ Fe(CN) ₆	Anode	1071	1 C	200	485
MIL-125(Ti)	Anode	310	2000	400	449
PBA Co ₃ [Co(CN) ₆] ₂	Anode	1465	300	50	431
N-rich Co-MOF	Anode	612	1000	500	470
N-doped carbon nanoweb Fe-ZIF	Anode	1741	1C	600	469

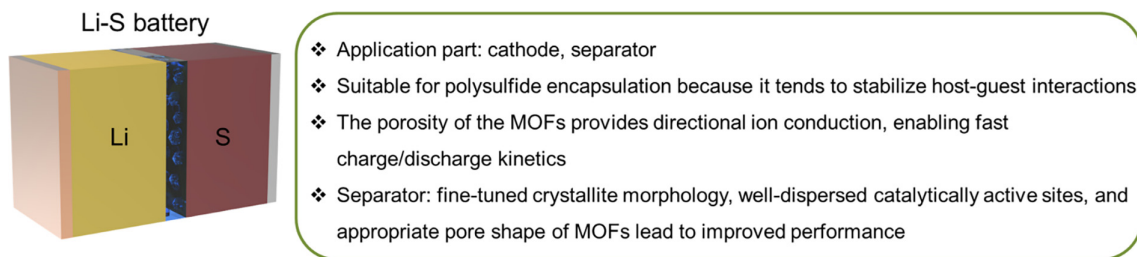


FIGURE 19 MOF-based materials applied in LSB components and notable features of MOFs, that play important roles in LSBs

heating temperature) and increased capacity was observed. Galvanostatic discharge–charge analysis was performed to estimate the electrochemical performance of the MIL-100(Cr)/S@155 composite. The MIL-100(Cr)/S@155/carbon showed excellent reversible capacity, which could be attributed to the unique pore shape (large pores but small windows) of MIL-100(Cr), and this inherently slowed down the diffusion of polysulfides.

The structures of MOFs are suitable for polysulfide encapsulation because they tend to stabilize host-guest interactions. Adjustable pore shapes and sizes can promote Li^+ diffusion, which is important for fast charging and discharging.⁵²⁷ Furthermore, the large volume expansion of S when reduced to Li_2S can accommodate due to the open and flexible structure of the MOFs. Therefore, the addition of MOFs to the cathode of an LSB could be a promising way to mitigate polysulfide leaching. Therefore, studies using MOFs to encapsulate S continued. After the first use of MIL-100(Cr), a LIB study using HKUST-1 was reported in 2013.⁵²⁸ HKUST-1, which has a medium pore space and open metal sites for enhanced S confinement, was used as the host material to trap S and reduce dissolution problems. HKUST-1 containing S (denoted as HKUST-1 \supset S) was prepared by heating sublimated S and activated HKUST-1. The crystal structure of HKUST-1 \supset S confirmed that a large amount of S could be trapped inside due to the appropriate pore space and open Cu^{2+} sites of HKUST-1. HKUST-1 \supset S showed a large initial discharge capacity of 1498 mAh g^{-1} due to the excellent electrical conductivity of Ketjenblack, and then it continuously suffered an irreversible decrease in capacity during the first 50 cycles, although from the 170th cycle, the capacity of 500 mAh g^{-1} remained almost unchanged. The strong binding of HKUST-1 to S played the most key role in the excellent performance of HKUST-1 \supset S cathode. As the pore structure and size within the porous MOFs can be systematically tuned and the functional sites can be reasonably tuned to recognize S, this material may offer potential and an alternative strategy as a novel cathode material for LSBs.

Studies using ZIF-8, one type of MOF, as a cathode material for LSBs have also been reported. In general, cage-shaped pores are more suitable for S encapsulation than straight channels.⁵²⁷ In 2014, Qian et al. reported the notable cycling characteristics that could be obtained by using ZIF-8 with cage-shaped pores.⁵²⁹ The dissolution of polysulfide was successfully mitigated due to the strong restraining effect on the S inside, with the cathode showing high capacity of 510 mAh g^{-1} at a 0.1 C after 100 cycles. Li et al. confirmed the S encapsulation characteristic of ZIF-8 compared with HKUST-1 and MIL-53 (Al).⁵³⁰ ZIF-8 showed the best capacity retention of 553 mAh g^{-1} at 0.5 C after 300 cycles and outstanding rate capability, which was due to the small window size of 3.4 \AA and the small and uniform particle size of 100–200 nm.

In 2015, Li et al. not only applied ZIF-8 as a cathode material for LSBs, but also conducted a study on the effects of ZIF-8 particles in LSBs.⁵³¹ A previous study had shown that decreasing the size of the active material can greatly facilitate the insertion and extraction of Li^+ due to the shorter distance for Li^+ transport within the particle.⁵³² The particle size of the host material affects both the transport and leaching properties of the polysulfide, which in turn affects the utilization and retention of S. In this study, ZIF-8, which had been proven to be promising for S storage in the LSB cathode, was selected as the prototype for proof-of-concept, and the size effect was investigated using ZIF-8 with various particle sizes. ZIF-8 particles with five different sizes, $\sim 2 \mu\text{m}$, $\sim 800 \text{ nm}$, $\sim 200 \text{ nm}$, $\sim 70 \text{ nm}$, and $\sim 15 \text{ nm}$, were synthesized by the solution synthesis method. A fast nucleation rate tends to produce small nanoparticles with a short reaction time, and a slow nucleation rate tends to produce large crystals with a long reaction time. Figure 20A shows a schematic model of a S@ZIF-8 particle under discharge. Unlike porous carbon and some conductive oxides, the S host ZIF-8 itself is not electrically conductive, so the electrochemical process occurs mainly in outer surface of the ZIF-8 particle which is active material can access both Li^+ delivering phase and electron delivering phase. The

small particle size, which promotes better contact with conductive additive, helps to increase the utilization of S by promoting electron/ion transport in short dimensions and consequently yields a maximum capacity. The prepared ZIF-8 composite was used as a cathode material and galvanostatic discharge-charge tests were performed at 0.5 C (837 mAh g⁻¹, based on S). In the high-voltage region, the delivered capacity is larger in the small size (~15 nm) compared to the large particle size (2 μm). The capacity ratio between the low voltage and high voltage regions increased from 2.50 (2 μm) to 2.85 (15 nm), confirming that the S was more thoroughly reduced in smaller ZIF-8 particles. Therefore, it is advantageous for the porous host to have a small particle size from the standpoint of maximizing S utilization. In the long-term cycling performance results of Figure 20B, ZIF-8 with a particle size of 15 nm showed a high capacity of 968 mAh g⁻¹, and ZIF-8 with a particle size of 2 μm reached a maximum capacity of 489 mAh g⁻¹. It can be seen that as the particle size increases, the maximum value of capacity is reached decreases. On the other hand, fading showed a different trend. Although fast fading was observed in small size samples, stable cycling was not achieved in large size samples with slow fading. Instead, the moderately sized 200 nm ZIF-8 provided superior capacity retention. There is an optimal “golden size” with less average attenuation while capacity is kept to a maximum. When the discharge starts, the S stored in the pores near the outer surface is first dissolved and then reduced to soluble higher-order polysulfides. The reduced polysulfide reduces the active material through indiffusion and allows it to escape from the leaching by ZIF-8. When ZIF-8 particles are large, it takes a long time for the initially formed polysulfides to transfer electrons and Li⁺ to the internal S. On the other hand, the ZIF-8, which has been reduced in size to a certain level, can react with S in the internal region to efficiently consume polysulfides through internal diffusion. A further reduction in the particle size of ZIF-8 (<20 nm) results in the rapid generation of many polysulfides, which can provide high doses, but quickly leave the porous host, as it has many external surfaces from which to escape. Thus, the polysulfide confinement effect created by the porous host eventually disappears. Therefore, the particles smaller than the “golden size” do not help to optimize the function of the porous host for cycling stability. The conclusion of this study suggests that it is necessary to find the optimal particle size that can maximize the utilization of S without sacrificing cycling stability, and it is expected that it will apply to other porous systems.

In a similar vein, Qian et al. demonstrated that MOF-525 has excellent performance as a cathode material

among S/MOF composites.⁵³³ The structure of MOF-525 (M) used in the study and MOF-525 host impregnated with S are shown in Figure 20C. MOF-525(2H) consisted of Zr₆(OH)₄O₄ clusters linked by MTCPP (M: H₂, Fe, Cu) ligands, while the materials composed of metal clusters of FeCl and Cu linked by TCPP ligands were called MOF-525(FeCl) and MOF-525(Cu) respectively. Zr₆(OH)₄O₄ clusters have the coordination of Zr(IV) atoms filled with O atoms, but the Zr(IV) centers cannot possible to supply accessible Lewis acid sites (LAS). To study the effect of LAS on LSB performance, MOF-525(2H), a material without a central metal site, and MOF-525(FeCl), and MOF-525(Cu), materials with metal sites, were compared. They can provide 0, 1, and 2 Lewis acid sites for S binding and including, respectively. MOF-525 series has cubic-shaped crystals structure, and the S impregnation of the MOF host was carried out through the melt diffusion method, which has the lowest viscosity for liquid S (expressed as S@MOF-525(M)). The unique pore structure and accessible sites of the MOF-525 series play an important role in S containment. Electrochemical tests of S@MOF-525 (2H), S@MOF-525(FeCl) and S@MOF-525(Cu) were performed to investigate the effects of LAS in MOF hosts on LSB performance. S@MOF-525(Cu) provides two possible to access sites per Cu²⁺ metal ion, making it valuable for S containment, and it showed improved electrochemical performance. Figure 20D shows the cycling performance of S@MOF-525(2H), S@MOF-525(FeCl), and S@MOF-525(Cu) at 0.5 C. After 200 cycles, the reversible capacities of S@MOF-525(2H), S@MOF-525(FeCl), and S@MOF-525(Cu) were 402, 616, and 704 mAh g⁻¹, respectively. S@MOF-525(2H) underwent rapid capacity decline during cycling, but the capacities of S@MOF-525 (Cu) and S@MOF-525(FeCl) only decreased 0.07% and 0.09% per cycle after the 10 cycles, respectively. S@MOF-525(FeCl) and S@MOF-525(Cu) showed good capacity recovery capability as well as high reversible capacity. The Lewis acid metal sites of S@MOF-525(FeCl) and S@MOF-525(Cu) have strong interactions with S, and these interactions can confine the S in the host, improving the cycling performance.

Previously, it was reported that mesopores with cage-like shape and pores with cross-like shape are advantageous for polysulfide imprisonment and Li⁺ diffusion,^{530,534} and this can be further improved by introducing polysulfide-interacting polarity to the pore surface. There have been studies applying MOFs composed of organic ligands with open metal moieties (OMS) or Lewis basic functional groups to host materials.^{533,535,536} Previous studies have shown that open metal sites in MOFs such as HKUST-1,⁵²⁸ Ni₆(BTB)₄(BP)₃ (BTB = 1,3,5-tris(4-carboxyphenyl)benzene, BP = 4,4'-

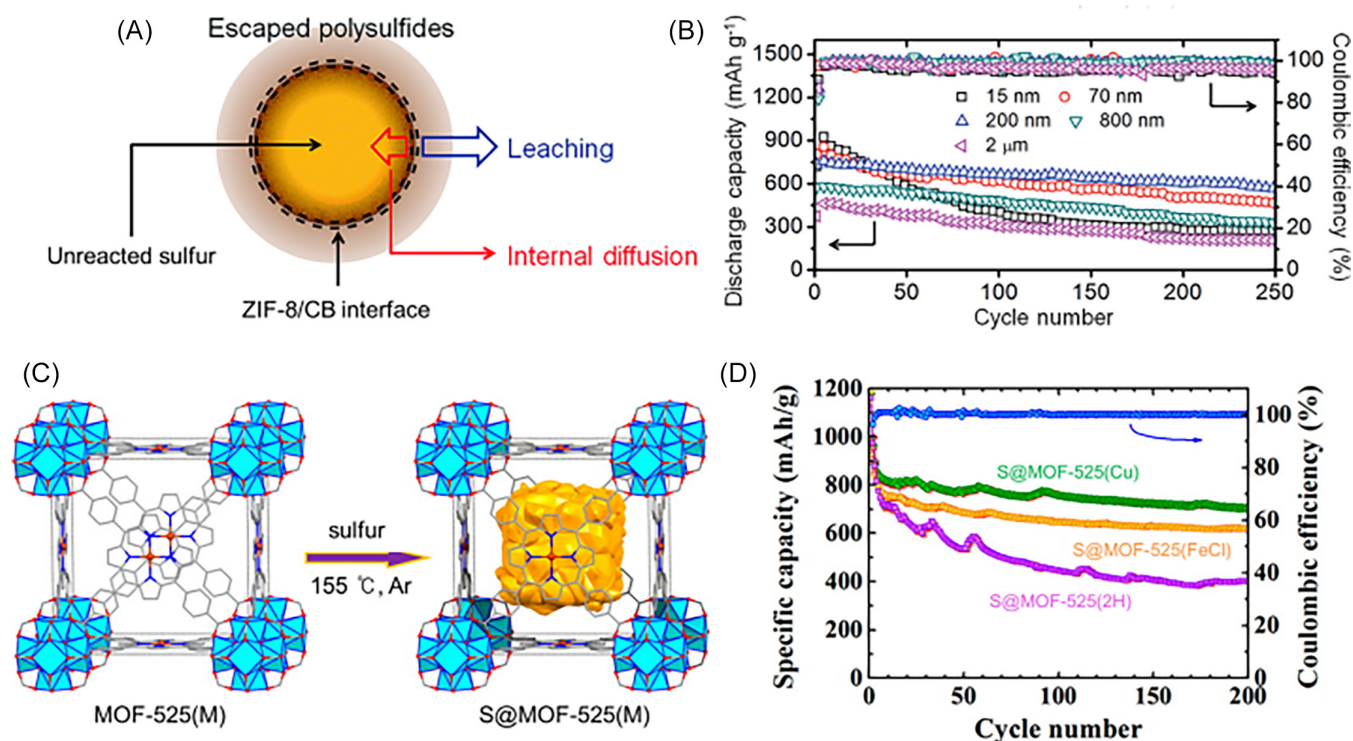


FIGURE 20 (A) Schematic illustration of S@ZIF-8 particle in discharge. The utilization of sulfur and its retention are determined by the internal diffusion and leaching of the polysulfides, respectively. (B) Long-term cycling performance at 0.5 C over 250 cycles for various particle sizes. Reproduced with permission.⁵³¹ Copyright 2015, ROYAL SOCIETY OF CHEMISTRY. (C) Schematic illustration of S@MOF-525(M) synthesized through the melt-diffusion method (M = 2H, FeCl, Cu). (D) Cycling performance and Coulombic efficiency of S@MOF-525(2H), S@MOF-525(FeCl), and S@MOF-525(Cu). Reproduced with permission.⁵³³ Copyright 2015, American Chemical Society

bipyridine),⁵³⁷ MOF-525,⁵³³ and Cu-TDPAT (H₆TDPAT = 2,4,6-tris(3,5-dicarboxylphenyl-amino)-1,3,5-triazine)⁵³⁵ can act as Lewis acidic sites and supply chemically compatible interaction with S and polysulfides. To further increase the affinity with negatively charged polysulfides, framework with coordinately unsaturated metal moieties used.^{536,538} Park et al. investigated 16 different metal substitution types of M2(dobdc) (dobdc = 1,4-dioxido-2,5-benzenedicarboxylate) computationally for the ability to anchor S₈, Li₂S₄, and Li₂S, and the calculation results confirmed that the dominant adsorption sites in the MOFs are the coordinately unsaturated metal sites.⁵³⁸ In the Li₂S₄ chain, the S atom is in contact with the OMS, while the terminal Li atom tends to get closer to the organic moiety (e.g., the oxygen anion or nitrogen group of the ligand).

Despite these advantages and possibilities, the practical applications of MOFs in LSBs are severely limited by their low electrical conductivity. This causes several serious problems, including slow redox reaction rates and limited S utilization, which results in reduced cycling stability and rate capability. The effective utilization of active S is limited due to the insulating properties of S and Li₂S, so conductive additives must be used for electrical contact. Conductive additives mainly used for

combining with MOF/S composites are carbon materials (e.g., rGO and CNT) and polymers (e.g., polypyrrole and poly[3,4-ethylenedioxythiophene]).^{527,534,539,540} Lin et al. presented thin film type MOF/CNT composite with interpenetrating 3D conductive network and a unique hierarchical porous structure, which not only improved the conductivity of the MOF, but also applied it in a foldable battery structure.⁵⁴⁰ By solid-precursor assisted-confinement conversion process, a hierarchically porous MOF/CNT composite thin film was prepared.⁵⁴¹ The MHN/CNT composite thin films were obtained by combining metal hydroxide nanostrands (MHN) and CNT, and immersed in organic ligand solution to obtain flexible MOF/CNT composite thin films. To analyze the effect of MOF pore size on LSB performance, HKUST-1, MOF-5, and ZIF-8 based CNT composite thin films with entrance sizes of 0.9, 0.8, and 0.34 nm, respectively, were prepared. All MOF/CNT composite films exhibited a typical layered structure with excellent self-support and foldability. Through large cavities of HKUST-1 and MOF-5, S₈ can easily access, whereas the cavity of ZIF-8 is difficult to access due to its comparative small entrance as shown in Figure 21A. The typical S mass content of S@MOF/CNT electrodes for coin cell cycling is ~40 wt%. The reason why no apparent crystalline S was not formed

after S loading is good pores were occupied by S in the MOFs. The cycling behavior of S@HKUST-1/CNT, S@MOF-5/CNT, and S@ZIF-8/CNT cathodes with a S loading of 1 mg cm^{-2} ($\sim 40 \text{ wt\%}$) is shown in Figure 21B. The S@MOF-5/CNT cathode indicates stable cycling behavior similar to the S@HKUST-1/CNT cathode, whereas the S@ZIF-8/CNT cathode exhibits much faster capacity fading during cycling. S in the form of an S_8 ring with a diameter of 0.68 nm is loaded into the MOFs thin film.⁵⁴² In ZIF-8 with an entrance size of 0.34 nm,⁵⁴³ S_8 is impossible to introduce and is dispersed on the surfaces of the ZIF-8 particles, which results in poor reaction rates, low S utilization, and fast capacity fading. On the other hand, MOF-5 and HKUST-1 have a comparative larger entrance size than S_8 molecules, which allows for easy access to pores and advantageous for uniform S bonding, and consequently acts favorably for electrochemical reactions. MOF-5 has a slightly smaller entrance size compared to HKUST-1, so less amount of S_8 loading inside the pore and more of S_8 loading on the exterior surface, resulting in faster capacity decline during initial few cycles. CNTs interpenetrate the MOF crystals to ensure easy access of electrons to the trapped S species, and enable excellent electron transport within the electrodes through conductive connections. The MOF/CNT composite thin film structure proposed in this study maintained limited active S electrical connections and accommodated large volume changes during cycling, giving the electrode excellent flexibility and integrity. As a result, the possibility of designing MOF-based flexible energy storage systems is presented.

In addition to CNTs, studies have also been reported to enhance the conductivity of MOFs by using conductive polymers and applying them in LSBs. Deng et al. designed a ppy-S-in-MOF structure by wrapping three MOFs containing S (S-in-MOF, MOF = MIL-53, MIL-101 and PCN-224) with the conductive polymer ppy.⁵²⁷ Ppy is a conductive polymer with the chemical formula $\text{H}(\text{C}_4\text{H}_2\text{NH})_n\text{H}$ and is widely used in electronics, optics, biology, and medicine. The proposed ppy-S-in-MOF is achieved in three steps, as shown in Figure 21C. First, each MOF is synthesized by a solvothermal reaction method, and then the solvent is removed in a vacuum to activate it. Subsequently, S molecules were successfully introduced into the pores of MOFs quantitatively via melt diffusion at 155°C , and the morphology of the MOF crystals was preserved. Finally, ppy-S-in-MOF was obtained by encapsulating the S-in-MOF sample with ppy via a solution-based chemical oxidative polymerization process. Electrical conductivity was measured by the two-electrode method and the conductivity of the pristine MOFs ranged from 1.4×10^{-5} to $5.7 \times 10^{-5} \text{ S m}^{-1}$. After improvement to the ppy-S-in-MOF structure, the

conductivity was 3.1×10^1 , 1.2×10^2 , and 6.7 S m^{-1} for ppy-S-in-MIL-101, ppy-S-in-MIL-53, and ppy-S-in-PCN-224, respectively, which showed a dramatic improvement of 6–7 times. Fine S particles coated with ppy (ppy-S), S-penetrated porous BP2000 (S-in-carbon), and S-impregnated MOF without ppy (S-in-MOF) were used as controls for electrochemical characterization. As shown in Figure 21D, discharge capacities of the ppy-S-in-MIL-53 cathode exhibited 1420, 1080, 960, and 830 mAh g^{-1} at rates of 0.1, 0.3, 0.5, and 1.0 C, respectively, which is higher performance than that of the S-in-MIL-53 cathode. The cycling performance of ppy-S-in-MIL-53 at the 0.5 C rate was 82% higher than that of S-in-MIL-53, maintaining a high capacity of 900 mAh g^{-1} after 100 cycles. Similar improvements in electrochemical performance were also observed for ppy-S-in-MIL-101 and ppy-S-in-PCN-224 compared to their original MOF counterparts. This demonstrates the importance of solving the conductivity problem in electrochemical applications of MOFs. In particular, among the three MOF composites, Zr-based PCN-224 with a porphyrin linker showed the best long-term battery performance even at the high current density of 10 C. In this study, it was confirmed that MOFs with short Li^+ transport pathways and large pores are suitable for long-term cycling stability under the high-rate operation of LSB, which showed that improving the conductivity of MOFs can broaden the scope of their electrochemical applications.

In addition to the combination of MOF/S composites and conductive additives, discover of MOFs which have electrically conductive opened up a new avenue for finding the optimal S host material for LSBs.⁵⁴⁴ In this study, first-principles calculations showed that Cu-benzenehexathial (BHT) satisfied the requirements of an ideal S host material for LSBs. The strong affinity of Cu-BHT for polysulfides can prevent the dissolution of polysulfides into the electrolyte. In addition, the directional deposition of Li_2S is advantageous for increasing the utilization of the active material and improving the fast conversion between Li_2S and Li polysulfides.

The insulating properties of MOFs can be advantageous when applied to separators in LSBs. This is because the use of multifunctional separator coatings to improve the performance of LSBs has recently proven to be an effective approach.^{545,546} The fact that most membranes, however, reported have irregular pore sizes and distributions that are difficult to control is problematic. In addition, modifying the surface by immobilizing various organic functional groups is also a challenge to promote ionic conductivity and achieve excellent interfacial properties.⁵⁴⁷ A separator coating material with a simple manufacturing process that suppresses the shuttle effect of polysulfides very efficiently but without compromising

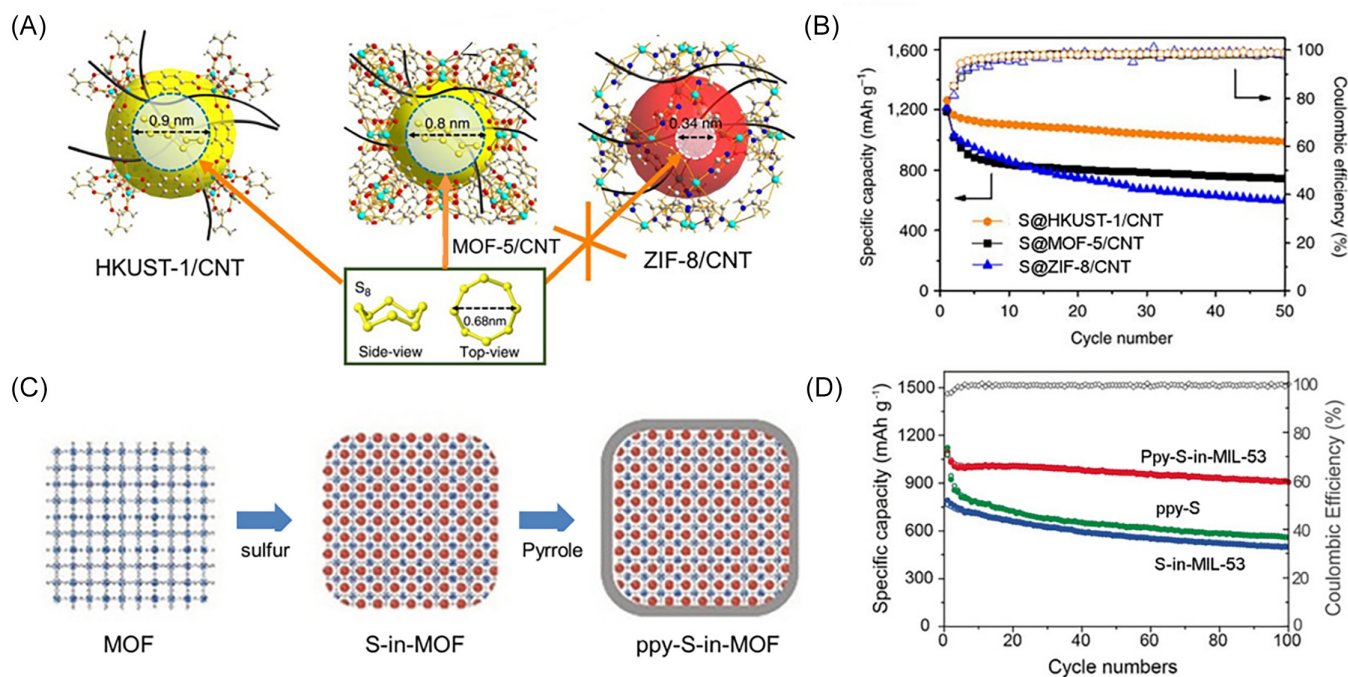


FIGURE 21 (A) Structure and pore entrance of HKUST-1/CNT, MOF-5/CNT, and ZIF-8/CNT. S₈ can easily access the cavities of HKUST-1 and MOF-5 through their large entrances, whereas the cavity of ZIF-8 is difficult to access due to its relatively small entrance. (B) Cycling performances of S@HKUST-1/CNT, S@MOF-5/CNT, and S@ZIF-8/CNT electrodes, respectively. Reproduced with permission.⁵⁴⁰ Copyright 2017, Springer Nature. (C) Schematic diagram showing the synthesis step of ppy-S in a MOF containing polypyrrole (ppy), a conductive polymer. (D) Cycling performance of ppy-S-in-MIL-53, ppy-S, and S-in-MIL-53 at the rate of 1.0 C in 100 cycles. Reproduced with permission.⁵²⁷ Copyright 2018, WILEY-VCH

Li⁺ transference is still highly desirable for realizing practical applications of LSBs. MOF-based separators have been developed as “ionic sieves” to transport Li⁺ while inhibiting the migration of solubilized polysulfides to the anode. Moreover, MOFs with highly ordered and tunable pore structure is advantageous in inhibiting the migration of soluble polysulfides as separators. Zhou et al. reported a MOF@GO membrane with 3D channels and 9 Å-sized aligned micropores through the combining of HKUST-1 with GO.⁵⁴⁸ An LSB fabricated using HKUST-1@GO membranes with mesoporous, S/carbon cathodes showed improved cycling stability with a capacity reduction of 0.019% per cycle during 1500 cycles. The results showed that HKUST-1 based separators can act as ionic sieves in LSBs to selectively filter Li⁺ ions while effectively inhibiting migration of unwanted polysulfides towards the anode. Park et al. coated PE membranes with sulfonated UiO-66 (UiO-66-S) and Nafion as functional separators for LSBs.⁵⁴⁹ The reason why UiO-66-S was used is as follows: (1) The pore sizes are much smaller than those of polysulfides (S_n²⁻, 4 < n ≤ 8); (2) Presence of sulfonated derivatives that promote electrostatic repulsion of polysulfide anions; (3) UiO-66-S promotes ion conduction for low polarization. An LSB cell with a UiO-66-S/Nafion hybrid coated separator exhibited capacity retention of 75.5% over 200 cycles and displayed a

discharge capacity of 1127.4 mAh g⁻¹ at 0.1 C. Because of the improved the redox kinetics and the reversibility, electrochemical properties with sharpest redox peak, the lowest voltage hysteresis of 0.20 eV, and high OCV retention of 98.4% were obtained. After the cycling test, the effect of preventing polysulfide dissolution of the UiO-66-S/Nafion hybrid-coated separator was confirmed by visually identifying and analyzing the surface and time-dependent morphological changes of the Li anode and rGO/S cathode. Consequently, the UiO-66/Nafion hybrid-coated separator improved the electrochemical performance of LSBs by inhibiting polysulfide transport. Zhou et al. fabricated a separator for LSB application using HKUST-1 and PVDF-co-hexafluoropropylene (PVDF-HFP), denoted as HKUST-1@PVDF-HFP membrane.⁵⁵⁰ Fabricated by multiple filtering of HKUST-1 and PVDF-HFP, this membrane was flexible. And it also inhibited polysulfides through physical barriers and lead to uniform Li deposition. Thus, the LSB with HKUST-1@PVDF-HFP membrane exhibited a high initial capacity of 1192 mAh g⁻¹ and maintained a reversible capacity of 802 mAh g⁻¹ even after 600 cycles.

Li et al. studied comparison of electrochemical performance of various MOF-based separators, including HKUST-1, ZIF-8, ZIF-7, and Y-FTZB ([Y₆(μ₃-OH)₈]¹⁰⁺ clusters with FTZB²⁻ 2-fluoro-4-(tetrazol-5-yl)benzoate)

ligands). Because they have different pore sizes and chemical structures, their effects on stability and shuttle inhibition during electrochemical cycling of LBS were studied.⁵⁵¹ Figure 22A shows the structure and SEM image of the four different types of MOFs used in this study, and the configuration of the battery. Because the size and shape of the MOF particles are different and varied, interfacial structure with MOF-based separator appear significantly different. The structures based on Y-FTZB consist mostly of large particles covering the surface area, so that the boundary space is densely filled with smaller particles, eventually forming a seamless dense film. While HKUST-1 exhibits a dense packing morphology, ZIF-7 and ZIF-8 layers have a regular stacking morphology due to well-defined grain size and shape. The ability of various MOF-based separators was evaluated from their cycling performance and rate, as shown in Figure 22B. LSBs with Y-FTZB coated separators showed the highest initial discharge capacity of 1101 mAh g⁻¹, followed by those of 1032, 1025, 989, and 925 mAh g⁻¹ for the samples with HKUST-1, ZIF-7, ZIF-8, and no MOF separator, respectively. The MOFs deposited on the separator acts as an additional barrier layer that suppresses the shuttle effect of polysulfides. After 300 cycles, the batteries configured based on Y-FTZB separators retained good capacity of 557 mAh g⁻¹, while the other batteries configured based on HKUST-1, CNT, ZIF, and ZIF-8 separators, respectively showed the capacity of 197, 380, 403, and 452 mAh g⁻¹. As shown in Figure 22C, the LSB with a Y-FTZB based separator presented a high capacity of 1480 mAh g⁻¹ at 0.1 C and maintained capacity of 987 mAh g⁻¹, even when the rate was increased to 0.25 C. In contrast, low CE and rapid capacity loss were showed in the LSB using the HKUST-1 separator. By analyzing the differences in electrochemical behavior, this tendency was explained in relation to the chemical stability. In the CV results, the battery using the Y-FTZB separator showed a relatively sharp peak, and the potential change with the scan rate was the smallest, proving its remarkable performance for the LSB. In addition, batteries with Y-FTZB separators have low Ohmic resistance values, indicating that polysulfides can return to the anode without migrating towards the cathode due to the dense layer. In the case of ZIF-8 and ZIF-7-based separators, the pores are not dense and abundant, making it difficult for polysulfide to penetrate into the anode, and reacts with metallic Li to form solid-phase Li₂S₂ and Li₂S. They are deposited on the Li surface, increasing the resistance and causing performance degradation. Since the HKUST-1 layer was denser than the ZIF-8 and ZIF-7 layers, more polysulfides were blocked. This study showed that different types of MOF-based separators can be applied to LSBs for suppression polysulfide shuttling,

thereby improving electrochemical performance. It is expected that the mechanism and analysis suggested here can be helpful in the development of advanced MOF-based separators in the future.

A barrier layer that improves performance by blocking the diffusion of polysulfides⁵⁵²⁻⁵⁵⁴ must satisfy the following conditions: (1) A layer should be crack-free and continuous membrane with a uniform pore structure; (2) They must be light and thin enough to prevent a reduction in the overall S content of the LSB; (3) A barrier layer must have high conductivity to act as an extended current collector. Fang et al. reported a study of using Ni₃(HITP)₂ (HITP = 2,3,6,7,10,11-hexaiminotriphenylene), one of the conductive MOFs, to fabricate a crack-free large-area microporous film and applied it as a separator for LSBs.⁵⁵⁵ Ni₃(HITP)₂ has an electrical conductivity of 4000 S m⁻¹, which is four times higher than porous graphite and activated carbon. Ni₃(HITP)₂ has a structure in which a Ni²⁺ center and a tritopic HITP ligand are coordinated forming a 2D layered structure with hexagonal holes in the *ab* plane. Packing of the 2D layer to produce a honeycomb structure with uniform 1D channels along the *c*-axis is rich in polar sites, favorably binding polar polysulfides.⁵⁵⁶ Figure 23A shows the structure of Ni₃(HITP)₂ and the LSB structure in which the Ni₃(HITP)₂/PP membrane, which PP is polypropylene, is applied to the separator by combining it with a commercial PP separator (Celgard 2400). By an interface-induced growth method that replaces the water-air interface with a water-solid interface, a high-quality Ni₃(HITP)₂ film was grown on one side of a PP separator. The formed Ni₃(HITP)₂/PP separator has both conductive Ni₃(HITP)₂ side and an insulating PP side. The conductivity of the Ni₃(HITP)₂ layer was 3720 S m⁻¹, which is much higher than that of powder pellets (50 S m⁻¹). The Ni₃(HITP)₂ membrane with conductive properties acts as a barrier layer and extended current collector, thereby inhibiting polysulfide shuttling and increasing the usage of S. The PP layer, which is a surface with insulating properties, prevents short circuit between the anode and the cathode. To evaluate the performance of the Ni₃(HITP)₂ membrane in LSBs, commercial carbon black (CB) was used as the S host material for the S/carbon cathode. PP, ZIF-8/PP, CNT/PP, and graphene (G)/PP were used for comparison with Ni₃(HITP)₂/PP. Figure 23B shows the cycling performances of PP, ZIF-8/PP, CNT/PP, G/PP, and Ni₃(HITP)₂/PP at 0.2 C. The initial discharge capacity of Ni₃(HITP)₂/PP was 1244 mAh g⁻¹, and after 100 cycles, it showed 1139 mAh g⁻¹, which is 92% of the initial capacity. The initial discharge capacities of PP, ZIF-8/PP, CNT/PP, and G/PP were 889, 945, 1082, and 1146 mAh g⁻¹, respectively, with discharge capacities of 342, 581, 703, and 838 mAh g⁻¹ after 100 cycles,

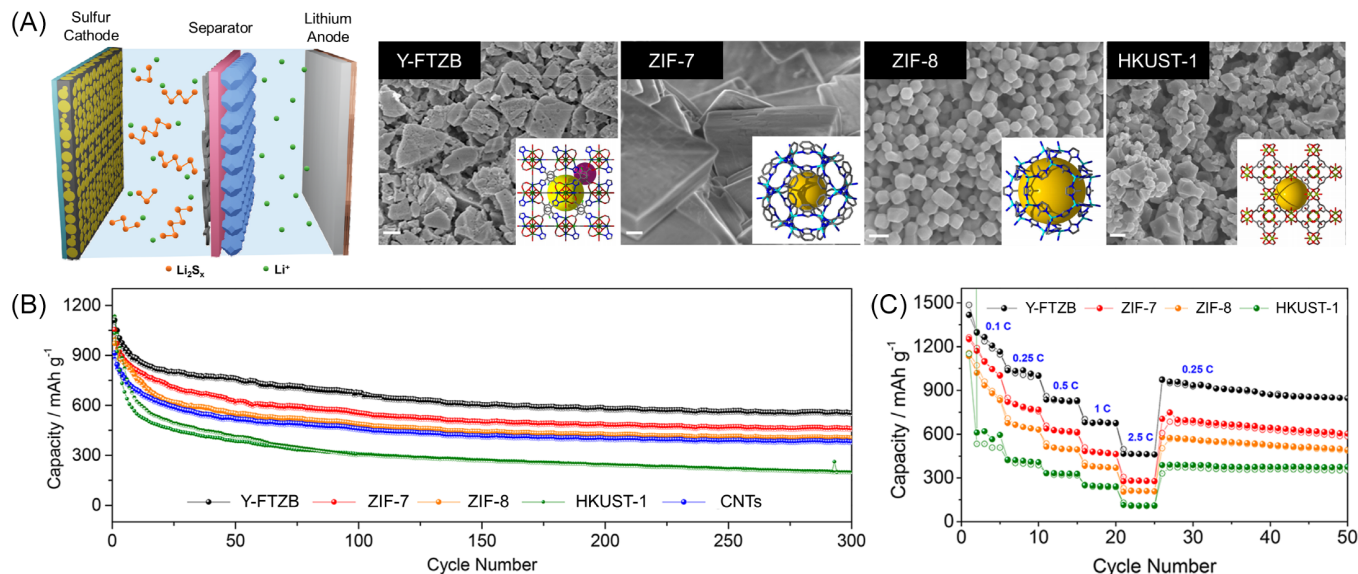


FIGURE 22 (A) Schematic illustration for the LSB configuration consisting of a sulfur cathode, a MOF/CNT modified separator, and a lithium anode. SEM images and structures (insets) of the morphologies of the four MOFs that were used: Y-FTZB, ZIF-7, ZIF-8, and HKUST-1. (B) Cycling performances of Y-FTZB, ZIF-7, ZIF-8, HKUST-1, and CNT. (C) Rate capabilities of batteries using different MOF-based separators under the rates of 0.1, 0.25, 0.5, 1, and 2.5 C. Reproduced with permission.⁵⁵¹ Copyright 2017, American Chemical Society

accounting for 38%, 61%, 65%, and 73% of the initial capacity, respectively. After cycling, the amount of dissolved polysulfide attached to the surface of the separator increased in the order of PP > ZIF-8/PP > CNT/PP > G/PP > Ni₃(HITP)₂/PP. This means that the ability of the Ni₃(HITP)₂ barrier to trap polysulfides is much higher than that of the other four types of membranes. Ni₃(HITP)₂/PP shows good stability under galvanostatic discharge/charge at different current rates. Its good conductivity, good ability to trap polysulfide, low density, and highly ordered micropores, make Ni₃(HITP)₂ membrane an ideal polysulfide barrier for optimizing high S loading LSBs. In this study, it was demonstrated that crystalline microporous membranes which has conductivity are advantageous barrier layers for high-performance LSBs. It also showed that the liquid–solid interface method provides a novel route to fabricate uniform and crack-free MOF membranes with very large areas and controlled thickness. After demonstrating that Ni-based crystalline microporous membranes have sufficient potential as separators for high-performance Li-S batteries, Zheng et al. confirmed that Ni₃(HITP)₂, which was easily synthesized by the facile filtration method and attached to the separator was effective in easing the shuttle effect and improving the rate performance of LSBs.⁵⁵⁷

The open metal sites of MOFs can act as catalytically active sites.^{558,559} MOFs have better catalytic performance than conventional nanocatalysts or inorganic porous catalysts because the catalytic sites are uniformly dispersed and the specific surface area is large. The recent research

findings that cerium(IV) oxide (CeO₂) nanoparticles are capable of adsorbing and catalyzing the conversion of polysulfides were to be an inspiration.⁵⁶⁰ Wang et al. reported a study on Ce-MOF/CNT composite which contain Ce(IV)-clusters as nodes and combined them with CNT and applied it as separator coating for LSBs.⁵⁶¹ CNT is one of the materials most widely used as a separator coating material, but its non-polar surface has a weak affinity for polysulfide, so it only physically blocks the polysulfide shuttle, resulting in low efficiency. In this study, it was found that Ce-MOF-808 (denoted as Ce-MOF-2) can rapidly adsorb polysulfides and effectively catalyze the conversion. So, Ce-MOF-2 was combined with the highly conductive CNTs and applied to the CNT separator. Figure 23C shows the structure of an LSB with Ce-MOF/CNTs as the separator and the structure of the Ce-MOF that was used. First, two Ce-MOFs with different open metal sites, Ce-MOF-2 and Ce-UiO-66-BPDC (denoted as Ce-MOF-1), were designed. The metallic Ce(IV)-clusters are nodes of these two Ce-MOFs, both of which are hexanuclear clusters, but differ in the number of coordination of their carboxyl ligands. Ce-MOF-1 has a structure in which a hexanuclear Ce(IV) clusters are completely surrounded by 12 carboxyl groups, whereas in Ce-MOF-2 has a structure in which a hexanuclear Ce(IV) clusters are coordinated with 6 carboxyl groups and 6 adsorption of polysulfides. The Ce-MOF-1/CNT and Ce-MOF-2/CNT composites were prepared by refluxing a mixture of cerium nitrate, BPDC, and CNT. The interaction between polysulfide and the synthesized

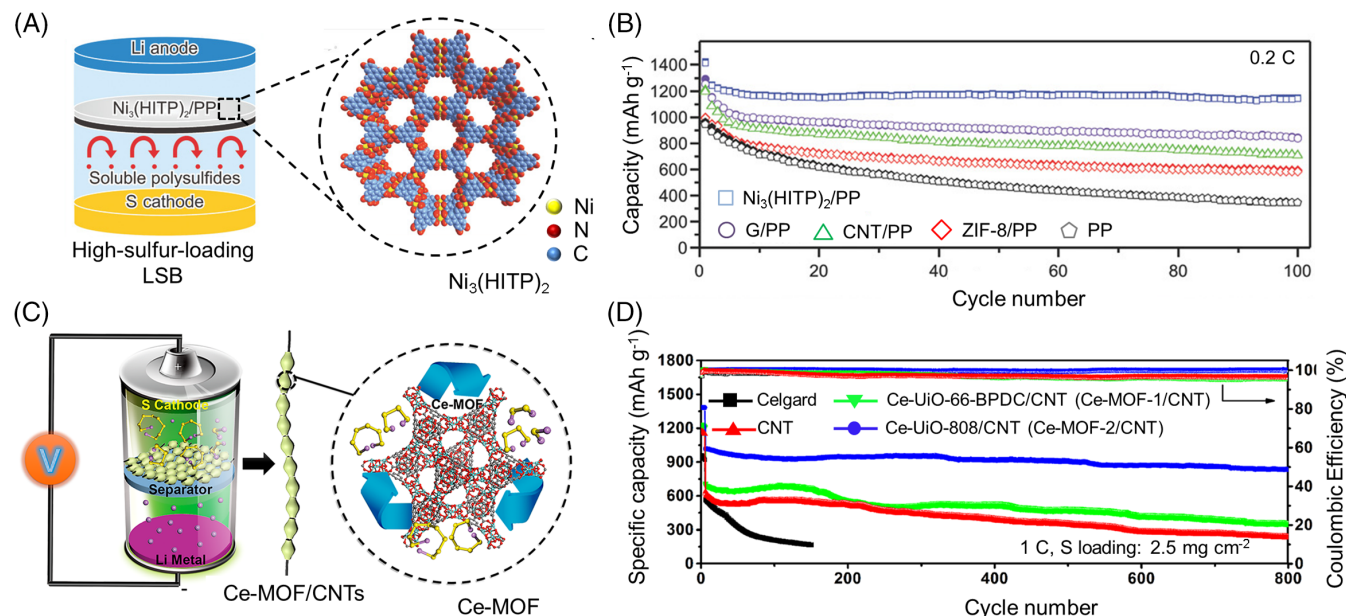


FIGURE 23 (A) Structure of Ni₃(HITP)₂ and the LSB structure in which the Ni₃(HITP)₂/PP membrane is applied to the separator. (B) Cycling performances of Ni₃(HITP)₂/PP, G/PP, CNT/PP, ZIF-8/PP, and PP at 0.2 C. Reproduced with permission.⁵⁵⁵ Copyright 2018, WILEY-VCH. (C) Schematic illustration of MOF/CNT composites offering catalysis of the conversion of polysulfides as the separator coating materials for LSBs. (D) Cycling performances of cells with different separators including Celgard, CNT, Ce-UiO-66-BPDC/CNT, and Ce-MOF-808/CNT, operated at 1 C for 800 cycles. Reproduced with permission.⁵⁶¹ Copyright 2019, American Chemical Society

materials was confirmed by adding an active Ce-MOF/CNT composite and CNTs to a Li₂S₆ solution and checking the color of the solution over time. As a result, the color of the Li₂S₆ solution mixed with Ce-MOF-2/CNT gradually changed to colorless, because the open metal sites of Ce-MOF-2/CNT adsorbed Li₂S₆ more efficiently. The charge transfer resistance values of Ce-MOF-1/CNT and CNT were similar, but the value of Ce-MOF-2/CNT was much smaller. Their difference in charge transfer resistance suggests that Ce-MOF-2/CNT effectively improved the reaction kinetics compared to Ce-MOF-1/CNT and CNT, thus promoting the conversion of polysulfides.⁵⁶² Figure 23D shows the cycling stability of cells using different separator coatings at 1 C with an S loading of 2.5 mg cm⁻². The initial specific capacity of the Ce-MOF-2/CNT coated cell was 1021.8 mAh g⁻¹, which is the highest among the samples, and after slowly decreasing to 838.8 mAh g⁻¹, it showed an almost 100% CE after 800 cycles. In contrast, after 800 cycles, the capacity of the Ce-MOF-1/CNT-based cells rapidly decreased from 701.8 to 349.4 mAh g⁻¹, and that of the CNT-based cells also rapidly decreased from 622.9 to 237.6 mAh g⁻¹. Through this, it was confirmed that the capacity retention of the Ce-MOF-2/CNT-coating containing cell was very high. This study is significant in that it showed a MOF-based material with catalytically active open metal sites, high dispersion, and a large specific surface area can effectively

improve the catalytic conversion and absorption of polysulfides.

Mixed-valent MOFs, in which two different valence states of metal ions exist simultaneously, have often shown promising properties in separation, catalysis, and biomedical applications.^{563–566} In particular, the redox behavior of mixed-valence MOFs can lead to unique catalytic and electrochemical properties due to changes in their metal ion oxidation states. Ce, one of the rare-earth metal elements that exist in abundance on earth and are inexpensive, has been widely studied in the field of catalysis-related research,⁵⁶⁷ and Ce-based materials are used as effective mediators to further enhance redox catalytic activity due to the unique oxidation capability of Ce^{IV}. The fact that the formation and stabilization of Ce^{IV}-based materials is readily possible by partial reduction of Ce^{IV} to Ce^{III} suggests potential applications of Ce-based materials in LSBs.⁵⁶⁸ The most Ce-MOFs reported so far, however, are Ce^{III}-MOFs because Ce^{IV} is a strong oxidizing agent that can be easily reduced during the synthesis of MOFs.^{569,570} Therefore, the preparation of mixed-valent MOFs with isolated Ce arrays remains an open challenge. Chao et al. synthesized mixed-valent Ce-MOFs with isolated Ce(IV, III) arrays following a sophisticated kinetic stability study of UiO-66(Ce), denoted as CSUST-1 (where CSUST stands for Changsha University of Science and Technology).⁵⁷¹ CSUST-1 is characterized by being rich in oxygen

vacancies and having open metal sites, and mechanism of its formation has been described. Then, CSUST-1 was combined with CNTs to form a CSUST-1/CNT composite, which was then applied to the separator of the LSB. The LSBs showed stable electrochemical performance, even after a long period of 1200 cycles, due to the efficient adsorption and fast redox conversion rate of polysulfides by CSUST-1, as well as improved Li^+ transport.

In addition to electrochemical compatibility, several other factors, such as resource abundance, environmental friendliness, and feasible technologies, must also be considered in the design of the separator for LSBs. In 2020, Liu et al. produced MIL-125(Ti), which used Ti, which is one of the abundant resources, as its metal ion and BDC as its ligand, through a solvothermal process and applied it on separators for LSBs.⁵⁷² A layer of MIL-125 (Ti) coated on a PP/PE membrane acted as an effective physical and chemical barrier region that could trap polysulfide species without affecting the facile transport of Li^+ . The 3D open framework of MIL-125(Ti) particles with a large surface area and uniform micropores ensured fast migration of Li^+ and was able to guide uniform Li plating/stripping. In addition, the strong bonding ability between the oxygen atoms of the BDC ligands of MIL-125(Ti) and the Li^+ of Li_2S_n led to the immobilization of S_n^{2-} . Due to their synergistic effect, the microporous PP/PE membrane modified with the MIL-125 (Ti) coating layer could effectively inhibit the polysulfide shuttle and Li dendrite growth, which was demonstrated in terms of good rate performance and high cycling stability.

Table 5 summarizes studies in which MOF-based materials have been used for cathodes and separators for LSBs.^{526–531,533–537,540,548–551,555,557,561,571–578} MOFs with tailored pore structures and sizes, as well as functional sites for S, offer possibilities and strategies for realizing novel cathode materials and separators for LSBs.

4.3 | Li-air battery

LABs are secondary batteries that use air (O_2) as their active material and Li as an anode material. Theoretically, LABs can realize an energy density that is 5–10 times higher than that of LIBs. Technical issues such as slow redox reaction rates and formation of solid discharge products (e.g., Li_2O and Li_2O_2) must be addressed to enhance low energy efficiency and cycling stability.^{579–581} Figure 24 briefly explains the application of MOF-based materials to the cathode of LABs, and the characteristic and notable features of MOFs, that play an important role in this case.

Because of their porous structure, tunable chemical functions, and regular channels, MOFs are considered promising materials, accommodating discharge products, facilitating mass transport, providing specific interactions, and accelerating redox reactions, as cathode materials for LABs. In 2014, Li et al. tried to solve the problems encountered in LABs by using a composite material containing two types of pores in the electrode material.⁵⁸² This study proposed a MOF material with larger mesopores in its carbon material to be lined with open metal sites where enhanced O_2 bonding and electrolyte diffusion could occur. HKUST-1, MOF-5, and M-MOF-74 (M = Mg, Mn, Co) were selected as suitable MOFs to serve as LAB electrode cathode materials, and the effects of their structural properties on performance were evaluated. These MOFs offer uniquely accessible metal sites, different structural topologies, and wide range of surface areas. MOF-5 has an infinite cubic framework structure and the pores of HKUST-1 are decorated with unsaturated Cu(II) coordination centers that provide binding sites for guests. M-MOF-74 is composed of various divalent metal ions and 2,5-dihydroxyterephthalic acid (H_4DOBDC) and has a hexagonal 1D pore structure. Both M-MOF-74 and HKUST-1 have lower surface areas than MOF-5 and have pores lined with open metal sites, so they show higher O_2 uptake. The open metal sites of these MOFs bind gas molecules and increase their absorption capacity. Therefore, it is believed that the presence of MOFs acts to compress the O_2 molecules in the pores, so that more O_2 can be utilized in LABs without increasing the volume and weight of the cathode. The performance evaluation of MOFs in LABs was conducted by coating a mixture of Super-P and M-MOF-74 using PVDF as a binder on carbon paper. These mixtures act as a cathode material. Figure 25A is a schematic illustration indicating the structure of the MOF-Super-P composite and its transport of O_2 . The discharge profiles with a current density of 50 mA g^{-1} for LAB cells using Super-P and various MOF-Super-P composites under O_2 atmosphere are shown in Figure 25B. The LAB using only Super-P had a discharge capacity of 2170 mAh g^{-1} , and the discharge capacities of batteries using HKUST-1, Mg-MOF-74, and Co-MOF-74 were 4170, 4560, and 3630 mAh g^{-1} , respectively. The discharge capacity of the battery containing Mn-MOF-74 was 9420 mAh g^{-1} , which is the highest value in this study, that is, a 330% improvement over the cell without MOFs. Here, it is clearly shown that the open metal sites of M-MOF-74 and HKUST-1 play a key role in capacity enhancement. MOFs as cathode materials induce O_2 enrichment in the electrodes by providing uniform pores with high surface area and a chemical environment that is tunable for specific interactions with

TABLE 5 Summary of recent studies in which MOFs or MOF derived materials were applied in the cathodes and separators for LSBs.

MOF	Application part	Reversible capacity (mAh g ⁻¹)	Rate (mA g ⁻¹)	Cycle number	Reference
MIL-100 (Cr)	Cathode	—	—	—	526
HKUST-1	Cathode	500	—	170	528
HKUST-1	Cathode	286	0.5 C	300	530
HKUST-1	Cathode	679	0.1 C	100	536
Ni based MOF (Ni ₆ (BTB) ₄ (BP) ₃)	Cathode	611	0.1 C	100	537
ZIF-8	Cathode	510	0.1 C	100	529
ZIF-8	Cathode	553	0.5 C	300	530
ZIF-8	Cathode	950	0.5 C	250	531
MIL-53 (Al)	Cathode	347	0.5 C	300	530
MOF-525(Cu)	Cathode	700	0.5 C	200	533
Cu-TDPAT	Cathode	745	1 C	500	535
nMOF-867	Cathode	788	835	500	573
ppy-S-in PCN-224	Cathode	670	10 C	200	527
NA ₂ Fe[Fe(CN) ₆]	Cathode	770	1 C	100	534
S@HKUST-1-CNT	Cathode	757	0.2 C	500	540
MIL-101	Cathode	695	0.1C	100	574
ZIF-67	Cathode	653	0.1 C	100	575
ZIF-67	Cathode	949	300	300	576
LPS-UiO-66	Cathode	375	100	600	577
HKUST-1@GO	Separator	855	1 C	1500	548
Y-FTZB	Separator	557	2.5 C	300	551
HKUST-1	Separator	197	2.5 C	300	551
HKUST-1@PVDF-HFP	Separator	802	2 C	600	550
ZIF-7	Separator	452	2.5 C	300	551
ZIF-8	Separator	403	2.5 C	300	551
UiO-66/Nafion	Separator	1056	0.1 C	200	549
Ni ₃ (HITP) ₂	Separator	716	1 C	500	555
Ni ₃ (HITP) ₂	Separator	1220	0.1 C	300	557
Ce-MOF-1 (Ce-UiO-66-BPDC)	Separator	349	0.1 C	800	561
Ce-MOF-2(Ce-MOF-808)/CNT	Separator	838	0.1 C	800	561
MIL-125(Ti)	Separator	1218	0.2 C	200	572
Co ₉ S ₈ nanostructure derived MOF	Separator	500	1 C	200	578
CSUST-1	Separator	538	2 C	1200	571

guests. These micropores are primarily for O₂ transport, and they cannot be fully occupied by larger molecules during battery operation. In conclusion, it has been shown that the proposed MOFs can increase the O₂ concentration in micropores by up to 18 times, and the combination of a MOF and Super-P as cathode materials

shows a higher discharge capacity than when Super-P is used alone.

Lee et al. applied a bimetallic MOF prepared by a simple hydrothermal reaction as a cathode material for LABs.⁵⁸³ The metal ions used were Mn and Co, and MnCo-MOF-74 with a ratio of Mn to Co of 1:4 was

synthesized. For comparison, the properties of monometallic Co-MOF-74 and Mn-MOF-74 were also confirmed, showing that they had only a single catalytic activity towards either LiOH formation or oxygen evolution reactions. On the other hand, the bimetallic MOFs showed improved reversibility and efficiency in both discharge and charge cycles. Co-MOF-74 and Mn-MOF-74 benefits from a porous structure that surpasses those of Mn-MOF-74 and Co-MOF-74, as well as the complementary contributions of Mn- and Co-metal clusters. Mn-metal clusters convert Li_2O_2 to LiOH, and Co-metal clusters efficiently decompose LiOH. The full discharge capacity of bimetallic MnCo-MOF-74 was $11\,150\text{ mAh g}^{-1}$, and it exhibited good cyclability with low overpotential at a limited capacity of 1000 mAh g^{-1} .

Li et al. reported on the effect of the size of MOF on the capacity of LABs with the aim of enabling better accessibility of active sites with short transport routes without losing high internal surface area.⁵⁸⁴ Modulators and various solvents were used to precisely control the grain size and morphology of the crystal,^{585–587} and it was possible to introduce intentional defects and active sites. Co-MOF-74 in three different sizes and shapes was synthesized by controlling the composition of the regulator and solvent through an easy solvothermal method. The MOFs obtained according to each synthesis condition were named Co-MOF-74-1400 (average length of $9.5\text{ }\mu\text{m}$ and a width of $\sim 1400\text{ nm}$), Co-MOF-74-800 ($\sim 6.5\text{ }\mu\text{m}$ in length and $\sim 800\text{ nm}$ in width), and Co-MOF-74-20 (average diameter of 20 nm and a length/

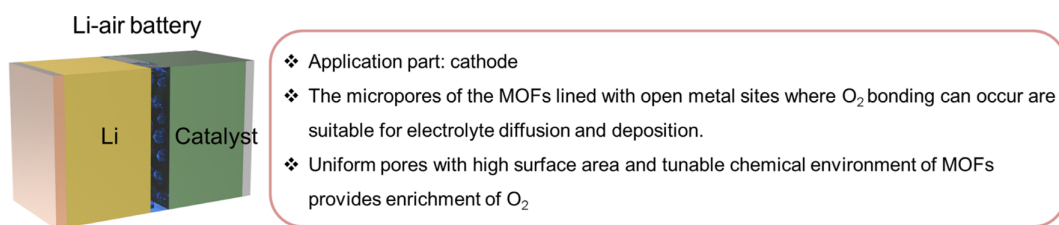


FIGURE 24 Application of MOF-based materials in LABs and notable features of the MOFs, which play important roles in LABs

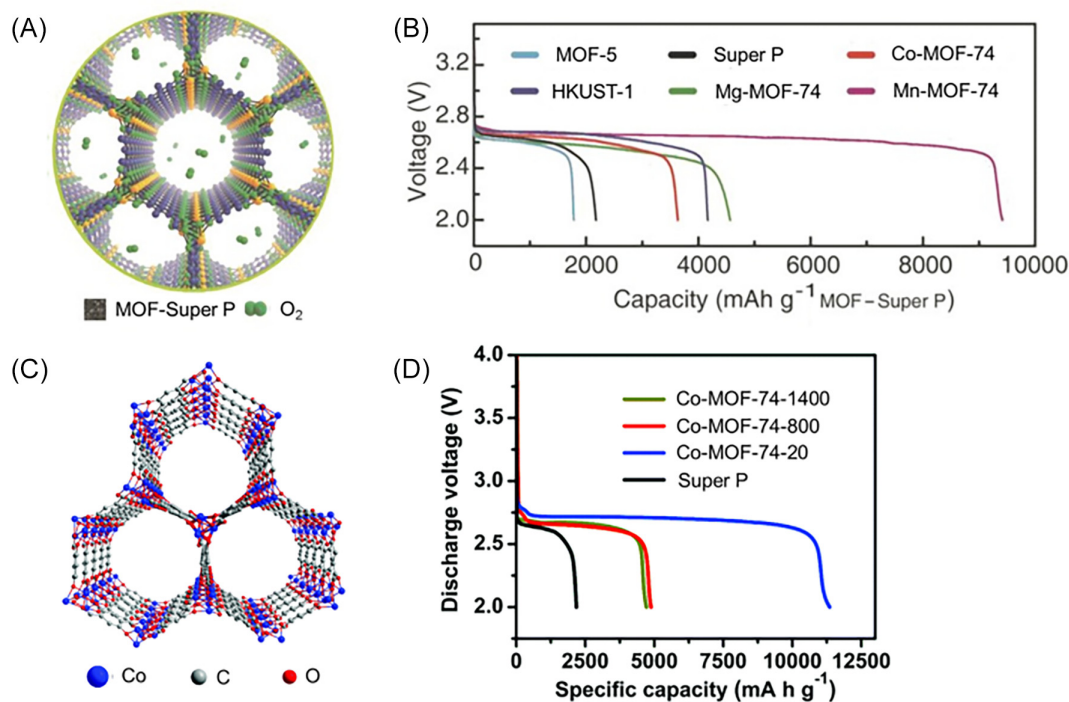


FIGURE 25 (A) Schematic illustration showing the structure of the MOF-Super-P composite and its transport of O_2 . (B) Discharge profiles of the Li- O_2 cells using Super-P, MOF-5, HKUST-1, Co-MOF-74, Mg-MOF-74, and Mn-MOF-74 with a current density of 50 mA g^{-1} . Reproduced with permission.⁵⁸² Copyright 2014, WILEY-VCH. (C) Structure of Co-MOF-74, which has 1D microporous hexagonal channels with high surface area, providing sufficient active sites to enhance O_2 adsorption and potential catalysis. (D) Discharge curves of LABs using both the MOF-Super-P composite electrodes and pure Super-P electrode at a cutoff voltage of 2.0 V and with a current density of 100 mA g^{-1} . Reproduced with permission.⁵⁸⁴ Copyright 2017, ROYAL SOCIETY OF CHEMISTRY

diameter ratio of 12), respectively. Figure 25C shows 1D microporous hexagonal channel structure of Co-MOF-74, which has a high surface area that provides sufficient active sites to enhance O₂ adsorption and potential catalysis. This unique structure makes it an advisable candidate as an O₂ electrode material. The pore diameter of Co-MOF-74 is ~12 Å,⁵⁸⁸ allowing free transport of Li⁺ and O₂ in the pores. As a result of evaluating the O₂ enrichment capacity of each sample through low-pressure oxygen adsorption isotherms, Co-MOF-74-800 and Co-MOF-74-20 showed similar adsorption capacity, whereas Co-MOF-74-1400 showed a significantly lower O₂ adsorption capacity. The reduction in O₂ adsorption is mainly caused by reduced surface area due to the use of modulators and the miniaturization of the material, which further affects the periodicity of the framework.⁵⁸⁹ The size of the crystals ensures accessibility of coordinating unsaturated metals and guest molecules entering the newly introduced defect site of Co-MOF-74. For electrochemical performance evaluation, LABs using Co-MOF-74-20, Co-MOF-74-800, and Co-MOF-74-1400 as cathode materials were fabricated, and pure Super-P was used as a control. Figure 25D shows the first discharge curves of the LABs using pure Super-P electrode and the Co-MOF-Super-P composite electrodes with different sizes at a cut-off voltage of 2.0 V and with a current density of 100 mA g⁻¹. The discharge capacity of the LAB using the pure Super-P-based cathode was 2090 mAh g⁻¹, and those of the batteries using Co-MOF-74-800 and Co-MOF-74-1400 were 4880 and 4710 mAh g⁻¹, respectively. Surprisingly, the Co-MOF-74-20-based battery provided a high capacity of 11 350 mAh g⁻¹. It was attributed to the short transport distance, accessibility of the active site, and the large electrode-electrolyte contact area of Co-MOF-74-20 resulting effectively promote the oxygen reduction reaction. Even when the current density was increased to 500 mA g⁻¹, the MOF-74-20 still had the best rate performance of the three MOFs. This means that making the smaller and less perfect crystals improves their electrochemical performance with a smaller surface area but more active sites. In other words, these results show that the electrochemical performance of cells can be further improved by facile designing of nanocrystals with specific internal diffusion pathways.

Table 6 summarizes studies on applying MOF-based materials as cathode materials for LABs.^{39,285,582–595} Compared to the LIBs and LSBs described above, LAB research using MOFs is still in its infancy. Although there is still a long way to go, we are confident that the porous structure and tunable chemical functions of MOFs can improve the capacity and cycle lifetime of LABs.

4.4 | Lithium-metal battery

The capacity of the anode active material increases in the order of carbon (including graphite), metal oxide, silicon-carbon composite, and Li metal. Li metal is attracting attention as a very interesting candidate material for anode because it has a high theoretical capacity up to 3860 mAh g⁻¹ and has the lowest standard reduction potential (3.04 V vs. standard hydrogen electrode [SHE]),^{596,597} although commercial applications suffer from the following problems: (1) safety issues (short circuits and thermal runaway) caused by uncontrolled Li dendrite growth during charging; (2) capacity and lifetime reduction issues caused by the accumulation of dead Li in the anode, which increases the internal resistance of the battery; (3) unstable and brittle SEI layer on the Li metal, which consumes much of the electrolyte and fresh Li; and (4) volume changes in the cycling process, which cause the intrinsic SEI layer to fall off the Li metal surface, further impairing the interfacial stability.⁹⁸ Numerous approaches have been proposed to resolve these issues^{598–601}: (1) construction of a 3D Li anode structure to reduce volume changes and enable dendrite-free Li deposition^{602–610}; (2) application of artificial SEI layers to reduce the consumption of organic electrolytes and fresh Li^{611–616}; (3) that can produce a tough physical layer as a coating to inhibit Li dendrite growth; (4) lithiophilic material to induce Li nucleation^{617,618}; (5) utilization of well-designed solid-state electrolytes (SSEs) with excellent chemical stability, a high Young's modulus and good Li⁺ conductivity^{619–621}; (6) the introduction of additives to help minimize side reactions and obtain a stable SEI layer^{622,623}; and (7) modification of the separator to provide a uniform channel for Li⁺ flux and induce uniform Li deposition, as well as preventing Li dendrite growth due to its mechanical strength.^{624–627} Figure 26 briefly explains the battery components of LMBs that can contain MOF-based materials, and the characteristic and notable features of the MOFs that play important roles in this case.

The porosity, tunability, and variety of combinations of MOFs provide an effective and attractive solution for application in LMBs. MOFs can be applied as SSEs, separators, electrodes, and anode structures for Li metal anode protection in LMBs. First, we describe studies using MOFs as SSEs. Development of a solid electrolyte which has high ionic conductivity and good usability with electrodes is important, and Long et al. first utilized MOFs as SSEs.²²¹ An Mg-MOF-74-based material with an open metal center was used, and it exhibited a high ionic conductivity of 3.1×10^{-4} S cm⁻¹, showing potential for application in SSEs. After that, the ionic conductivity of other MOFs, such as ZIF-8,⁶²⁸ Al-Td-MOF-1,²²²

TABLE 6 Summary of recent studies in which MOFs or MOF derived materials were applied as cathode materials for LABs.

MOF	Application part	Reversible capacity (mAh g ⁻¹)	Rate (mA g ⁻¹)	Cycle number	References
Mn-MOF-74	Cathode	9420 (primary capacity)	—	—	582
Bimetallic MOF	Cathode	11 150	—	44	583
Aliphatic-ligand based Co-MOF	Cathode	500	200	320	590
Fe(III)-MOF-5	Cathode	5000	300	15	591
MIL-100 (Fe)	Cathode	600	0.1 (mA cm ⁻²)	30	592
MIL-100 (Cr)	Cathode	800	100	50	593
Mn ₃ [Co(CN) ₆] ₂ ·9H ₂ O	Cathode	500	0.16 (mA cm ⁻²)	100	594
Co-MOF-74	Cathode	11 350 (primary capacity)	100	-	584
Bimetallic ZIF	Cathode	354–756	-	-	285
Zn-MOF-5	Cathode	1437 (initial discharge capacity)	0.2 (mA cm ⁻²)	-	39
Zn ₄ Co ₁ -C/CNT composite	Cathode	16 000		137	595

UiO-66,²²³ UiO-67,⁶²⁹ and Massachusetts Institute of Technology (MIT)-20⁶³⁰ were also reported, suggesting the possibility of application in SSEs. Chen et al. reported a novel ionogel that was prepared by using ZIF-67 obtained by simple ball milling as a host and mixing with ionic liquid electrolyte (ILE) (referred to as ILE@MOF).⁶³¹ Ionogel, a new type of semi-solid electrolyte that combines the unique properties of ionic liquids and solid materials, was used in this study. The ILE has high ionic conductivity and thermal stability, ensuring excellent electrochemical performance in high-temperature environments.^{632,633} An organically modified SiO₂-based ionogel electrolyte was fabricated using the sol-gel method, and the cycling performance with a Li metal anode was investigated. To improve the thermal stability of the ionogel, ZIF-67 was chosen as the scaffold. MOFs are novel candidates for establishing electrolytes that are good ionic conductors because they have insulating properties and provides a tunable porous structure that facilitates ion transport. The ILE, mixture of N-propyl-N-methylpyrrolidinium bis(trifluoromethylsulfonyl)imide ([Py₁₃][TFSI]) and LiTFSI, was used in this study. The ILE encapsulated in ZIF-67 channels maintained high ionic conductivity without losing dynamic mobility. Figure 27A shows a schematic diagram of the ILE@ZIF-67 synthesis method and the Li⁺ transport pathways. The ionic conductivity of the material was analyzed using electrochemical impedance spectroscopy method with

stainless-steel electrode. As the content of ILE increased, the ionic conductivity also increased, and the conductivity level of $2.29 \times 10^{-3} \text{ S cm}^{-1}$ obtained at 2.0 g was sufficient for practical application in batteries. The high temperature stability of the ILE@MOF was evaluated because the thermal stability of the electrolyte, which is directly related to the safety of the battery, is a very important factor. ILE@MOF was indicated excellent thermal stability, starting decomposition at 325 °C. In addition, ILE@MOF significantly suppressed the growth of Li dendrites, a cause of degradation of batter, by forming a particle-rich coating on the Li metal anode. The electrochemical compatibility of Li and the ILE@MOF was explored by Li plating/stripping examinations. The Li metal surface of the Li/ILE@MOF/Li cell had a thin layer preventing the growth of Li dendrites after 100 h of cycling. Due to the thermal stability of the ILE@MOF electrolyte at high temperatures, even at 150 °C, the Li/ILE@MOF/Li cell generated an overall overpotential of less than 700 mV under a current density of 0.5 mA cm⁻² for 1200 h without major voltage fluctuations. Li/ILE@MOF/Li cells exhibited stable plating/stripping voltages, confirming ILE@MOF ionogel electrolyte are promising materials for LMBs at high-temperature operation. Figure 27B shows the cycling performance of Li/Li-Ni_{0.33}Mn_{0.33}Co_{0.33}O₂ cells using ILE@MOF electrolyte at 60, 90, and 120 °C under 2.0 C (1.0 C = 140 mA g⁻¹). As the temperature increased, the initial discharge capacity

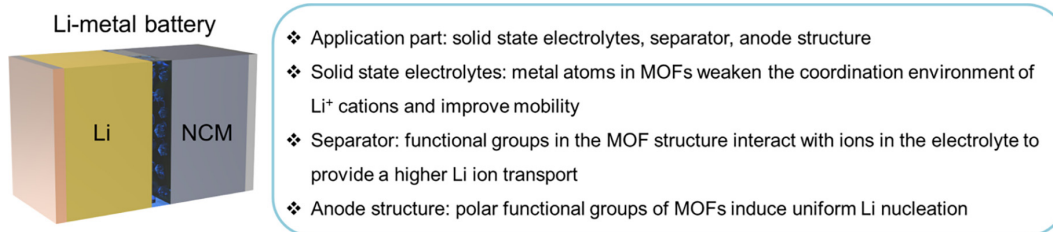


FIGURE 26 Application of MOF-based materials in LMBs and notable features of the MOFs that play important roles in LMBs

also increased due to the decrease of the interfacial impedance. Stable lithiation/delithiation capacity was observed with a high CE of 98% at 60 and 90 °C over 50 cycles. In conclusion, the ILE@MOF electrolyte proposed in this study represents a promising approach to reduce the problem of Li dendrite growth in extreme situations, and it will enable the development of efficient and durable high-temperature LMBs by accelerating the transport of Li^+ .

Sun et al. reported a new type of cationic MOF (CMOF) formed by the nucleophilic substitution grafted with pyridine N based on UiO-66, and applied them to a solid polymer electrolyte (SPEs).⁶³⁴ Numerous strategies have been used to enhance the conductivity of SPEs.^{635–637} Despite much progress, the growth of Li dendrites penetrating through the SPE is dangerous and still greatly hinders the practical application of all solid-state batteries (ASSBs).^{638–640} The electrochemical performance of polymer electrolytes was improved by introducing MOF-5 into poly(ethylene oxide) (PEO) polymer. The large surface-to-volume of MOF-5 helps to stabilize the interface between the electrolyte and the Li metal.⁶⁴¹ MOFs further enhance the anion absorption and tightly trap anions around the surface, leading to a higher transference number (t_+) than that of ceramic particles. First, 2-aminoterephthalic acid (H_2ATA), 2,5-pyridinedicarboxylic acid, and zirconium (IV) chloride were added to anhydrous DMF, and acetic acid was used as a mineralizer. The mixture was stirred and then heated at 120 °C for 24 h. After the reaction, the producing suspension was centrifuged, washed, and vacuum dried to obtain UiO-66 (named D-UiO-66- NH_2). The dual ligand composed of H_2ATA and 2,5-pyridinedicarboxylic acid replacing the BDC linker led to the formation of the intermediate MOF, D-UiO-66- NH_2 . The - NH_2 groups achieved a stable structure of the composite electrolyte and promoted the subsequent linkage of the PEO chains with the etheric oxygen. Cationic D-UiO-66- NH_2 (CMOF) was obtained by immersing D-UiO-66- NH_2 in DMF and CHCl_3 to activate it by guest exchange and removal. The CMOFs immobilize anions through electrostatic interactions of charge carriers, which are more effective than covalent bonds in

polymers and Lewis acid–base interactions in metal oxides. P@CMOF membranes were manufactured by uniformly mixing CMOF powder, PEO, and LiTFSI and grinding the mixture in a mortar to obtain small rough balls, sandwiching the coarse balls between two pieces of PTFE and pressing. Figure 27C is a schematic illustration showing the structure of the manufactured P@CMOF membrane and the improved electrical flow. The smooth and clean surface of P@CMOF can firmly bond with the electrode, reducing the interfacial resistance. The optimal conductivity was achieved by controlling the content of CMOF, and when the content was 12.5 vol%, the optimal conductivity was $3.1 \times 10^{-5} \text{ S cm}^{-1}$. Conductivity as a function of temperature was also investigated, reaching $6.3 \times 10^{-4} \text{ S cm}^{-1}$ at 60 °C, which was confirmed to be sufficient for ASSB applications. To investigate the long-term electrochemical stability of anion-immobilized P@CMOF, Li symmetric cells were assembled. The resistance values of the Li/P@CMOF/Li cells did not change significantly before and after 10 days at 60 °C, confirming the chemical stability of P@CMOF. Figure 27D shows the cycling performance of LiFePO_4 (LFP)/P@CMOF/Li cells at 1 C and 60 °C. The initial CE of the cell with P@CMOF was 93.7% and it provided a discharge capacity of 126.4, 106.3, 88.0, and 67.4 mAh g^{-1} at the current density of 0.5, 1, 2, and 5 C, respectively. Even after high current densities, the discharge capacity could be restored when the current density returned to 1 C. Using P@CMOF and a dendrite-free Li anode, an ASSB with LFP cathode could be charged and discharged 300 times at 1 C with a capacity retention of 85.4%. P@CMOF exhibited an electrochemical window of up to 4.97 V due to its stable composite structure at high voltage. The anion-immobilized CMOF was dispersed in a PEO/LiTFSI matrix to produce a P@CMOF composite electrolyte by a hot-pressing method, providing 10 times higher conductivity than pure PEO electrolyte. Dendrite-free Li anode and the anion trapping ability were brought about by the synergistic effect of CMOF and the polymer. The formation of a large electric field was prevented due to the small concentration gradient of Li^+ in the composite electrolyte. These

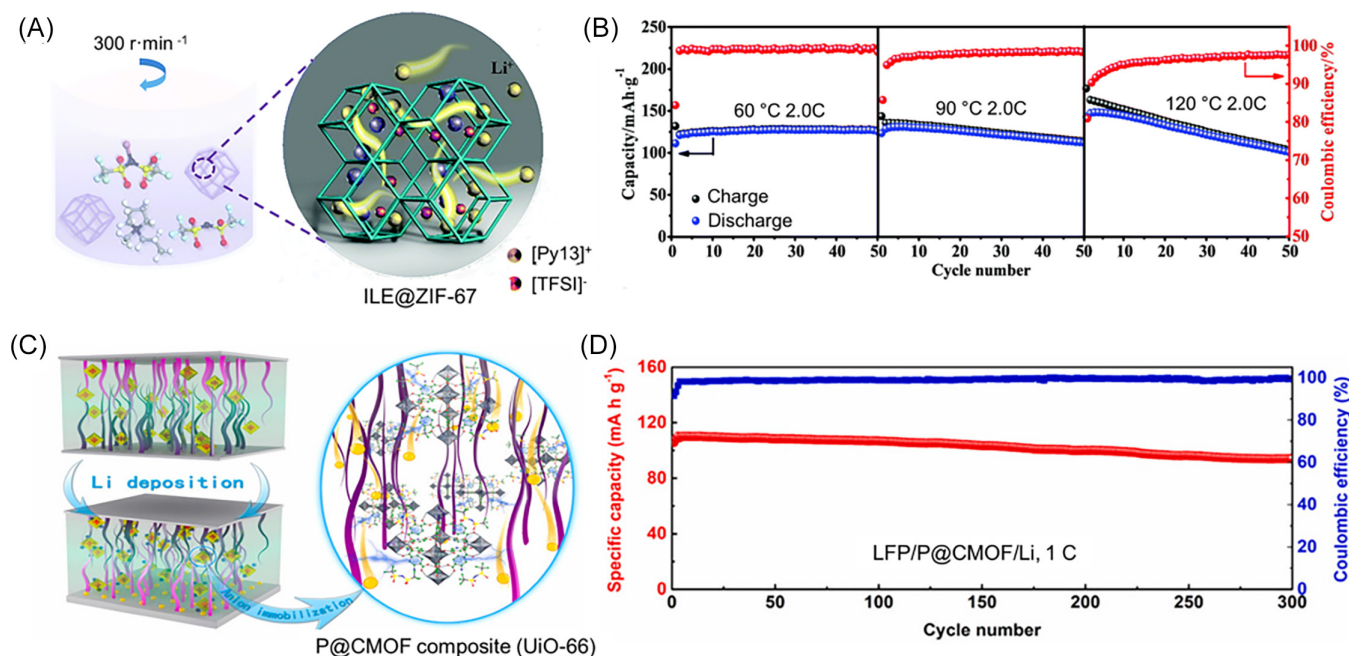


FIGURE 27 (A) Schematic diagram of the ILE@ZIF-67 synthesis method and the Li⁺ transport pathways. (B) Cycling performance of Li/LiNi_{0.33}Mn_{0.33}Co_{0.33}O₂ cells using ILE@MOF electrolyte at 60, 90, and 120 °C under 2.0 C (1.0 C = 140 mA g⁻¹). Reproduced with permission.⁶³¹ Copyright 2019, ROYAL SOCIETY OF CHEMISTRY. (C) Schematic diagram showing the structure of the manufactured P@CMOF membrane and the improved electrical flow. (D) Cycling performance of LiFePO₄ (LFP)/P@CMOF/Li cells at 1 C. Reproduced with permission.⁶³⁴ Copyright 2019, Elsevier

anion-fixed electrolytes used in Li metal cells with LiFePO₄ and LiFe_{0.15}Mn_{0.85}PO₄ cathode exhibited excellent rate and cycling performance.

There are also studies using MOF-based materials as separators for LMBs. The role of the separator is to provide an ion pathway and prevent short circuits. The performance of Li metal anodes can be improved by optimizing the separator through any strategic method. Coating them with inorganic materials such as polydopamine improves the electrolyte wetting and electrolyte absorption capacity of PE separators, which directly affects the power performance of batteries.⁶⁴² MOFs with increased stability of the Li metal anode have been proposed by including an organic ligand and an inorganic metal ion as modifiers of the separator. Wang et al. were the first to report a composite separator capable of high-density Li deposition and long-term reversible Li plating/stripping without additional electrochemical input through coating NH₂-MIL-125(Ti) MOFs on Celgard 3501, a commercial separator.⁶⁴³ After coating, NH₂-MIL-125 (Ti) without obvious cracks was uniformly distributed in the separator and the symmetrical cell with the NH₂-MIL-125(Ti) coated separator showed stable cycling properties for over 1200 h. It was found that the amine functional groups in the MOF structure interact with ions in the electrolyte to accelerate a higher Li⁺ transport and induce uniform Li nucleation and growth, making an important contribution to good electrochemical

performance. As a separator modifier, the use of MOFs with polar functional groups has verified to be an important strategy for obtaining long-life batteries with the dendrite-free anode. Another trend to utilize MOFs for separators of LMS is the use of functionalized MOFs by carboxylation, amination, hydroxylation, and sulfonation.

In addition to improving the separator through coating with MOFs, a method using the MOF itself as the separator was also devised. In 2018, Zhou et al. proposed a MOF-based separator with a structure capable of inhibiting polysulfide diffusion as well as dendrite formation due to the porous structure of the MOF.⁶⁴⁴ Theoretically, a crystalline MOF lattice with ordered porous can achieve the transport of desired molecules as they would have suitable properties to host guest liquid/gas species.⁶⁴⁵ From the pore chemistry point of view, the application of compatible pores of MOF species to liquid electrolytes can force ordered ion transport, resulting in stable and uniform Li deposition as shown in Figure 28A. Considering the size of the TFSI⁻ anion (anion of the LTFSI), HKUST-1 was selected as an appropriate host candidate. It was expected that the pore width of HKUST-1 (8 Å) and that of TFSI⁻ anion (7.9 Å) could serve as a 3D pathways for ion transport. By utilizing angstrom-scale MOF pores to limit TFSI⁻ anion transport, it is expected that stable Li electrodeposition under real high current conditions will be feasible based on this. To evaluate ion diffusivity of this battery electrode/

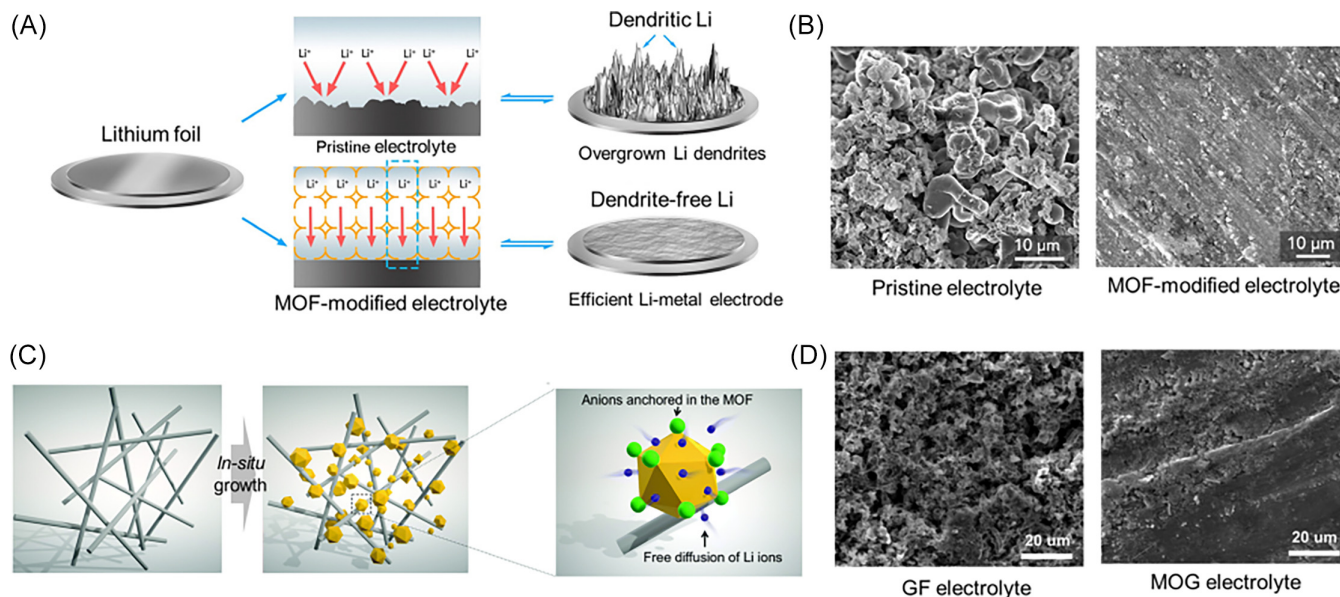


FIGURE 28 (A) Schematic illustration of dendritic Li growth on pristine electrolyte and MOF-modified electrolyte. (B) SEM images that can confirm the presence of Li dendrites after symmetric cell operation in pristine electrolyte and MOF-modified electrolyte. Reproduced with permission.⁶⁴⁴ Copyright 2018, Elsevier. (C) Process of obtaining a MOF-GF composite membrane by modifying a commercially available GF membrane with MOFs nanoparticles. (D) SEM image of a post-cycling Li electrode harvested from a LiFePO₄|Li cell after operation at 1C (100 cycles). Reproduced with permission.⁶⁴⁶ Copyright 2019, ROYAL SOCIETY OF CHEMISTRY

electrolyte combination, a molecular dynamics (MD) simulation based on density functional theory (DFT) (DFT-MD) was performed. In the results of the diffusion kinetics analysis of pristine and MOF-modified electrolyte by DFT-MD, both Li⁺ and TFSI⁻ anions exhibited significant diffusion behavior according to the general observation that they could freely move inside. The MOF host was involved in the solvation process of Li⁺, whereas binding behavior between MOF host and the TFSI⁻ anion was not monitored during the MD simulation. In the pure electrolyte, Li⁺ and TFSI⁻ anions diffuse rapidly, causing non-uniform Li-stripping behavior on the Li metal surface and inducing the growth of Li dendrites through a self-amplifying mechanism. In the MOF-modified electrolyte, on the other hand, well-ordered angstrom-scale pores imposed spatial restrictions on TFSI⁻ anion transport, transforming it into a state with highly mobile Li⁺ and nearly “caged” TFSI⁻ anions and finally prevent the growth of Li dendrites. The uniform distribution of Li⁺ immobilized on the MOF-modified electrolyte was insensitive to the non-uniformity of the Li metal surface due to the suppressed TFSI⁻ anion diffusion. In other words, the “cage” electrolyte anions within the MOF induce a homogeneous Li⁺ flux, which inhibits the formation of harmful dendrites and achieves stable Li deposition. The pristine and MOF-modified electrolytes were implemented in a Li||Li symmetric cell (2032-type) to investigate the role of the MOFs during Li eposition. A symmetrical cell of MOF-modified electrolyte was

operated under an areal capacity of 2.5 mAh cm⁻² and a current density of 5.0 mA cm⁻². At the 100th hour, the overpotential was only ~30 mV versus Li/Li⁺, and it remained almost constant for the next 900 h. The final voltage hysteresis reached ~35 mV at the end of the test. A uniformly flat voltage profile indicated a stable Li plating/stripping process, demonstrating the containment of Li dendrite growth. To confirm the reliability of the MOF-modified electrolyte at substantially high current densities, the areal capacity was increased up to 10 mAh cm⁻². The initial voltage hysteresis was ~107 mV, followed by a gentle increase to ~114 mV at 120 h. When the test time was extended to 800 h, the voltage profile remained consistent and stable at ~100 mV. On the other hand, the cells with pure electrolyte showed a sharp increase in overpotential from the initial value of ~420 to ~1000 mV after 120 h, which was due to a short circuit caused by overgrown Li dendrites. Through the SEM images in Figure 28B, the existence of Li dendrites was confirmed with a direct image after the operation of the symmetric cell. In the case of the pristine electrolyte, significant fragments and randomly oriented Li dendrites ~10 μm in length were generated on the Li metal surface after operation under areal capacity of 10 mAh cm⁻² over 120 cycles. On the other hand, no Li dendrites could be found in the case of MOF-modified electrolyte operated under the same conditions, and the smooth and undamaged Li surface could be identified even under more harsh operating conditions of

2.5 mAh cm⁻² after 1000 h. Consequently, this study showed that the MOF-modified electrolyte could significantly inhibit the growth of Li dendrites by modulating the ion transport behavior and eventually provide stable and flat Li deposition. Furthermore, it was highlighted that MOFs can play a promising role in realizing tunable ion transport, which is widely applicable in energy storage devices and other fields that involve ion conduction.

Lu et al. demonstrated a new type of advanced separator that can improve Li⁺ transference in liquid electrolytes by transforming glass fiber (GF) into a host for a MOF to fabricate a functional separator with high thermal stability and mechanical robustness.⁶⁴⁶ Figure 28C shows the process of obtaining a MOF-GF composite membrane by modifying a commercially available GF membrane with MOF nanoparticles. Here, the functionalized MOF was UiO-66-NH₂ with an octahedral structure composed of Zr₆O₄(OH)₄ and NH₂-BDC. The μ₃-OH capped on Zr₆O₄(OH)₄ generates OMS on Zr₆O₆ through dehydration upon thermal activation. The resulting OMS with Lewis acidity serves as an anchoring point for anionic species in the liquid electrolyte, increasing the Li⁺ transference number (t_{Li^+}). GF, which has the advantages of high chemical stability, good thermal stability, and low cost, was chosen as the porous matrix. In-situ growth of UiO-66-NH₂ nanoparticles on GF was accomplished by infiltrating the MOF precursor into the GF porous membrane followed by heat treatment. The nanocomposite functional separators which were synthesized by GF membranes with UiO-66-NH₂ were named MOGs. The pristine GF membrane has the morphology of entangled fibers, and after in-situ growth of the MOFs, the GF maintains its fibrous structure decorated with nanoparticles. To confirm the role of MOG as a functional separator, an electrochemical evaluation was performed using 1 M LiClO₄ in propylene carbonate (LPC) as a liquid electrolyte. The t_{Li^+} was evaluated using a Li|Li symmetric cell by the Bruce-Vincent method. Cells containing MOG and LPC showed a high t_{Li^+} of 0.67, which was twice that of commercial polyolefin separators or GF membranes. The electrochemical stability window was evaluated using stainless-steel (SS) plate as the working electrode and Li as the counter/reference electrode (SS|Li). Cells with MOG maintain substantially smaller peak currents (continuously less than 0.02 mA cm⁻²), demonstrating the significant inhibition of electrolyte collapse at the interface between the electrode and the LPC-saturated MOG. To mimic the practical situation of lithium batteries, galvanostatic tests were carried out under areal capacity of 3 at 1.5 mA cm⁻² for each cycle. Cells using GFs underwent polarization, resulting in a sharp increase in cell voltage (rapid increase from 50 to 800 mV over 200 h), which is an archetypal sign of Li

dendrite growth and increased interfacial resistance. In comparison, cells using MOG showed stable operation for up to 350 h with a small overpotential (~55 mV). This result demonstrates the advantage of MOGs in inhibiting the growth of Li dendrites and improving the resistance of interfacial with Li. Prototype cells using LiFePO₄ as cathode and Li metal as anode (LiFePO₄|Li) to indicate the potential use of MOG separators in LMBs were assembled. Cells using MOG showed a high t_{Li^+} and relaxed concentration polarization under high-rate operation and also showed good rate capability. A cell with MOG showed ~80% cycling stability under areal capacity of 2.1 mAh cm⁻² at a current density of 1 C (2.5 mA cm⁻²) after operation for 200 cycles, while a control cell with GF exhibited a sharp decrease in capacity at the 106th cycle, suggesting dendritic Li growth. This can be seen in Figure 28D, which shows an SEM image of a cycled Li electrode harvested from a LiFePO₄|Li cell at 1 C (100 cycles). The surface of the Li from the cell using GF showed a completely dendritic morphology, whereas the surface of the Li from the cell using MOG showed a smooth and dense surface without Li dendrites. This study is significant in that it improved the performance of LMBs by applying a MOG-based separator that can modulate the ion transport behavior of liquid electrolytes, and demonstrated that this method can be a general and practically viable approach.

The current collector affects the Li anode performance,⁶⁴⁷ and depositing Li on an existing current collector leads to the growth of Li dendrites. An electrode modified using MOFs that has good chemical compatibility with Li metal and stable electrochemical properties inhibits the growth of Li dendrites due to its high surface area and abundant polar functional groups. Lin et al. designed an electrode modified with Cu-MOF to inhibit Li dendrite growth.⁶⁴⁸ MOF nanosheets were prepared by the hydrothermal method using BDC and cobalt nitrate. The MOF-nanosheet modified electrode (denoted as Cu-MOFs electrode) was fabricated by the simple method of coating the dispersed MOF nanosheets on Cu foil using a doctor blade. In the TEM image of Figure 29A, clear MOF nanosheets can be confirmed. 2D nanosheets facilitate electrolyte adsorption and Li⁺ adhesion due to their unique structural periodicity, uniform thickness of nanostructures, and exposure of polar functional groups and ligands. The electrochemical stability of the Cu-MOFs electrode was evaluated using CV and linear sweep voltammetry (LSV) methods. Bare Cu electrodes without MOFs were used for comparison. The low current density in the CV and the large electrochemical stability window in the LSV indicate that the Cu-MOFs electrode is more stable towards the electrolyte during the electrochemical cycling, which helps to reduce side

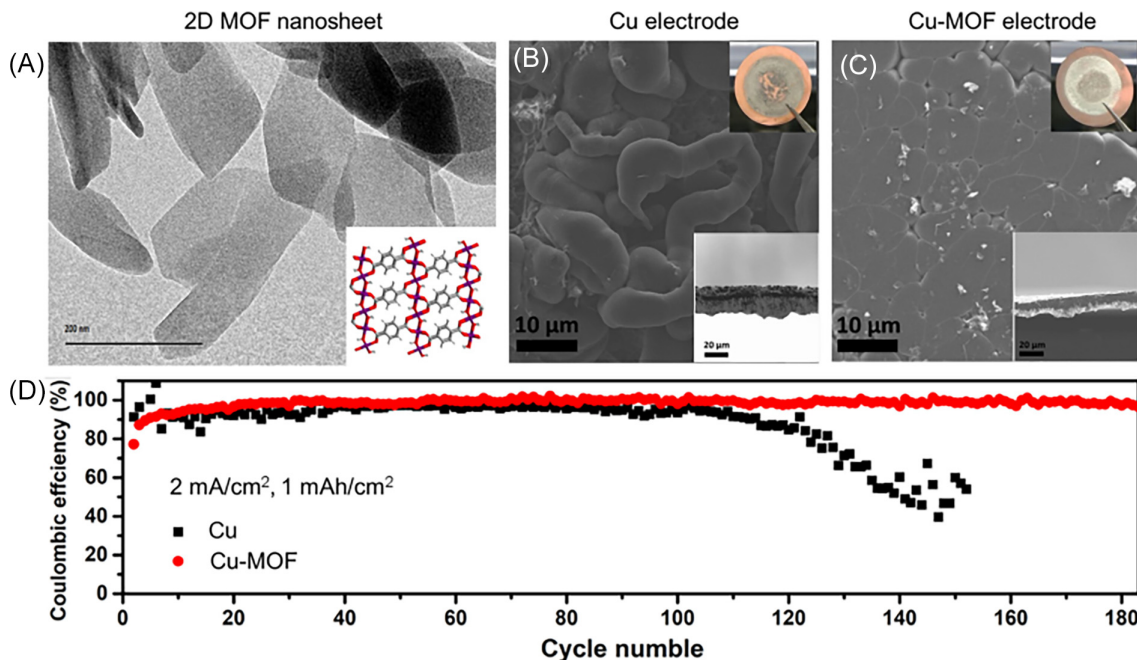


FIGURE 29 (A) TEM image of 2D MOF nanosheet and schematic diagram of the structure. (B) SEM images of the surface and cross-sectional (lower inset) morphologies of bare Cu electrode with 1.0 mAh cm^{-2} Li deposition at a current density of 0.5 mA cm^{-2} . (C) SEM images of the surface and cross-sectional (lower inset) morphologies of Cu-MOF electrode with 1.0 mAh cm^{-2} Li deposition at a current density of 0.5 mA cm^{-2} . The upper insets of C and D are photographs of the electrodes. (D) Cycling performances of bare Cu electrode and Cu-MOFs electrode at the current density of 2 mA cm^{-2} with a lithiation capacity of 1 mAh cm^{-2} . Reproduced with permission.⁶⁴⁸ Copyright 2018, Elsevier

reactions. The improved electrolyte absorption capacity of MOF nanosheets can be confirmed by dropping an ether-based electrolyte on the Cu electrode and Cu-MOFs electrode to investigate the contact angles. The enhanced affinity of the MOF nanosheets reduces the Li^+ concentration gradient and inhibits the growth of dendrites, which in turn allows the electrolyte to remain stable on the electrode surface. Figure 29B,C show the surface and cross-sectional (inset images) morphologies of Li deposited on the bare Cu electrode and Cu-MOFs electrode, respectively. After 5 cycles limited to the capacity of 1 mAh cm^{-2} at a current density of 0.5 mA cm^{-2} , the bare Cu electrode showed a very uneven shape, whereas the Cu-MOFs electrode showed a relatively flat surface. The optical images (inset images in the upper right of Figure 29B,C) of Li deposited on these two electrodes also show significant differences. A typical dark gray Li deposit called Elton's gray layer was observed on the bare Cu electrode. Coin-type batteries were used to observe the cycling stability of Li plating/stripping. As shown in Figure 29D, the Cu-MOFs electrode maintained a CE of about 98.4% for more than 180 cycles under the condition of a lithiation capacity of 1 mAh cm^{-2} and a current density of 2 mA cm^{-2} . On the other hand, the bare Cu electrode exhibits an unstable CE and short cycle life under the same operating condition, representing an inferior electrochemical cycle. The results of this study open the

possibility of designing LMBs with high energy density due to the advantages that they offer of high electrolyte absorption, high surface area, polar functional groups, and tunable pore structure with a high content of MOFs as an electrode modifier. Also, shortly, this approach will also apply to other metal secondary batteries.

Utilizing a 3D host framework as a Li storage medium has generated great interest as an effective approach to solve the technical problems related to the formation of Li dendrites and volume changes.^{649,650} The 3D host framework can be endowed with high Li storage capacity by providing abundant interior space for hosting metallic Li plating, so that it will not undergo any appreciable volume changes during Li plating/stripping. A 3D host framework with a high surface area can modulate the electric field for Li^+ transport to significantly reduce the effective current density and mitigate the nucleation and growth of Li dendrites.⁶⁵¹ Indeed, the efficacy of using carbon nanofibers/nanotubes,⁶⁵¹ graphene,⁶⁵² polymers,⁶⁵³ and metallic Ni and Cu^{647,654} as 3D host materials has been demonstrated. Liang et al. reported the experimental results of a Li-scaffold composite electrode fabricated using the method of Li melt implantation on a porous carbon matrix deposited with lithiophilic Li.⁶⁵⁵ The resulting composite electrode showed low overpotential for Li plating-stripping and consequently high structural stability and stable cycling performance. Li

et al. reported a porous carbon with 3D structure forming a strong SEI with doped fluorine species by promoted uniform distribution of current density with graphene shuttle. This porous carbon network structure can effectively suppress the formation of Li dendrites and maintain a high CE of 99%.

Preparing a 3D-structured anode is one of effective and easy approach to control the volume changes of the Li metal anode and suppress the Li dendrites.^{607,654,656} Cui et al. reported experimental findings of significant differences in Li metal nucleation barriers among 11 types of metal substrate materials (Cu, C, Zn, Mg, Al, Ni, Si, Sn, Au, Ag, and Pt), and reported the Li nucleation overpotentials in these substrates.⁶⁵⁷ It has been shown that no overpotential is required to nucleate Li metal in Mg, Zn, Ag, and Au, which can be explained in terms of solubility of Li metal in these substrates. The principle of Li metal nucleation in various metal substrates has laid the basis for designing 3D structures of Li metal anodes that are Li dendrite-free. To reduce the formation of Li dendrites and lead to a more uniform deposition of Li, it is necessary to use a lithiophilic material with large surface area and low nucleation overpotential with respect to Li.

In addition to the porous and large surface area properties of MOFs, their polar functional groups can induce uniform Li nucleation.^{658–663} Wang et al. proposed a dual lithiophilic MOF structure composed of HKUST-1 impregnated with conductive lithiophilic Au nanoparticles (expressed as Ag@HKUST-1) to induce the uniform deposition of Li.⁶⁶⁴ Due to the large surface area and abundant O sites of the MOFs, the binding energy for Li is increased, followed by low nucleation overpotentials leading to a uniform distribution of Li nuclei. When Au particles with highly conductive lithiophilic are integrated with MOFs, the binding energy to Li is increases, and the nucleation overpotential approaches almost zero. Consequently, Li plating and stripping of Ag@HKUST-1 substrate exhibited a 97% of CE and had a high areal capacity of 5 mAh cm⁻² without the formation of Li dendrites.

Yang et al. reported Li-cMOFs (cMOFs: carbonized MOFs) hybrid 3D anode structures and studied their electrochemical performance.⁶⁶⁵ The MOF used in this study was ZIF-8, which is tetrahedrally coordinated by Zn²⁺ and imidazolate, and was transformed into a unique microporous carbon with well-constrained metal clusters after simple heat treatment.^{666–668} Carbonized ZIF-8 demonstrated that it was an ideal lithiophilic host for metallic Li, providing that easily molten Li can be implanted into the matrix to form a homogeneous lithium carbide MOF (Li-cMOF) hybrid. Since numerous Zn clusters were uniformly dispersed in the matrix and thermodynamically well matched with Li, which can

overcome the nucleation barrier, they acted like pre-planted nucleation seeds, leading to uniform Li deposition. At the same time, the 3D conductive porous structure in ZIF-8 dramatically homogenized the distributions of electric field and Li⁺ flux, preventing the formation of Li dendrites. In addition, the unlimited volume changes of Li due to plating and stripping could also be well handled by the porous ZIF-8. These characteristics make Li-cMOF a promising rechargeable Li anode material with excellent electrochemical performance, including a very low voltage hysteresis of 29 mV at 1 mA cm⁻² and a long lifetime of up to 350 cycles.

Similarly, Zhang et al. reported a ZnO/carbon/Li advanced anode using ZIF-8 that provided excellent battery performance.⁶⁶⁹ With the help of abundant ZnO, and carbonyl and N-containing surface functional groups, a free-standing and current-collector-free Li electrode in which molten Li was injected into the framework, was created. The structure has two notable advantages. First, the ZnO/carbon framework provides a stable scaffold for Li plating/stripping, greatly alleviating volume changes during cycling at the electrode level. Second, the excellent affinity of the ZnO/carbon framework with a large surface area ensures deposition and infusion of Li during synthesis and cycling. Due to these advantages, the ZnO/carbon/Li electrode shows good stability during cycling, even at a high current density of 10 mA cm⁻², which can significantly improve the electrochemical performance.

Recently, Park et al. proposed a dual function for Li storage in a porous carbon host using a ZIF-8-derived porous carbon framework (PCF).⁶¹⁰ Without using other templates, the ZIF-8 product was obtained by a simple method of dissolving and mixing Zn ions and 2-MIM in a solution, and a porous carbon structure was obtained through an easy carbonization process. The obtained porous carbon framework was denoted as PCF, and the product obtained by removing the residual Zn with HCl solution was called PCF-E, respectively. The reason why ZIF-8-based porous carbon material was selected in this study is that it has the following attributes: (1) carbon structure to absorb Li⁺, (2) large pore volume to accommodate metallic Li, (3) large surface area to reduce the effective current density, and (4) lithiophilic heteroelements to promote the nucleation kinetics. Based on the atomic model, the Li lattice gap formation energy for the Zn dopant was calculated by DFT, and the results showed that Zn donates excess electrons and further lowers the activation energy for Li adsorption and metallic Li formation, promoting lithiation and metallization of Li. Figure 30A is a schematic illustration showing dual-phase Li storage in a PCF structure. It can be seen that Li metal is stored in the pores of PCF and that Li⁺ are intercalated on the PCF surface. The reaction

mechanisms are as follows. During charging, Li^+ is inserted into the carbon structure and a lithiation reaction occurs. When PCF is fully lithiated, the surface becomes more lithiophilic, which mainly serves to lower the activation energy for Li adsorption and induce a uniform surface reaction inside the nanopores. The metallization reaction occurs as Li is plated inside the nanopores through the nucleation-growth process after the lithiation process. To confirm the electrochemical behavior, the galvanostatic charge–discharge curves of Super-P, PCF, and PCF-E were investigated. Super-P, which is a conductive and non-porous carbon material was used for comparison. PCF-E with a larger pore volume exhibited high reversibility and low overpotential for Li stripping during subsequent discharge. These results indicate that, in addition to lithiophilic element coordination, the porous structure of PCF is a major factor in accommodating the metallic Li phase. The electrochemical behavior of the metallization reaction was performed for full lithiation after 3 cycles in the voltage range of 0.01–2.0 V versus Li/Li^+ , discharging to 0 V versus Li/Li^+ . Then, a constant cathodic current (0.5 mA cm^{-2}) was applied to drive the metallization reaction, and the potential was monitored from that moment until the capacity reached 1.0 mAh cm^{-2} . PCF showed a flat voltage profile with a significant decrease in overpotential during Li plating at the same current density. Figure 30B,C are cross-sectional field emission SEM (FESEM) images of Super-P and PCF-E obtained after charging to 1.0 mAh cm^{-2} . It is clear that Super-P is covered with a thick layer of metallic Li moss-like fibers, whereas in PCF-E there is no Li dendrite growth. The reversibility of Li plating and stripping processes was determined by characterizing and comparing the cycling performance of Super-P and PCF-based anodes. For the cycling test, the cell was first charged to 2.0 mAh cm^{-2} and cycled at a constant capacity of 0.2 at 0.2 mA cm^{-2} . In the cycling results shown in Figure 30D, the $\text{Li}||\text{Super-P}$ cell using Super-P as an electrode showed very high overpotential and CE fluctuation after 88 cycles, suggesting dendritic Li growth or cell failure by Li exhaustion. The $\text{Li}||\text{PCF-E}$ cell using PCF-E as an electrode showed stable cycling behavior with no signs of failure over 350 cycles. The results of this study showed that MOF-derived PCF can act as a promising metallic Li storage material with dimensional stability, high capacity, and excellent circulation in application to LMBs.

The achievable rate capability and reversible capacity of ZIF-8 is limited, however, in terms of electrolyte access and Li^+ migration by its structural features, which are mainly composed of micropores (<2 nm). Therefore, the pore structure of the porous material becomes a major factor in determining the electrochemical performance in

Li storage, as the Li^+ conduction kinetics in the electrolyte must be considered for effective metallization of Li in a given pore structure.^{670,671} It is also necessary to establish a porous material and an open path with internal pores of appropriate size for homogeneous metallization of Li throughout the electrode. Otherwise, the internal pores will be electrochemically deactivated, eventually resulting in reduced reversible capacity and long-term cyclability. Park et al. created craters on the surfaces of ZIF-8 to secure an open path and investigated the role of the craters in improving the reversibility of plating and peeling when using ZIF-8 as a host for LMBs.⁶⁷² First, poly(vinylpyrrolidone) (PVP, $[\text{C}_6\text{H}_9\text{NO}]_n$) was dissolved in deionized (DI) water, and colloidal silica (SiO_2) solution was added to the PVP solution under stirring for 24 h. Then, a solution of zinc acetate dihydrate and 2-MIM dissolved in DI water as precursors were mixed with a PVP- SiO_2 solution and maintained without stirring. The precipitate was collected, washed, dried, and then the resulting powder was heat-treated in an Ar atmosphere. After etching with hydrofluoric acid solution to remove chemical residues, washing and drying were performed to obtain the final product. The structure without surface craters was named PCF, and the structure with surface craters was named SC-PCF. The surface structures of PCF and SC-PCF are shown in Figure 31A. The surface of SC-PCF, which is cratered due to silica particles, shows noticeable morphological changes and large pores are formed. PCF particles with surface craters have a typical amorphous carbon structure, and various chemical states of N exist, such as quaternary N, pyrrolic N, and pyridinic N, which play an key role in stable Li metal formation. The function of surface craters in modulating the Li storage response was analyzed using two different AC impedance measurements. From the impedance results, the MacMullin number (N_M) was estimated for both PCF electrodes, as shown in Figure 31B. N_M is defined as the ratio of the ionic conductivity (κ) of an electrolyte solution to the effective ionic conductivity (κ_{eff}) of an electrolyte-filled porous electrode, and indicates how effectively ions are transported through the electrode.⁶⁷³ The N_M value of SC-PCF was estimated to be 2.18 and that of PCF to be 4.47, which means that the integration of surface craters in SC-PCF helps to provide robust pathways for facile Li^+ transport through the electrode. PCFs are mainly composed of micropores, which provide a narrow path for the movement of Li^+ , resulting in high ionic resistance. This prevents the transport of Li^+ deep into the pores, causing preferential plating of Li at the pore orifice, which provides only limited utilization of the internal pores during charge the process. SC-PCF regulates Li^+ transport by reducing ionic resistance through the electrode due to the craters on the particle

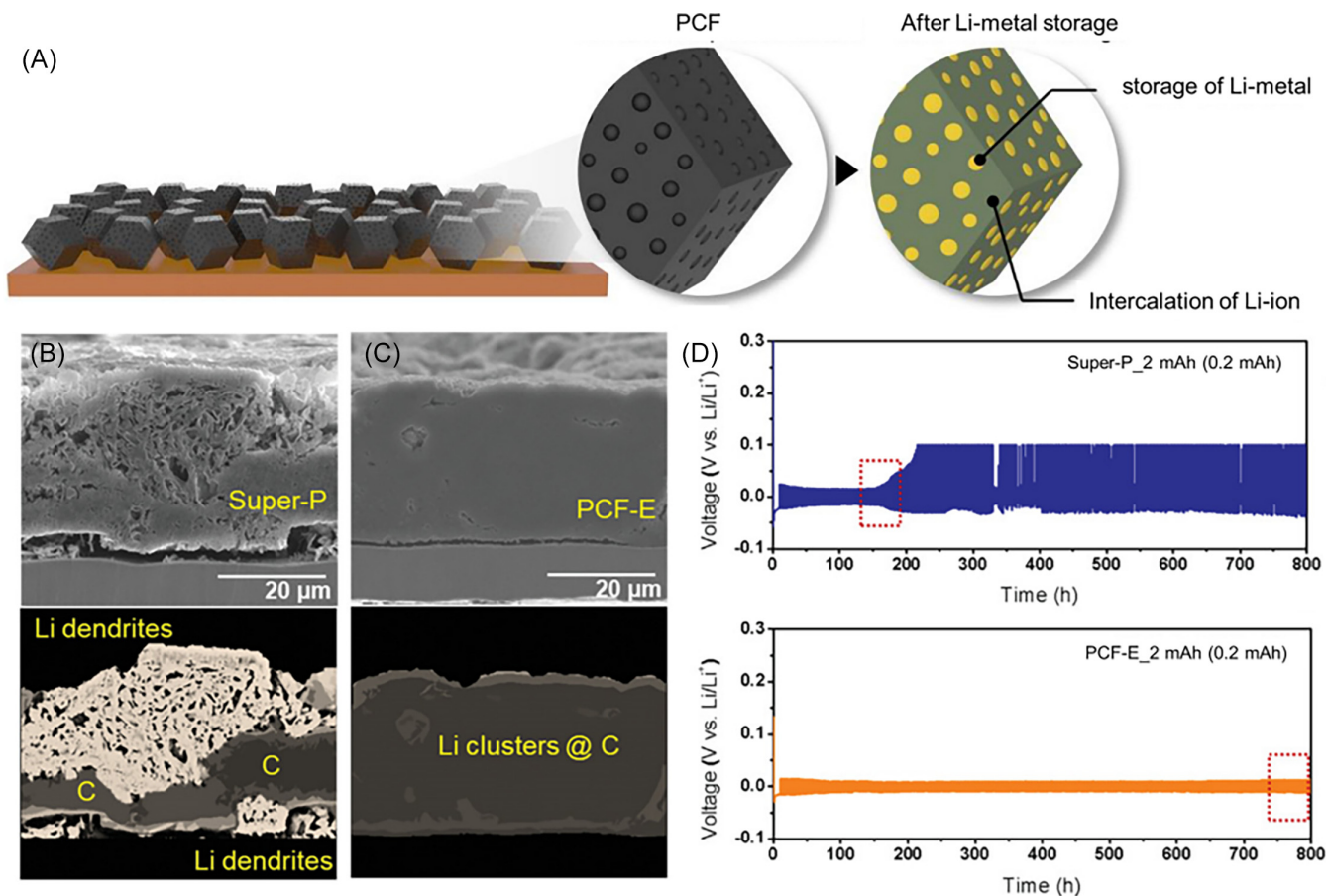


FIGURE 30 (A) Schematic illustration showing dual-phase Li storage in a porous carbon framework (PCF) structure. Li metal is stored in the pores of PCF, and Li⁺ are intercalated on the PCF surface. (B) Cross-sectional SEM images of Super-P obtained after charging to 1.0 mAh cm⁻². (C) Cross-sectional SEM images of PCF-E obtained after charging to 1.0 mAh cm⁻². (D) Cycling performances of Super-P and PCF-E at a constant capacity of 0.2 at 0.2 mA cm⁻². Reproduced with permission.⁶¹⁰ Copyright 2020, WILEY-VCH

surfaces, while also allowing Li⁺ to migrate into the internal pores to be plated. When the inner pores are filled with Li, the surface craters provide additional space for Li storage, allowing efficient use of both the inner pores and the surface craters, and enhancing the reversibility of Li plating and stripping. To clarify the role of surface craters for Li storage, the results for the electrochemical behavior during Li plating and stripping of PCF and SC-PCF are shown in Figure 31C. Both the PCF and the SC-PCF electrodes were galvanostatically charged to an areal capacity of 2 mAh cm⁻² with a current density of 0.2 mA cm⁻². They were initially lithiated (>0 V vs. Li/Li⁺) during charging (Li plating) and then metallic Li (<0 V vs. Li/Li⁺) was plated into the internal pores. During discharging (Li stripping), PCF and SC-PCF exhibited different behavior, and the initial CE of SC-PCF electrode was ~90.5%, much higher than that of PCF (~72.7%) because a larger amount of Li was removed from the SC-PCF electrode. This is because more of the pore space of the SC-PCF was effectively utilized as a reservoir for metallic Li during cycling. In

conclusion, the full cell composed of PCF anode with surface craters introduced noticeable improvements in speed and cycling performance compared to the original PCF full cell. This demonstrates that tuning the surface structure of PCFs can be novel strategy to enhance the electrochemical performance and cycle life of advanced host materials for LMBS.

The Zn atoms, which are metal ions constituting ZIF-8, plays a role in promoting stable Li metal formation in the host by increasing lipophilicity. Moreover, dual-phase lithiation and metallization can be realized in a single anode electrode, enabling a large amount of Li storage. Reinforcing weaknesses such as less stable surface chemistry causing dead-Li growth, however, still remains a challenge to be solved. Kim et al. proposed a structure in which Co nanoparticles are embedded in a porous N-doped graphite material derived from ZIF-8 as part of a study to improve this.⁶⁷⁰ Zn-based ZIF-derived carbon (ZC) and bimetallic ZIF-derived carbon (BZC) were synthesized by controlling the ratio of Zn to Co. Figure 32A shows the Li metal growth behavior in

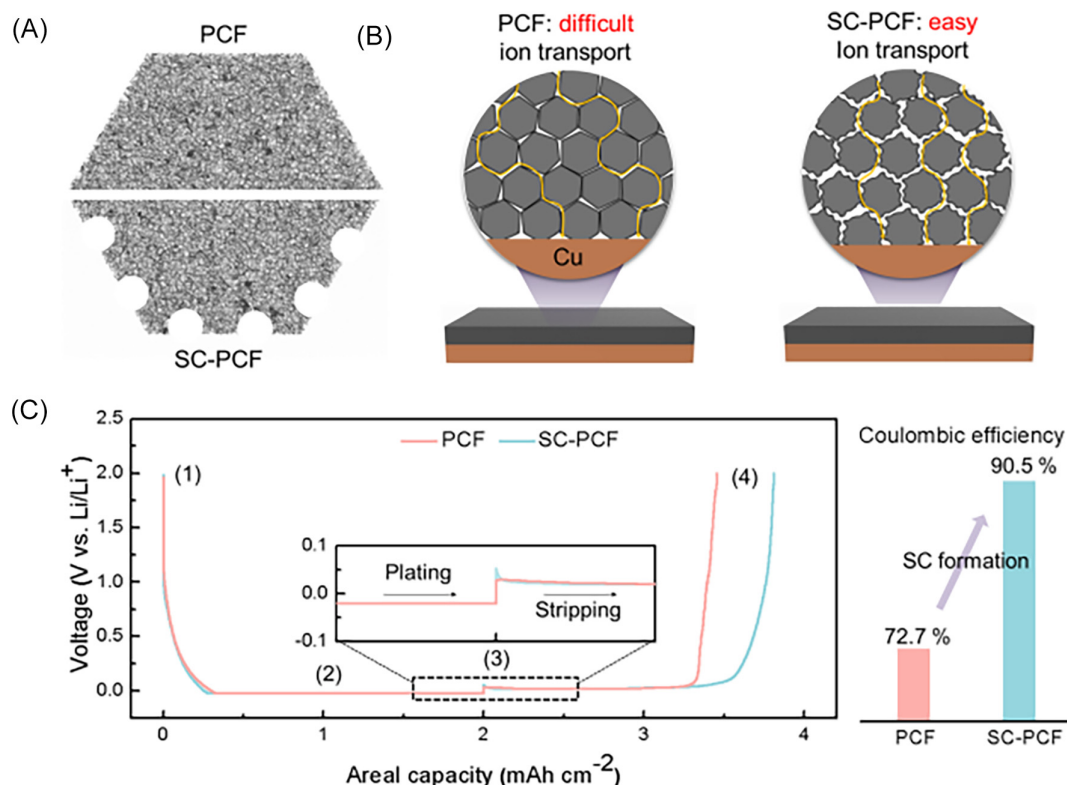


FIGURE 31 (A) Surface structures of porous carbon framework (PCF) and structure with surface craters (SC-PCF). (B) Schematic illustrations showing the ion transport, which was used to calculate the MacMullin numbers of PCF and SC-PCF electrodes. (C) The Li plating and stripping behavior of PCF and SC-PCF electrodes. Reproduced with permission.⁶⁷² Copyright 2021, Elsevier

ZC and BZC. It is well known that simple carbonization of ZIF synthesized with a Zn-ion precursor yields Zn-N-amorphous carbon, which exhibits excellent Li metal storage performance due to its high porosity and high conductivity. As shown in the TEM images located on the right of Figure 32A, it can be confirmed that a large number of Li metal whiskers had grown on the surface of the ZC after charging to 2 mAh cm⁻². On the other hand, Co-N-graphitic carbon derived from bimetallic Zn/Co-ZIF showed stable axial Li metal growth on the surface. It can be expected that, due to the catalytic effect of Co ions, many N dopants are bound to the graphite defects, resulting in excellent Li metal anode performance.^{674,675} DFT calculations were performed to investigate the causes of different types of Li metal growth behavior and to explore the optimal carbon structure in terms of the lithiophilicity of the surface chemistry. As shown in Figure 32B, the Li interstitial formation energy for various dopant elements was calculated based on the atomic model.⁶⁷⁶ in amorphous and graphite carbon structures. Elemental doping can effectively lowered the Li interstitial formation energy, and the N dopant forms the lowest Li interstitial energy in the graphite structure among various single dopants. From these discoveries, it was concluded that the best candidate for a Li metal host should

be rich in N-doped graphitic carbon with a high pore volume and acceptable electrical conductivity. Experimentally, the sample with the ratio of Co to Zn of 2:1 (expressed as BZC-2:1) had the highest pore volume (0.63 cc g⁻¹) and high electrical conductivity (16.7 S cm⁻¹), so it was sufficient for use as a metal host anode. The important role of Co was investigated by analyzing the charge density difference (ρ_{diff}) of Li adsorption on Co-N-doped graphite and N-doped graphite. The charge transfer by Li insertion occurring in Li-C and Li-N is shown in the yellow part of the isosurface in Figure 32C,D. The marked with cyan region represents charge depletion, which may be the driving force for local charge separation during polarization. When Co is doped, charge depletion is observed near the Co atom, and the donated charge participates in the creation of chemical bonds to Li. Co-N doped graphite allows the accumulation of delocalized electrons from surrounding electrons. Therefore, the interaction between Li and Co-N doped graphite is enhanced by Co. With planar Li plating, it is expected that the effect of Co-N extends to the second nearest neighbor of the C atom and that N affects only the nearest neighbor C atom. Using charge analysis, it was found that Li atoms provide charge to Co-N doped graphite which almost completely ionizes Li atoms.

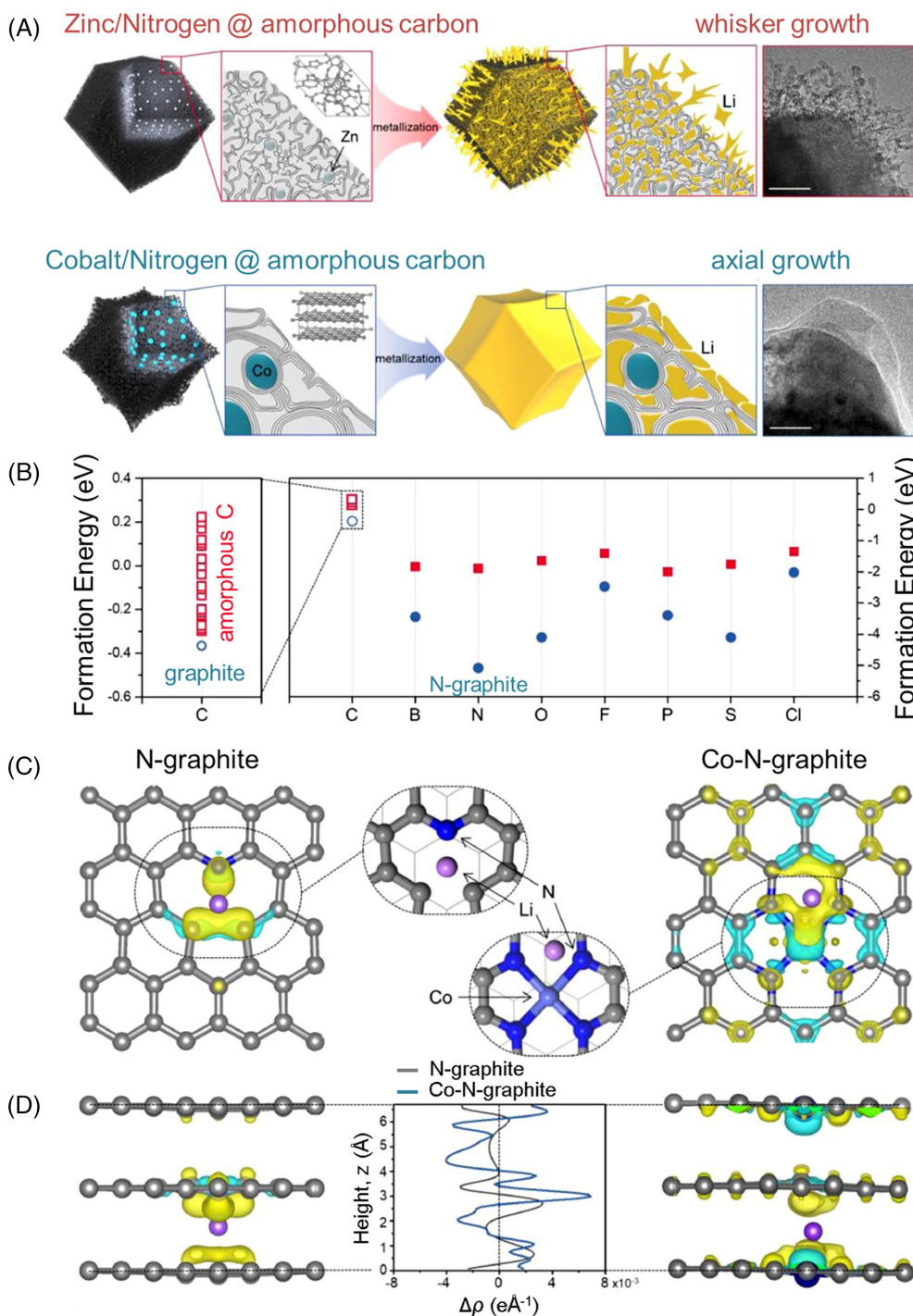


FIGURE 32 (A) Schematic illustration and TEM images of Li metal growth behavior in Zn/N @ amorphous carbon and Co/N @ amorphous carbon. (B) Density functional theory (DFT) calculations of the Li formation energies on amorphous and graphite carbon structures with possible hetero-atom dopants. (C) Transferred charge behavior on N-graphite and Co-N-graphite. (D) Charge deficiency about the z-axis hexagonal structure of graphite. Reproduced with permission.⁶⁷⁰ Copyright 2021, Elsevier

Saturation of electron-deficient Co-N bonds creates strong chemical bonds between graphite and Li^+ . In conclusion, the highly mesoporous N-graphite with Co nanoparticles proposed in this study showed noticeably high electrochemical performance without the formation of dead Li. This provides possibilities and understanding of the application of ZIF as an LMB anode material for next-generation lithium battery applications.

All the results based on using the porous carbon obtained from ZIF-8 as host material confirmed that it suppresses volume expansion as it does not form Li dendrites

during Li plating/stripping. Furthermore, they showed that N and Zn (or ZnO) nanoparticles within the host structure had enhanced affinity with Li and caused favorable nucleation and stable growth of Li metal. In conclusion, the ZIF-derived carbon hosts showed dramatically improved cycling performance compared to Li metal or non-porous carbon materials. So far, more than 30 000 MOFs with various structures and properties composed of different metal ions or clusters and ligands have been reported, which show tremendous potential to obtain carbonized composites that can be used as templates or precursors.

Metals, metal oxides, and metal sulfides act as lithophilic sites for Li nucleation and deposition. In addition to constructing a standalone carbonized MOF anode, other methods such as hot-pressing methods can be used to introduce MOFs into the network.^{677,678} The introduction of electrolyte additives can improve the cycling stability of LMBs,^{679–681} and several MOFs have been proposed for this purpose. The introduction of the additive usually results from the in-situ formation of a strong but thin SEI when the degradable additive comes into contact with Li, as is the case with LiNO₃ and fluoroethylene carbonate.^{616,623} Because sufficient porosity and thin-grain self-assembly are important in electrolyte fillers,⁶⁸² the search for flexible or modifiable additives that are full of multi-scale pores, functional groups, or building blocks is essential for the advancement of Li metal anodes. Additives are used to protect the anode by reacting with Li to form an SEI layer, and to inhibit the growth of Li dendrite.⁶⁸³ Li et al. proposed three MOFs (UiO-66, HKUST-1, NH₂-MIL-101) as electrolyte solid additives to inhibit the growth of Li dendrite.⁶⁸⁴ The MOF-based additives were synthesized by mixing with common carbonate electrolytes. Among them, Zr-based MOF additives (UiO-66) had the best electrical conductivity compared to other Cu-based MOFs (HKUST-1) and Al-based MOFs (NH₂-MIL-101). The system with UiO-66 enabled very long cycling of Li plating/stripping with a small voltage gap of 75–150 mV up to 1400 h at an areal capacity of 1.5 mAh cm⁻², based on a Li-Li symmetric cell. The robustness, porosity and electrochemical stability of the MOF additives promote the concentration of LiF in the SEI to reduce unwanted side reactions. It makes an important contribution to good Li anode performance by homogenizing the distribution and size of the Li⁺ flux and suppressing the extrusion of Li deposits. Table 7 summarizes the studies where MOFs were applied as an electrolyte, separator, and host in LMBs.^{223,549,550,610,629,631,634,644,646,664,665,669,670,672,685–687}

MOFs show tremendous potential for broad application in LMBs. In spite of the existing difficulties, we believe that the targeted and definite design of MOFs for LMBs will make increasingly valuable progress and make clean energy a reality in the near future.

5 | CONCLUSION AND PERSPECTIVE

There is no doubt that secondary batteries will provide a technical solution to resolve various social problems arising from energy crises as well as environmental issues. Therefore, it is crucial to develop highly reliable batteries with high energy density and long cycle lifetimes. Table 8 outlines the key features of advanced batteries in terms

of energy density, stability, processing, and cost. Given that the achievable energy density and performance of batteries would strongly depend on the choice of materials, continuous efforts should be made to find and develop advanced electrode/electrolyte materials for batteries. As discussed in this review, MOFs provide potential advantages as battery components, over conventional carbon and inorganic materials: for example, good ion mobility, gentle chemical interactions, open porous channels, and chemical/electrochemical compatibility with carbon-based electrodes. Furthermore, the easy crystallographic control of the constituent elements of the MOF increases the porosity and availability, resulting in improved performance. The multifaceted nature of MOFs offers great opportunities to develop battery materials with high thermal and mechanical stability, thereby pushing the limits of the current technology towards safe battery operations under extreme conditions.

The unique compositional and structural features of MOFs will provide more opportunities to improve the electrochemical performance of next-generation batteries, as summarized below:

1. Lithium-ion battery: MOFs can be used as advanced cathode and anode materials that offer higher Li storage capability than those of commercial materials. When MOFs are employed as cathode materials, they exhibit reversible Li storage behaviors based on the redox reactions of transition metals coordinated in the given structures during cycling. The crystal structures of MOFs can host a large amount of Li⁺ with excellent structural stability. In addition, the feasibility of MOFs has been examined as potential anode materials for LIBs. The porous structure of MOF is beneficial for boosting interfacial reaction kinetics as well as for improving dimensional stability (regarded as practical limitations of high-capacity anode materials), as demonstrated by superior rate capability and cycling stability. The large irreversible capacity of MOFs, however, still remains an open problem to be resolved. Comprehensive studies on structural modifications and optimizations are required to make MOFs more valuable in the development of high-energy LIBs. Recently, MOFs have been utilized as functional materials for separators owing to their porous structure and ion selectivity. They can be directly deposited on the polymeric membranes, providing various functionalities such as high permeability, high strength, and high heat resistance for improving the performance and safety of LIBs.
2. Lithium-metal battery: MOFs can be utilized as promising host materials for metallic Li storage in LMBs. The porous structure of MOFs offers sufficient free spaces and facile pathways for charge transport,

TABLE 7 Summary of recent studies in which MOFs or MOF derived materials were applied as electrolyte, separator, and host materials for LMBs.

MOF	Application part	Reversible capacity (mAh g ⁻¹)	Rate (mA g ⁻¹)	Cycle number	References	Note
ILE@ZIF-67	Solid state electrolyte	151	2 C	60	631	
SLE-UiO-66	Solid state electrolyte	129	0.1 C	100	223	
Li-IL@MOF (UiO-67)	Solid state electrolyte	140	0.1 C	150	629	
MOF-525(Cu)	Solid state electrolyte	145	0.1 C	100	685	
LPC@HKUST-1	Solid state electrolyte	106	1 C	500	685	
cationic MOF (CMOF)	Solid state electrolyte	100	1 C	300	634	
PEO-n-UIO	Solid state electrolyte	140	0.5 C	100	686	
NH ₂ -UiO-66	Solid state electrolyte	121	0.2 C	100	687	
UiO-66-S/Nafion	Separator	1127	0.1 C	200	549	
HKUST-1	Separator	135	5 C	2000	644	
HKUST-1	Separator	802	2 C	600	550	
Ag@HKUST-1	Host material	—	—	300	664	Long cycle life with a high CE over 97% at a current density of 0.5 mA cm ⁻²
ZIF-8	Host material	—	—	350	665	Overpotential of 29 mV at a current density of 1 mA cm ⁻² with the areal capacity of 1 mAh cm ⁻²
ZIF-8	Host material	—	—	200	669	Overpotential of ~14 mV at a current density of 1 mA cm ⁻² with the areal capacity of 1 mAh cm ⁻²
ZIF-8	Host material	—	—	350	610	Overpotential of 24.4 mV at a current density of 0.5 mA cm ⁻² with the areal capacity of 1 mAh cm ⁻²
ZIF-8	Host material	991	—	120	672	Overpotential of ~36 mV at a current density of 0.2 mA cm ⁻² with the areal capacity of 0.6 mAh cm ⁻²
Bimetallic ZIF	Host material	—	—	200	670	100% of coulombic efficiency even over 100 cycles at 0.4 mAh cm ⁻²

enabling reversible storage of metallic Li. This approach can effectively suppress the dendritic growth of metallic Li without volume changes during cycling. Moreover, a wide range of heteroatoms can be easily incorporated into the structure of MOFs during synthesis, and they would regulate interfacial reactions of

MOFs, allowing for more stable Li plating and stripping during cycling. Based on these merits of MOFs, current researches focus on the practical design of MOF electrodes for realizing highly reliable LMBs.

3. Lithium-sulfur battery: The large surface area and tunable porosity of MOFs are also advantageous for

TABLE 8 Outline of the types of batteries and a technology overview according to the most important aspect of performance of the battery.

Focusing performance	Aspect of performance	Technical overview
High energy	Li-S battery	<ol style="list-style-type: none"> Using sulfur as a cathode material and lithium as an anode material. Possible to realize an energy density three times higher than that of a LIB. Eco-friendly and low cost because uses sulfur waste, a by-product of crude oil refining.
	Li-air battery	<ol style="list-style-type: none"> Air (oxygen) is used as the cathode material and lithium is used as the anode material. Energy density equivalent to 5–10 times that of LIBs can be realized.
Stability	Solid-state battery	<ol style="list-style-type: none"> A battery in which all of the battery's components are solidified by replacing the electrolyte, which is generally a liquid type, with a solid electrolyte. Remarkably lowering the risk of ignition/explosion of LIBs, dramatically improving stability of the battery.
Function convenience	Flexible battery	<ol style="list-style-type: none"> A technical field that collectively refers to flexible and bendable batteries. Rather than being an independent field, flexible batteries are composed of a technology that provides mechanical flexibility by grafting it onto other battery fields. (Example: flexible all-solid-state battery, flexible LSB, etc.)
Manufacturing innovation	Printable battery	<ol style="list-style-type: none"> A technical field that refers to batteries manufactured through the printing process. A technology for printing batteries by grafting it to other battery technical fields, rather than being an independent field. (Example: printable LIB, printable all-solid-state battery, etc.)
Low cost of resource	Redox flow battery	<ol style="list-style-type: none"> A battery that charges and discharges through oxidation–reduction reactions using aqueous solutions of vanadium as positive and negative electrolytes. Longer lifespan (more than 10 times) and lower-cost (one-third the level) than of LIBs. Difficult to miniaturize due to its large volume and has disadvantages in that energy efficiency is lower than that of LIBs.
	Sodium-ion battery	<ol style="list-style-type: none"> A battery that uses sodium ions as ion carriers instead of lithium ions. Low-cost battery production is possible by replacing lithium, which is vulnerable to price and supply stability.
	Zn-air battery	<ol style="list-style-type: none"> Air (oxygen) is used as the anode material, and zinc is used as the anode material. No risk of explosion because it uses an aqueous electrolyte, and low-cost battery manufacturing is possible due to the use of zinc.

use as cathode materials for LSBs. In LSBs, a cathode is generally composed of solid sulfur and conductive carbon materials. Here, conductive carbon plays an important role in securing electrical conduction pathways as well as absorbing soluble polysulfide molecules. In this respect, MOFs have received great attention as promising cathode materials for LSBs because of their porous structure and excellent electrical conductivity. The solid sulfur and polysulfide molecules can be effectively confined in the free-space of MOFs, resulting in reduced side reactions (e.g., polysulfide shuttling). In addition, they can be used as absorbents for polysulfide molecules on the separator, leading to the improved reversibility of LSBs. Currently, various structural modifications of MOFs are in progress to improve the electrochemical performance of LSBs.

- Lithium air battery: In the development of LABs, MOFs have been considered as cathode materials owing to the large surface area and pore volumes. In principle, the charge transfer reactions occur on the surface of MOFs,

and discharge products (e.g., Li_2O_2) can be accommodated in the free spaces of MOFs. These structural features of MOFs can improve the reversibility of LABs by lowering the overpotentials mainly arising from the decomposition of discharge products upon charging. In addition, current efforts to enhance the electrical conductivity of MOFs via elemental doping and microstructural engineering would be essential for developing advanced cathode materials for LABs.

In this review, we overviewed and discussed the important characteristics of MOFs for use in electrochemical energy storage as well as their applications in next-generation batteries especially LIB, LSB, LAB, and LMB. The unique properties of MOFs in terms of porosity, stability, and synthetic tunability provide effective solutions to overcome technical bottlenecks in the development of high-performance and stable battery components (electrode, electrolyte, and separator). MOFs have emerged as effective materials for lithium storage applications due to

their special structural properties such as aligned channels and tunable open metal sites. The OMS of MOFs restrain the movement of anions and accelerate the transfer of Li^+ , showing excellent performance. Despite their great potentials, there is still much to be learned about the effective application of MOFs in energy storage devices. The chemical inertia of MOFs towards lithium needs to be systematically studied, as the interactions between different types of OMS or functional groups and lithium anions are not clear. Additionally, there are a large number of contact interfaces in each battery, and the improvement in Li^+ transport dynamics at these interfaces should also be fully accounted and studied. Understanding of these will provide guidance for future research. The strategies being studied and developed so far can inspire the identification and discovery of MOF materials with novel compositions and nanoarchitectures/nanoarchitectonics. In conclusion, the basic and applied knowledge gained from this review will help realize advanced MOF-based energy storage technology.

ACKNOWLEDGMENTS

This research was supported by the Technology Development Program to Solve Climate Changes through the National Research Foundation of Korea funded by the Ministry of Science, ICT (NRF-2021M1A2A2038145), Republic of Korea.

CONFLICT OF INTEREST

The authors declare no conflicts of interest.

ORCID

Jung Ho Kim  <https://orcid.org/0000-0003-4931-3553>

REFERENCES

- Li X, Jiang H, Liu Y, et al. Hierarchically porous membranes for lithium rechargeable batteries: recent progress and opportunities. *EcoMat*. 2022;4(1):e12162.
- Wang Z, Wang H, Qi S, et al. Structural regulation chemistry of lithium ion solvation for lithium batteries. *EcoMat*. 2022;4(4):e12200.
- Liu J, Yuan H, Tao X, et al. Recent progress on biomass-derived ecomaterials toward advanced rechargeable lithium batteries. *EcoMat*. 2020;2(1):e12019.
- Wu F, Maier J, Yu Y. Guidelines and trends for next-generation rechargeable lithium and lithium-ion batteries. *Chem Soc Rev*. 2020;49(5):1569-1614.
- Xu G, Nie P, Dou H, Ding B, Li L, Zhang X. Exploring metal organic frameworks for energy storage in batteries and supercapacitors. *Mater Today*. 2017;20(4):191-209.
- Wang H, Wang C, Tang Y. Interface engineering toward high-efficiency alloy anode for next-generation energy storage device. *EcoMat*. 2021;3(6):e12172.
- Zhao Y, Song Z, Li X, et al. Metal organic frameworks for energy storage and conversion. *Energy Storage Mater*. 2016;2:35-62.
- Weiss M, Ruess R, Kasnatscheew J, et al. Fast charging of lithium-ion batteries: a review of materials aspects. *Adv Energy Mater*. 2021;11(33):211126.
- Shadike Z, Tan S, Wang Q-C, et al. Review on organosulfur materials for rechargeable lithium batteries. *Mater Horiz*. 2021;8(2):471-500.
- Zhang W, Sun H, Hu P, Huang W, Zhang Q. Double-effect of highly concentrated acetonitrile-based electrolyte in organic lithium-ion battery. *EcoMat*. 2021;3(5):e12128.
- Li Y, Du Y-F, Sun G-H, et al. Self-standing hard carbon anode derived from hyper-linked nanocellulose with high cycling stability for lithium-ion batteries. *EcoMat*. 2021;3(2):e12091.
- Wang J, Kong H, Zhang J, Hao Y, Shao Z, Ciucci F. Carbon-based electrocatalysts for sustainable energy application. *Prog Mater Sci*. 2021;116:100717.
- Kshetri T, Tran DT, Le HT, et al. Recent advances in MXene-based nanocomposites for electrochemical energy storage applications. *Prog Mater Sci*. 2021;117:100733.
- He X, Bresser D, Passerini S, et al. The passivity of lithium electrodes in liquid electrolytes for secondary batteries. *Nat Rev Mater*. 2021;6(11):1036-1052.
- Galos J, Pattarakunnan K, Best AS, Kyratzis IL, Wang C-H, Mouritz AP. Energy storage structural composites with integrated lithium-ion batteries: a review. *Adv Mater Technol*. 2021;6(8):2001059.
- Lu C, Chen X. Learn from nature: bio-inspired structure design for lithium-ion batteries. *EcoMat*. 2022;4(3):e12181.
- Zhao H, Deng N, Yan J, et al. A review on anode for lithium-sulfur batteries: Progress and prospects. *Chem Eng J*. 2018;347:343-365.
- Zhao C-X, Chen W-J, Zhao M, et al. Redox mediator assists electron transfer in lithium-sulfur batteries with sulfurized polyacrylonitrile cathodes. *EcoMat*. 2021;3(1):e12066.
- Song Y, Gao H, Wang M, et al. Deciphering the defect micro-environment of graphene for highly efficient Li-S redox reactions. *EcoMat*. 2022;4(3):e12182.
- Rana M, Ahad SA, Li M, et al. Review on areal capacities and long-term cycling performances of lithium sulfur battery at high sulfur loading. *Energy Storage Mater*. 2019;18:289-310.
- Zhang M, Chen W, Xue L, et al. Adsorption-catalysis design in the lithium-sulfur battery. *Adv Energy Mater*. 2020;10(2):1903008.
- Li J, Niu Z, Guo C, Li M, Bao W. Catalyzing the polysulfide conversion for promoting lithium sulfur battery performances: a review. *J Energy Chem*. 2021;54:434-451.
- Guo W, Zhang W, Si Y, Wang D, Fu Y, Manthiram A. Artificial dual solid-electrolyte interfaces based on in situ organothiol transformation in lithium sulfur battery. *Nat Commun*. 2021;12(1):3031.
- Li Y, Guo S. Material design and structure optimization for rechargeable lithium-sulfur batteries. *Matter*. 2021;4(4):1142-1188.
- Shin H, Baek M, Gupta A, Char K, Manthiram A, Choi JW. Recent progress in high donor electrolytes for lithium-sulfur batteries. *Adv Energy Mater*. 2020;10(27):2001456.
- Subramanian K, Alexander GV, Karthik K, et al. A brief review of advances in garnet structured solid electrolyte based lithium metal batteries. *J Energy Storage*. 2021;33:102157.
- Shan X, Zhong Y, Zhang L, et al. A brief review on solid electrolyte interphase composition characterization technology

- for lithium metal batteries: challenges and perspectives. *J Phys Chem C*. 2021;125(35):19060-19080.
28. Alexander GV, Indu MS, Murugan R. Review on the critical issues for the realization of all-solid-state lithium metal batteries with garnet electrolyte: interfacial chemistry, dendrite growth, and critical current densities. *Ionics*. 2021;27(10):4105-4126.
 29. Wang Q, Liu B, Shen Y, et al. Confronting the challenges in lithium anodes for lithium metal batteries. *Adv Sci*. 2021;8(17):2101111.
 30. Wang C, Liang J, Luo J, et al. A universal wet-chemistry synthesis of solid-state halide electrolytes for all-solid state lithium-metal batteries. *Sci Adv*. 2021;7(37):eabh1896.
 31. Ren W, Zheng Y, Cui Z, Tao Y, Li B, Wang W. Recent progress of functional separators in dendrite inhibition for lithium metal batteries. *Energy Storage Mater*. 2021;35:157-168.
 32. Chen S, Dai F, Cai M. Opportunities and challenges of high-energy lithium metal batteries for electric vehicle applications. *ACS Energy Lett*. 2020;5(10):3140-3151.
 33. Hyeon Y, Lee J, Qutaish H, et al. Lithium metal storage in zeolitic imidazolate framework derived nanoarchitectures. *Energy Storage Mater*. 2020;33:95-107.
 34. Shi P, Zhang X-Q, Shen X, Zhang R, Liu H, Zhang Q. A review of composite lithium metal anode for practical applications. *Adv Mater Technol*. 2020;5(1):1900806.
 35. Varzi A, Thanner K, Scipioni R, et al. Current status and future perspectives of lithium metal batteries. *J Power Sources*. 2020;480:228803.
 36. Liu T, Vivek JP, Zhao EW, Lei J, Garcia-Araez N, Grey CP. Current challenges and routes forward for nonaqueous lithium-air batteries. *Chem Rev*. 2020;120(14):6558-6625.
 37. Kang J-H, Lee J, Jung J-W, et al. Lithium-air batteries: air-breathing challenges and perspective. *ACS Nano*. 2020;14(11):14549-14578.
 38. Lai J, Xing Y, Chen N, Li L, Wu F, Chen R. Electrolytes for rechargeable lithium-air batteries. *Angew Chem Int Ed*. 2020;59(8):2974-2997.
 39. Shin S, Yoon H, Yoon Y, Park S, Shin MW. Porosity tailoring of the Zn-MOF-5 derived carbon materials and its effects on the performance as a cathode for lithium-air batteries. *Microporous Mesoporous Mat*. 2021;311:110726.
 40. Imanishi N, Yamamoto O. Perspectives and challenges of rechargeable lithium-air batteries. *Mater Today Adv*. 2019;4:100031.
 41. Pan J, Tian XL, Zaman S, et al. Recent progress on transition metal oxides as bifunctional catalysts for lithium-air and zinc-air batteries. *Batter Supercaps*. 2019;2(4):336-347.
 42. Kwak W-J, Rosy SD, et al. Lithium-oxygen batteries and related systems: potential, status, and future. *Chem Rev*. 2020;120(14):6626-6683.
 43. Jung J-W, Cho S-H, Nam JS, Kim I-D. Current and future cathode materials for non-aqueous Li-air (O₂) battery technology—a focused review. *Energy Storage Mater*. 2020;24:512-528.
 44. Wang J, Fan M, Tu W, Chen K, Shen Y, Zhang H. In situ growth of Co₃O₄ on nitrogen-doped hollow carbon nanospheres as air electrode for lithium-air batteries. *J Alloy Compd*. 2019;777:944-953.
 45. Hong Y-S, Zhao C-Z, Xiao Y, et al. Safe lithium-metal anodes for Li-O₂ batteries: from fundamental chemistry to advanced characterization and effective protection. *Batteries Supercaps*. 2019;2(7):638-658.
 46. Wang F, Li X, Hao X, Tan J. Review and recent advances in mass transfer in positive electrodes of aprotic Li-O₂ batteries. *ACS Appl Energy Mater*. 2020;3(3):2258-2270.
 47. Zhao W, Mu X, He P, Zhou H. Advances and challenges for aprotic lithium-oxygen batteries using redox mediators. *Batteries Supercaps*. 2019;2(10):803-819.
 48. Kwak W-J, Chae S, Feng R, et al. Optimized electrolyte with high electrochemical stability and oxygen solubility for lithium-oxygen and lithium-air batteries. *ACS Energy Lett*. 2020;5(7):2182-2190.
 49. Zhu Y, Cao K, Cheng W, et al. A non-Newtonian fluidic cellulose-modified glass microfiber separator for flexible lithium-ion batteries. *EcoMat*. 2021;3(4):e12126.
 50. Xia J, Chen W, Yang Y, et al. In-situ growth of ultrathin sulfur microcrystal on MXene-based 3D matrix for flexible lithium-sulfur batteries. *EcoMat*. 2022;4(3):e12183.
 51. Zhao Y, Guo J. Development of flexible Li-ion batteries for flexible electronics. *InfoMat*. 2020;2(5):866-878.
 52. Chang J, Huang Q, Zheng Z. A figure of merit for flexible batteries. *Joule*. 2020;4(7):1346-1349.
 53. Qian G, Liao X, Zhu Y, Pan F, Chen X, Yang Y. Designing flexible lithium-ion batteries by structural engineering. *ACS Energy Lett*. 2019;4(3):690-701.
 54. Zhu Y-H, Yang X-Y, Liu T, Zhang X-B. Flexible 1D batteries: recent progress and prospects. *Adv Mater*. 2020;32(5):1901961.
 55. Dai C, Sun G, Hu L, Xiao Y, Zhang Z, Qu L. Recent progress in graphene-based electrodes for flexible batteries. *InfoMat*. 2020;2(3):509-526.
 56. Hager MD, Esser B, Feng X, Schuhmann W, Theato P, Schubert US. Polymer-based batteries-flexible and thin energy storage systems. *Adv Mater*. 2020;32(39):2000587.
 57. Costa CM, Gonçalves R, Lanceros-Méndez S. Recent advances and future challenges in printed batteries. *Energy Storage Mater*. 2020;28:216-234.
 58. Zeng L, Qiu L, Cheng H-M. Towards the practical use of flexible lithium ion batteries. *Energy Storage Mater*. 2019;23:434-438.
 59. Huang Y, Yang H, Xiong T, et al. Adsorption energy engineering of nickel oxide hybrid nanosheets for high areal capacity flexible lithium-ion batteries. *Energy Storage Mater*. 2020;25:41-51.
 60. Yang T, Xia J, Piao Z, et al. Graphene-based materials for flexible lithium-sulfur batteries. *ACS Nano*. 2021;15(9):13901-13923.
 61. Wu Z, Wang Y, Liu X, et al. Carbon-nanomaterial-based flexible batteries for wearable electronics. *Adv Mater*. 2019;31(9):1800716.
 62. Yim H, Yu S-H, Baek SH, Sung Y-E, Choi J-W. Directly integrated all-solid-state flexible lithium batteries on polymer substrate. *J Power Sources*. 2020;455:227978.
 63. Li X, Sun X, Hu X, et al. Review on comprehending and enhancing the initial Coulombic efficiency of anode materials in lithium-ion/sodium-ion batteries. *Nano Energy*. 2020;77:105143.
 64. Perveen T, Siddiq M, Shahzad N, Ihsan R, Ahmad A, Shahzad MI. Prospects in anode materials for sodium ion

- batteries-a review. *Renew Sustain Energy Rev.* 2020;119:109549.
65. Chen G, Huang Q, Wu T, Lu L. Polyanion sodium vanadium phosphate for next generation of sodium-ion batteries-a review. *Adv Funct Mater.* 2020;30(34):2001289.
 66. Yu P, Tang W, Wu F-F, et al. Recent progress in plant-derived hard carbon anode materials for sodium-ion batteries: a review. *Rare Metals.* 2020;39(9):1019-1033.
 67. Chang G, Zhao Y, Dong L, et al. A review of phosphorus and phosphides as anode materials for advanced sodium-ion batteries. *J Mater Chem A.* 2020;8(10):4996-5048.
 68. Liu X-H, Lai W-H, Chou S-L. The application of hollow micro-/nanostructured cathodes for sodium-ion batteries. *Mater Chem Front.* 2020;4(5):1289-1303.
 69. Liang Y, Lai W-H, Miao Z, Chou S-L. Nanocomposite materials for the sodium-ion battery: a review. *Small.* 2018;14(5):1702514.
 70. Vaalma C, Buchholz D, Weil M, Passerini S. A cost and resource analysis of sodium-ion batteries. *Nat Rev Mater.* 2018;3(4):18013.
 71. Sun M, Jiang Y, Ni J, Li L. Application of materials based on group VB elements in sodium-ion batteries: a review. *J Mater Sci Technol.* 2018;34(11):1969-1976.
 72. Su H, Jaffer S, Yu H. Transition metal oxides for sodium-ion batteries. *Energy Storage Mater.* 2016;5:116-131.
 73. Zhu X, Wang L. Advances in materials for all-climate sodium-ion batteries. *EcoMat.* 2020;2(3):e12043.
 74. Delmas C. Sodium and sodium-ion batteries: 50 years of research. *Adv Energy Mater.* 2018;8(17):1703137.
 75. Douka AI, Yang H, Huang L, et al. Transition metal/carbon hybrids for oxygen electrocatalysis in rechargeable zinc-air batteries. *EcoMat.* 2021;3(1):e12067.
 76. Hosseini S, Soltani SM, Li Y-Y. Current status and technical challenges of electrolytes in zinc-air batteries: An in-depth review. *Chem Eng J.* 2021;408:127241.
 77. Zhao Z, Fan X, Ding J, Hu W, Zhong C, Lu J. Challenges in zinc electrodes for alkaline zinc-air batteries: obstacles to commercialization. *ACS Energy Lett.* 2019;4(9):2259-2270.
 78. Zhang W, Liu Y, Zhang L, Chen J. Recent advances in isolated single-atom catalysis for zinc air batteries: a focus review. *Nanomaterials.* 2019;9(10):1402.
 79. Gu P, Zheng M, Zhao Q, Xiao X, Xue H, Pang H. Rechargeable zinc-air batteries: a promising way to green energy. *J Mater Chem A.* 2017;5(17):7651-7666.
 80. Riede J-C, Turek T, Kunz U. Critical zinc ion concentration on the electrode surface determines dendritic zinc growth during charging a zinc air battery. *Electrochim Acta.* 2018;269:217-224.
 81. Lao-atiman W, Oлару S, Arpornwichanop A, Kheawhom S. Discharge performance and dynamic behavior of refuellable zinc-air battery. *Sci Data.* 2019;6:168.
 82. Zhang Y, Deng Y-P, Wang J, et al. Recent progress on flexible Zn-air batteries. *Energy Storage Mater.* 2021;35:538-549.
 83. Mainar AR, Iruin E, Colmenares LC, et al. An overview of progress in electrolytes for secondary zinc-air batteries and other storage systems based on zinc. *J Energy Storage.* 2018;15:304-328.
 84. Yang J, Ganesan P, Ishihara A, Nakashima N. Carbon nanotube-based non-precious metal electrode catalysts for fuel cells, water splitting and zinc-air batteries. *Chem-CatChem.* 2019;11(24):5929-5944.
 85. Chen X, Zhou Z, Karahan HE, Shao Q, Wei L, Chen Y. Recent advances in materials and design of electrochemically rechargeable zinc-air batteries. *Small.* 2018;14(44):1801929.
 86. Zhu X, Hu C, Amal R, Dai L, Lu X. Heteroatom-doped carbon catalysts for zinc-air batteries: progress, mechanism, and opportunities. *Energy Environ Sci.* 2020;13(12):4536-4563.
 87. Lee J, Choi JW. Block copolymer binders with hard and soft segments for scalable fabrication of sulfide-based all-solid-state batteries. *EcoMat.* 2022;4(4):e12193.
 88. Zheng F, Kotobuki M, Song S, Lai MO, Lu L. Review on solid electrolytes for all-solid-state lithium-ion batteries. *J Power Sources.* 2018;389:198-213.
 89. Gurung A, Pokharel J, Baniya A, et al. A review on strategies addressing interface incompatibilities in inorganic all-solid-state lithium batteries. *Sustain Energy Fuels.* 2019;3(12):3279-3309.
 90. Nolan AM, Zhu Y, He X, Bai Q, Mo Y. Computation-accelerated design of materials and interfaces for all-solid-state lithium-ion batteries. *Joule.* 2018;2(10):2016-2046.
 91. Zhang F, Huang Q-A, Tang Z, et al. A review of mechanics-related material damages in all-solid-state batteries: mechanisms, performance impacts and mitigation strategies. *Nano Energy.* 2020;70:10454.
 92. Chen C, Jiang M, Zhou T, et al. Interface aspects in all-solid-state Li-based batteries reviewed. *Adv Energy Mater.* 2021;11(13):2003939.
 93. Wu Z, Xie Z, Yoshida A, et al. Utmost limits of various solid electrolytes in all-solid-state lithium batteries: a critical review. *Renew Sustain Energy Rev.* 2019;109:367-385.
 94. Tan DHS, Banerjee A, Chen Z, Meng YS. From nanoscale interface characterization to sustainable energy storage using all-solid-state batteries. *Nat Nanotechnol.* 2020;15(3):170-180.
 95. Xu H, Yu Y, Wang Z, Shao G. First principle material genome approach for all solid-state batteries. *Energy Environ Mater.* 2019;2(4):234-250.
 96. Wu Y, Wang S, Li H, Chen L, Wu F. Progress in thermal stability of all-solid-state-Li-ion-batteries. *InfoMat.* 2021;3(8):827-853.
 97. Chu J, Wang Y, Zhong F, et al. Metal/covalent-organic frameworks for electrochemical energy storage applications. *EcoMat.* 2021;3(5):e12133.
 98. Zhao G, Sun Y, Yang Y, Zhang C, An Q, Guo H. Molecular engineering regulation redox-dual-active-center covalent organic frameworks-based anode for high-performance Li storage. *EcoMat.* 2022;e212221. doi:10.1002/eom.2.12221
 99. Reddy RCK, Lin J, Chen Y, et al. Progress of nanostructured metal oxides derived from metal-organic frameworks as anode materials for lithium-ion batteries. *Coord Chem Rev.* 2020;420:213434.
 100. Kumar P, Pournara A, Kim K-H, Bansal V, Rapti S, Manos MJ. Metal-organic frameworks: challenges and opportunities for ion-exchange/sorption applications. *Prog Mater Sci.* 2017;86:25-74.
 101. Hankari SE, Bousmina M, Kadib AE. Biopolymer@metal-organic framework hybrid materials: a critical survey. *Prog Mater Sci* 2019; 106:100579.
 102. Li W. Metal-organic framework membranes: production, modification, and applications. *Prog Mater Sci.* 2019;100:21-63.

103. Gao X, Dong Y, Li S, Zhou J, Wang L, Wang B. MOFs and COFs for batteries and supercapacitors. *Electrochem Energy Rev.* 2020;3(1):81-126.
104. Xu Y, Li Q, Xue H, Pang H. Metal-organic frameworks for direct electrochemical applications. *Coord Chem Rev.* 2018;376:292-318.
105. Baumann AE, Burns DA, Liu B, Thoi VS. Metal-organic framework functionalization and design strategies for advanced electrochemical energy storage devices. *Comm Chem.* 2019;2:86.
106. Liang Z, Zhao R, Qiu T, Zou R, Xu Q. Metal-organic framework-derived materials for electrochemical energy applications. *EnergyChem.* 2019;1(1):100001.
107. Mehtab T, Yasin G, Arif M, et al. Metal-organic frameworks for energy storage devices: batteries and supercapacitors. *J Energy Storage.* 2019;21:632-646.
108. Zhao R, Liang Z, Zou R, Xu Q. Metal-organic frameworks for batteries. *Joule.* 2018;2(11):2235-2259.
109. Zhu JP, Wang XH, Zuo XX. The application of metal-organic frameworks in electrode materials for lithium-ion and lithium-sulfur batteries. *R Soc Open Sci.* 2019;6(7):190634.
110. Lee JY, Farha OK, Roverts J, Scheidt KA, Nguyen SBT, Hupp JT. Metal-organic framework materials as catalysts. *Chem Soc Rev.* 2009;38(5):1450-1459.
111. Zhu Q-L, Xu Q. Metal-organic framework composites. *Chem Soc Rev.* 2014;43(16):5468-5512.
112. Li H, Eddaoudi M, O'Keeffe M, Yaghi OM. Design and synthesis of an exceptionally stable and highly porous metal-organic framework. *Nature.* 1999;402(6759):276-279.
113. Xuan W, Zhu C, Liu Y, Cui Y. Mesoporous metal-organic framework materials. *Chem Soc Rev.* 2012;41(5):1677-1695.
114. Li B, Wen H-M, Cui Y, Zhou W, Qian G, Chen B. Emerging multifunctional metal-organic framework materials. *Adv Mater.* 2016;28(40):8819-8860.
115. Wang S, McGuirk CM, d'Aquino A, Mason JA, Mirkin CA. Metal-organic framework nanoparticles. *Adv Mater.* 2018;30(37):1800202.
116. Chakraborty G, Park I-H, Medishetty R, Vittal JJ. Two-dimensional metal-organic framework materials: synthesis, structures, properties and applications. *Chem Rev.* 2021;121(7):3751-3891.
117. Sanati S, Abazari R, Alberio J, et al. Metal-organic framework derived bimetallic materials for electrochemical energy storage. *Angew Chem Int Ed.* 2021;60(20):11048-11067.
118. Rodenas T, Luz I, Prieto G, et al. Metal-organic framework nanosheets in polymer composite materials for gas separation. *Nat Mater.* 2015;14(1):48-55.
119. Lin R-B, Xiang S, Zhou W, Chen B. Microporous metal-organic framework materials for gas separation. *Chem.* 2020;6(2):337-363.
120. Qiu S, Xue M, Zhu G. Metal-organic framework membranes: from synthesis to separation application. *Chem Soc Rev.* 2014;43(16):6116-6140.
121. Kang Z, Fan L, Sun D. Recent advances and challenges of metal-organic framework membranes for gas separation. *J Mater Chem A.* 2017;5(21):10073-10091.
122. Fonseca J, Choi S. Synthesis of a novel amorphous metal organic framework with hierarchical porosity for adsorptive gas separation. *Microporous Mesoporous Mat.* 2021;310:110600.
123. Wang C, Kaneti YV, Bando Y, et al. Metal-organic framework-derived one-dimensional porous or hollow carbon-based nanofibers for energy storage and conversion. *Mater Horiz.* 2018;5(3):394-407.
124. Xie X-C, Huang K-J, Wu X. Metal-organic framework derived hollow materials for electrochemical energy storage. *J Mater Chem A.* 2018;6(16):6754-6771.
125. Zhu L, Liu N, Lv X, Zhang Z, Yu L, Li X. A novel metal-organic framework derived carbon nanoflower with effective electromagnetic microwave absorption and high-performance electrochemical energy storage properties. *Chem Commun.* 2021;57(20):2539-2542.
126. Lu XF, Fang Y, Luan D, Lou XWD. Metal-organic frameworks derived functional materials for electrochemical energy storage and conversion: a mini review. *Nano Lett.* 2021;21(4):1555-1565.
127. Majumder M, Santosh MS, Viswanatha R, Thakur AK, Dubal DP, Jayaramulu K. Two-dimensional conducting metal-organic frameworks enabled energy storage devices. *Energy Storage Mater.* 2021;37:396-416.
128. Li S, Lin J, Xiong W, et al. Design principles and direct applications of cobalt-based metal-organic frameworks for electrochemical energy storage. *Coord Chem Rev.* 2021;438:213872.
129. Wang X, Wang Y, Ying Y. Recent advances in sensing applications of metal nanoparticle/metal-organic framework composites. *Trac-Trends Anal Chem.* 2021;143:116395.
130. Yan B. Luminescence response mode and chemical sensing mechanism for lanthanide-functionalized metal-organic framework hybrids. *Inorg Chem Front.* 2021;8(1):201-233.
131. Fang X, Zong B, Mao S. Metal-organic framework-based sensors for environmental contaminant sensing. *Nano-Micro Lett.* 2018;10(4):64.
132. Amini A, Kazemi S, Safarifard V. Metal-organic framework-based nanocomposites for sensing applications-a review. *Polyhedron.* 2020;177:114260.
133. Lei J, Qian R, Ling P, Cui L, Ju H. Design and sensing applications of metal-organic framework composites. *Trac-Trends Anal Chem.* 2014;58:71-78.
134. Kumar P, Deep A, Kim K-H. Metal organic frameworks for sensing applications. *Trac-Trends Anal Chem.* 2015;73:39-53.
135. Qiu Q, Chen H, Wang Y, Ying Y. Recent advances in the rational synthesis and sensing applications of metal-organic framework biocomposites. *Coord Chem Rev.* 2019;387:60-78.
136. Wang Y, Gao X, Wu M, Tsubaki N. Thermocatalytic hydrogenation of CO₂ into aromatics by tailor-made catalysts: recent advancements and perspectives. *EcoMat.* 2021;3(1):e12080.
137. Chen W, Duan X, Zhou X, Chen D. Design and tailoring of advanced catalytic probes for light alkanes upgrading. *EcoMat.* 2021;3(2):e12095.
138. Wei Y-S, Zhang M, Zou R, Xu Q. Metal-organic framework-based catalysts with single metal sites. *Chem Rev.* 2020;120(21):12089-12174.
139. Goetjen TA, Liu J, Wu Y, et al. Metal-organic framework (MOF) materials as polymerization catalysts: a review and recent advances. *Chem Commun.* 2020;56(72):10409-10418.
140. Chen L, Xu Q. Metal-organic framework composites for catalysis. *Matter.* 2019;1(1):57-89.

141. Konnerth H, Matsagar BM, Chen SS, Prechtl MHG, Shieh F-K, Wu KC-W. Metal-organic framework (MOF)-derived catalysts for fine chemical production. *Coord Chem Rev.* 2020;416:213319.
142. Huang Y-B, Liang J, Wang X-S, Cao R. Multifunctional metal-organic framework catalysts: synergistic catalysis and tandem reaction. *Chem Soc Rev.* 2017;46(1):126-157.
143. Sun Y, Zheng L, Yang Y, et al. Metal-organic framework nanocarriers for drug delivery in biomedical applications. *Nano-Micro Lett.* 2020;12(1):103.
144. Osterrieth JWM, Fairen-Jimenez D. Metal-organic framework composites for theragnostics and drug delivery applications. *Biotechnol J.* 2021;16(2):2000005.
145. Wu M-X, Yang Y-W. Metal-organic framework (MOF)-based drug/cargo delivery and cancer therapy. *Adv Mater.* 2017;29(23):1606134.
146. Hashemzadeh A, Drummen GPC, Avan A, et al. When metal-organic framework mediated smart drug delivery meets gastrointestinal cancers. *J Mater Chem B.* 2021;9(19):3967-3982.
147. Zhang S, Pei X, Gao H, Chen S, Wang J. Metal-organic framework-based nanomaterials for biomedical applications. *Chin Chem Lett.* 2020;31(5):1060-1070.
148. Xu Q, Li C, Chen Y, Zhang Y, Lu B. Metal-organic framework-based intelligent drug delivery systems for cancer theranostic: a review. *Front Mater Sci.* 2021;15(3):374-390.
149. Cai W, Wang J, Chu C, Chen W, Wu C, Liu G. Metal-organic framework-based stimuli-responsive systems for drug delivery. *Adv Sci.* 2019;6(1):1801526.
150. Sarker M, Song JY, Jung SH. Adsorptive removal of anti-inflammatory drugs from water using graphene oxide/metal-organic framework composites. *Chem Eng J.* 2018;335:74-81.
151. Oh H, Li T, An J. Drug release properties of a series of adenine-based metal-organic frameworks. *Chem A Eur J.* 2015;21(47):17010-17015.
152. Jarai BM, Stillman Z, Attia L, Decker GE, Bloch ED, Fromen CA. Evaluating UiO-66 metal-organic framework nanoparticles as acid-sensitive carriers for pulmonary drug delivery applications. *ACS Appl Mater Interfaces.* 2020;12(35):38989-39004.
153. Lu L, Ma M, Gao C, et al. Metal organic framework@oosylsesequioxane core/shell-structured nanoplatfor for drug delivery. *Pharmaceutics.* 2020;12(2):98.
154. Lawson HD, Walton SP, Chan C. Metal-organic frameworks for drug delivery: a design perspective. *ACS Appl Mater Interfaces.* 2021;13(6):7004-7020.
155. Jia X, Yang Z, Wang Y, et al. Hollow mesoporous silica@metal-organic framework and applications for pH-responsive drug delivery. *ChemMedChem.* 2018;13(5):400-405.
156. Haber RG, Ebnöther A, Schmid H. Die synthesis von (\pm)-elutherol. Inhaltsstoffe aus eleutherine bulbosa (mill.) Urb. VII. *Helv Chim Acta.* 1956;39(6):1529.
157. Friedman L, Shechter H. Dimethylformamide as a useful solvent in preparing nitriles from aryl halides and cuprous cyanide; improved isolation techniques^{1a}. *J Org Chem.* 1961;26(7):2522-2524.
158. Newman MS, Phillips DK. The synthesis of 1-bromobenzo [c] phenanthrene¹. *J Am Chem Soc.* 1959;81(14):3667-3670.
159. Hoskins BF, Robson R. Infinite polymeric frameworks consisting of three dimensionally linked rod-like segments. *J Am Chem Soc.* 1989;111(15):5962-5964.
160. Yaghi OM, Li G, Li H. Selective binding and removal of guests in a microporous metal-organic framework. *Nature.* 1995;378(6558):703-706.
161. Rosi NL, Eckert J, Eddaoudi M, et al. Hydrogen storage in microporous metal-organic frameworks. *Science.* 2003;300(5622):1127-1129.
162. Stock N, Biswas S. Synthesis of metal-organic frameworks (MOFs): routes to various MOF topologies, morphologies, and composites. *Chem Rev.* 2012;112(2):933-969.
163. Liu W, Yin R, Xu X, Zhang L, Shi W, Cao X. Structural engineering of low-dimensional metal-organic frameworks: synthesis, properties, and applications. *Adv Sci.* 2019;6(12):1802373.
164. Li S, Wang Y, Qi C, et al. 3D energetic metal-organic frameworks: synthesis and properties of high energy materials. *Angew Chem Int Ed.* 2013;52(52):14031-14035.
165. Cai X, Xie Z, Li D, Kassymova M, Zang S-Q, Jiang H-L. Nano-sized metal-organic frameworks: synthesis and applications. *Coord Chem Rev.* 2020;417:213366.
166. Zhou H-C, Long JR, Yaghi OM. Introduction to metal-organic frameworks. *Chem Rev.* 2012;112(2):673-674.
167. Zhou H-C, Kitagawa S. Metal-organic frameworks (MOFS). *Chem Soc Rev.* 2014;43(16):5415-5418.
168. Lu W, Wei Z, Gu Z-Y, et al. Tuning the structure and function of metal-organic frameworks via linker design. *Chem Soc Rev.* 2014;43(16):5561-5593.
169. Yaghi OM, O'Keeffe M, Sckwig NW, Chae HK, Eddaoudi M, Kim J. Reticular synthesis and the design of new materials. *Nature.* 2003;423(6941):705-714.
170. Barthelet K, Marrot J, Riou D, Férey G. A breathing hybrid organic-inorganic solid with very large pores and high magnetic characteristics. *Angew Chem Int Ed.* 2001;41(2):281-284.
171. Millange F, Serre C, Férey G. Synthesis, structure determination and properties of MIL-53as and MIL-53ht: the first Cr^{III} hybrid inorganic-organic microporous solids: Cr^{III}(OH) \cdot {O₂C-C₆H₄-CO₂} \cdot {HO₂C-C₆H₄-CO₂H}_x. *Chem Commun.* 2002;(8):822-823.
172. Serre C, Millange F, Thouvenot C, et al. Very large breathing effect in the first nanoporous chromium(III)-based solids: MIL-53 or Cr^{III}(OH) \cdot {O₂C-C₆H₄-CO₂} \cdot {HO₂C-C₆H₄-CO₂H}_x \cdot H₂O_y. *J Am Chem Soc.* 2002;124(45):13519-13526.
173. Loiseau T, Serre C, Huguenaud H, et al. A rationale for the large breathing of the porous aluminum terphthalate (MIL-53) upon hydration. *Chem A Eur J.* 2004;10(6):1373-1382.
174. Chui SS, Lo SM, Charmant JP, Orpen AG, Williams ID. A chemically functionalizable nanoporous material [Cu₃(TMA)₂(H₂O)₃]_n. *Science.* 1999;283(5405):1148-1150.
175. Zhang XX, Chui SS-Y, Williams D. Cooperative magnetic behavior in the coordination polymers [Cu₃(TMA)₂L₃] (L=H₂O, pyridine). *J Appl Phys.* 2000;87(9):6007.
176. Mellot-Draznieks C, Dutour J, Férey G. Hybrid organic-inorganic frameworks: routes for computational design and structure prediction. *Angew Chem Int Ed.* 2004;43(46):6290-6296.
177. Xie L, Liu S, Gao C, et al. Mixed-valence iron(II,III) trimesates with open frameworks modulated by solvents. *Inorg Chem.* 2007;46(19):7782-7788.
178. Zhang Z, Zhang L, Wojtas L, Eddaoudi M, Zaworotko MJ. Template-directed synthesis of nets based upon

- octahemioctahedral cages that encapsulate catalytically active metalloporphyrins. *J Am Chem Soc.* 2012;134(2):928-933.
179. Llewellyn PL, Horcajada P, Maurin G, et al. Complex adsorption of short linear alkanes in the flexible metal-organic-framework MIL-53(Fe). *J Am Chem Soc.* 2009;131(36):13002-13008.
 180. Ba Y, Guo D, Duan CY, Dang DB, Meng QJ. A three dimensional porous metal-organic framework $[\text{Fe}_4\text{L}_6(\text{DMF})_3(\text{H}_2\text{O})_{10}]$ constructed from neutral discrete Fe_4L_6 pyramids [$\text{H}_2\text{L} = 1,3$ bensodihydroxamic acid]. *Chem Commun.* 2004;(2):186-187.
 181. Whitfield TR, Wang X, Liu L, Jacobson AJ. Metal-organic frameworks based on iron oxide octahedral chains connected by benzenedicarboxylate dianions. *Solid State Sci.* 2005;7(9):1096-1103.
 182. Murray LJ, Dinca M, Yano J, et al. Highly-selective and reversible O_2 binding in $\text{Cr}_3(1,3,5\text{-benzenetricarboxylate})_2$. *J Am Chem Soc.* 2010;132(23):7856-7857.
 183. Mulder FM, Assfour B, Huot J, Dingemans TJ, Wagemaker M, Ramirez-Cuesta AJ. Hydrogen in the metal-organic framework Cr MIL-53. *J Phys Chem C.* 2010;114(23):10648-10655.
 184. Bourrelly S, Moulin B, Rivera A, et al. Explanation of the adsorption of polar vapors in the highly flexible metal organic framework MIL-53(Cr). *J Am Chem Soc.* 2010;132(27):9488-9498.
 185. Trung TK, Trens P, Tanchoux N, et al. Hydrocarbon adsorption in the flexible metal organic frameworks MIL-53(Al, Cr). *J Am Chem Soc.* 2008;130(50):16926-16932.
 186. Rosenbach N Jr, Jobic H, Ghoufi A, et al. Quasi-elastic neutron scattering and molecular dynamics study of methane diffusion in metal organic frameworks MIL-47(V) and MIL-53(Cr). *Angew Chem Int Ed.* 2008;47(35):6611-6615.
 187. Maniam P, Stock N. Investigation of porous Ni-based metal-organic frameworks containing paddle-wheel type inorganic building units via high-throughput methods. *Inorg Chem.* 2011;50(11):5085-5097.
 188. Kozachuk O, Yussenko K, Noei H, et al. Solvothermal growth of a ruthenium metal-organic framework featuring HKUST-1 structure type as thin films on oxide surfaces. *Chem Commun.* 2011;47(30):8509-8511.
 189. Zhang W, Freitag K, Wannapaiboon S, et al. Elaboration of highly porous $\text{Ru}^{\text{II,III}}$ analogue of HKUST-1. *Inorg Chem.* 2016;55(24):12492-12495.
 190. Xu G, Zhang X, Guo P, Pan C, Zhang H, Wang C. Mn^{II} -based MIL-53 analogues: synthesis using neutral bridging μ_2 -ligands and application in liquid-phase adsorption and separation of C6–C8 aromatics. *J Am Chem Soc.* 2010;132(11):3656-3657.
 191. Moon HR, Kobayashi N, Suh MP. Porous metal-organic framework with coordinatively unsaturated Mn^{II} sites: sorption properties for various gases. *Inorg Chem.* 2006;45(21):8672-8676.
 192. Dincă M, Dailly A, Liu Y, Brown CM, Neumann DA, Long JR. Hydrogen storage in microporous metal-organic framework with exposed Mn^{2+} coordination sites. *J Am Chem Soc.* 2006;128(51):16876-16883.
 193. Wang X-W, Dong Y-R, Zheng Y-Q, Chen J-Z. A novel five-connected BN topological network metal-organic framework $\text{Mn}(\text{II})$ cluster complex. *Cryst Growth des.* 2007;7(4):613-615.
 194. Rosi NL, Kim J, Eddaoudi M, Chen B, O'keeffe M, Yaghi OM. Rod packings and metal-organic frameworks constructed from rod-shaped secondary building units. *J Am Chem Soc.* 2005;127(5):1504-1518.
 195. Salles F, Maurin G, Serre C, et al. Multistep N_2 breathing in the metal-organic framework $\text{co}(1,4\text{-benzenedipyrzolate})$. *J Am Chem Soc.* 2010;132(39):13782-13788.
 196. Cheon YE, Suh MP. Selective gas adsorption in a microporous metal-organic framework constructed of CoII_4 clusters. *Chem Commun.* 2009;(17):2296-2298.
 197. An J, Geib SJ, Rosi N. High and selective CO_2 uptake in a cobalt aeninate metal-organic framework exhibiting pyrimidine- and amino- decorated pores. *J Am Chem Soc.* 2010;132(1):38-39.
 198. Kandiah M, Usseglio S, Svelle S, Olsbye U, Lillerud KP, Tilsted M. Post-synthetic modification of the metal-organic-framework compound UiO-66. *J Mater Chem.* 2010;20(44):9848-9851.
 199. Venturi DM, Campana F, Marmottini F, Costantino F, Vaccaro L. Extensive screening of green solvents for safe and sustainable UiO-66 synthesis. *ACS Sustainable Chem Eng.* 2020;8(46):17154-17164.
 200. Chavan S, Vitillo JG, Gianolio D, et al. H_2 storage in isostructural UiO-67 and UiO-66 MOFs. *Phys Chem Chem Phys.* 2012;14(5):1614-1626.
 201. Tan C, Han X, Li Z, Liu Y, Cui Y. Controlled exchange of achiral linkers with chiral linkers in Zr-based UiO-68 metal-organic framework. *J Am Chem Soc.* 2018;140(47):16229-16236.
 202. Ahnfeldt T, Guillou N, Gunzelmann D, et al. $[\text{Al}_4(\text{O}-\text{H})_2(\text{OCH}_3)_4(\text{H}_2\text{N}-\text{bdc})_3] \cdot x\text{H}_2\text{O}$: a 12-connected porous metal-organic framework with an unprecedented aluminum-containing brick. *Angew Chem Int Ed.* 2009;48(28):5163-5166.
 203. Reinsch H, Krüger M, Wack J, et al. A new aluminium-based microporous metal-organic framework: Al(BTB) (BTB = 1,3,5-benzenetrisbenzoate). *Microporous Mesoporous Mat.* 2012;157:50-55.
 204. Benecke J, Grape ES, Engesser TA, Inge AK, Reinsch H. Observation of three different linker conformers in a scandium ferrocenedicarboxylate coordination polymer. *CrystEngComm.* 2020;22(34):5569-5575.
 205. Phan A, Doonan CJ, Uribe-Romo FJ, Knobler CB, O'Keeffe M, Yaghi OM. Synthesis, structure, and carbon dioxide capture properties of zeolitic imidazolate framework. *Acc Chem Res.* 2010;43(1):58-67.
 206. Férey G, Serre C, Mellot-Draznieks C, et al. A hybrid solid with giant pores prepared by a combination of targeted chemistry, simulation, and powder diffraction. *Angew Chem Int Ed.* 2004;43(46):6296-6301.
 207. Juan-Alcañiz J, Goesten MG, Ramos-Fernandez EV, Gascon J, Kapteijn F. Towards efficient polyoxometalate encapsulation in MIL-100(Cr): influence of synthesis conditions. *New J Chem.* 2012;36(4):977-987.
 208. Jia X, Yuan N, Wang L, Yang J, Li J. $(\text{CH}_3)_2\text{NH}$ -assisted synthesis of high-purity Ni-HKUST-1 for the adsorption of CO_2 , CH_4 , and N_2 . *Eur J Inorg Chem.* 2018;2018(8):1047-1052.
 209. Ko N, Noh K, Sung S, Park HJ, Park SY, Kim J. Connection of zinc paddle-wheels in a pto-type metal-organic framework with 2-methylimidazolate and subsequent incorporation of charged organic guests. *Chem Commun.* 2014;50(51):6785-6788.
 210. Pirmohammadi Z, Bahrami A, Nematollahi D, Alizadeh S, Shahna FG, Rahimpour R. Determination of urinary

- methylhippuric acids using MIL-53-NH₂ (Al) metal-organic framework in microextraction by packed sorbent followed by HPLC-UV analysis. *Biomed Chromatogr.* 2020;34(1):e4725.
211. Diniz J, Soe E, Lu JE, et al. Oxygen reduction reaction catalyzed by metal-nitrogen-carbon hybrids derived from metal-organic frameworks: optimized performance by zinc porogen. *Sci Adv Mater.* 2020;12(11):1591-1600.
 212. Kramer M, Schwarz U, Kaskel S. Synthesis and properties of the metal-organic framework Mo₃(BTC)₂ (TUDMOF-1). *J Mater Chem.* 2006;16(23):2245-2248.
 213. Feldblyum JI, Liu M, Gidley DW, Matzger AJ. Reconciling the discrepancies between crystallographic porosity and guest access as exemplified by Zn-HKUST-1. *J Am Chem Soc.* 2011;133(45):18257-18263.
 214. Leclerc H, Devic T, Devautour-Vinot S, et al. Influence of the oxidation state of the metal center on the flexibility and adsorption properties of a porous metal organic framework: MIL-47(V). *J Phys Chem C.* 2011;115(40):19828-19840.
 215. Anokhina EV, Vougo-Zanda M, Wang X, Jacobson AJ. In (OH)BDC-0.75BDCH₂ (BDC = benzenedicarboxylate), a hybrid inorganic-organic Vernier structure. *J Am Chem Soc.* 2005;127(43):15000-15001.
 216. Vougo-Zanda M, Huang J, Anokhina E, Wang X, Jacobson AJ. Tossing and turning: guests in the flexible frameworks of metal(III) dicarboxylates. *Inorg Chem.* 2008;47(24):11535-11542.
 217. Li X, Cheng F, Zhang S, Chen J. Shape-controlled synthesis and lithium storage study of metal-organic frameworks Zn₄O(1,35-benzenetribenzoate)₂. *J Power Sources.* 2006;160:542-547.
 218. Fateeva A, Horcajada P, Devic T, et al. Synthesis, structure, characterization, and redox properties of the porous MIL-68 (Fe) solid. *Eur J Inorg Chem.* 2010;2010(24):3789-3794.
 219. Du M, Rui K, Chang Y, et al. Carbon necklace incorporated electroactive reservoir constructing flexible papers for advanced lithium-ion batteries. *Small.* 2018;14(2):1702770.
 220. Dan-Hardi M, Serre C, Fort T, et al. A new photoactive crystalline highly porous titanium(IV) dicarboxylate. *J Am Chem Soc.* 2009;131(31):10857-10859.
 221. Wiers BM, Foo M-L, Balsara NP, Long JR. A solid lithium electrolyte via addition of lithium isopropoxide to a metal-organic framework with open metal sites. *J Am Chem Soc.* 2011;133(37):14522-14525.
 222. Fischer S, Roeser J, Lin TC, et al. A metal-organic framework with tetrahedral aluminate sites as a single-ion Li⁺ solid electrolyte. *Angew Chem Int Ed.* 2018;57(51):16683-16687.
 223. Wang K, Yang L, Wang Z, et al. Enhanced lithium dendrite suppressing capability enabled by a solid-like electrolyte with different-sized nanoparticles. *Chem Commun.* 2018;54(93):13060-13063.
 224. Morris W, Voloskiy B, Demir S, et al. Synthesis, structure, and metalation of two new highly porous zirconium metal-organic frameworks. *Inorg Chem.* 2012;51(12):6443-6445.
 225. Babae S, Zarei M, Sepehrmansourie H, Zolfigol MA, Rostamnia S. Synthesis of metal-organic frameworks MIL-101 (Cr)-NH₂ containing phosphorous acid functional groups: application for the synthesis of N-amino-2-pyridone and pyrano [2,3-c]pyrazole derivatives via a cooperative vinylogous anomeric-based oxidation. *ACS Omega.* 2020;5(12):6240-6249.
 226. Peter IJ, Ramachandran K, Vijaya S, Anandan S, Nithiananthi P. Effect of phosphor on the efficiency of TiO₂/CdS/Ag₂S heterostructure based solar cells. *Mater Lett.* 2019;240:291-294.
 227. Xing X-S, Fu Z-H, Zhang N-N, Yu X-Q, Wang M-S, Guo G-C. High proton conduction in an excellent water-stable gadolinium metal-organic framework. *Chem Commun.* 2019;55(9):1241-1244.
 228. Mirkovic I, Lei L, Ljubic D, Zhu S. Crystl growth of metal-organic framework-5 around cellulose-based fibers having a necklace morphology. *ACS Omega.* 2019;4(1):169-175.
 229. Sun T, Xu L, Wang D, Li Y. Metal organic frameworks derived single atom catalysts for electrocatalytic energy conversion. *Nano Res.* 2019;12(9):2067-2080.
 230. Guo Z, Panda DK, Gordillo MA, et al. Lowering band gap of an electroactive metal-organic framework via complementay guest intercalation. *ACS Appl Mater Interfaces.* 2017;9(38):32413-32417.
 231. Kampouri S, Nguyen TN, Spodaryk M, et al. Concurrent photocatalytic hydrogen generation and dye degradation using MIL-125-NH₂ under visible light irradiation. *Adv Funct Mater.* 2018;28(52):1806368.
 232. Hendon CH, Tiana D, Fontecave M, et al. Engineering the optical response of the titanium-MIL-125 metal-organic framework through ligand functionalization. *J Am Chem Soc.* 2013;135(30):10942-10945.
 233. Yang L-M, Vajeeston P, Ravindran P, Fjellvåg H, Tilset M. Theoretical investigations on the chemical bonding, electronic structure, and optical properties of the metal-organic framework MOS-5. *Inorg Chem.* 2010;49(22):10283-10290.
 234. Li J, Musho T, Bright J, Wu N. Functionalization of a metal-organic framework semiconductor for tuned band structure and catalytic activity. *J Electrochem Soc.* 2019;166(5):H3029-H3034.
 235. Ravon U, Domine ME, Gaudillère C, Desmartin-Chomel A, Farrusseng D. MOFs as acid catalysts with shape selectivity properties. *New J Chem.* 2008;32(6):937-940.
 236. Pang J, Kang Z, Wang R, et al. Exploring the sandwich anti-bacterial membranes based on UiO66/graphene oxide for forward osmosis perfoamance. *Carbon.* 2019;144:321-332.
 237. Li L, Zhang S, Ruffley JP, Johnson JK. Energy efficient formaldehyde synthesis by direct hydrogenation of carbon monoxide in functionalize metal-organic frameworks. *ACS Sustainable Chem Eng.* 2019;7(2):2508-2515.
 238. Wang C-Y, Yu B, Fu H, Wang P, Wang C-C. A mixed valence Tb(III)/Tb(IV) metal-organic framework: crystal structure, luminescence property and selective detection of naproxen. *Polyhedron.* 2019;159:298-307.
 239. Wang Q, Liu DJ, Cui LL, Hu X-L, Wang X-L, Su Z-M. A 3D pillared-layer metal-organic framework with fluorescence property for detection of nitroaromatic explosives. *New J Chem.* 2019;43(2):963-969.
 240. Mahmoodi NM, Taghizadeh M, Taghizadeh A. Activated carbon/metal-organic framework composite as a bio-based novel green adsorbent: preparation and mathematical pollutant removal modeling. *J Mol Liq.* 2019;277:310-322.
 241. Mohaghegh N, Faraji M, Abedini A. Highly efficient multi-functional ag/TiO₂ nanotubes/Ti plate coated with MIL-88B (Fe) as a photocatalyst, adsorbent, and disinfectant in water treatment. *Appl Phys A-Mater Sci Process.* 2019;125(1):25.
 242. Kim M-K, Kim SH, Park M, Ryu SG, Jung H. Degradation of chemical warfare agents over cotton fabric functionalized with UiO-66-NH₂. *RSC Adv.* 2018;8(72):41633-41638.

243. Shen J, Wang N, Wang YG, Yu D, Ouyang X-K. Efficient adsorption of Pb(II) from aqueous solutions by metal organic framework (Zn-BDC) coated magnetic montmorillonite. *Polymers*. 2018;10(12):1383.
244. Esmailzadeh M. A composite prepared from a metal-organic framework of type MIL-101(Fe) and morin-modified magnetite nanoparticles for extraction and speciation of vanadium(IV) and vanadium(V). *Microchim Acta*. 2019;186(1):14.
245. Zhang L, Li S, Xin J, et al. A non-enzymatic voltammetric xanthine sensor based on the use of platinum nanoparticles loaded with a metal-organic framework of type MIL-101(Cr). Application to simultaneous detection of dopamine, uric acid, xanthine and hypoxanthine. *Microchim Acta*. 2019;186(1):9.
246. Henrique A, Rodrigues AE, Silva JAC. Separation of hexane isomers in ZIF-8 by fixed bed adsorption. *Ind Eng Chem Res*. 2019;58(1):378-394.
247. Chen X-Y, Zhao B, Shi W, et al. Microporous metal-organic frameworks built on a Ln3 cluster as a six-connecting node. *Chem Mater*. 2005;17(11):2866-2874.
248. Wang D, He H, Chen X, Feng X, Niu Y, Sun D. A 3D porous metal-organic framework constructed of 1D zigzag and helical chains exhibiting selective anion exchange. *CrystEngComm*. 2010;12(4):1041-1043.
249. Wu J-Y, Chao T-C, Zhong M-S. Influence of counteranions on the structural modulation of silver-Di(3-pyridylmethyl)amine coordination polymers. *Cryst Growth des*. 2013;13(7):2953-2964.
250. Li H, Davis CE, Groy TL, Kelley DG, Yaghi OM. Coordinatively unsaturated metal centers in the extended porous framework of $Zn_3(BDC)_3 \cdot 6CH_3OH(BDC = 1,4 \text{ benzenedicarboxylate})$. *J Am Chem Soc*. 1998;120(9):2186-2187.
251. Piñero-López L, Arcís-Castillo Z, Muñoz MC, Real JA. Clathration of five-membered aromatic rings in the bimetallic spin crossover metal-organic framework $[Fe(TPT)_{2/3}\{ml(CN)_2\}_2] \cdot G$ (ml = ag, au). *Cryst Growth des*. 2014;14(12):6311-6319.
252. Qi Y, Luo F, Che Y, Zheng J. Hydrothermal synthesis of metal-organic frameworks based on aromatic polycarboxylate and flexible bis(imidazole) ligands. *Cryst Growth des*. 2008;8(2):606-611.
253. Mu Y, Fu J, Song Y, Li Z, Hou H, Fan Y. Hydrothermal syntheses of metal-organic frameworks constructed from aromatic polycarboxylate and 4,4'-Bis(1,2,4-triazol-1-ylmethyl) biphenyl. *Cryst Growth des*. 2011;11(6):2183-2193.
254. Zhang L, Yao Y-L, Che Y-X, Zheng J-M. Hydrothermal synthesis of a series of interpenetrated metal-organic frameworks based on long multicarboxylate and long heterocyclic aromatic ligands. *Cryst Growth des*. 2010;10(2):528-533.
255. Sun L-X, Qi Y, Che Y-X, Batten SR, Zheng J-M. Three unprecedented entangled metal-organic frameworks: self-penetration and hydrothermal in situ ligand formation. *Cryst Growth des*. 2009;9(7):2995-2998.
256. Phang WJ, Lee WR, Yoo K, Ryu DW, Kim BS, Hong CS. pH-dependent proton conducting behavior in a metal-organic framework material. *Angew Chem*. 2014;126(32):8523-8527.
257. Jung SH, Yoon JW, Hwang J-S, Cheetham AK, Chang J-S. Facile synthesis of nanoporous nickel phosphates without organic templates under microwave irradiation. *Chem Mater*. 2005;17(17):4455-4460.
258. Jung SH, Chang J-S, Hwang JS, Park S-E. Selective formation of SAPO-5 and SAPO-34 molecular sieves with microwave irradiation and hydrothermal heating. *Microporous Mesoporous Mat*. 2003;64(1-3):33-39.
259. Hwang YK, Chang J-S, Park S-E, et al. Microwave fabrication of MFI zeolite crystals with a fibrous morphology and their applications. *Angew Chem Int Ed*. 2005;44(4):556-560.
260. Ni Z, Masel RI. Rapid production of metal-organic frameworks via microwave-assisted solvothermal synthesis. *J Am Chem Soc*. 2006;128(38):12394-12395.
261. Sabouni R, Kazemian H, Rohani S. Microwave synthesis of the CPM-5 metal organic framework. *Chem Eng Technol*. 2012;35(6):1086-1092.
262. Mueller U, Schubert M, Teich F, Puetter H, Schierle-Arndt K, Pastré J. Metal-organic frameworks-prospective industrial applications. *J Mater Chem*. 2006;16(7):626-636.
263. Van Assche TRC, Desmet G, Ameloot R, De Vos DE, Terryn H, Denayer JFM. Electrochemical synthesis of thin HKUST-1 layers on copper mesh. *Microporous Mesoporous Mat*. 2012;158:209-213.
264. Campagnol N, Souza ER, De Vos DE, Binnemans K, Franssaer J. Luminescent terbium-containing metal-organic framework films: new approaches for the electrochemical synthesis and application as detectors for explosives. *Chem Commun*. 2014;50(83):12545-12547.
265. Pichon A, Lazuen-Garay A, James SL. Solvent-free synthesis of a microporous metal-organic framework. *CrystEngComm*. 2006;8(3):211-214.
266. James SL, Adams CJ, Bolm C, et al. Mechanochemistry: opportunities for new and cleaner synthesis. *Chem Soc Rev*. 2012;41(1):413-447.
267. Masoomi MY, Morsali A, Junk PC. Rapid mechanochemical synthesis of two new Cd(II)-based metal-organic frameworks with high removal efficiency of Congo red. *CrystEngComm*. 2015;17(3):686-692.
268. Morsali A, Monfared HH, Morsali A, Janiak C. Ultrasonic irradiation assisted syntheses of one-dimensional di(azido)dipyridylamine Cu(II) coordination polymer nanoparticles. *Ultrason Sonochem*. 2015;23:208-211.
269. Jung D-W, Yang D-A, Kim J, Kim J, Ahn W-S. Facile synthesis of MOF-177 by a sonochemical method using 1-methyl-2-pyrrolidinone as a solvent. *Dalton Trans*. 2010;39(11):2883-2887.
270. Son W-J, Kim J, Kim J, Ahn W-S. Sonochemical synthesis of MOF-5. *Chem Commun*. 2008;(47):6336-6338.
271. Haque E, Khan NA, Park JH, Jung SH. Synthesis of a metal-organic framework material, iron terephthalate, by ultrasound, microwave, and conventional electric heating: a kinetic study. *Chem A Eur J*. 2010;16(3):1046-1052.
272. Jin L-N, Liu Q, Sun W-Y. An introduction to synthesis and application of nanoscale metal-carboxylate coordination polymers. *CrystEngComm*. 2014;16(19):3816-3828.
273. Bauer S, Serre C, Devic T, et al. High-throughput assisted rationalization of the formation of metal organic frameworks in the iron(III) aminoterephthalate solvothermal system. *Inorg Chem*. 2008;47(17):7568-7576.
274. Long P, Wu H, Zhao Q, Wang Y, Dong J, Li J. Solvent effect on the synthesis of MIL-96(Cr) and MIL-100(Cr). *Microporous Mesoporous Mat*. 2011;142(2-3):489-493.

275. Brozek CK, Bellarosa L, Soejima T, Clark TV, López N, Dincă. Solvent-dependent cation exchange in metal-organic frameworks. *Chem A Eur J*. 2014;20(23):6871-6874.
276. Yang D-A, Cho H-Y, Kim J, Yang S-T, Ahn W-S. CO₂ capture and conversion using mg-MOF-74 prepared by a sonochemical method. *Energ Environ Sci*. 2012;5(4):6465-6473.
277. Cho H-Y, Yang D-A, Kim J, Jeong S-Y, Ahn W-S. CO₂ adsorption and catalytic application of CO-MOF-74 synthesized by microwave heating. *Catal Today*. 2012;185(1):35-40.
278. Wu X, Bao Z, Yuan B, et al. Microwave synthesis and characterization of MOF-74 (M = Ni, mg) for gas separation. *Micropor Mesopor Mater*. 2013;180:114-122.
279. Chen Y, Lv D, Wu J, et al. A new MOF-505@GO composite with high selectivity for CO₂/CH₄ and CO₂/N₂ separation. *Chem Eng J*. 2017;308:1065-1072.
280. Lee Y-R, Kim J, Ahn W-S. Synthesis of metal-organic frameworks: a mini review. *Korean J Chem Eng*. 2013;30(9):1667-1680.
281. Loiseau T, Mellot-Draznieks C, Muguerra H, Férey G, Haouas M, Taulelle F. Hydrothermal synthesis and crystal structure of a new three-dimensional aluminum-organic framework MIL-69 with 2,6-naphthalenedicarboxylate (ndc), Al(OH)(ndc)·H₂O. *C R Chim*. 2005;8(3-4):765-772.
282. Banerjee R, Phan A, Wang B, et al. High-throughput synthesis of zeolitic imidazolate frameworks and application to CO₂ capture. *Science*. 2008;319(5865):939-943.
283. Stock N. High-throughput investigations employing solvothermal syntheses. *Micropor Mesopor Mater*. 2010;129(3):287-295.
284. Li M, Dong C, Yang J, et al. Solvothermal synthesis of La-based metal-organic frameworks and their color-tunable photoluminescence properties. *J Mater Sci-Mater Electron*. 2021;32(8):9903-9911.
285. Han SA, Lee J, Shim K, et al. Strategically designed zeolitic imidazolate frameworks for controlling the degree of graphitization. *Bull Chem Soc Jpn*. 2018;91(10):1474-1480.
286. Eddaoudi M, Kim J, Rosi N, et al. Systematic design of pore size and functionality in isoreticular MOFs and their application in methane storage. *Science*. 2002;295(5554):469-472.
287. Caskey SR, Wong-Foy AG, Matzger AJ. Dramatic tuning of carbon dioxide uptake via metal substitution in a coordination polymer with cylindrical pores. *J Am Chem Soc*. 2008;130(33):10870-10871.
288. Kamal K, Bustam MA, Ismail M, Grekov D, Shariff AM, Pré P. Optimization of washing processes in solvothermal synthesis of nickel-based MOF-74. *Materials*. 2020;13(12):2741.
289. Thomas-Hillman I, Laybourn A, Dodds C, Kingman SW. Realising the environmental benefits of metal-organic frameworks: recent advances in microwave synthesis. *J Mater Chem A*. 2018;6(25):11564-11581.
290. Cheng W, Wang Y, Ge S, Ding X, Cui Z, Shao Q. One-step microwave hydrothermal preparation of cd/Zr-bimetallic metal-organic frameworks for enhanced photochemical properties. *Adv Compos Hybrid Mater*. 2021;4(1):150-161.
291. Nguyen HTT, Tran KNT, Tan LV, et al. Microwave-assisted solvothermal synthesis of bimetallic metal-organic framework for efficient photodegradation of organic dyes. *Mater Chem Phys*. 2021;272:125040.
292. Appelhans LN, Hughes L, McKenzie B, et al. Facile microwave synthesis of zirconium metal-organic framework thin films on gold and silicon and application to sensor functionalization. *Microporous Mesoporous Mat*. 2021;323:111133.
293. Gaikwad R, Gaikwad S, Kim Y, Han S. Electrospun fiber mats with multistep seeded growth of UTSA-16 metal organic frameworks by microwave reaction with excellent CO₂ capture performance. *Microporous Mesoporous Mat*. 2021;323:111233.
294. Panda AB, Glaspell G, El-Shall MS. Microwave synthesis of highly aligned ultra narrow semiconductor rods and wires. *J Am Chem Soc*. 2006;128(9):2790-2791.
295. Gensheimer M, Becker M, Brandis-Heep A, Wendorff JH, Thauer RK, Greiner A. Novel biohybrid materials by electrospinning: nanofibers of poly(ethylene oxide) and living bacteria. *Adv Mater*. 2007;19(18):2480-2482.
296. Gong G, Zhou C, Wu J, Jin X, Jiang L. Nanofibrous adhesion: the twin of gecko adhesion. *ACS Nano*. 2015;9(4):3721-3727.
297. Xu S, Ren L-F, Zhou Q, Bai H, Li J, Shao J. Facile ZIF-8 functionalized hierarchical micronanofiber membrane for high-efficiency separation of water-in-oil emulsions. *J Appl Polym Sci*. 2018;135(27):46462.
298. Quirós J, Boltes K, Aguado S, Villoria de RG, Vilatela JJ, Rosal R. Antimicrobial metal-organic frameworks incorporated into electrospun fibers. *Chem Eng J*. 2015;262:189-197.
299. Kohsari I, Shariatnia Z, Pourmortazavi SM. Antibacterial electrospun chitosan-polyethylene oxide nanocomposite mats containing ZIF-8 nanoparticles. *Int J Biol Macromol*. 2016;91:778-788.
300. Peterson GW, Lu AX, Epps TH. Tuning the morphology and activity of electrospun polystyrene/UiO-66-NH₂ metal-organic framework composites to enhance chemical warfare agent removal. *ACS Appl Mater Interfaces*. 2017;9(37):32248-32254.
301. Liu F, Xu H. Development of a novel polystyrene/metal-organic framework-199 electrospun nanofiber adsorbent for thin film microextraction of aldehydes in human urine. *Talanta*. 2017;162:261-267.
302. Efome JE, Rana D, Matsuura T, Lan CQ. Insight studies on metal-organic framework nanofibrous membrane adsorption and activation for heavy metal ions removal from aqueous solution. *ACS Appl Mater Interfaces*. 2018;10(22):18619-18629.
303. Hong Y, Liu C, Cao X, et al. Process evaluation of the metal-organic frameworks for the application of personal protective equipment with filtration function. *Polymers*. 2018;10(12):1386.
304. Gaikwad S, Kim S-J, Han S. Novel metal-organic framework of UTSA-16 (Zn) synthesized by a microwave method: outstanding performance for CO₂ capture with improved stability to acid gases. *J Ind Eng Chem*. 2020;87:250-263.
305. Peh SB, Wang Y, Zhao D. Scalable and sustainable synthesis of advanced porous materials. *ACS Sustainable Chem Eng*. 2019;7(4):3647-3670.
306. Ameloot R, Stappers L, Franssaer J, Alaerts L, Sels BF, De Vos DE. Patterned growth of metal-organic framework coatings by electrochemical synthesis. *Chem Mater*. 2009;21(13):2580-2582.
307. Teo WL, Zhou W, Qian C, Zhao Y. Industrializing metal-organic frameworks: scalable synthetic means and their transformation into functional materials. *Mater Today*. 2021;47:170-186.
308. Zhou S, Wei Y, Li L, et al. Paralyzed membrane: current-driven synthesis of a metal-organic framework with sharpened propene/propane separation. *Sci Adv*. 2018;4(10):eaau1393.

309. Campagnol N, Assche TV, Boudewijns T, et al. High pressure, high temperature electrochemical synthesis of metal–organic frameworks: films of MIL-100 (Fe) and HKUST-1 in different morphologies. *J Mater Chem A*. 2013;1(19):5827-5830.
310. Joaristi AM, Juan-Alcañiz J, Serra-Crespo P, Kapteijn F, Gascon J. Electrochemical synthesis of some archetypical Zn^{2+} , Cu^{2+} , and Al^{3+} metal organic frameworks. *Cryst Growth des*. 2012;12(7):3489-3498.
311. Liu Y, Wei Y, Liu M, et al. Electrochemical synthesis of large area two-dimensional metal-organic framework films on copper anodes. *Angew Chem Int Ed*. 2021;60(6):2887-2891.
312. Makiura R, Motoyama S, Umemura Y, Yamanaka H, Sakata O, Kitagawa H. Surface nano-architecture of a metal–organic framework. *Nat Mater*. 2010;9(7):565-571.
313. Zhong Y, Cheng B, Park C, et al. Wafer-scale synthesis of monolayer two-dimensional porphyrin polymers for hybrid superlattices. *Science*. 2019;366(6471):1379-1384.
314. Liu J, Wöll C. Surface-supported metal–organic framework thin films: fabrication methods, applications, and challenges. *Chem Soc Rev*. 2017;46(19):5730-5770.
315. Adamas M, Kozłowska M, Baroni N, et al. Highly efficient one-dimensional triplet exciton transport in a palladium–porphyrin-based surface-anchored metal-organic framework. *ACS Appl Mater Interfaces*. 2019;11(17):15688-15697.
316. Chen D, Zhao J, Zhang P, Dai S. Mechanochemical synthesis of metal–organic frameworks. *Polyhedron*. 2019;162:59-64.
317. Yuan W, Garay AL, Pichon A, et al. Study of the mechanochemical formation and resulting properties of an archetypal MOF: $Cu_3(BTC)_2$ ($BTC = 1,3,5$ -benzenetricarboxylate). *CrstEngComm*. 2010;12(12):4063-4065.
318. Klimakow M, Klobes P, Thünemann AF, Rademann K, Emmerling F. Mechanochemical synthesis of metal-organic frameworks: a fast and facile approach toward quantitative yields and high specific surface areas. *Chem Mater*. 2010;22(18):5216-5221.
319. Klimakow M, Klobes P, Rademann K, Emmerling F. Characterization of mechanochemically synthesized MOFs. *Microporous Mesoporous Mater*. 2012;154:113-118.
320. Masoomi MY, Beheshti S, Morsali A. Mechanochemical synthesis of new azine-functionalized Zn(II) metal–organic frameworks for improved catalytic performance. *J Mater Chem A*. 2014;2(40):16863-16866.
321. Masoomi MY, Stylianou KC, Morsali A, Retailleau P, Maspoche D. Selective CO_2 capture in metal-organic frameworks with azine-functionalized pores generated by mechanochemical synthesis. *Cryst Growth des*. 2014;14(5):2092-2096.
322. Tanaka S, Kida K, Nagaoka T, Ota T, Miyake Y. Mechanochemical dry conversion of zinc oxide to zeolitic imidazolate framework. *Chem Commun*. 2013;49(72):7884-7886.
323. Zhang P, Li H, Veith GM, Dai S. Soluble porous coordination polymers by mechanochemistry: from metal-containing films/membranes to active catalysts for aerobic oxidation. *Adv Mater*. 2015;27(2):234-239.
324. Bowmaker GA. Solvent-assisted mechanochemistry. *Chem Commun*. 2013;49(4):334-348.
325. Delogu F, Gorrasi G, Sorrentino A. Fabrication of polymer nanocomposites via ball milling: present status and future perspectives. *Prog Mater Sci*. 2017;86:75-126.
326. Braga D, Giuffreda SL, Grepioni F, et al. Mechanochemical preparation of molecular and supramolecular organometallic materials and coordination networks. *Dalton Trans*. 2006;37(10):1249-1263.
327. Friščić T, Childs SL, Rizvi SAA, Jones W. The role of solvent in mechanochemical and sonochemical cocrystal formation: a solubility-based approach for predicting cocrystallisation outcome. *CrstEngComm*. 2009;11(3):418-426.
328. Beldon PJ, Fábíán L, Stein RS, Thirumurugan A, Cheetham AK, Friščić T. Rapid room-temperature synthesis of zeolitic imidazolate frameworks by using mechanochemistry. *Angew Chem Int Ed*. 2010;49(50):9640-9643.
329. Kang L, Sun S-X, Kong L-B, Lang J-W, Luo Y-C. Investigating metal-organic framework as a new pseudo-capacitive material for supercapacitors. *Chin Chem Lett*. 2014;25(6):957-961.
330. Wang D, Ni W, Pang H, Lu Q, Huang Z, Zhao J. Preparation of mesoporous NiO with a bimodal pore size distribution and application in electrochemical capacitors. *Electrochim Acta*. 2010;55(22):6830-6835.
331. Chen L, Bai J, Wang C, Pan Y, Scheer M, You X. One-step solid-state thermolysis of a metal–organic framework: a simple and facile route to large-scale of multiwalled carbon nanotubes. *Chem Commun*. 2008;(13):1581-1583.
332. Du P, Dong Y, Liu C, Wei W, Liu D, Liu P. Fabrication of hierarchical porous nickel based metal-organic framework (Ni-MOF) constructed with nanosheets as novel pseudo-capacitive material for asymmetric supercapacitor. *J Colloid Interface Sci*. 2018;518:57-68.
333. Jin L-N, Liu Q, Sun W-Y. Room temperature solution-phase synthesis of flower-like nanostructures of $[Ni_3(BTC)_2 \cdot 12H_2O]$ and their conversion to porous NiO. *Chin Chem Lett*. 2013;24(8):663-667.
334. Friščić T. Supramolecular concepts and new techniques in mechanochemistry: cocrystals, cages, rotaxanes, open metal–organic frameworks. *Chem Soc Rev*. 2012;41(9):3493-3510.
335. Pichon A, James SL. An array-based study of reactivity under solvent-free mechanochemical conditions—insights and trends. *CrstEngComm*. 2008;10(12):1839-1847.
336. Katsenis AD, Puškarić A, Štrukil V, et al. In situ X-ray diffraction monitoring of a mechanochemical reaction reveals a unique topology metal-organic framework. *Nat Commun*. 2015;6:6662.
337. Yuan W, O'Connor J, James SL. Mechanochemical synthesis of homo- and hetero-rare-earth(III) metal–organic frameworks by ball milling. *CrstEngComm*. 2010;12(11):3515-3517.
338. Prochowicz D, Sokotowski K, Justyniak I, et al. A mechanochemical strategy for IRMOF assembly based on pre-designed oxo-zinc precursors. *Chem Commun*. 2015;51(19):4032-4035.
339. Pilloni M, Padella F, Ennas G, et al. Liquid-assisted mechanochemical synthesis of an iron carboxylate metal organic framework and its evaluation in diesel fuel desulfurization. *Microporous Mesoporous Mat*. 2015;213:14-21.
340. Julien PA, Užarević K, Katsenis AD, et al. In situ monitoring and mechanism of the mechanochemical formation of a microporous MOF-74 framework. *J Am Chem Soc*. 2016;138(9):2929-2932.
341. Stolar T, Batzdorf L, Lukin S, et al. In situ monitoring of the mechanochemical synthesis of the archetypal metal–organic framework

- HKUST-1: effect of liquid additives on the milling reactivity. *Inorg Chem.* 2017;56(11):6599-6608.
342. Liu W, Zhu K, Teat SJ, Deibert BJ, Yuan W, Li J. A mechanochemical route toward the rational, systematic, and cost-effective green synthesis of strongly luminescent copper iodide based hybrid phosphors. *J Mater Chem C.* 2017;5(24):5962-5969.
343. Chen Y, Wu H, Liu Z, Sun X, Xia Q, Li Z. Liquid-assisted mechanochemical synthesis of copper based MOF-505 for the separation of CO₂ over CH₄ or N₂. *Ind Eng Chem Res.* 2018;57(2):703-709.
344. Zhang R, Tao C-A, Chen R, Wu L, Zou X, Wang J. Ultrafast synthesis of Ni-MOF in one minute by ball milling. *Nanomaterials.* 2018;8(12):1067.
345. Park KS, Ni Z, Côté AP, et al. Exceptional chemical and thermal stability of zeolitic imidazolate frameworks. *Proc Natl Acad Sci USA.* 2006;103(27):10186-10191.
346. Low JJ, Benin AI, Jakubczak P, Abrahamian JF, Faheem SA, Willis RR. Virtual high throughput screening confirmed experimentally: porous coordination polymer hydration. *J Am Chem Soc.* 2009;131(43):15834-15842.
347. Chen Y-Z, Wang C, Wu Z-Y, et al. From bimetallic metal-organic framework to porous carbon: high surface area and multicomponent active dopants for excellent electrocatalysis. *Adv Mater.* 2015;27(34):5010-5016.
348. Lü Y, Zhou Q, Chen L, et al. Templated synthesis of diluted magnetic semiconductors using transition metal ion-doped metal-organic frameworks: the case of co-doped ZnO. *CrstEngComm.* 2016;18(22):4121-4126.
349. Kaur G, Rai RK, Tyagi D, et al. Room-temperature synthesis of bimetallic co-Zn based zeolitic imidazolate frameworks in water for enhanced CO₂ and H₂ uptakes. *J Mater Chem A.* 2016;4(39):14932-14938.
350. Friščić T, Fábián L. Mechanochemical conversion of a metal oxide into coordination polymers and porous frameworks using liquid-assisted grinding (LAG). *CrstEngComm.* 2009;11(5):743-745.
351. Friščić T, Reid DG, Halasz I, Stein RS, Dinnebier RE, Duer MJ. Ion- and liquid-assisted grinding: improved mechanochemical synthesis of metal-organic frameworks reveals salt inclusion and anion templating. *Angew Chem Int Ed.* 2010;49(4):712-715.
352. Imawaka K, Sugita M, Takewaki T, Tanaka S. Mechanochemical synthesis of bimetallic CoZn-ZIFs with sodalite structure. *Polyhedron.* 2019;158:290-295.
353. Tanaka S, Nagaoka T, Yasuyoshi A, Hasegawa Y, Denayer JFM. Hierarchical pore development of ZIF-8 MOF by simple salt-assisted mechanosynthesis. *Cryst Growth des.* 2018;18(1):274-279.
354. Bang JH, Suslick KS. Applications of ultrasound to the synthesis of nanostructured materials. *Adv Mater.* 2010;22(10):1039-1059.
355. Kim J, Yang S-T, Choi SB, Sim J, Kim J, Ahn W-S. Control of catenation in CuTATB-n metal-organic frameworks by sonochemical synthesis and its effect on CO₂ adsorption. *J Mater Chem.* 2011;21(9):3070-3076.
356. Masoomi MY, Morsali A. Sonochemical synthesis of nanoplates of two cd(II) based metal-organic frameworks and their applications as precursors for preparation of nano-materials. *Ultrason Sonochem.* 2016;28:240-249.
357. Armstrong MR, Senthilnathan S, Balzer CJ, Shan B, Chen L, Mu B. Particle size studies to reveal crystallization mechanisms of the metal organic framework HKUST-1 during sonochemical synthesis. *Ultrason Sonochem.* 2017;34:365-370.
358. Masoomi MY, Bagheri M, Morsali A. High adsorption capacity of two Zn-based metal-organic frameworks by ultrasound assisted synthesis. *Ultrason Sonochem.* 2016;33:54-60.
359. Gao W-Y, Chrzanowski M, Ma S. Metal-metalloporphyrin frameworks: a resurging class of functional materials. *Chem Soc Rev.* 2014;43(16):5841-5866.
360. Day NU, Wamser CC, Walter MG. Porphyrin polymers and organic frameworks. *Polym Int.* 2015;64(7):833-857.
361. Huh S, Kim S-J, Kim Y. Porphyrinic metal-organic frameworks from custom-designed porphyrins. *CrstEngComm.* 2016;18(3):345-368.
362. Yuan S, Feng L, Wang K, et al. Stable metal-organic frameworks: design, synthesis, and applications. *Adv Mater.* 2018;30(37):1704303.
363. Feng L, Wang K-Y, Joseph E, Zhou H-C. Catalytic porphyrin framework compounds. *Trends Chem.* 2020;2(6):555-568.
364. Su C-H, Kung C-W, Chang T-H, Lu H-C, Ho K-C, Liao Y-C. Inkjet-printed porphyrinic metal-organic framework thin films for electrocatalysis. *J Mater Chem A.* 2016;4(28):11094-11102.
365. Hod I, Sampson MD, Deria P, Kubiak CP, Farha O, Hupp JT. Fe-porphyrin-based metal-organic framework films as high-surface concentration, heterogeneous catalysts for electrochemical reduction of CO₂. *ACS Catal.* 2015;5(11):6302-6309.
366. Sasan K, Lin Q, Mao CY, Feng P. Incorporation of iron hydrogenase active sites into a highly stable metal-organic framework for photocatalytic hydrogen generation. *Chem Commun.* 2014;50(72):10390-10393.
367. Liu Y, Howarth AJ, Hupp JT, Farha OK. Selective photooxidation of a mustard-gas simulant catalyzed by a porphyrinic metal-organic framework. *Angew Chem Int Ed.* 2015;54(31):9001-9005.
368. Xu H-Q, Hu J, Wang D, et al. Visible-light photoreduction of CO₂ in a metal-organic framework: boosting electron-hole separation via electron trap states. *J Am Chem Soc.* 2015;137(42):13440-13443.
369. Meng A-N, Chaihu L-X, Chen H-H, Gu Z-Y. Ultrahigh adsorption and singlet-oxygen mediated degradation for efficient synergetic removal of bisphenol a by a stable zirconium-porphyrin metal-organic framework. *Sci Rep.* 2017;7:6297.
370. Howarth AJ, Liu Y, Li P, et al. Chemical, thermal and mechanical stabilities of metal-organic frameworks. *Nat Rev Mater.* 2016;1(3):15018.
371. Chen Y, Hoang T, Ma S. Biomimetic catalysis of a porous iron-based metal-metalloporphyrin framework. *Inorg Chem.* 2012;51(21):12600-12602.
372. Zhang H, Wei J, Dong J, et al. Efficient visible-light-driven carbon dioxide reduction by a single-atom implanted metal-organic framework. *Angew Chem Int Ed.* 2016;55(46):14310-14314.
373. Xu H-Q, Wang K, Ding M, Feng D, Jiang H-L, Zhou H-C. Seed-mediated synthesis of metal-organic frameworks. *J Am Chem Soc.* 2016;138(16):5316-5320.
374. Kelty ML, Morris W, Gallagher AT, et al. High-throughput synthesis and characterization of nanocrystalline porphyrinic

- zirconium metal–organic frameworks. *Chem Commun.* 2016; 52(50):7854–7857.
375. Shaikh SM, Usov PM, Zhu J, Cai M, Alatis J, Morris AJ. Synthesis and defect characterization of phase-pure Zr-MOFs based on meso-tetracarboxyphenylporphyrin. *Inorg Chem.* 2019;58(8):5145–5153.
376. Gong X, Noh H, Gianneschi NC, Farha OK. Interrogating kinetic versus thermodynamic topologies of metal–organic frameworks via combined transmission electron microscopy and X-ray diffraction analysis. *J Am Chem Soc.* 2019;141(15):6146–6151.
377. Yu K, Lee Y-R, Seo JY, Baek K-Y, Chung Y-M, Ahn W-S. Sonochemical synthesis of Zr-based porphyrinic MOF-525 and MOF-545: enhancement in catalytic and adsorption properties. *Microporous Mesoporous Mat.* 2021;316:110985.
378. Wang K, Feng D, Liu T-F, et al. A series of highly stable mesoporous metalloporphyrin Fe-MOFs. *J Am Chem Soc.* 2014;136(40):13983–13986.
379. Israr F, Chun D, Kim Y, Kim DK. High yield synthesis of Ni-BTC metal–organic framework with ultrasonic irradiation: role of polar aprotic DMF solvent. *Ultrason Sonochem.* 2016; 31:93–101.
380. Choi H-Y, Kim J, Kim S-N, Ahn W-S. High yield 1-L scale synthesis of ZIF-8 via a sonochemical route. *Microporous Mesoporous Mater.* 2013;169:180–184.
381. Sargazi G, Afzali D, Mostafavi A. A novel synthesis of a new thorium (IV) metal organic framework nanostructure with well controllable procedure through ultrasound assisted reverse micelle method. *Ultrason Sonochem.* 2018;41:234–251.
382. Paseta L, Potier G, Sorribas S, Coronas J. Solventless synthesis of MOFs at high pressure. *ACS Sustainable Chem Eng.* 2016;4(7):3780–3785.
383. Garzón-Tovar L, Cano-Sarabia M, Carné-Sánchez A, Carbonell C, Imaz I, MasPOCH D. A spray-drying continuous-flow method for simultaneous synthesis and shaping of microspherical high nuclearity MOF beads. *React Chem Eng.* 2016;1(5):533–539.
384. Yoshida J, Takahashi Y, Nagaki A. Flash chemistry: flow chemistry that cannot be done in batch. *Chem Commun.* 2013;49(85):9896–9904.
385. Liu Z, Zhu J, Peng C, Wakihara T, Okubo T. Continuous flow synthesis of ordered porous materials: from zeolites to metal–organic frameworks and mesoporous silica. *React Chem Eng.* 2019;4(10):1699–1720.
386. Myers RM, Fitzpatrick DE, Turner RM, Ley SV. Flow chemistry meets advanced functional materials. *Chem A Eur J.* 2014; 20(39):12348–12366.
387. Rubio-Martinez M, Avci-Camur C, Thornton AW, Imaz I, MasPOCH D, Hill MR. New synthetic routes towards MOF production at scale. *Chem Soc Rev.* 2017;46(11):3453–3480.
388. Batten MP, Rubio-Martinez M, Hadley T, et al. Continuous flow production of metal–organic frameworks. *Curr Opin Chem Eng.* 2015;8:55–59.
389. Faustini M, Kim J, Jeong G-Y, et al. Microfluidic approach toward continuous and ultrafast synthesis of metal–organic framework crystals and hetero structures in confined microdroplets. *J Am Chem Soc.* 2013;135(39):14619–14626.
390. Yamamoto D, Maki T, Watanabe S, Tanaka H, Miyahara MT, Mae K. Synthesis and adsorption properties of ZIF-8 nanoparticles using a micromixer. *Chem Eng J.* 2013;227:145–150.
391. Watanabe S, Ohsaki S, Hanafusa T, et al. Synthesis of zeolitic imidazolate framework-8 particles of controlled sizes, shapes, and gate adsorption characteristics using a central collision-type microreactor. *Chem Eng J.* 2017;313:724–733.
392. Munn AS, Dunne PW, Tang SVY, Lester EH. Large-scale continuous hydrothermal production and activation of ZIF-8. *Chem Commun.* 2015;51(64):12811–12814.
393. Parulkar A, Brunelli NA. High-yield synthesis of ZIF-8 nanoparticles using stoichiometric reactants in a jet-mixing reactor. *Ind Eng Chem Res.* 2017;56(37):10384–10392.
394. Carraro F, Williams JD, Linares-Moreau M, et al. Continuous-flow synthesis of ZIF-8 biocomposites with tunable particle size. *Angew Chem Int Ed.* 2020;59(21):8123–8127.
395. Bustamante EL, Fernández JL, Zamaro JM. Influence of the solvent in the synthesis of zeolitic imidazolate framework-8 (ZIF-8) nanocrystals at room temperature. *J Colloid Interface Sci.* 2014;424:37–43.
396. Wang Z, Wang J, Li M, Sun K, Liu C. Three-dimensional printed acrylonitrile butadiene styrene framework coated with Cu-BTC metal–organic frameworks for the removal of methylene blue. *Sci Rep.* 2014;4:5939.
397. Crawford D, Casaban J, Haydon R, Giri N, McNally T, James SL. Synthesis by extrusion: continuous, large-scale preparation of MOFs using little or no solvent. *Chem Sci.* 2015;6(3):1645–1649.
398. Silva P, Vilela SMF, Tomé JPC, Paz FAA. Multifunctional metal–organic frameworks: from academia to industrial applications. *Chem Soc Rev.* 2015;44(19):6774–67803.
399. Ren J, Dyosiba X, Musyoka NM, Langmi HW, Mathe M, Liao S. Review on the current practices and efforts towards pilot-scale production of metal–organic frameworks (MOFs). *Coord Chem Rev.* 2017;352:187–219.
400. He Q, Zhan F, Wang H, Xu W, Wang H, Chen L. Recent progress of industrial preparation of metal–organic frameworks: synthesis strategies and outlook. *Mater Today Sustain.* 2022; 17:100104.
401. Seoane B, Castellanos S, Dikhtiarenko A, Kapteijn F, Gascon J. Multi-scale crystal engineering of metal organic frameworks. *Coord Chem Rev.* 2016;307:147–187.
402. Bon V, Kavooosi N, Senkovska I, et al. Tuning the flexibility in MOFs by SBU functionalization. *Dalton Trans.* 2016;45(10): 4407–4415.
403. Halder A, Ghoshal D. Structure and properties of dynamic metal–organic frameworks: a brief accounts of crystalline-to-crystalline and crystalline-to-amorphous transformations. *CrystEngComm.* 2018;20(10):1322–1345.
404. Sun L, Hendon CH, Minier MA, Walsh A, Dinca M. Million-fold electrical conductivity enhancement in Fe₂(DEBDC) versus Mn₂(DEBDC) (E = S, O). *J Am Chem Soc.* 2015;137(19): 6164–6167.
405. Kung C-W, Platero-Prats AE, Drout RJ, et al. Inorganic “conductive glass” approach to rendering mesoporous metal–organic frameworks electronically conductive and chemically responsive. *ACS Appl Mater Interfaces.* 2018;10(36):30532–30540.
406. Wang TC, Hod I, Audu CO, et al. Rendering high surface area, mesoporous metal–organic frameworks electronically conductive. *ACS Appl Mater Interfaces.* 2017;9(14):12584–12591.
407. Phang WJ, Jo H, Lee WR, et al. Superprotonic conductivity of a UiO-66 framework functionalized with sulfonic acid groups

- by facile postsynthetic oxidation. *Angew Chemie Int Ed.* 2015; 54(17):5142-5146.
408. Kim SR, Joarder B, Hurd JA, et al. Achieving superprotonic conduction in metal-organic frameworks through iterative design advances. *J Am Chem Soc.* 2018;140(3):1077-1082.
 409. Sun L, Hendon CH, Park SS, et al. Is iron unique in promoting electrical conductivity in MOFs? *Chem Sci.* 2017;8(6): 4450-4457.
 410. Shen L, Wu HB, Liu F, et al. Creating lithium-ion electrolytes with biomimetic ionic channels in metal-organic frameworks. *Adv Mater.* 2018;30(23):1707476.
 411. Chen Z, Hanna SL, Redfern LR, Alezi D, Islamoglu T, Farha OK. Reticular chemistry in the rational synthesis of functional zirconium cluster-based MOFs. *Coord Chem Rev.* 2019;386:32-49.
 412. Isaeva VI, Kustov LM. Microwave activation as an alternative production of metalorganic frameworks. *Russ Chem Bull.* 2013;65(9):2103-2114.
 413. Shekhah O, Wang H, Zacher D, Fischer RA, Wöll C. Growth mechanism of metal-organic frameworks: insights into the nucleation by employing a step-by-step route. *Angew Chem Int Ed.* 2009;48(27):5038-5041.
 414. Meilikhov M, Yusenko K, Schollmeyer E, Mayer C, Buschmann H-J, Fischer RA. Stepwise deposition of metal organic frameworks on flexible synthetic polymer surfaces. *Dalton Trans.* 2011;40(18):4838-4841.
 415. Shekhah O, Liu J, Fischer RA, Wöll C. MOF thin films: existing and future applications. *Chem Soc Rev.* 2011;40(2):1081-1106.
 416. Goodenough JB, Kim Y. Challenges for rechargeable Li batteries. *Chem Mater.* 2010;22(3):587-603.
 417. Zheng D, Zhang X, Wang J, Qu D, Yang X, Qu D. Reduction mechanism of sulfur in lithium-sulfur battery: from elemental sulfur to polysulfide. *J Power Sources.* 2016;301:312-316.
 418. Wu Y, Yan D, Zhang Z, Matsushita MM, Awaga K. Electron highways into nanochannels of covalent organic frameworks for high electrical conductivity and energy storage. *ACS Appl Mater Interfaces.* 2019;11(8):7661-7665.
 419. Férey G, Millange F, Morcrette M, et al. Mixed-valence Li/Fe-based metal-organic frameworks with both reversible redox and sorption properties. *Angew Chem Int Ed.* 2007;46(18):3259-3263.
 420. Combarieu G, Morcrette M, Millange F, et al. Influence of the benzoquinone sorption on the structure and electrochemical performance of the MIL-53(Fe) hybrid porous material in a lithium-ion battery. *Chem Mater.* 2009;21(8):1602-1611.
 421. Combarieu G, Hamelet S, Millange F, et al. In situ Fe XAFS of reversible lithium insertion in a flexible metal organic framework material. *Electrochem Commun.* 2009;11(10):1881-1884.
 422. Combelles C, Yahia MB, Pedesseau L, Doublet M-L. Fe^{II}/Fe^{III} mixed-valence state induced by Li-insertion into the metal-organic-framework Mil53(Fe): a DFT+U study. *J Power Sources.* 2011;196:3426-3432.
 423. Fateeva A, Horcajada P, Devic T, et al. Synthesis, structure, characterization, and redox properties of the porous MIL-68 (Fe) solid. *Eur. J Inorg Chem.* 2010;2010(24):3789-3794.
 424. Yamada T, Shiraishi K, Kitagawa H, Kimizuka N. Applicability of MIL-101(Fe) as a cathode of lithium ion batteries. *Chem Commun.* 2017;53(58):8215-8218.
 425. Zhang Z, Yoshikawa H, Awaga K. Monitoring the solid-state electrochemistry of cu(2,7-AQDC) (AQDC = anthraquinone Dicarboxylate) in a lithium battery: coexistence of metal and ligand redox activities in a metal-organic framework. *J Am Chem Soc.* 2014;136(46):16112-16115.
 426. Peng Z, Yi X, Liu Z, Shang J, Wang D. Triphenylamine-based metal-organic frameworks as cathode materials in lithium-ion batteries with coexistence of redox active sites, high working voltage, and high rate stability. *ACS Appl Mater Interfaces.* 2016;8(23):14578-14585.
 427. Nguyen TLA, Demir-Cakan R, Devic T, et al. 3-D coordination polymers based on the tetrathiafulvalenetetracarboxylate (TTF-TC) derivative: synthesis, characterization, and oxidation issues. *Inorg Chem.* 2010;49(15):7135-7143.
 428. Asakura D, Okubo M, Mizuno Y, et al. Fabrication of a cyanide-bridged coordination polymer electrode for enhanced electrochemical ion storage ability. *J Phys Chem C.* 2012;116(15):8364-8369.
 429. Okubo M, Asakura D, Mizuno Y, et al. Switching redox-active sites by valence tautomerism in Prussian blue analogues A_xM_n[Fe(CN)₆]_n·nH₂O (a: K, Rb): robust frameworks for reversible Li storage. *J Phys Chem Lett.* 2010;1(14):2063-2071.
 430. Nanba Y, Asakura D, Okubo M, et al. Configuration-interaction full-multiplet calculation to analyze the electronic structure of a cyano-bridged coordination polymer electrode. *J Phys Chem C.* 2012;116(47):24896-24901.
 431. Hu L, Yan N, Chen Q, et al. Fabrication based on the kirkendall effect of Co₃O₄ porous nanocages with extraordinarily high capacity for lithium storage. *Chem A Eur J.* 2012;18(29):8971-8977.
 432. Ohkoshi S, Tokoro H, Hashimoto K. Temperature- and photo-induced phase transition in rubidium manganese hexacyanoferrate. *Coord Chem Rev.* 2005;249(17-18):1830-1840.
 433. Asakura D, Li CH, Mizuno Y, Okubo M, Zhou H, Talham DR. Bimetallic cyanide-bridged coordination polymers as lithium ion cathode materials: Core@shell nanoparticles with enhanced cyclability. *J Am Chem Soc.* 2013;135(7):2793-2799.
 434. Wang X-J, Krumeich F, Nesper R. Nanocomposite of manganese ferrocyanide and graphene: a promising cathode material for rechargeable lithium ion batteries. *Electrochem Commun.* 2013;34:246-249.
 435. Nitta N, Wu F, Lee JT, Yushin G. Li-ion battery materials: present and future. *Mater Today.* 2015;18(5):252-264.
 436. Nunes GG, Seisenbaeva GA, Kessler VG. Crystal engineering of nanomorphology for complex oxide materials via thermal decomposition of metal-organic frameworks. Case study of sodium tantalate. *Cryst Growth des.* 2011;11(4):1238-1243.
 437. Dash R, Pannala S. Theoretical limits of energy density in silicon-carbon composite anode based lithium ion batteries. *Sci Rep.* 2016;6:27449.
 438. Chan CK, Peng H, Liu G, et al. High-performance lithium battery anodes using silicon nanowires. *Nat Nanotechnol.* 2008;3(1):31-35.
 439. Machill S, Shodai T, Sakurai Y, Yamaki J. Electrochemical and structural investigations of the reaction of lithium with tin-based composite oxide glasses. *J Solid State Electrochem.* 1999;3(2):97-103.

440. Li M, Li W, Hu Y, et al. New insights into the high-performance black phosphorus anode for lithium-ion batteries. *Adv Mater*. 2021;33(35):2101259.
441. Hu X, Li C, Lou X, et al. Controlled synthesis of $\text{Co}_x\text{Mn}_{3-x}\text{O}_4$ nanoparticles with a tunable composition and size for high performance lithium-ion batteries. *RSC Adv*. 2016;6(59):54270-54276.
442. Li C, Chen T, Xu W, et al. Mesoporous nanostructured Co_3O_4 derived from MOF template: a high-performance anode material for lithium-ion batteries. *J Mater Chem A*. 2015;3(10):5585-5591.
443. Yang SJ, Nam S, Kim T, et al. Preparation and exceptional lithium anodic performance of porous carbon-coated ZnO quantum dots derived from a metal-organic framework. *J Am Chem Soc*. 2013;135(20):7394-7397.
444. Zou G, Jia X, Huang Z, et al. Cube-shaped porous carbon Derived from MOF-5 as advanced material for sodium-ion batteries. *Electrochim Acta*. 2015;196:413-421.
445. Jia D, Tong R, Ning L, et al. BN nanosheets in-situ mosaic on MOF-5 derived porous carbon skeleton for high-performance lithium-ion batteries. *J Alloy Compd*. 2021;857:157571.
446. Zhang G, Hou S, Zhang H, et al. High-performance and ultra-stable lithium-ion batteries based on MOF-derived ZnO@ZnO quantum dots/C core-shell nanorod arrays on a carbon cloth anode. *Adv Mater*. 2015;27(14):2400-2405.
447. Xu W, Cui X, Xie Z, Dietrich G, Wang Y. Integrated $\text{Co}_3\text{O}_4/\text{TiO}_2$ composite hollow polyhedrons prepared via cation-exchange metal-organic framework for superior lithium-ion batteries. *J Alloy Compd*. 2016;20:1021-1028.
448. Wang L, Wang Z, Xie L, Zhu L, Cao X. ZIF-67-derived N-doped co/C nanocubes as high-performance anode materials for lithium-ion batteries. *ACS Appl Mater Interfaces*. 2019;11(18):16619-16628.
449. Xiu Z, Kim D, Alfaruqi MH, et al. Porous TiN nanoparticles embedded in a N-doped carbon composite derived from metal-organic frameworks as a superior anode in lithium-ion batteries. *J Mater Chem A*. 2016;4(13):4706-4710.
450. Zhu JP, Chen X, Wang X, Zuo XX, Li J. Disc-shaped $\text{Li}_{4-x}\text{K}_x\text{Ti}_5\text{O}_{12}$ derived from MIL-125(Ti) as an anode material with high performance for lithium-ion batteries. *J Electron Mater*. 2021;50(7):4066-4074.
451. Gou L, Hao L-M, Shi Y-X, et al. One-pot synthesis of a metal-organic framework as an anode for Li-ion batteries with improved capacity and cycling stability. *J Solid State Chem*. 2014;210(1):121-124.
452. Hu H, Lou X, Li C, et al. A thermally activated manganese 1,4-benzenedicarboxylate metal organic framework with high anodic capability for Li-ion batteries. *New J Chem*. 2016;40(11):9746-9752.
453. Maiti S, Pramanik A, Manju U, Mahanty S. $\text{Cu}_3(1,3,5\text{-benzenetricarboxylate})_2$ metal-organic framework: a promising anode material for lithium-ion battery. *Micropor Mesopor Mater*. 2016;226:353-359.
454. Hu X, Lou X, Li C, et al. Facile synthesis of the Basolite F300-like nanoscale Fe-BTC framework and its lithium storage properties. *RSC Adv*. 2016;6(115):114483-114490.
455. Li C, Lou X, Shen M, et al. High anodic performance of co 1,3,5-benzenetricarboxylate coordination polymers for Li-ion battery. *ACS Appl Mater Interfaces*. 2016;8(24):15352-15360.
456. Dong C, Xu L. Cobalt- and cadmium-based metal-organic frameworks as high-performance anodes for sodium ion batteries and lithium ion batteries. *ACS Appl Mater Interfaces*. 2017;9(8):7160-7168.
457. Lou X, Hu X, Li C, et al. Room-temperature synthesis of a cobalt 2,3,5,6-tetrafluoroterephthalic coordination polymer with enhanced capacity and cycling stability for lithium batteries. *New J Chem*. 2017;41(4):1813-1819.
458. An Q, Lv F, Liu Q, et al. Amorphous vanadium oxide matrixes supporting hierarchical porous Fe_3O_4 /graphene nanowires as a high-rate lithium storage anode. *Nano Lett*. 2014;14(11):6250-6256.
459. Bai J, Li X, Liu G, Qian Y, Xiong S. Unusual formation of ZnCo_2O_4 3D hierarchical twin microspheres as a high-rate and ultralong-life lithium-ion battery anode material. *Adv Funct Mater*. 2014;24(20):3012-3020.
460. Qin J, He C, Zhao N, et al. Graphene networks anchored with Sn@graphene as lithium ion battery anode. *ACS Nano*. 2014;8(2):1728-1738.
461. Zou F, Chen Y-M, Liu K, et al. Metal organic frameworks derived hierarchical hollow NiO/Ni/graphene composites for lithium and sodium storage. *ACS Nano*. 2016;10(1):377-386.
462. Xu X, Cao R, Jeong S, Cho J. Spindle-like mesoporous $\alpha\text{-Fe}_2\text{O}_3$ anode material prepared from MOF template for high-rate lithium batteries. *Nano Lett*. 2012;12(9):4988-4991.
463. Guo W, Sung W, Wang Y. Multilayer CuO@NiO hollow spheres: microwave-assisted metal-organic-framework derivation and highly reversible structure-matched stepwise lithium storage. *ACS Nano*. 2015;9(11):11462-11471.
464. Li C, Hu X, Lou X, et al. The organic-moiety-dominated Li+ intercalation/deintercalation mechanism of a cobalt-based metal-organic framework. *J Mater Chem A*. 2016;4(41):16245-16251.
465. Gong T, Lou X, Gao E-Q, Hu B. Pillared-layer metal-organic frameworks for improved lithium-ion storage performance. *ACS Appl Mater Interfaces*. 2017;9(26):21839-21847.
466. Xiong P, Zeng G, Zeng L, Wei M. Prussian blue analogues $\text{Mn}[\text{Fe}(\text{CN})_6]_{0.6667}\cdot n\text{H}_2\text{O}$ cubes as an anode material for lithium-ion batteries. *Dalton Trans*. 2015;44(38):16746-16751.
467. Li Y, Xu Y, Yang W, Shen W, Xue H, Pang H. MOF-derived metal oxide composites for advanced electrochemical energy storage. *Small*. 2018;14(25):1704435.
468. Hu C, Chen L, Hu Y, et al. Optimizing $\text{SnO}_2\text{-x}/\text{Fe}_2\text{O}_3$ heteronano-crystals toward rapid and highly reversible lithium storage. *Small*. 2021;17(49):2103532.
469. Wang Y, Gao Y, Shao J, et al. Ultrasmall Fe_3O_4 nanodots within N-doped carbon frameworks from MOFs uniformly anchored on carbon nanowebs for boosting Li-ion storage. *J Mater Chem A*. 2018;6(8):3659-3666.
470. Han X, Chen W-M, Han X, Tan Y-Z, Sun D. Nitrogen-rich MOF derived porous $\text{Co}_3\text{O}_4/\text{N-C}$ composites with superior performance in lithium-ion batteries. *J Mater Chem A*. 2016;4(34):13040-13045.
471. Li W-Y, Xu L-N, Chen J. Co_3O_4 nanomaterials in lithium-ion batteries and gas sensors. *Adv Funct Mater*. 2005;15(5):851-857.
472. Du N, Zhang H, Chen B, et al. Porous Co_3O_4 nanotubes derived from $\text{Co}_4(\text{CO})_{12}$ clusters on carbon nanotube

- templates: a highly efficient material for Li-battery applications. *Adv Mater.* 2007;19(24):4505-4509.
473. Choi SH, Kang YC. Fe₃O₄-decorated hollow graphene balls prepared by spray pyrolysis process for ultrafast and long cycle-life lithium ion batteries. *Carbon.* 2014;79:58-66.
 474. Mei J, Liao T, Ayoko GA, Bell J, Sun Z. Cobalt oxide-based nanoarchitectures for electrochemical energy applications. *Prog Mater Sci.* 2019;103:596-677.
 475. Geng H, Zhou Q, Pan Y, Gu H, Zheng J. Preparation of fluorine-doped, carbon-encapsulated hollow Fe₃O₄ spheres as an efficient anode material for Li-ion batteries. *Nanoscale.* 2014;6(7):3889-3894.
 476. Xia H, Wan Y, Yuan G, Fu Y, Wang X. Fe₃O₄/carbon core-shell nanotubes as promising anode materials for lithium-ion batteries. *J Power Sources.* 2013;241:486-493.
 477. Ding Y-L, Wen Y, Wu C, van Aken PA, Maier J, Yu Y. 3D V₆O₁₃ nanotextiles assembled from interconnected nanogrooves as cathode materials for high-energy lithium ion batteries. *Nano Lett.* 2015;15(2):1388-1394.
 478. He Y, Huang L, Cai J-S, Zheng X-M, Sun S-G. Structure and electrochemical performance of nanostructured Fe₃O₄/carbon nanotube composites as anodes for lithium ion batteries. *Electrochim Acta.* 2010;55(3):1140-1144.
 479. Yang S, Cui G, Pang S, et al. Fabrication of cobalt and cobalt oxide/graphene composites: towards high-performance anode materials for lithium ion batteries. *ChemSusChem.* 2010;3(2):236-239.
 480. Han F, Ma L, Sun Q, Lei C, Lu A. Rationally designed carbon-coated Fe₃O₄ coaxial nanotubes with hierarchical porosity as high-rate anodes for lithium ion batteries. *Nano Res.* 2014;7(11):1706-1717.
 481. Kim IT, Magasinski A, Jacob K, Yushin G, Tannenbaum R. Synthesis and electrochemical performance of reduced graphene oxide/maghemite composite anode for lithium ion batteries. *Carbon.* 2013;52:56-64.
 482. Eskandari M, Shahbazi N, Marcos AV, Malekfar R, Taboada P. Facile MOF-derived NiCo₂O₄/r-GO nanocomposites for electrochemical energy storage applications. *J Mol Liq.* 2022;348:118428.
 483. Zhang X, Li D, Zhu G, Lu T, Pan L. Porous CoFe₂O₄ nanocubes derived from metal-organic frameworks as high-performance anode for sodium ion batteries. *J Colloid Interface Sci.* 2017;499:145-150.
 484. Moon JH, Oh MJ, Nam MG, et al. Carbonization/oxidation-mediated synthesis of MOF-derived hollow nanocages of ZnO/N-doped carbon interwoven by carbon nanotubes for lithium-ion battery anodes. *Dalton Trans.* 2019;48(31):11941-11950.
 485. Tan J, Hussain S, Ge C, et al. ZIF-67 MOF-derived unique double-shelled Co₃O₄/NiCo₂O₄ nanocages for superior gas-sensing performances. *Sens Actuator B-Chem.* 2020;303:127251.
 486. Wang M, Huang Y, Zhu Y, et al. Synthesis of porous Zn_xCo_{3-x}O₄ hollow nanoboxes derived from metal-organic frameworks for lithium and sodium storage. *Electrochim Acta.* 2020;335:135694.
 487. Xu J, Li Y, Wang L, et al. High-energy lithium-ion hybrid supercapacitors composed of hierarchical urchin-like WO₃/C anodes and MOF-derived polyhedral hollow carbon cathodes. *Nanoscale.* 2016;8(37):16761-16768.
 488. Bian Z, Li A, He R, et al. Metal-organic framework-templated porous SnO/C polyhedrons for high-performance lithium-ion batteries. *Electrochim Acta.* 2018;289:389-396.
 489. Wang F, Feng T, Jin X, et al. Atomic co/Ni active sites assisted MOF-derived rich nitrogen-doped carbon hollow nanocages for enhanced lithium storage. *Chem Eng J.* 2021;420:127583.
 490. Yuan YF, Chen F, Ye LW, et al. Construction of Co₃O₄@TiO₂ heterogeneous mesoporous hollow nanocage-in-nanocage from metal-organic frameworks with enhanced lithium storage properties. *J Alloy Compd.* 2019;790:814-821.
 491. Park M-S, Wang G-X, Kang Y-M, Wexler D, Dou S-X, Liu H-K. Preparation and electrochemical properties of SnO₂ nanowires for application in lithium-ion batteries. *Angew Chem Int Ed.* 2007;46(5):750-753.
 492. Li W, Sun X, Yu Y. Si-, Ge-, Sn-based anode materials for lithium-ion batteries: from structure design to electrochemical performance. *Small Methods.* 2017;1(3):1600037.
 493. Liu K, Li C, Yan L, et al. MOFs and their derivatives as Sn-based anode materials for lithium/sodium ion batteries. *J Mater Chem A.* 2021;9(48):27234-27251.
 494. Li Q, Li W, Feng Q, et al. Thickness-dependent fracture of amorphous carbon coating on SnO₂ nanowire electrodes. *Carbon.* 2014;80:793-798.
 495. Cui C, Liu X, Wu N, Sun Y. Facile synthesis of core/shell-structured Sn/onion-like carbon nanocapsules as high-performance anode material for lithium-ion batteries. *Mater Lett.* 2015;143:35-37.
 496. Guo J, Li P, Chai L, Su Y, Diao J, Guo X. Silica template-assisted synthesis of SnO₂@porous carbon composites as anode materials with excellent rate capability and cycling stability for lithium-ion batteries. *RSC Adv.* 2017;7(48):30070-30079.
 497. Li A, Song H, Bian Z, Shi L, Chen X, Zhou J. ZnO nanosheet/squeezebox-like porous carbon composites synthesized by in situ pyrolysis of a mixed-ligand metal-organic framework. *J Mater Chem A.* 2017;5(12):5934-5942.
 498. Huang H, Shen K, Chen F, Li Y. Metal-organic frameworks as a good platform for the fabrication of single-atom catalysts. *ACS Catal.* 2020;10(12):6579-6586.
 499. Li Y, Fu Y, Chen S, Huang Z, Wang L, Song Y. Porous Fe₂O₃/Fe₃O₄@carbon octahedron arrayed on three-dimensional graphene foam for lithium-ion battery. *Compos PtB-Eng.* 2019;171:130-137.
 500. Ji D, Zhou H, Tong Y, et al. Facile fabrication of MOF-derived octahedral CuO wrapped 3D graphene network as binder-free anode for high performance lithium-ion batteries. *Chem Eng J.* 2017;313:1623-1632.
 501. Shao J, Zhou H, Zhu M, Feng J, Yuan A. Facile synthesis of metal-organic framework-derived Co₃O₄ with different morphologies coated graphene foam as integrated anodes for lithium-ion batteries. *J Alloy Compd.* 2018;768:1049-1057.
 502. Sui Z-Y, Zhang P-Y, Xu M-Y, Liu Y-W, Wei Z-X, Han B-H. Metal-organic framework-derived metal oxide embedded in nitrogen-doped graphene network for high-performance lithium-ion batteries. *ACS Appl Mater Interfaces.* 2017;9(49):43171-43178.
 503. Ma J, Kong Y, Liu S, et al. Flexible phosphorus-doped graphene/metal-organic framework-derived porous Fe₂O₃ anode for

- lithium-ion battery. *ACS Appl Energy Mater.* 2020;3(12):11900-11906.
504. Karthikeyan P, Elanchezhiyan SSD, Banu HAT, Farzana MH, Park CM. Hydrothermal synthesis of hydroxyapatite-reduced graphene oxide (1D-2D) hybrids with enhanced selective adsorption properties for methyl orange and hexavalent chromium from aqueous solutions. *Chemosphere.* 2021;276:130200.
505. Thirupathi A, van der Zalm J, Zeng L, Salverda M, Wood PC, Chen A. Effective microwave-hydrothermal reduction of graphene oxide for efficient energy storage. *J Energy Storage.* 2022;48:103962.
506. Sui Z-Y, Wang C, Yang Q-S, et al. A highly nitrogen-doped porous graphene – an anode material for lithium ion batteries. *J Mater Chem A.* 2015;3(35):18229-18237.
507. Cai Y, Fang G, Zhou J, et al. Metal-organic framework-derived porous shuttle-like vanadium oxides for sodium-ion battery application. *Nano Res.* 2018;11(1):449-463.
508. Jiang T, Bu F, Feng X, Shakir I, Hao G, Xu Y. Porous Fe₂O₃ nanoframeworks encapsulated within three-dimensional graphene as high-performance flexible anode for lithium-ion battery. *ACS Nano.* 2017;11(5):5140-5147.
509. Sun Y, Xing Z, Jiang S, et al. Rapid preparation of crosslinked N-doped graphene by burning method for high-performance electrochemical capacitors. *Electrochim Acta.* 2016;92:243-250.
510. Yin D, Huang G, Zhang F, et al. Coated/sandwiched rGO/CoSx composites derived from metal-organic frameworks/GO as advanced anode materials for lithium-ion batteries. *Chem A Eur J.* 2016;22(4):1467-1474.
511. Guo D, Guo H, Ke Y, et al. Facile one-step mechanochemical synthesis of [Cu(tu)]Cl·1/2H₂O nanobelts for high-performance supercapacitor. *RSC Adv.* 2015;5(48):38527-38532.
512. Xia G, Su J, Li M, Jiang P, Yang Y, Chen Q. A MOF-derived self-template strategy toward cobalt phosphide electrodes with ultralong cycle life and high capacity. *J Mater Chem A.* 2017;5(21):10321-10327.
513. Wang Y, Wu Y, Liu LZ, et al. Bimetallic MOF-derived CoSe₂ embedded within N-doped carbon with enhanced lithium storage properties. *Solid State Ion.* 2021;370:115747.
514. Jin R, Zhou J, Guan Y, Liu H, Chem G. Mesocrystal Co₉S₈ hollow sphere anodes for high performance lithium ion batteries. *J Mater Chem A.* 2014;2(33):13241-13244.
515. Wang X, Kim H-M, Xiao Y, Sun Y-K. Nanostructured metal phosphide-based materials for electrochemical energy storage. *J Mater Chem A.* 2016;4(39):14915-14931.
516. Huang Q, Wei T, Zhang M, et al. A highly stable polyoxometalate-based metal-organic framework with π - π stacking for enhancing lithium ion battery performance. *J Mater Chem A.* 2017;5(18):8477-8483.
517. Saravanan K, Nagarathinam M, Balaya P, Vittal JJ. Lithium storage in a metal organic framework with diamondoid topology – a case study on metal formates. *J Mater Chem.* 2010;20(38):8329-8335.
518. Maiti S, Pramanik A, Manju U, Mahanty S. Reversible lithium storage in manganese 1,3,5-benzenetricarboxylate metal-organic framework with high capacity and rate performance. *ACS Appl Mater Interfaces.* 2015;7(30):16357-16363.
519. Xiao P, Bu F, Zhao R, Aboud MFA, Shakir I, Xu Y. Sub-5 nm ultrasmall metal-organic framework nanocrystals for highly efficient electrochemical energy storage. *ACS Nano.* 2018;12(4):3947-3953.
520. Zhu M, Zhou H, Shao J, Feng J, Yuan A. Prussian blue nanocubes supported on graphene foam as superior binder-free anode of lithium-ion batteries. *J Alloys Compd.* 2018;749:811-817.
521. Fang G, Zhou J, Liang C, et al. MOFs nanosheets derived porous metal oxide-coated three-dimensional substrates for lithium-ion battery applications. *Nano Energy.* 2016;26:57-65.
522. Zhang L, Wu HB, Madhavi S, Hng HH, Lou XW. Formation of Fe₂O₃ microboxes with hierarchical shell structures from metal-organic frameworks and their lithium storage properties. *J Am Chem Soc.* 2012;134(42):17388-17391.
523. Zhang L, Wu BW, Lou XW. Metal-organic-frameworks-derived general formation of hollow structures with high complexity. *J Am Chem Soc.* 2013;135(29):10664-10672.
524. Chen Z, Wu R, Wang H, et al. Construction of hybrid hollow architectures by in-situ rooting ultrafine ZnS nanorods within porous carbon polyhedra for enhanced lithium storage properties. *Chem Eng J.* 2017;326:680-690.
525. Huang S, Wang Z, Lim YV, et al. Recent advances in Heterostructure engineering for lithium-sulfur batteries. *Adv Energy Mater.* 2021;11(10):2003689.
526. Demir-Cakan R, Morcrette M, Nouar F, et al. Cathode composites for Li-S batteries via the use of oxygenated porous architectures. *J Am Chem Soc.* 2011;133(40):16154-16160.
527. Jiang H, Liu X-C, Wu Y, et al. Metal-organic frameworks for high charge-discharge rates in lithium-sulfur batteries. *Angew Chem Int Ed.* 2018;57(15):3916-3921.
528. Wang Z, Li X, Cui Y. A metal-organic framework with open metal sites for enhanced confinement of sulfur and lithium-sulfur battery of long cycling life. *Cryst Growth des.* 2013;13(11):5116-5120.
529. Wang Z, Dou Z, Cui Y, Yang Y, Wang Z, Qian G. Sulfur encapsulated ZIF-8 as cathode material for lithium-sulfur battery with improved cyclability. *Microporous Mesoporous Mater.* 2014;185:92-96.
530. Zhou J, Li R, Fan X, et al. Rational design of a metal-organic framework host for sulfur storage in fast, long-cycle Li-S batteries. *Energ Environ Sci.* 2014;7(8):2715-2724.
531. Zhou J, Yu X, Fan X, et al. The impact of the particle size of a metal-organic framework for sulfur storage in Li-S batteries. *J Mater Chem A.* 2015;3(16):8272-8275.
532. Bruce PG, Scrosati B, Tarascon J-M. Nanomaterials for rechargeable lithium batteries. *Angew Chem Int Ed.* 2008;47(16):2930-2946.
533. Wang Z, Wang B, Yang Y, et al. Mixed-metal-organic framework with effective Lewis acidic sites for sulfur confinement in high-performance lithium-sulfur batteries. *ACS Appl Mater Interfaces.* 2015;7(37):20999-21004.
534. Su D, Cortie M, Fan H, Wang G. Prussian blue nanocubes with an open framework structure coated with PEDOT as high-capacity cathodes for lithium-sulfur batteries. *Adv Mater.* 2017;29(48):1700587.
535. Hong X-J, Tan T-X, Guo Y-K, et al. Confinement of polysulfides within bi-functional metal-organic frameworks for high performance lithium-sulfur batteries. *Nanoscale.* 2018;10(6):2774-2780.

536. Baumann AE, Aversa GE, Roy A, Falk ML, Bdeford NM, Thoi VS. Promoting sulfur adsorption using surface Cu sites in metal-organic frameworks for lithium sulfur batteries. *J Mater Chem A*. 2018;6(11):4811-4821.
537. Zheng J, Tian J, Wu D, et al. Lewis acid-base interactions between polysulfides and metal organic framework in lithium sulfur batteries. *Nano Lett*. 2014;14(5):2345-2352.
538. Park H, Seigel DJ. Tuning the adsorption of Polysulfides in lithium-sulfur batteries with metal-organic frameworks. *Chem Mater*. 2017;29(11):4932-4939.
539. Jin W-W, Li H-J, Zou J-Z, et al. Conducting polymer-coated MIL-101/S composite with scale-like shell structure for improving Li-S batteries. *RSC Adv*. 2018;8(9):4786-4793.
540. Mao Y, Li G, Guo Y, et al. Foldable interpenetrated metal-organic frameworks/carbon nanotubes thin film for lithium-sulfur batteries. *Nat Commun*. 2017;8:14628.
541. Mao Y, Li J, Cao W, et al. General incorporation of diverse components inside metal-organic framework thin films at room temperature. *Nat Commun*. 2014;5:5532.
542. Lim J, Pyun F, Char K. Recent approaches for the direct use of elemental sulfur in the synthesis and processing of advanced materials. *Angew Chem Int Ed*. 2015;54(11):3249-3258.
543. Hughes JT, Sava DF, Nenoff TM, Navrotsky A. Thermochemical evidence for strong iodine chemisorption by ZIF-8. *J Am Chem Soc*. 2013;135(44):16256-16259.
544. Li F, Zhang X, Liu X, Zhao M. Novel conductive metal-organic framework for a high-performance lithium-sulfur battery host: 2D Cu-benzenehexathial (BHT). *ACS Appl Mater Interfaces*. 2018;10(17):15012-15020.
545. Wang Z, Feng M, Sun H, et al. Constructing metal-free and cost-effective multifunctional separator for high-performance lithium-sulfur batteries. *Nano Energy*. 2019;59:390-398.
546. Yang Y, Wang W, Li L, Li B, Zhang J. Stable cycling of Li-S batteries by simultaneously suppressing Li-dendrite growth and polysulfide shuttling enabled by a bioinspired separator. *J Mater Chem A*. 2020;8(7):3692-3700.
547. She ZW, Sun Y, Zhang Q, Cui Y. Designing high-energy lithium-sulfur batteries. *Chem Soc Rev*. 2016;45(20):5605-5634.
548. Bai S, Liu X, Zhu L, Wu S, Zhou H. Metal-organic framework-based separator for lithium-sulfur batteries. *Nat Energy*. 2016;1:16094.
549. Kim SH, Yeon JS, Kim R, Choi KM, Park HS. A functional separator coated with sulfonated metal-organic framework/Nafion hybrids for Li-S batteries. *J Mater Chem A*. 2018;6(48):24971-24978.
550. He Y, Chang Z, Wu S, et al. Simultaneously inhibiting lithium dendrites growth and polysulfides shuttle by a flexible MOF-based membrane in Li-S batteries. *Adv Energy Mater*. 2018;8(34):1802130.
551. Li M, Wan Y, Huang J-K, et al. Metal-organic framework-based separators for enhancing Li-S battery stability: mechanism of mitigating polysulfide diffusion. *ACS Energy Lett*. 2017;2(10):2362-2367.
552. Pei F, Lin L, Fu A, et al. A two-dimensional porous carbon-modified separator for high-energy-density Li-S batteries. *Joule*. 2018;2(2):323-336.
553. Ghazi ZA, He X, Kahttak AM, et al. MoS₂/celgard separator as efficient polysulfide barrier for long-life lithium-sulfur batteries. *Adv Mater*. 2017;29(21):1606817.
554. Sun J, Sun Y, Pasta M, et al. Entrapment of polysulfides by a black-phosphorus-modified separator for lithium-sulfur batteries. *Adv Mater*. 2016;28(44):9797-9803.
555. Zang Y, Pei F, Huang J, Fu Z, Xu G, Fang X. Large-area preparation of crack-free crystalline microporous conductive membrane to upgrade high energy lithium-sulfur batteries. *Adv Energy Mater*. 2018;8(31):1802052.
556. Pang Q, Liang X, Kwok CY, Nazar LF. Advances in lithium-sulfur batteries based on multifunctional cathodes and electrolytes. *Nat Energy*. 2016;1:16132.
557. Chen H, Xiao Y, Chen C, et al. Conductive MOF-modified separator for mitigating the shuttle effect of lithium-sulfur battery through a filtration method. *ACS Appl Mater Interfaces*. 2019;11(12):11459-11465.
558. Huang N, Wang K, Drake H, et al. Tailor-made pyrazolide-based metal-organic frameworks for selective catalysis. *J Am Chem Soc*. 2018;140(20):6383-6390.
559. Chen S, Li K, Zhao F, et al. A metal-organic cage incorporating multiple light harvesting and catalytic centres for photochemical hydrogen production. *Nat Commun*. 2016;7:13169.
560. Ma L, Chen R, Zhu G, et al. Cerium oxide nanocrystal embedded bimodal microporous nitrogen-rich carbon nanospheres as effective sulfur host for lithium-sulfur batteries. *ACS Nano*. 2017;11(7):7274-7283.
561. Hong X-J, Song C-L, Yang Y, et al. Cerium based metal-organic frameworks as an efficient separator coating catalyzing the conversion of polysulfides for high performance lithium-sulfur batteries. *ACS Nano*. 2019;13(2):1923-1931.
562. Pu J, Shen Z, Zheng J, et al. Multifunctional Co₃S₄@sulfur nanotubes for enhanced lithium-sulfur battery performance. *Nano Energy*. 2017;37:7-14.
563. Liang L, Luo D, Zuo T, Zhou X-P, Li D. Control over the synthesis of homovalent and mixed-valence cubic cobalt-imidazolite cages. *Chem Commun*. 2019;55(35):5103-5106.
564. Park JG, Aubrey ML, Oktawiec J, et al. Charge delocalization and bulk electronic conductivity in the mixed-valence metal-organic framework Fe(1,2,3-triazolate)₂(BF₄)_x. *J Am Chem Soc*. 2018;140(27):8526-8534.
565. Tran VA, Do HH, Ha TDC, et al. Metal-organic framework for lithium and sodium-ion batteries: Progress and perspective. *Fuel*. 2022;319:123856.
566. Chen H, Liu Y, Cai T, et al. Boosting photocatalytic performance in mixed-valence MIL-53(Fe) by changing FeII/FeIII ratio. *ACS Appl Mater Interfaces*. 2019;11(32):28791-28800.
567. Montini T, Melchionna M, Monai M, Fornasiero P. Fundamentals and catalytic applications of CeO₂-based materials. *Chem Rev*. 2016;116(10):5987-6041.
568. Paier J, Penschke C, Sauer J. Oxygen defects and surface chemistry of ceria: quantum chemical studies compared to experiment. *Chem Rev*. 2013;113(6):3949-3985.
569. Smolders S, Struyf A, Reinsch H, et al. A precursor method for the synthesis of new Ce(IV) MOFs with reactive tetracarboxylate linkers. *Chem Commun*. 2018;54(8):876-879.
570. Kateshali AF, Dogaheh SG, Soleimannejad J, Blake AJ. Structural diversity and applications of Ce(III)-based coordination polymers. *Coord Chem Rev*. 2020;419:213392.
571. Jin H-G, Wang M, Wen J-X, et al. Oxygen vacancy-rich mixed-valence cerium MOF: An efficient separator coating to

- high-performance lithium-sulfur batteries. *ACS Appl Mater Interfaces*. 2021;13(3):3899-3910.
572. Qi C, Xu L, Wang J, et al. Titanium-containing metal-organic framework modified separator for advanced lithium-sulfur batteries. *ACS Sustainable Chem Eng*. 2020;8(34):12968-12975.
573. Park JH, Choi KM, Lee DK, et al. Encapsulation of redox polysulphides via chemical interaction with nitrogen atoms in the organic linkers of metal-organic framework nanocrystals. *Sci Rep*. 2016;6:25555.
574. Zhao Z, Wang S, Liang R, Li Z, Shi Z, Chen G. Graphene-wrapped chromium-MOF(MIL-101)/sulfur composite for performance improvement of high-rate rechargeable Li-S batteries. *J Mater Chem A*. 2014;2(33):13509-13512.
575. Zhang J, Hu H, Li Z, Lou XW. Double-shelled nanocages with cobalt hydroxide inner shell and layered double hydroxides outer shell as high-efficiency polysulfide mediator for lithium-sulfur batteries. *Angew Chem Int Ed*. 2016;55(12):3982-3986.
576. Li Z, Li C, Ge X, et al. Reduced graphene oxide wrapped MOFs-derived cobalt-doped porous carbon polyhedrons as sulfur immobilizers as cathodes for high performance lithium sulfur batteries. *Nano Energy*. 2016;23:15-26.
577. Baumann AE, Han X, Butala MM, Thoi VS. Lithium thiophosphate functionalized zirconium MOFs for Li-S batteries with enhanced rate capabilities. *J Am Chem Soc*. 2019;141(44):17891-17899.
578. Wang Q, Zhao H, Li B, et al. MOF-derived Co₉S₈ nano-flower cluster array modified separator towards superior lithium sulfur battery. *Chin Chem Lett*. 2021;32(3):1157-1160.
579. Zhang P, Zhao Y, Zhang X. Functional and stability orientation synthesis of materials and structures in aprotic Li-O₂ batteries. *Chem Soc Rev*. 2018;47(8):2921-3004.
580. Jung KN, Kim J, Yamauchi Y, et al. Rechargeable lithium-air batteries: a perspective on the development of oxygen electrodes. *J Mater Chem A*. 2016;4(37):14050-14068.
581. Yu H, Liu D, Feng X, Zhang Y. Mini review: recent advances on flexible rechargeable Li-air batteries. *Energy Fuel*. 2021;35(6):4751-4761.
582. Wu D, Guo Z, Yin X, et al. Metal-organic frameworks as cathode materials for Li-O₂ batteries. *Adv Mater*. 2014;26(20):3258-3262.
583. Kim SH, Lee YJ, Kim DH, Lee YJ. Bimetallic metal-organic frameworks as efficient cathode catalysts for Li-O₂ batteries. *ACS Appl Mater Interfaces*. 2018;10(1):660-667.
584. Yan W, Guo Z, Xu H, Lou Y, Chen J, Li Q. Downsizing metal-organic frameworks with distinct morphologies as cathode materials for high-capacity Li-O₂ batteries. *Mater Chem Front*. 2017;1(7):1324-1330.
585. Cheng X, Zhang A, Hou K, et al. Size- and morphology-controlled NH₂-MIL-53(Al) prepared in DMF-water mixed solvents. *Dalton Trans*. 2013;42(37):13698-13705.
586. Wan X, Jiang F, Chen L, et al. Structural diversity modulated by the ratios of a ternary solvent mixture: syntheses, structures, and luminescent properties of five zinc(II) metal-organic frameworks. *Cryst Growth des*. 2015;15(3):1481-1491.
587. Zhang B, Zhang J, Liu C, et al. Solvent determines the formation and properties of metal-organic frameworks. *RSC Adv*. 2015;5(47):37691-37696.
588. Bae Y-S, Lee CY, Kim KC, et al. High propene/propane selectivity in isostructural metal-organic frameworks with high densities of open metal sites. *Angew Chem Int Ed*. 2012;51(8):1857-1860.
589. Wang F, Guo H, Chai Y, Li Y, Liu C. The controlled regulation of morphology and size of HKUST-1 by "coordination modulation method". *Microporous Mesoporous Mater*. 2013;173:181-188.
590. Song MJ, Kim IT, Kim YB, Kim J, Shin MW. Metal-organic frameworks-derived porous carbon/Co₃O₄ composites for rechargeable lithium-oxygen batteries. *Electrochim Acta*. 2017;230:73-80.
591. Yin W, Shen Y, Zou F, Hu X, Chi B, Huang Y. Metal-organic framework derived ZnO/ZnFe₂O₄/C nanocages as stable cathode material for reversible lithium-oxygen batteries. *ACS Appl Mater Interfaces*. 2015;7(8):4947-4954.
592. Chen W, Zhang Z, Bao W, et al. Hierarchical mesoporous γ -Fe₂O₃/carbon nanocomposites derived from metal organic frameworks as a cathode electrocatalyst for rechargeable Li-O₂ batteries. *Electrochim Acta*. 2014;134:293-301.
593. Gan Y, Lai Y, Zhang Z, Chen W, Du K, Li J. Hierarchical Cr₂O₃@OPC composites with octahedral shape for rechargeable nonaqueous lithium-oxygen batteries. *J Alloys Compd*. 2016;665:365-372.
594. Zhang J, Wang L, Xu L, et al. Porous cobalt-manganese oxide nanocubes derived from metal organic frameworks as a cathode catalyst for rechargeable Li-O₂ batteries. *Nanoscale*. 2015;7(2):220-226.
595. Pham HTT, Yun J, Kim SY, et al. Nanoarchitectonics of the cathode to improve the reversibility of Li-O₂ batteries. *Beilstein J Nanotechnol*. 2022;13:689-698.
596. Sun Y, Liu N, Cui Y. Promises and challenges of nanomaterials for lithium-based rechargeable batteries. *Nat Energy*. 2016;1:16071.
597. Cheng X-B, Zhang Q. Dendrite-free lithium metal anodes: stable solid electrolyte interphases for high-efficiency batteries. *J Mater Chem A*. 2015;3(14):7207-7209.
598. Shen X, Liu H, Cheng X-B, Yan C, Huang J-Q. Beyond lithium ion batteries: higher energy density battery systems based on lithium metal anodes. *Energy Storage Mater*. 2018;12:161-175.
599. Cui J, Zhan T-G, Zhang KD, Chen D. The recent advances in constructing designed electrode in lithium metal batteries. *Chin Chem Lett*. 2017;28(12):2171-2179.
600. Zhang X-Q, Zhao C-Z, Huang J-Q, Zhang Q. Recent advances in energy chemical engineering of next-generation lithium batteries. *Engineering*. 2018;4(6):831-847.
601. Xu X, Wang S, Wang H, et al. Recent progresses in the suppression method based on the growth mechanism of lithium dendrite. *J Energy Chem*. 2018;27(2):513-527.
602. Sun Z, Jin S, Jin H, et al. Robust expandable carbon nanotube scaffold for ultrahigh-capacity lithium-metal anodes. *Adv Mater*. 2018;30(32):1800884.
603. Liu Y, Lin D, Liang Z, Zhao J, Yan K, Cui Y. Lithium-coated polymeric matrix as a minimum volume-change and dendrite-free lithium metal anode. *Nat Commun*. 2016;7:10992.
604. Liu K, Kong B, Liu W, et al. Stretchable lithium metal anode with improved mechanical and electrochemical cycling stability. *Joule*. 2018;2(9):1857-1865.
605. Zhang R, Chen X, Shen X, et al. Coralloid carbon fiber-based composite lithium anode for robust lithium metal batteries. *Joule*. 2018;2(4):764-777.

606. Zuo T-T, Wu X-W, Yang C-P, et al. Graphitized carbon fibers as multifunctional 3D current collectors for high areal capacity Li anodes. *Adv Mater.* 2017;29(29):1700389.
607. Yun J, Park B-K, Won E-S, et al. Bottom-up lithium growth triggered by interfacial activity gradient on porous framework for lithium-metal anode. *ACS Energy Lett.* 2020;5(10):3108-3114.
608. Han SA, Qutaish H, Park M-S, Moon J, Kim JH. Strategic approaches to the dendritic growth and interfacial reaction of lithium metal anode. *Chem Asian J.* 2021;16(24):4010-4017.
609. Lee J, Park M-S, Kim JH. Stabilizing Li-metal host anode with LiF-rich solid electrolyte interphase. *Nano Converg.* 2021;8(1):18.
610. Kim J, Lee J, Yun J, et al. Functionality of dual-phase lithium storage in a porous carbon host for lithium-metal anode. *Adv Funct Mater.* 2020;30(15):1910538.
611. Yuan Y, Wu F, Bai Y, et al. Regulating Li deposition by constructing LiF-rich host for dendrite-free lithium metal anode. *Energy Storage Mater.* 2019;16:411-418.
612. Lopez J, Pei A, Oh JY, Wang GJN, Cui Y, Bao Z. Effects of polymer coatings on electrodeposited lithium metal. *J Am Chem Soc.* 2018;140(37):11735-11744.
613. Li N-W, Yin Y-X, Yang C-P, Guo Y-G. An artificial solid electrolyte interphase layer for stable lithium metal anodes. *Adv Mater.* 2016;28(9):1853-1858.
614. Zhu B, Jin Y, Hu X, et al. Poly(dimethylsiloxane) thin film as a stable interfacial layer for high-performance lithium-metal battery anodes. *Adv Mater.* 2017;29(2):1603755.
615. Liang X, Pang Q, Kochetkoov IR, et al. A facile surface chemistry route to a stabilized lithium metal anode. *Nat Energy.* 2017;2(9):17119.
616. Yan C, Cheng X-B, Tian Y, et al. Dual-layered film protected lithium metal anode to enable dendrite-free lithium deposition. *Adv Mater.* 2018;30(25):1707629.
617. Liu Y, Qin X, Zhang S, et al. Oxygen and nitrogen co-doped porous carbon granules enabling dendrite-free lithium metal anode. *Energy Storage Mater.* 2019;18:320-327.
618. Cheng X-B, Hou T-Z, Zhang R, et al. Dendrite-free lithium deposition induced by uniformly distributed lithium ions for efficient lithium metal batteries. *Adv Mater.* 2016;28(15):2888-2895.
619. Manthiram A, Yu X, Wang S. Lithium battery chemistries enabled by solid-state electrolytes. *Nat Rev Mater.* 2017;2(4):16103.
620. Chen R, Qu W, Guo X, Li L, Wu F. The pursuit of solid-state electrolytes for lithium batteries: from comprehensive insight to emerging horizons. *Mater Horiz.* 2016;3(6):487-516.
621. Yang C, Fu K, Zhang Y, Hitz E, Hu L. Protected lithium-metal anodes in batteries: from liquid to solid. *Adv Mater.* 2017;29(36):1701169.
622. Zhang H, Eshetu GG, Judez X, Li C, Rodriguez-Martínez LM, Armand M. Electrolyte additives for lithium metal anodes and rechargeable lithium metal batteries: Progress and perspectives. *Angew Chem Int Ed.* 2018;57(46):15002-15027.
623. Zhang X-Q, Cheng X-B, Chen X, Yan C, Zhang Q. Fluoroethylene carbonate additives to render uniform Li deposits in lithium metal batteries. *Adv Funct Mater.* 2017;27(10):1605989.
624. Li C, Liu S, Shi C, et al. Two-dimensional molecular brush-functionalized porous bilayer composite separators toward ultrastable high-current density lithium metal anodes. *Nat Commun.* 2019;10:1363.
625. Bai S, Zhu K, Wu S, et al. A long-life lithium–Sulphur battery by integrating zinc–organic framework based separator. *J Mater Chem A.* 2016;4(43):16812-16817.
626. Lee H, Ren X, Niu C, et al. Suppressing lithium dendrite growth by metallic coating on a separator. *Adv Funct Mater.* 2017;27(45):1704391.
627. Chi M, Shi L, Wang Z, et al. Excellent rate capability and cycle life of Li metal batteries with ZrO₂/POSS multilayer-assembled PE separators. *Nano Energy.* 2016;28:1-11.
628. Fujie K, Ikeda R, Otsubo K, Tamada T, Kitagawa H. Lithium ion diffusion in a metal–organic framework mediated by an ionic liquid. *Chem Mater.* 2015;27(21):7355-7361.
629. Wang Z, Wang Z, Yang L, et al. Boosting interfacial Li⁺ transport with a MOF-based ionic conductor for solid-state batteries. *Nano Energy.* 2018;49:580-587.
630. Park SS, Tulchinsky Y, Dincă M. Single-ion Li⁺, Na⁺, and Mg²⁺ solid electrolytes supported by a mesoporous anionic copper-azolate metal–organic framework. *J Am Chem Soc.* 2017;139(38):13260-13263.
631. Chen N, Li Y, Dai Y, et al. A Li⁺ conductive metal organic framework electrolyte boosts the high-temperature performance of dendrite-free lithium batteries. *J Mater Chem A.* 2019;7(16):9530-9536.
632. Shikinaka K, Taki N, Kaneda K, Tominaga Y. Quasi-solid electrolyte: a thixotropic gel of imogolite and an ionic liquid. *Chem Commun.* 2017;53(3):613-616.
633. MacFarlane DR, Forsyth M, Howlett PC, et al. Ionic liquids and their solid-state analogues as materials for energy generation and storage. *Nat Rev Mater.* 2016;1(2):15005.
634. Huo H, Wu B, Zhang T, et al. Anion-immobilized polymer electrolyte achieved by cationic metal-organic framework filler for dendrite-free solid-state batteries. *Energy Storage Mater.* 2019;18:59-67.
635. Lin D, Liu W, Liu Y, et al. High ionic conductivity of composite solid polymer electrolyte via in situ synthesis of monodispersed SiO₂ nanospheres in poly(ethylene oxide). *Nano Lett.* 2016;16(1):459-465.
636. Vignarooban K, Dissanayake MAKL, Albinsson I, Mellander B-E. Effect of TiO₂ nano-filler and EC plasticizer on electrical and thermal properties of poly(ethylene oxide) (PEO) based solid polymer electrolytes. *Solid State Ion.* 2014;266:25-28.
637. Heyer WH. Polymer electrolytes for lithium-ion batteries. *Adv Mater.* 1998;10(6):439-448.
638. Wen S, Luo C, Wang Q, et al. Integrated design of ultrathin crosslinked network polymer electrolytes for flexible and stable all-solid-state lithium batteries. *Energy Storage Mater.* 2022;47:453-461.
639. Lou S, Zhang F, Fu C, et al. Interface issues and challenges in all-solid-state Batteries: lithium, sodium, and beyond. *Adv Mater.* 2021;33(6):2000721.
640. Albertus P, Anandan V, Ban C, et al. Challenges for and pathways toward Li-metal-based all-solid-state Batteries. *ACS Energy Lett.* 2021;6(4):1399-1404.
641. Yuan C, Li J, Han P, Lai Y, Zhang Z, Liu J. Enhanced electrochemical performance of poly(ethylene oxide) based composite polymer electrolyte by incorporation of nano-sized metal-organic framework. *J Power Sources.* 2013;240:653-658.

642. Tan L, Sun Y, Wei C, et al. Design of Robust, Lithiophilic, and flexible inorganic-polymer protective layer by separator engineering enables dendrite-free lithium metal batteries with $\text{LiNi}_{0.8}\text{Mn}_{0.1}\text{Co}_{0.1}\text{O}_2$ cathode. *Small*. 2021;17(13):2007717.
643. Liu W, Mi Y, Weng Z, Zhong Y, Wu Z, Wang H. Functional metal-organic framework boosting lithium metal anode performance via chemical interactions. *Chem Sci*. 2017;8(6):4285-4291.
644. Bai S, Sung Y, Yi J, He Y, Qiao Y, Zhou H. High-power Li-metal anode enabled by metal-organic framework modified electrolyte. *Joule*. 2018;2(10):2117-2132.
645. Pang J, Yuan S, Qin J, et al. Control the structure of Zr-tetracarboxylate frameworks through steric tuning. *J Am Chem Soc*. 2017;139(46):16939-16945.
646. Shen L, Wu HB, Liu F, et al. Anchoring anions with metal-organic framework-functionalized separators for advanced lithium batteries. *Nanoscale Horiz*. 2019;4(3):705-711.
647. Li Q, Zhu S, Lu Y. 3D porous Cu current collector/Li-metal composite anode for stable lithium-metal batteries. *Adv Funct Mater*. 2017;27(18):1606422.
648. Jiang Z, Liu T, Yan L, et al. Metal-organic framework nanosheets-guided uniform lithium deposition for metallic lithium batteries. *Energy Storage Mater*. 2018;11:267-273.
649. Yu Y, Gu L, Zhu C, Tsukimoto S, van Aken PA, Maier J. Reversible storage of lithium in silver-coated three-dimensional macroporous silicon. *Adv Mater*. 2010;22(20):2247-2250.
650. Zheng G, Lee SW, Liang Z, et al. Interconnected hollow carbon nanospheres for stable lithium metal anodes. *Nat Nanotechnol*. 2014;9(8):618-623.
651. Zhang C, Liu S, Li G, Zhang C, Liu X, Luo J. Incorporating ionic paths into 3D conducting scaffolds for high volumetric and areal capacity, high rate lithium-metal anodes. *Adv Mater*. 2018;30(33):1801328.
652. Deng W, Zhou X, Fang Q, Liu Z. Microscale lithium metal stored inside cellular graphene scaffold toward advanced metallic lithium anodes. *Adv Energy Mater*. 2018;8(12):1703152.
653. Fan L, Zhuang HL, Zhang W, Fu Y, Liao Z, Lu Y. Stable lithium electrodeposition at ultra-high current densities enabled by 3D PMF/Li composite anode. *Adv Energy Mater*. 2018;8(15):1703360.
654. Chi S-S, Liu Y, Song W-L, Fan L-Z, Zhang Q. Pre-storing lithium into stable 3D nickel foam host as dendrite-free lithium metal anode. *Adv Funct Mater*. 2017;27(24):1700348.
655. Liang Z, Lin D, Zhao J, et al. Composite lithium metal anode by melt infusion of lithium into a 3D conducting scaffold with lithiophilic coating. *Proc Natl Acad Sci U S A*. 2016;113(11):2862-2867.
656. Hafez AM, Jiao Y, Shi J, et al. Stable metal anode enabled by porous lithium foam with superior ion accessibility. *Adv Mater*. 2018;30(3):1802156.
657. Yan K, Lu Z, Lee H-W, et al. Selective deposition and stable encapsulation of lithium through heterogeneous seeded growth. *Nat Energy*. 2016;1:16010.
658. Eom GH, Han SA, Suh JH, Kim JH, Park M-S. Enriched cavities to ZIF-8-derived porous carbon for reversible metallic lithium storage. *ACS Appl Energy Mater*. 2021;4(12):14520-14525.
659. Chu F, Hu J, Tian J, Zhou X, Li Z, Li C. In situ plating of porous Mg network layer to reinforce anode dendrite suppression in Li-metal batteries. *ACS Appl Mater Interfaces*. 2018;10(15):12678-12689.
660. Wang Y, Wang Z, Lei D, et al. Spherical Li deposited inside 3D Cu skeleton as anode with ultrastable performance. *ACS Appl Mater Interfaces*. 2018;10(24):20244-20249.
661. Foroozan T, Soto FA, Yurkiv V, et al. Synergistic effect of graphene oxide for impeding the dendritic plating of Li. *Adv Funct Mater*. 2018;28(15):1705917.
662. Jin C, Sheng O, Luo J, et al. 3D lithium metal embedded within lithiophilic porous matrix for stable lithium metal batteries. *Nano Energy*. 2017;37:177-186.
663. Zhao H, Lei D, He Y-B, et al. Compact 3D copper with uniform porous structure derived by electrochemical dealloying as dendrite-free lithium metal anode current collector. *Adv Energy Mater*. 2018;8(19):1800266.
664. Yuan S, Bao JL, Li C, Xia Y, Truhlar DG, Wang Y. Dual lithiophilic structure for uniform Li deposition. *ACS Appl Mater Interfaces*. 2019;11(11):10616-10623.
665. Zhu M, Li B, Li S, Du Z, Gong Y, Yang S. Dendrite-free metallic lithium in lithiophilic carbonized metal-organic frameworks. *Adv Energy Mater*. 2018;8(18):1703505.
666. Li Y, Fan J, Zhang J, et al. A honeycomb-like $\text{Co}@N-C$ composite for ultrahigh sulfur loading Li-S batteries. *ACS Nano*. 2017;11(11):11417-11424.
667. Jagadeesh RV, Murugesan K, Alshammari AS, et al. MOF-derived cobalt nanoparticles catalyze a general synthesis of amines. *Science*. 2017;358(6361):326-332.
668. Lee KJ, Lee JH, Jeoung S, Moo HR. Transformation of metal-organic frameworks/coordination polymers into functional nanostructured materials: experimental approaches based on mechanistic insights. *Acc Chem Res*. 2017;50(11):2684-2692.
669. Wang L, Zhu X, Guan Y, et al. ZnO/carbon framework derived from metal-organic frameworks as a stable host for lithium metal anodes. *Energy Storage Mater*. 2018;11:191-196.
670. Lee J, Choi SH, Qutaish H, et al. Structurally stabilized lithium-metal anode via surface chemistry engineering. *Energy Storage Mater*. 2021;37:315-324.
671. Qutaish H, Han SA, Rehman Y, Konstantiov K, Park M-S, Kim JH. Porous carbon architectures with different dimensionalities for lithium metal storage. *Sci Technol Adv Mater*. 2022;23(1):169-188.
672. Choi SH, Hyeon Y, Shin HR, et al. Critical role of surface craters for improving the reversibility of Li metal storage in porous carbon frameworks. *Nano Energy*. 2021;88:106243.
673. Landesfeind J, Hattendorff J, Ehrl A, Wall WA, Gasteiger HA. Tortuosity determination of battery electrodes and separators by impedance spectroscopy. *J Electrochem Soc*. 2016;163(7):A1373-A1387.
674. Kim J, Young C, Lee J, et al. CNTs grown on nanoporous carbon from zeolitic imidazolate frameworks for supercapacitors. *Chem Commun*. 2016;52(88):13016-13019.
675. Qutaish H, Lee J, Hyeon Y, et al. Design of cobalt catalysed carbon nanotubes in bimetallic zeolitic imidazolate frameworks. *Appl Surf Sci*. 2021;547:149134.
676. Perdew JP, Burke K, Ernzerhof M. Generalized gradient approximation made simple. *Phys Rev Lett*. 1996;77(18):3865-3868.

677. Chen Y, Li S, Pei X, et al. A solvent-free hot-pressing method for preparing metal-organic-framework coatings. *Angew Chem Int Ed.* 2016;55(10):3419-3423.
678. Gao X, Du Y, Zhou J, et al. Large-scale production of MOF-derived coatings for functional interlayers in high-performance Li-S batteries. *ACS Appl Energy Mater.* 2018;1(12):6986-6991.
679. Liu Z-C, Xu J-J, Yuan S, et al. Artificial protection film on lithium metal anode toward long-cycle-life lithium-oxygen batteries. *Adv Mater.* 2015;27(35):5241-5247.
680. Zhang X, Zhang Q, Wang X-G, et al. An extremely simple method for protecting lithium anodes in Li-O₂ batteries. *Angew Chem Int Ed.* 2018;57(39):12814-12818.
681. Pang Q, Liang X, Shyamsunder A, Nazar LF. An in vivo formed solid electrolyte surface layer enables stable plating of Li metal. *Joule.* 2017;1(4):870-886.
682. Hu J, Tian J, Li C. Nanostructured carbon nitride polymer-reinforced electrolyte to enable dendrite-suppressed lithium metal batteries. *ACS Appl Mater Interfaces.* 2017;9(13):11615-11625.
683. Chen L, Connell JG, Nie A, et al. Lithium metal protected by atomic layer deposition metal oxide for high performance anodes. *J Mater Chem A.* 2017;5(24):12297-12309.
684. Chu F, Hu J, Wu C, et al. Metal-organic frameworks as electrolyte additives to enable ultrastable plating/stripping of Li anode with dendrite inhibition. *ACS Appl Mater Interfaces.* 2019;11(4):3869-3879.
685. Wang Z, Tan R, Wang H, et al. A metal-organic-framework-based electrolyte with nanowetted interfaces for high-energy-density solid-state lithium battery. *Adv Mater.* 2018;30(2):1704436.
686. Wu J-F, Guo X. MOF-derived nanoporous multifunctional fillers enhancing the performances of polymer electrolytes for solid-state lithium batteries. *J Mater Chem A.* 2019;7(6):2653-2659.
687. Wang Z, Wang S, Wang A, et al. Covalently linked metal-organic framework (MOF)-polymer all-solid-state electrolyte membranes for room temperature high performance lithium batteries. *J Mater Chem A.* 2018;6(35):17227-17234.

AUTHOR BIOGRAPHIES



Sang A. Han received her PhD degree (2016) at SKKU Advanced Institute of Nanotechnology (SAINT), Sungkyunkwan University (SKKU), Republic of Korea. Her research interests are synthesis and characterizations of nanomaterials and their energy storage applications. Now she is a Postdoctoral Fellow at University of Wollongong (UOW), Australia.



Jong-Won Lee is an Associate Professor at Daegu Gyeongbuk Institute of Science and Technology (DGIST). He received his PhD (2005) in Materials Science from KAIST, and then he worked as a Research Assistant Professor at the University of South Carolina. He was a Research Scientist at Samsung Advanced Institute of Technology and Korea Institute of Energy Research and an Assistant Professor at Chosun University before joining DGIST in 2020. His current research is focused on functional materials for next-generation energy storage systems.



Min-Sik Park is currently Associate Professor at Advanced Materials Engineering for Information and Electronics, Kyung Hee University, Republic of Korea. After his PhD at University of Wollongong, Australia (2008), he was a research scientist at Samsung Advanced Institute of Technology (SAIT) and Korea Electronics Technology Institute (KETI). His current research focuses on advanced materials for energy storage systems such as lithium-ion batteries and post-lithium systems for future energy solutions.



Jung Ho Kim is currently tenured Professor at the Institute for Superconducting and Electronic Materials (ISEM), Australian Institute for Innovative Materials (AIIM), University of Wollongong, Australia. He received his Bachelor's (1998), Master's (2000), and PhD (2005) degrees from Sungkyunkwan University, Korea. His major research is the rational design of materials for energy storage and harvesting applications.

How to cite this article: Han SA, Qutaish H, Lee J-W, Park M-S, Kim JH. Metal-organic framework derived porous structures towards lithium rechargeable batteries. *EcoMat.* 2023;5(2):e12283. doi:10.1002/eom2.12283